Stony Brook University

Synthesis and Structural Characterization of Carboxylate-Based Metal-Organic Frameworks and Coordination Networks

A Dissertation Presented

by

Paul Calderone

to

The Graduate School

in Partial Fulfillment of the

Requirements

for the Degree of

Doctor of Philosophy

in

Chemistry

Stony Brook University

August 2012

Stony Brook University

The Graduate School

Paul Calderone

We, the dissertation committee for the above candidate for the

Doctor of Philosophy degree, hereby recommend

acceptance of this dissertation.

John B. Parise, Ph. D., Advisor
Distinguished Professor, Departments of Chemistry and Geosciences, Stony Brook University

Benjamin S. Hsiao, Ph. D., Chairperson
Professor, Department of Chemistry
Vice President for Research, Stony Brook University

Staislaus S. Wong, Ph. D., Third Member
Professor, Department of Chemistry, Stony Brook University

Ivor Bull, Ph.D., Outside Member
BASF Corporation, Inorganic Materials

This dissertation is accepted by the Graduate School

Charles Taber
Interim Dean of the Graduate School

Abstract of the Dissertation

Synthesis and Structural Characterization of Carboxylate-Based Metal-Organic Frameworks and Coordination Networks

by

Paul Calderone

Doctor of Philosophy

in

Chemistry

Stony Brook University

2012

Coordination networks (CNs) and metal-organic frameworks (MOFs) are crystalline materials composed of metal ions linked by multifunctional organic ligands. From these connections, infinite arrays of one-, two-, or three-dimensional networks can be formed. Exploratory synthesis and research of novel CNs and MOFs is of current interest because of their many possible industrial applications including gas storage, catalysis, magnetism, and luminescence.

A variety of metal centers and organic ligands can be used to synthesize MOFs and CNs under a range of reaction conditions, leading to extraordinary structural diversity. The characteristics of the metals and linkers, such as properties and coordination preferences, play the biggest role in determining the structure and properties of the resulting network. Thus, the choice of metal and linker is dictated by the desired traits of the target network. The pervasive use of transition metal centers in MOF synthesis stems from their well-known coordination behavior with carboxylate-based linkers, thus facilitating design strategies. Conversely, CNs and

MOFs based on *s*-block and lanthanide metals are less studied because each group presents unique challenges to structure prediction. Lanthanide metals have variable coordination spheres capable of accommodating up to twelve atoms, while the bonding in *s*-block metals takes on a mainly ionic character. In spite of these obstacles, lanthanide and *s*-block CNs are worthwhile synthetic targets because of their unique properties. Interesting photoluminescent and sensing materials can be developed using lanthanide metals, whereas low atomic weight *s*-block metals may afford an advantage in gravimetric advantages for gas storage applications.

The aim of this research was to expand the current understanding of carboxylate-based CN and MOF synthesis by varying the metals, solvents, and temperatures used. To this end, magnesium-based CNs were examined using a variety of aromatic carboxylate linkers, solvents, and temperatures. Since the coordination chemistry of Zn^{2+} is similar to that of Mg^{2+}, a zinc metal center is a reasonable proxy for magnesium CN design. Solvent and temperature proved to be the key factors in the synthesis as the topologies that formed depended on the amount of solvent incorporation and the temperature of the synthesis. Exploratory synthesis of magnesium CNs if often conducted with gas storage applications in mind, but the photoluminescence (PL) properties are rarely investigated because Mg^{2+} is a closed shell metal ion. However, since CN linkers can also contribute to the PL emission of the network, an appropriate choice in linker can lead to the development of a lightweight PL or sensing material. Fluorescence studies on the magnesium CNs illustrate that the PL activity of is not only dependent on the properties and makeup of the linker, but the overall structure and solvent effects as well.

Carboxylate-based MOFs were further investigated with the use of lanthanide metal centers. The variable coordination spheres of lanthanide metals leads to a wide range structural topologies not possible with more common metal centers. Additionally, the network linkers used

can also double as antenna ligands that further sensitize the metal centers and produce interesting photoluminescence (PL) properties. The photoactive ligand 2,5-thiophenedicarboxylate was used in this work to link four lanthanide MOFs using the metals Dy, Er, Nd, and Tb. Fluorescence studies show that the thiophene linker is a very good antenna ligand, as the Dy and Tb frameworks exhibit their characteristic lanthanide emissions.

Finally, a series of transition metal formate MOFs were explored using ionothermal synthesis, a synthetic method that employs an ionic liquid solvent containing an anion and cation to template the desired network. This method proved to be another synthetic route to producing transition metal MOFs with magnetic properties. Anionic formate networks resulting from the ionthermal syntheses possess topologies dictated by the cationic species of the ionic liquid, which is incorporated to provide charge balance. Magnetic studies revealed that these transition metal formate MOFs behave similarly to related formate compounds in that they order as canted antiferromagnets.

Table of Contents

List of Abbreviations

AC	Alternating Current magnetic field
BTC	Trimesate (1,3,5-benzenetricarboxylate)
CCD	Charge-coupled device
CN	Coordination Network
DC	Direct Current magnetic field
DMA	Dimethylamine
DMF	N,N-dimethylformamide
EtOH	Ethanol
IL	Ionic liquid
IPA	Isophthalate (1,3-benzenedicarboxylate)
Ln	Lanthanide
MOF	Metal-Organic Framework
NDC	1,4-napthalenedicarboxylate
PL	Photoluminescence
SDB	Sulfonyldibenzoate
TGA	Thermogravimetric analysis
TDC	2,5-thiophenedicarboxylate
UV-Vis	Ultraviolet-Visible
XRD	X-ray diffraction

List of Structures

List of Figures

List of Tables

List of Publications

Calderone, P. J.; Forster, P. M.; Borkowski, L. A.; Teat, S. J.; Feygenson, M.; Aronson, M. C.; Parise, J. B. *Inorg. Chem.* **2011**, *50*, 2159.

Calderone, P. J.; Banerjee, D.; Borkowski, L. A.; Parise, J. B. *Inorg. Chem. Commun.* **2011**, *14*, 741.

Calderone, P. J.; Banerjee, D.; Santulli, A. C.; Wong, S. S.; Parise, J. B. *Inorg. Chim. Acta* **2011**, *378*, 109.

Calderone, P. J.; Banerjee, D.; Nizami, Q.; LaDuca, R. L.; Parise, J. B. *Polyhedron* **2012**, *37*, 42.

Calderone, P. J.; Banerjee, D.; Plonka, Anna M.; Kim, S. J.; Parise, J. B. *Inorg. Chim. Acta*. **Submitted**

Calderone, P. J.; Plonka, Anna M.; Banerjee, D.; Nizami, Quddus A.; Parise, J. B. *Solid State Sci*. **Submitted**.

.

Acknowledgements

This dissertation is the culmination of five years of work that would not have been possible without the support and assistance of a number of important individuals and organizations. My most sincere gratitude goes to my advisor, Prof. John Parise, for his patience, encouragement, and guidance throughout my graduate career. The challenge of participating in his research group has given me confidence and skills that will be invaluable to my future in science. I would also like to thank my Stony Brook University Chemistry committee members, Prof. Benjamin Hsiao and Prof. Stanislaus Wong, for their help and support. I am also thankful for the participation and contribution of time by Dr. Ivor Bull as the external member of my dissertation committee.

Many thanks also go to Prof. Paul Forster (UNLV Chemistry), a former Post-Doctoral Researcher who helped me get my start in the Parise group and worked with me to learn a number of techniques and strategies. Much of the work reported in this dissertation would not have been possible without my collaboration with many people, including Dr. Alex Santulli, Dr. Mikhail Feygenson, Dr. Meigan Aronson (Brookhaven National Lab and Stony Brook University Physics), Dr. Yu-Sheng Chen (Advanced Photon Source, Argonne National Laboratory), and Dr. Simon Teat (Advanced Light Source, Lawrence Berkeley National Laboratory).

One of the biggest reasons for my success is the rapport and camaraderie I've shared with past and present Parise Group members: Lauren Borkowski, Richard Harrington, Wenqian Xu, William Woerner, Lena Lazareva, Xianyin Chen, Quddus Nizami, Anna Plonka, and Debasis Banerjee. I'm very lucky to have had the opportunity to work with such talented scientists. I am

especially grateful for my many collaborative efforts with Quddus Nizami, Anna Plonka, and Debasis Banerjee.

This work would not have been possible without funding from the Division of Materials Research of the National Science Foundation (DMR-0800415).

Finally, I would like to thank my friends, family, and future family for their support, especially my parents, whose constant encouragement throughout my life has helped me to get where I am. To my fiancée Colleen: You have played the biggest part in my success these past two years through your ability to be a calming influence during an otherwise very stressful time. I know that whatever I'll face in my future, I'll have you to help me though.

Chapter 1

Overview of Metal-Organic Frameworks and Coordination Networks

Within the short time frame of a few decades, research focusing on the synthesis, characterization, and properties of metal-organic frameworks (MOFs) and coordination networks (CNs) has blossomed into a very important area of synthetic chemistry.[1-2] MOFs and CNs, subsets of hybrid inorganic-organic materials, are constructed by linking metal centers with multifunctional organic ligands into extended arrays or networks.[3-4] Exploitation of industrially relevant properties such as gas storage,[5-9] magnetism,[10-14] and photoluminescence[15-16] is the driving force behind much of the exploration for new network materials. Nomenclature use is often up to the preference of the researcher, but in general, "CN" is used to describe main group metal networks while "MOF" refers to other metal networks (e.g. lanthanides, transitions). Both terms will be used in this dissertation.

The discovery of novel and functional MOFs and CNs proceeds along several interrelated lines of research. A wide range of metals, linkers, and synthetic conditions can be employed to construct networks, and the seemingly infinite number of possible combinations makes systematic searches a challenge. However, this same variety also holds the prospect of directing MOFs and CNs toward desired structure types, topologies, and properties. One-dimensional chains, two-dimensional layers, or three-dimensional frameworks can be formed depending on the behavior of the solvent, geometry of the linker, and the coordination preferences of the metal.

A brief review of the rationale and tactics adopted for exploratory synthesis is presented in the remainder of this introduction. Specifically emphasized is the close relation of the structure and functions of MOFs and CNs to the properties of their component parts and

synthetic designs. For instance, the combination of a linker with a transition metal often leads to a network with magnetic properties. Likewise, lanthanide metals or photoactive linkers are desired for potential photoluminescent networks and sensing materials. Also discussed is the role of synthetic conditions, such as solvent and temperature, play in network formation. Metal-coordinated solvent molecules may control the assembly of the structure and temperature changes can lead to variations in connectivity.

Yaghi et al stimulated the search for non-cyano based[17] MOFs with the well-known report of the porosity of MOF-5.[18] In that compound, terephthalate linkers form a cage-like structure based on tetrahedral Zn_4 carboxylate clusters. A large surface area measurement of 2900 m^2/g implied a high potential for other functional hybrid networks. Structural analogs of MOF-5 were subsequently produced with a change of metal center or organic linker. An example is IRMOF-3,[19] (IR=isoreticular) in which terephthalte was substituted out for the amino-functionalized 2-aminoterephthalate (Fig. 1.1). This concept of "Reticular Chemistry"[20] grew out of the synthesis of MOF-5 and led to a series of related Zn_4-based structures with various dicarboxylate ligands. Throughout the series, the basic cubic network seen in MOF-5 is maintained, but the length and sterics of the linker used dictated the size of the cage. Notably, each successive change in component brought about a corresponding change in physical or chemical properties. These discoveries allowed for the rational design of MOFs and CNs and the possibility for networks to be devised with specific structures and uses in mind.

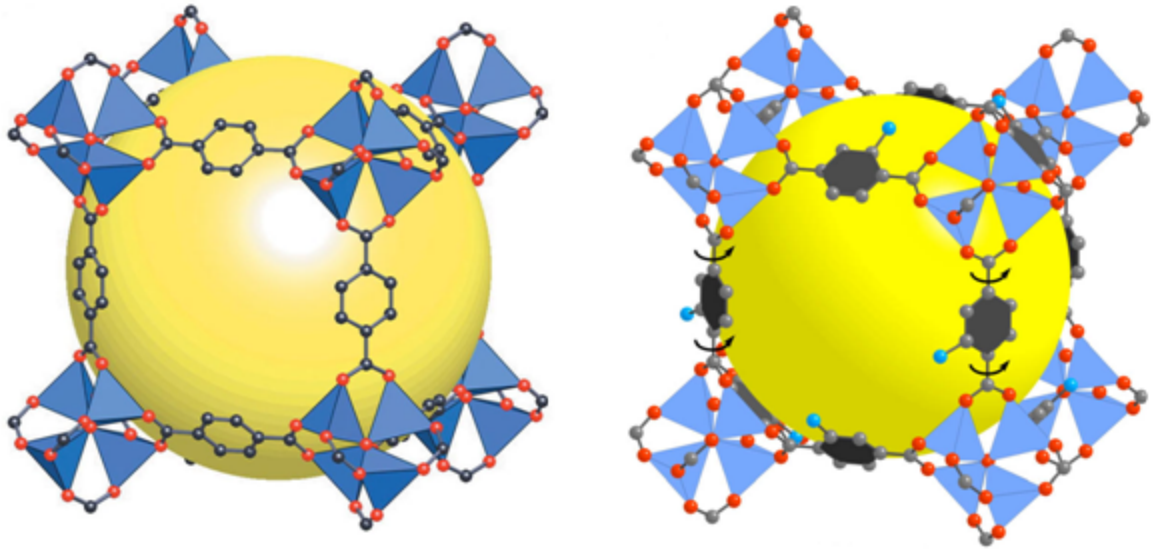

Figure 1.1. Comparison of MOF-5[18] (left) constructed using terephthalate linkers and its reticular analog of IRMOF-3[19] (right) formed with 2-aminoterephthalate linkers. The yellow spheres represent the pore sizes of the respective structures.

Aromatic polycarboxylate ligands, such as the terephthalate linkers found in MOF-5, are commonly used linkers in the construction of MOFs and CNs. The rigidity of the ligand as well as the strong bonding interactions between carboxylate oxygen atoms and most metal ions offer a high degree of structural stability. Transition metals are the most common CN metal centers paired with carboxylates in literature. This familiarity affords a high degree of synthetic predictability for the transition metal-carboxylate bonding interaction and allows various types of carboxylate linkers to be chosen to fit the needs of the structure. Magnetic MOFs are an example of this targeted synthesis with transition metals. Linkers can be selected based on their efficiency in transferring charge between metal centers.[10,21] Simple carboxylate ligands such as formate could be a better option in order to utilize the stability of the transition metal-oxygen interaction and take advantage of a short ligand bridge. Several varieties of magnetic transition metal formate CNs have been described. Gao et al first reported the synthesis and magnetic properties for a series of perovskite-related transition metal formates.[22] The three-dimensional

anionic cage is charge balanced by a disordered hydrogen-bound dimethylammonium cation and exhibits weak antiferromagnetism. Gao followed with a related antiferromagnetic formate CNs in which N,N′-dimethylethylenediammonium serves as the charge balancing counter ion.[23] Wang et al contributed two additional varieties of magnetic formate CNs. One series reports antiferromagnetic networks charge balanced by an ammonium cation[24] while the related series behaved as a permanently porous neutral network.[25]

Despite the disadvantage in predictability, there has been a recent increase in research targeting polycarboxylate networks that are based on lanthanide and *s*-block metal centers in order to expand the area and access properties not available from transition metal MOFs. In lanthanide MOFs, the appropriate linker could function as an effective antenna ligand and sensitize the metal ion to create a useful photoluminescent material.[16] Likewise, a porous CN based on an *s*-block metal center with a low atomic weight could maximize gravimetric storage capacity and be used as a potential gas storage material. Challenges to the strategy of using less studied metal centers can arise because of the distinct differences in preferred coordination spheres and electonegativity.[26] This makes structure prediction for lanthanide and *s*-block networks much more complex compared to transition metals. In the case of lanthanide metal ions, coordination spheres can be variable due to the lanthanide contraction effect, in which ionic radius decreases across the series. The valence electron configuration of *s*-block metals causes their bonding to take on a more ionic character when coordinating. As a result, the orientation of the linker in lanthanide and *s*-block CNs plays a much more profound role in the metal-linker interaction than coordination preference.

Photoluminescence is a key property available from lanthanide-based MOFs and should a network be microporous, it has the possibility for many uses including light-emitting

applications and selective sensing.[15-16,27] Generally, lanthinde ions are poor absorbers of light and are often paired with organic antenna ligands in order to boost the efficiency of metal sensitization. Provided the triplet energy level of the ligand is at or above the level of the lanthanide metal, absorbed energy will be transferred and the photoluminescence of the metal will be enhanced. The advantage of MOFs based on Ln metals is the ability to utilize the organic linkers as antenna ligands (Fig 1.2). A notable example comes from Serre et al who used trimesate to facilitate ligand-to-metal charge transfer in MIL-78, a mixed Y/Eu network.[28] Doping other metals such as Dy and Tb into the material produced noticeable optical changes.

Heterocyclic aromatic rings are also common ligands in photoactive materials because the higher localization of electrons can lead to significant PL responses. The heterocyclic 2,4,6-pyridinetricarboxylate linker was used by Wang et al who constructed and tested a series of Ln MOFs, noting that Er and Yb displayed additional emissions in the UV region.[29] Oftentimes it is beneficial to use a linker whose free acid state is known to be emissive as in the case of 2,5 thiophenedicarboxylate (TDC).[30-32] The H_2TDC form is photoactive due to the large localization of the S atom, and the "V" shape of the ligand offers a variety of coordination modes to build topologies. Pore-occupying guests can also play the role of sensitizers as de Lill reported in lanthanide MOFs of Tb and a Eu/Tb mixture.[33] In this case the network used a guest molecule of 4,4´-dipyridyl to sensitize the metal. While a characteristic Tb emission was observed in the Tb only network, curiously, the Tb emission Eu/Tb mixed metal network was quenched, and the transferred energy enhanced the Eu emission.

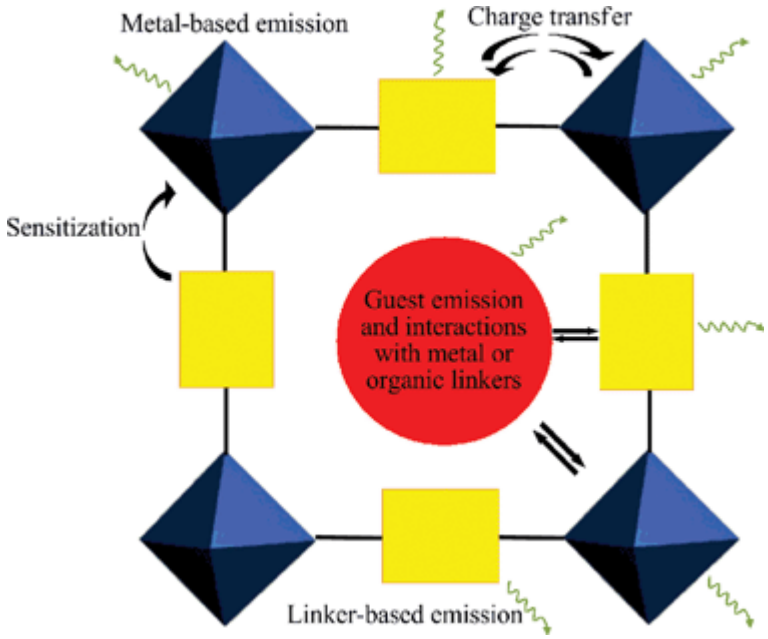

Figure 1.2. Schematic of different sensitizations and emissions that are possible in luminescent metal-organic frameworks and coordination networks.[15]

As mentioned earlier, *s*-block metals present challenges in the design and discovery of microporous CNs. Banerjee et al reported multiple lightweight lithium CNs and significantly expanded the field, but the preferred tetrahedral coordination of Li often led to the formation of dense networks.[34-36] Magnesium, however, is comparable to other more frequently used metal centers, such as zinc. Mg^{2+} and Zn^{2+} are similar in ionic radii,[37] affinity for carboxylate ligands, and octahedral coordination, making zinc an appealing proxy in targeting new magnesium networks. Porous magnesium CNs are especially sought after because of the implications for gas storage materials. Mg is a lightweight metal center and can theoretically store more gas per unit weight of material than a similar structure constructed with a heavier transition metal. Long et al introduced the first microporous CN based on Mg using 2,6-naphthalenedicarboxylate as the organic linker.[38] While a BET surface area of only 190 m^2/g was reported for the desolvated compound, the magnesium network was a structural analog to Zn network reported in the same

work. This demonstrated the ability of Mg to substitute for Zn in CNs. Dietzel and co-workers took this idea further, and synthesized a porous magnesium CN, $Mg_2(dhtp)(H_2O)]\cdot 8H_2O$ (Mg/DOBDC), based on 2,5-dihydroxoterephthalate.[39] Upon removal of guest water molecules, the structure was found to retain porosity. The same compound, later studied by Caskey, was found to have a Langmuir surface area of 1905 m2/g and a CO_2 uptake of 35.2 weight percent at 1 atm of pressure (Fig 3).[40]

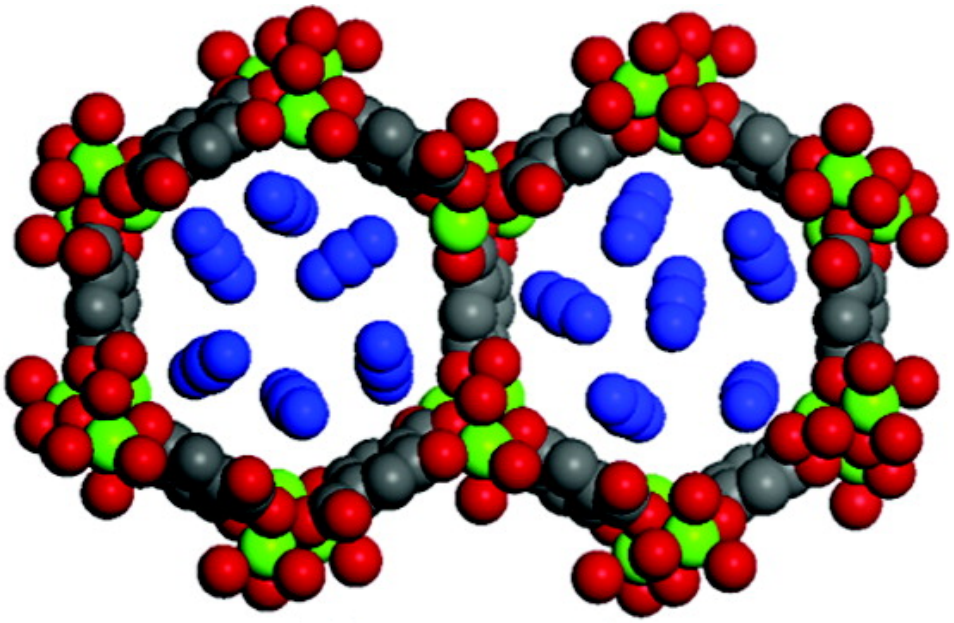

Figure 1.3. Space filling figure showing the pores of Mg/DOBDC occupied by CO_2 molecules (blue).[40]

While much of the exploration for new magnesium CNs is propelled by potential gas storage applications, the photoluminescence properties of these materials are virtually ignored in the literature. Main group metal CNs in general share this fate, with the exceptions being reports of a few bismuth[41], lead[42-43] and indium[44] CNs. One reason for the lack of reports for magnesium is that it a closed shell metal, and will contribute little—if at all—to the photoactivity of its networks. Yet other work has shown that the network linker can play a considerable role in

generating PL properties. Specifically, linkers that have a high degree of conjugation or contain aromatic rings can provide interesting results when subjected to fluorescence measurements, and networks based on Zn and Cd have shown ligand-based photoluminescence. Bauer et al reported two zinc CNs based on *trans*-stilbenedicarboxylate and showed that incorporation of the linker into the network increased linker emission over the free stilbenedicarboxylic acid. Likewise, trimesate linkers in a Cd-based CN were found by Fan et al to have a blue emission when used to link the network.[45] The same linker-based emission in magnesium CNs could lead to a lightweight sensing material.

Zhang and coworkers were the first to examine the photoluminescence properties of a magnesium CN based on the aromatic 1,2,4,5-benzenetetracarboxylate.[46] The work suggested the possibility of ligand-to-metal charge transfer and the fluorescence was likely due to the interaction of ring systems and π stacking. Later, Jayaramulu et al. reported the permanently porous network Mg(DHT)(DMF)2 (DHT = 2,5-dihydroxyterephthalate).[47] The ligand-based multicolor emission could be tuned by guest solvent molecules within the pores of the network. Apart from other work that will be highlighted in later chapters of this dissertation, [48-49] there are no other reports of PL magnesium CNs.

As previously alluded to, topology in a MOF or CN is highly dependent on the coordination preference of the metal center and the geometry of the ligand. Other synthetic parameters affecting topology include the choice of solvent and temperature, which may have drastic effects on the final product. For example, solvent molecules may become part of the network through metal coordination or guest inclusion,[50] thereby influencing the network by hindering extra-dimensional connection. Solvent breakdown and subsequent incorporation of the byproducts into the network often leads to unanticipated chemistries. For example, the

perovskite-related series of transition metal formates reported by Guo[22] is synthesized through the breakdown of solvent DMF and incorporation of the resulting formate anion and dimethyammonium cation. Banerjee et al. varied synthetic solvent in a series of magnesium 3,5-pyridinedicarboxylate networks, finding that coordination of solvent molecules to the metal centers dictated the topologies of the structure.[51] Temperature is also a key determinant of network dimensionality. Forster et al. noted that for a series of cobalt succinate networks, an increase in temperature led to increased metal-oxygen connectivity and a decrease in incorporated solvent (Fig. 1.4).[52] Similarly, Gurunatha and coworkers,[53] noted an increase in temperature leads to an increase in network connectivity.

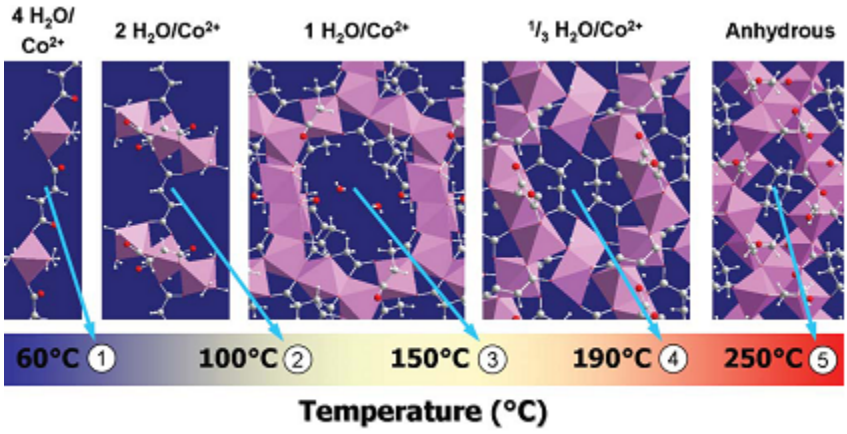

Figure 1.4. The work of Forster et al. on a series of cobalt succinates demonstrated the effect of increasing temperature on network connectivity, dimensionality, and solvent inclusion.[52]

Solvothermal and hydrothermal synthesis are indeed tried and true methods for producing MOFs and CNs, with nearly all reports citing some form of the hydro-/solvothermal technique as an experimental method. In contrast, ionothermal synthesis has recently been recognized as a potential MOF synthetic technique.[54] Where hydrothermal or solvothermal syntheses rely on solvents such as water or DMF, the ionothermal method employs an ionic liquid (IL) to act as

both the solvent and structural template (Fig. 1.5). This implies an increased measure of control and design since the solvent being used can also be a preferred structural component. Thus, ionothermal synthesis can largely eliminate undesirable solvent effects such as guest incorporation and breakdown. Additionally, the need for autoclave vessels for reactions can be eliminated due to reactions taking place at more ambient temperatures. Since ILs are essentially salts in liquid form at or near room temperature, they have high reactivity and do not necessarily require additional thermal activation energy. Jin et al reported the first successful use of an IL to produce a MOF. The use of the 1-butyl-3-methylimidazolium cation led to its incorporation into the $Cu(bpp)BF_4$ [bpp = 1,3-bis(4-pyridyl)propane] network.[55]

Morris reported the first use of a now very common IL, 1-ethyl, 3-methylimidazolium (EMI) bromide, in the synthesis of a series of aluminophosphate networks.[56] The relatively low synthetic temperature was touted as a safer alternative to the high pressures and temperatures of hydrothermal autoclave synthesis. The vast majority of ionic liquids used in ionothermal synthesis are commercially available and contain a bulky cation like EMI and a halide anion such as bromide. The synthesis of the trimesate network, [EMI][Cd(BTC)], by Laio and coworkers used the EMI^+Br^- ionic liquid to template the structure.[57] Ionothermal synthesis can also provide access to structures not accessible by conventional routes. The work of Hulvey et al yielded two perflorinated nickel succinates using EMI that were unable to be produced using hydrothermal synthesis.[58]

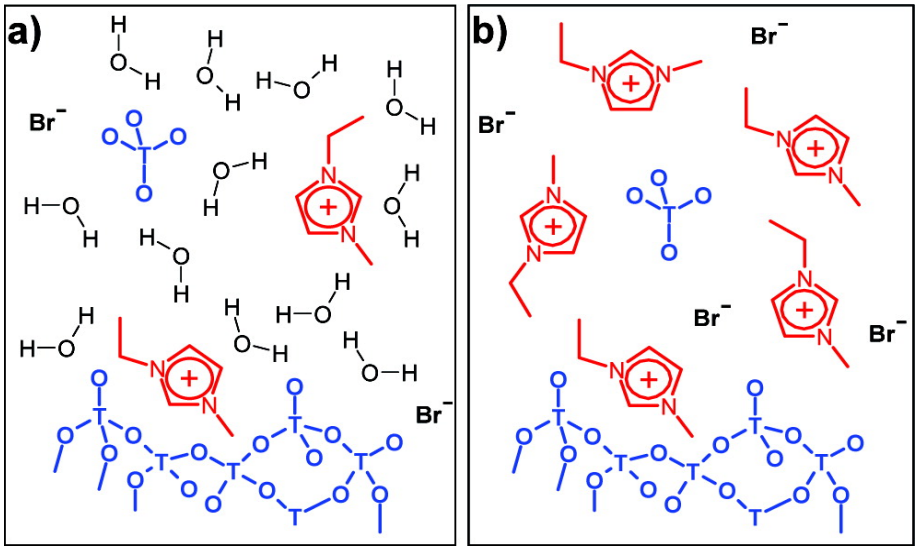

Figure 1.5. Representation of differences between the hydro-/solvothermal method (a), in which a solvent is required in reaction (H_2O), and the ionothermal method (b), in which the ionic liquid serves as the solvent and contains the framework components.[54]

Control over IL components is key to ionothermal synthesis, as both cations and anions may assist in structure direction. Two important examples of this influence come from Lin et al. who explored the effects of the anionic species. In a report of the $(BMIm)_2[Ni(TMA\text{-}H)_2(H_2O)_2]$ network, the use of the chiral anion L-aspertate in the ionic liquid induces chirality in the structure.[59] While the aspertate ion does not coordinate in the structure, it does guide the production of a "single-handed" network. In another case, the use of three different counter ions of EMI leads to a series of three Co MOFs with different structures and polarity/hydrophobicity.[60] This control offers a unique opportunity to exploit a tailor-made ionic liquid for synthetic use.

Hydrogen bonding also affects the structure as demonstrated in another report by Lin, in which hydrogen bonding from ammonium species in a cobalt imidizolate framework help bridge the structure into a three-dimensional network (Fig. 1.6).[61] The EMI^+ cations of the ionic liquid sit within the final structure. In later chapters of this dissertation, this control and hydrogen

bonding effects will be explored further as it relates to the synthesis of magnetic CNs. The magnetic transition metal formates previously mentioned by Gao and Wong rely on the formate anion and the charge balancing organic cation. The possibility of controlling and incorporating both species into the structure through the use of an ionic liquid is an important concept in design. This idea was the starting point for a formate-based ionic liquid series in which the cation is varied to produce a variety of structures.[62]

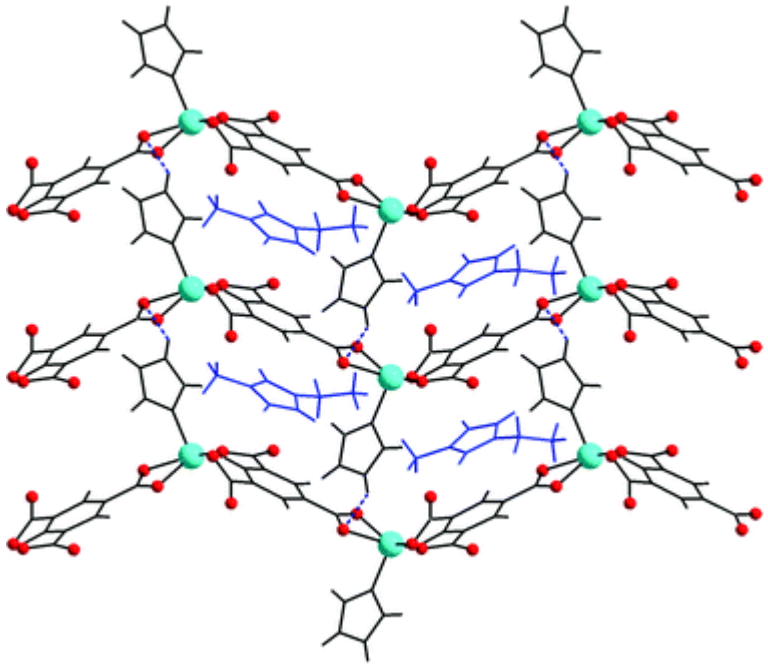

Figure 1.6. The cobalt imidizolate network synthesized by Lin et al. exhibits hydrogen-bonding effects from the imidizolate linkers to bridge the network.[61] EMI cations from the ionic liquid (blue) sit within the nework

In the work described in this dissertation, the synthesis and properties of three types of carboxylate-based networks are explored. Specifically highlighted is how the choice of metal center, linker, and synthetic conditions determine the structure and properties of the reported compounds. First, solvothermal synthesis of an assortment of magnesium carboxylate CNs and their photoluminescent properties are described. Photoluminescence properties are also reported for a series of of a series of lanthinde-based thiophenedicarboxylate MOFs. Next, the ionothermal synthesis and magnetic properties of a series of transition metal formate MOFs is

examined. Finally, the synthesis of a magnesium-lithium heterometallic network and novel potassium CNs are discussed, along with the implications for *s*-block metal chemistry. All structures of the reported compounds have been characterized using single crystal X-ray, and thermal properties were determined with thermogravimetric anaylsis and differential scanning calorimetry.

Chapter 2

Experimental Methods

2.1. Synthesis of Coordination Networks and Metal-Organic Frameworks

Hydrothermal and solvothermal techniques are normally used in the synthesis of metal-organic frameworks (MOFs) and coordination networks (CNs).[26,63-64] The distinction between hydrothermal and solvothermal synthesis is simply whether water or another organic solvent, such as DMF or ethanol, is being used. In a typical procedure, a metal salt, organic linker, and solvent are sealed inside a Teflon-lined stainless steel Parr Autoclave (Fig. 2.1) that is rated for temperatures of up to 250° C and pressures of ~ 150 bars. The autoclaves must be sealed tightly and able contain the autogenous pressure created during the reaction since the crystallization of desired products often require temperatures above the boiling point of the solvents. Crystals are recovered upon cooling the assembly to room temperature. It is often advantageous to stir the reactants to the point of dissolution before heating to reduce the likelihood of recrystalized reactants. Thus, a general knowledge of the solubility of the metal salts and organic ligand in the solvent of choice is required. Often, metal nitrates or other highly soluble metal salts provide the source of the metal ions in solution.

Figure 2.1. The Teflon liner (left) and Parr autoclave (right) in which the liner is sealed.

Varying the reaction temperature and solvent can be used to synthesize a number of different topologies for a given combination of metal ion and ligand. In hydrothermal and solvothermal syntheses, the normal temperature range used is 100° C to 180° C, with the general trend being an increase in network dimensionality with each increase in temperature.[52] On the other hand, solvent effects depend on factors such as solvent dielectric constant and molar ratio of solvent to reactants. Solvents are frequently found to play active roles in the assembly of the structure through metal coordination or inclusion as a guest molecule.[51] As an example, all magnesium-based CNs reported in this work that are synthesized with DMF share the common trait of metal-coordinated DMF molecules. Metal-coordinated solvent molecules also stabilize the structure of the CN and attempts to remove them through thermal activation often result in the collapse of the network.

The work detailed in this dissertation used solvothermal syntheses and in the procedures reported, the temperature does not exceed 180° C. Solutions were stirred in a Teflon liner until homogeneity of the solution was achieved. Both polar protic (H_2O, ethanol) and polar aprotic

(DMF) solvents were used in the synthesis. The liners were sealed in Parr autoclaves for a period of up to five days and after cooling, crystals were recovered and washed with DMF and ethanol.

Ionothermal synthesis can also be used as an alternative synthetic route when product crystallization occurs below 100° C.[56] In this method, an ionic liquid replaces the use of conventional solvents and serves as both solvent and structural template, affording a high degree of flexibility in design.[58-59,65] The main advantage to the ionothermal method is the low reaction temperature. As ionic liquids have negligible vapor pressures, ionothermal reactions can take place in capped glass vials rather than sealed autoclaves. Additionally, since the ionic liquid contains no molecular solvents, only cations and anions, its use eliminates many undesired solvent effects.[66] This allows for additional measures of control in the synthesis of the targeted network.

For ionothermal synthesis, the ionic liquid must first be synthesized through a reaction of an organic acid and organic base. In the case of the transition metal formates reported herein, ionic liquids were produced in glass vials with the reaction of formic acid and a number of amines (Fig. 2.2). Varying the amine led to a number of formate-based ionic liquids which were then used for synthesis of formate MOFs. The metal salt was added to the ionic liquid, and the vial was capped and heated to the desired temperature. Resulting crystals were filtered and washed with methanol.

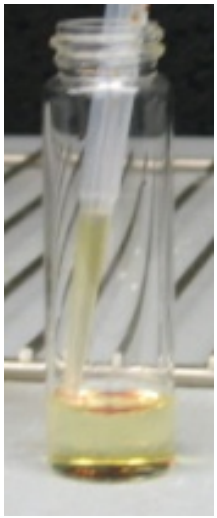

Figure 2.2. Typical ionic liquid used for the ionothermal synthesis reported in this work.

2.2. Powder X-ray Diffraction

A crystalline sample contains a large number of microcrystalline particles in random orientation. When the orientation satisfies Bragg's law, $\lambda = 2d\sin\theta$, the diffraction condition is met. Powder x-ray diffraction (XRD) data is collected as a two-dimensional diffractrogram where the intensity of diffraction (I) is plotted against the scattering angle 2θ.

In this work, powder XRD was used to confirm crystallinity and phase purity for the reported compounds. Data were collected with Cu Kα (λ = 1.5405 Å) radiation using either a Scintag PAD-X or a Rigaku® Ultima-IV diffractometer. The standard collection parameters were $5° \leq 2\theta \leq 40°$, a counting time of 1s/step, and a stepsize of 0.02 degrees θ. The powder diffractometers use Bragg-Brentano parfocusing geometry, where the incident beam and take-off geometry are fixed at θ/θ configuration. X-rays were generated at 40KV and 25 mA for the Scintag and 40KV and 44mA for the Rigaku Ultima diffractometer. Compunds were considered

phase pure if the powder diffraction patterns that were experimentally obtained were a match for the simulated powder diffraction patterns based on single-crystal data.

2.3. Single Crystal X-ray Diffraction

Due to the complex structural topologies of MOFs and CNs, powder XRD is generally not able to provide data of good resolution and accuracy for detailed structural information. Thus, single crystal XRD is a crucial tool in structural characterization. Good quality, single crystals are essential for the straightforward determination of MOF and CN structures.

Two laboratory single crystal instruments were used for data collection in this work, both of which use a Mo X-ray tube (λ = 0.71073 Å). A Bruker four circle P4 diffractometer equipped with a smart 1K CCD area detector was used to collect data at room temperature. X-rays were generated at 50 KV and 30 mA. The raw intensity data were collected using SMART software.[67] The data were further integrated and corrected for Lorentz and Polarization effects using SAINT.[68] Single crystal data at both room and low temperature (<150 K) were collected using a four-circle kappa Oxford Gemini diffractometer equipped with an Atlas detector. X-rays were generated at 50 KV and 40 mA. The raw intensity data were collected and integrated using CrysAlis PRO software.[69] Absorption corrections for data collected using either instrument were applied using SADABS.[70] Structure solution and least-squares refinements were carried out using direct methods and SHELXTL.[70] Heavy atoms were located first and other atom positions (C, N, O) were determined from the Fourier difference map, with all non-hydrogen atoms being refined anisotropically. Hydrogen atoms were placed in their theoretical positions using geometrical constraints.

It is sometimes difficult to obtain the desired materials in the form of large, good quality single crystals under applied synthetic conditions. If the as-synthesized materials are microcrystalline in nature (10-100μm in dimension), it is not possible to characterize the structure using a laboratory diffractometer. In these particular cases, X-ray diffraction setups at different synchrotron light sources are used for structure determination purposes. The increased brightness, tunability and low divergence of X-ray beams at a synchrotron source can provide good quality data for crystals as small as ~ 5μm. Synchrotron radiation is ten orders of magnitude brighter than standard laboratory instrument and has a spectral distribution of energy in the range of 5-40Kev.

Single crystal data were collected at the 15-ID ChemMatCARS beamline, Advanced Photon Source, Argonne National Laboratory. The beamline is equipped with a Bruker D8 diffractometer with a Bruker APEXII detector. Monochromatic X-ray radiation is achieved using a diamond (111) crystal (λ =0.41328 Å). Data collection was performed at 100K using a N2 cryostat. Single crystal data were also collected at the 11.3.1 beamline at Advanced Light Source, Lawrence Berkeley National Laboratory using a similar experimental setup but a different X-ray wavelength (λ =0.7749 Å). In both cases, data were integrated using APEXII suite of software[71] and processed using SHELXTL[70] in the same manner as the laboratory-collected data.

2.4. Thermogravimetric Analysis/Differential Scanning Calorimetry

Thermogravimetric analysis (TGA) and differential scanning calorimetry provide valuable information about the thermal stability of the synthesized compound, a property crucial for many advanced applications. The shape of the TGA curve provides information about the

network interactions and losses of guest or coordinated solvent molecules and can also be used to confirm the purity of the material by matching theoretical component losses with observed weight losses. TGA curves are also useful for determining a suitable temperature for activation, or removal of coordinated solvent used in porosity and surface area measurments. The thermal data of the synthesized materials described herein was collected using a Netzsch 449C Jupiter instrument. The instrument is equipped with a SiC furnace with a temperature range of RT to 1500°C and a microbalance with an accuracy of ± 0.01mg. In a typical experiment, a correction curve with an empty alumina crucible is collected first. Following this step, the as-synthesized sample (5-10 mg) was placed in an alumina crucible and heated between RT and 750°C under N_2 atmosphere at a rate of 10°C/min. The materials with either coordinated or free solvent molecules show multistep weight-losses. The first weight losses are due to the evacuation of the solvent molecules and normally lead to the breakdown of the network. The evacuation temperature depends on multiple factors, including the nature of the solvent and network topologies. The final weight-loss step corresponds to the pyrolysis of the organic linker.

2.5. Magnetic Property Measurements

Magnetism as described in this work is defined as the response of materials when subjected to an applied magnetic field. Common magnets are said to be ferromagnetic and have a permanent magnetic field under normal conditions, but in the presence of an applied magnetic field, most materials respond to some degree by entering a magnetic “phase”. In some cases, a material will be attracted to the magnetic field and are classified as paramagnetic, while materials which are repulsed from the field are classified as diamagnetic. The magnetic phase of a material can vary under conditions such as temperature and pressure meaning that a given

material can have multiple magnetic phases. Some materials, including those highlighted in this work, exhibit an antiferromagnetic response at low temperature. This behavior will be explained shortly.

The source of magnetism is the orbital angular motion and intrinsic magnetic moment of the electrons and in ordinary cases, the magnetic moments or "directionality" of the electrons in these materials will be cancelled out by electron pairing or pointing in random directions. For some materials in the presence of an applied magnetic field, the magnetic moments align and a magnetic field is produced.[72] Because electron configuration is an important factor in magnetic behavior, atoms or ions with unfilled electron shells are necessary to observe a response. Transition metal ions that have one or more unpaired *d* electrons normally have paramagnetic behavior, but the magnetic state depends on other factors such as charge, electron spin state, and metal-coordination geometry. The transiton-metal based compounds studied here, [7.1 – 7.5], are all have octahedral metal center coordination and are in the M^{2+} oxidation state (M=Co,Ni,Mn). When certain materials are sufficiently cooled, the thermal energy can be suppressed enough to allow a transition other magnetic phases. Antiferromagnetism is one such phase that normally occurs at cooling and is characterized by an electron alignment in which neighboring spins point in the opposite direction, resulting in zero net magnetic moment. Below the Néel temperature T_N, paramagnetic materials become antiferromagnetic.[73]

A Superconducting Quantum Interference Device (SQUID) is a sensitive magnetometer and is used to measure the magnetic fields that come from materials as a function of the applied magnetic field at varying temperatures.[74-75] Two types of SQUID measurements, DC and AC, are possible and discussed in this work. In DC measurements, current flows around a semiconductor loop and electrons that tunnel through Josephson junctions are able to interfere.

The magnetic field passing through the loop cause a phase difference between the electrons which affects the current through the loop. The potential differences between currents flowing through and around the loop are measured. For DC analysis, the temperature T and magnetic field H dependencies of the dc magnetizations $M(T,H)$ are measured. AC measurements, also known as RF (radio frequency) measurements, use a radio frequency oscillating current to measure the interactions between the superconducting ring and an external resonant circuit. Temperature dependencies of the real (in-phase) χ' and imaginary (out-of-phase) χ'' parts of the AC susceptibility $\chi(T)$ are determined. AC measurements are useful in the case of antiferromagnetic ordering since AC is more sensitive to changes in *M(H)*. Slope, rather than absolute value of *M(H)* is measured and this allows small magnetic shifts to be detected. Antiferromagnetic phase transitions are distinguished by a peak in the temperature derivative of the real part of the ac susceptibility χ' at T_N.

AC susceptibility and DC magnetization measurements of each sample presented were carried out using the Quantum Design Magnetic Property Measurement System (model XL-7). The powdered sample was contained in a standard gelatin capsule and was introduced into the magnetometer at room temperature. After subsequent cooling to 2 K in zero magnetic field, the magnetization was measured as a function of applied magnetic fields in the range -50 to 50 kOe at temperatures of 2, 30, 150 and 300 K, respectively. The temperature dependent dc magnetization was measured using standard zero–field cooled (ZFC) and field–cooled (FC) protocols in an applied field of 500 Oe in the temperature range 2 – 300 K. The temperature dependence of the ac susceptibility was measured in a 17 Hz ac field, with a root mean square amplitude of 4.17 Oe. The diamagnetic background of the gelatin capsule was measured to be $\sim 10^{-5}$ emu, and is only weakly temperature dependent. Since this amounts to no more than 5% of

the total measured sample+capsule magnetization in any sample at any temperature, we report here the entire sample + capsule magnetization. The values of the AC susceptibilities and DC magnetizations were normalized by the nominal masses of the moment bearing atoms (i.e. Co,Ni,Mn).

2.6. Photoluminescence Property Measurements

Photoluminescence (PL) occurs when a material absorbs photons from a source and then re-emits photons itself.[76] The process occurring in this transition is quantum mechanical in nature and involves the promotion of electrons to an excited or higher energy state and a corresponding relaxation to a lower energy state, which is accompanied by photon emission. The two basic types of photoluminescence are fluorescence and phosphorescence. Fluorescence refers to the emission of light between energy states of spin-allowed transitions and has typical lifetimes last no more than 10 ns. Conversely, phosphorescence is spin-forbidden transition and has lifetimes that can be as long as several seconds. Allowed and forbidden transitions are described as such because of quantum mechanical probabilities. In a forbidden transition, the relaxation of electrons does not follow the path of the path of least resistance (i.e., singlet-to-singlet emission) and instead the electron is “trapped” in the triplet state before returning to the singlet state (Fig. 2.3).

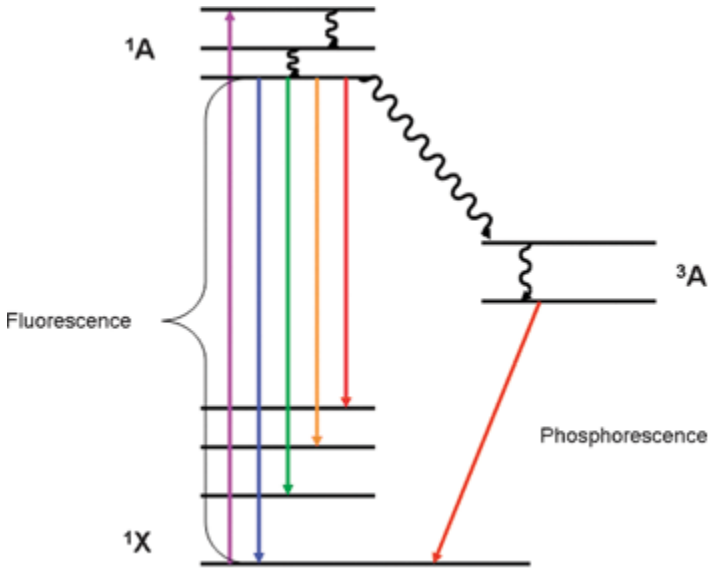

Figure 2.3. Path of relaxation of electrons leading to fluorescence or phosphorescence.[15]

Excitation of conjugated organic linkers usually occurs through the allowed singlet–singlet transition and most of the emission occurs from the lowest excited singlet state, unless there is an efficient non-radiative energy transfer to lower-lying triplet state. The difference in between positions of the band maxima of the absorption and emission spectra of the same electronic transition is known as the Stokes Shift. When a molecule or atom absorbs light, it enters an excited electronic state. The Stokes shift occurs because the molecule loses a small amount of the absorbed energy before re-releasing the rest of the energy as fluorescence depending on the time between the absorption and the re-emission. Stokes fluorescence is the reemission of longer wavelength (lower frequency) photons (energy) by a molecule that has absorbed photons of shorter wavelengths. Both absorption and radiation of energy are unique characteristics of a particular molecule or structure during the fluorescence process.[77]

Lanthanide (Ln) metals are commonly utilized for PL properties, but due to their small molar absorption coefficients (ε), only small amounts of photons are actually absorbed by the *4f*

levels of the ion.[78] Thus the PL intensity is weak as well. To remedy this, Ln ions are often paired with antenna molecules to increase the metal ion sensitivity. The antenna effect was first described by Crosby and Whan[79] who noted that coordinated organic molecules are more efficient absorbers of light and are able to indirectly lead to lanthanide excitation through intersystem crossing energy transfer. In Ln MOFs and CNs, the linkers of the network can also behave as antenna ligands.[15-16] However, in order for energy to transfer, the triplet state of the ligand must be at or above the triplet state of the metal.[76,80]

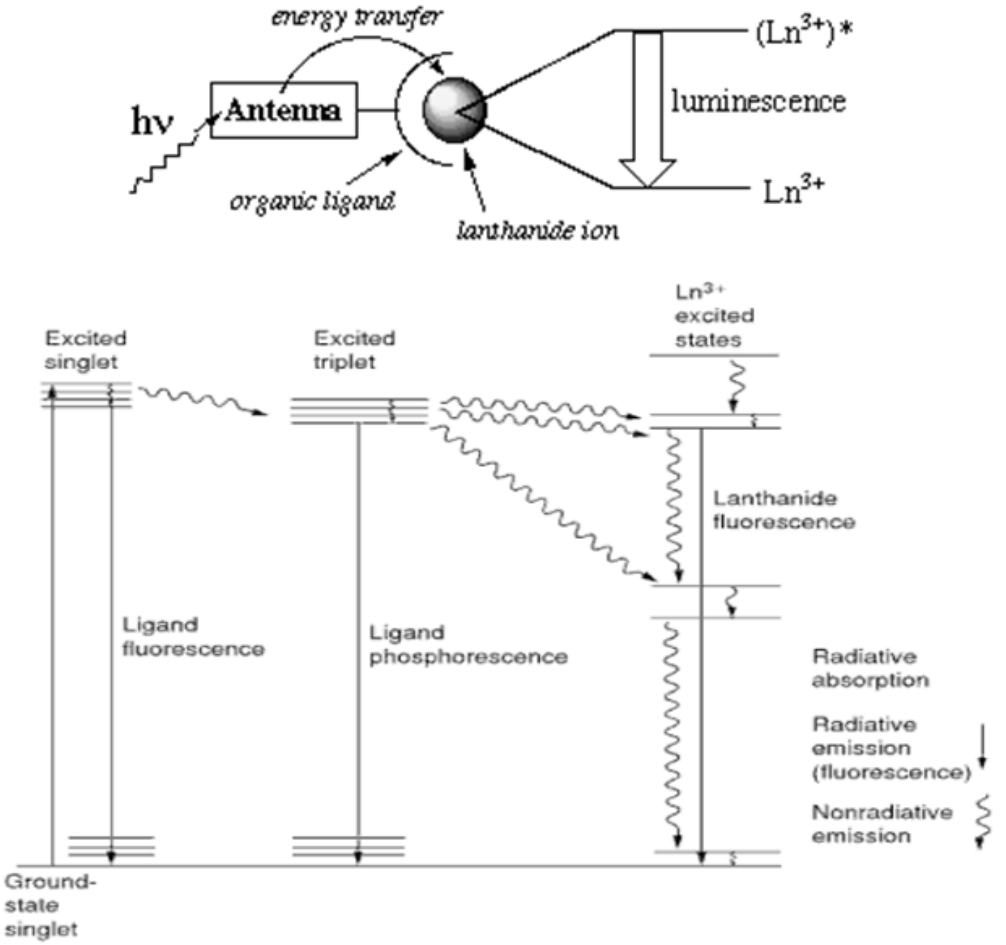

Figure 2.4. Top: Representation of the mechanism of the antenna effect. Bottom: General schematic of energy levels of both ligands and lanthanide ions highlighting the possible routes to PL materials.[80]

The complementary methods of fluorescence and UV-Vis absorption are presented in this work. Where fluorescence deals with the transition from excited to ground state, UV-Vis

absorption measures the ground to excited state transition. Two different fluorescence instruments were used to generate data for this work. In each case, the maximum excitation wavelength was determined by measuring the linker in its free acid state. This wavelength was used for subsequent measurements of fluorescence emission for network compounds. For samples [3.1], [3.2], [5.1], and [5.2], powder samples were uniformly packed into the sample holder of a Jobin Yvon Spex Fluorolog 3, and a 10 s integration time was used for analysis.

For samples [4.1 – 4.3] and [6.1 – 6.3], both fluorescence and UV-Vis analyses were done and a different sample preparation method was used. Solid samples were ground into powder. Quartz slides of dimension 16mm x 60mm were first rinsed with de-ionized water and ethanol, dried, and then scotch (black) tape was applied to the lower half of the dried slide. The tape was then removed to leave behind a small amount of adhesive, onto which a continuous thin layer of sample was sprinkled. Excess sample was removed by gently tapping the slide face down. The effect of glass slide and adhesive was evaluated and found to be negligible. Fluorescence measurements for were done on a Varian Cary Eclipse fluorescence spectrophotometer. UV-Vis measurements were done Shimadzu UV-Vis spectrophotometer equipped with an integrating sphere.

Chapter 3

Synthesis, Characterization, and Luminescence Properties of Magnesium Coordination Networks using a Thiophene-based Linker

3.1. Abstract

By varying the solvents and temperatures used in solvothermal synthesis, two new magnesium-based coordination networks were produced using 2,5-thiophenedicarbxoylate as a linker. Mg(TDC)(DMF) ([3.1]; TDC=2,5 thiophenedicarboxylate; space group $P2_1/c$, a=17.747(4) Å, b=9.805(2) Å, c=21.359(4) Å, β=103.13(3)°] is constructed from a combination of magnesium polyhedral trimers, which are connected by the TDC^{2-} linkers to form a 3-D network. Coordinated DMF molecules are present within the channels. $Mg(TDC)(H_2O)_2$ ([3.2]; space group *P*nma, a=7.296(4) Å, b=17.760(4) Å, c=6.6631(3) Å] is formed by 1-D chains of magnesium octahedra connected by the TDC^{2-} linker. Water molecules are coordinated at the axial positions of the magnesium octahedra. Compound [3.1] is formed using DMF as the synthesis solvent at 180°C, while compound [3.2] is formed using ethanol as the synthesis solvent at 100°C. Both compounds show enhanced photoluminescence intensity when excited at 397nm compared to the free TDC ligand, suggesting a charge transfer between the ligand and the magnesium metal center. Portions of the work described in this chapter, including the synthesis protocols, structures, and characterization have been published: Calderone, P. J.; Banerjee, D.; Santulli, A. C.; Wong, S. S.; Parise, J. B. *Inorg. Chim. Acta* **2011**, *378*, 109.

3.2. Introduction

Synthetic strategies aimed at constructing specific coordination networks possessing desirable properties continue to evolve due to the diverse use of metal centers and multifunctional organic ligands available to researchers.[1-2] The variety of structural topologies that can result from the use of appropriate network components drives research toward targeting topologies for specific uses, leading to many coordination networks with potentially important applications. For example, open frameworks with specific pore sizes are sought for gas storage/separation,[20,81-82] structures with unsaturated metal sites for catalytic applications,[83-84] and materials which take advantage of charge transfer between ligands and metals are desired for luminescence properties.[15,76]

The properties of coordination networks necessarily depend on the metal coordination geometry and the nature of the ligands apart from other synthetic parameters like reaction temperature and solvent. Rigid aromatic linkers can impart structural strength, and are frequently chosen as building blocks for structures requiring high thermal stability. Indeed, coordination networks that feature aromatic carboxylate ligands linked by first row *3d* metals such as Mn,[85] Co,[86-87] and Zn[88-90] continue to be the most prevalent in the literature, because of the well understood bonding interaction between the metal and carboxylate oxygen atoms.

Choices of reaction conditions like solvent[91] and temperature[52] have a fundamental effect on the final product, as the extent of solvent involvement can impact the assembly of the structure. Recently there has been an increase in reports featuring lightweight metal coordination network materials based on s-block metals such as lithium [34-36,92] and magnesium.[40,46,93-94] The possible increase in gravimetric gas storage capacity implied by constructing a network using a lightweight metal with high charge density, such as Li^+, drives much of this exploratory research.

However, assembling networks based on the divalent Mg^{2+} ion offers a dual advantage of using a lightweight metal and a metal ion that behaves similarly in a number of ways to well described *3d* coordination networks of Zn^{2+}. Much like Zn^{2+}, the Mg^{2+} ion is commonly observed to adopt octahedral coordination, has a comparable ionic size (0.72 pm for Mg^{2+}; 0.74 pm for Zn^{2+}),[37] and has a similar affinity for rigid aromatic carboxylate linkers.

As a building block, the 2, 5-thiophenedicarboxylate ligand is an ideal aromatic linker choice for assembling new coordination networks. The diverse coordination modes of the carboxylate groups suggest a range of possible topologies, while the rigidity of the ligand plays a key role in the stability of the network. In addition, free 2, 5-thiophenedicarboxylic acid is a photoluminescent molecule because the large radius of the sulfur atom contributes to the localization of the S electron pair within the heterocyclic thiophene ring. Therefore, utilizing TDC as a building block in coordination networks affords the possibility of unique luminescence properties. Some examples of this approach have been tried with a number of lanthanide,[30-32] transition,[95-97] and post-transition [98-99] metals. This study reports the synthesis, characterization and luminescence studies of two new magnesium-thiophenedicarboxylates, Mg(TDC)(DMF) and Mg(TDC)$(H_2O)_2$, produced using the solvents DMF and ethanol, respectively. Our current findings suggest that linking magnesium with the photoluminescent ligand 2,5 TDC facilitates charge transfer with the metal and enhances the luminescence of the ligand.

3.3. Experimental

3.3.1. Synthesis

Compounds [3.1] and [3.2] were synthesized under solvothermal conditions using Teflon®-lined 23-mL Parr stainless steel autoclaves. Magnesium nitrate hexahydrate

($Mg(NO_3)_2 \cdot 6H_2O$ Acros-organics, 99%), 2,5-thiophenedicarboxylic acid ($C_6H_4O_4S$, 2,5-TDC, Sigma-Aldrich, 95%), ethanol (Fisher 95%), pyridine (Fluka 99%), and N,N'-dimethylformamide (Sigma-Aldrich, 99%) were purchased and used as received.

Synthesis of [3.1], Mg(TDC)(DMF)

In a 23 ml Teflon liner, 0.194g (0.75 mmol) $Mg(NO_3)_2 \cdot 6H_2O$, and 0.147g (0.85 mmol) 2,5 TDC were dissolved in 8.83 g of DMF (ratio of metal salt: linker: solvent=1:1:160). The liner was transferred to a stainless steel autoclave and heated at 180°C for a period of 5 days. After cooling to room temperature, the resulting crystalline product was vacuum filtered and washed with DMF and ethanol. Elemental analysis for C, H, and N found 40.22% C, 3.63% H, 4.99% N (calc. 40.40%C, 3.39% H, 5.23% N).

Synthesis of [3.2], $Mg(TDC)(H_2O)_2$

In a 23 ml Teflon liner, 0.065g (0.25 mmol) $Mg(NO_3)_2 \cdot 6H_2O$, 0.044g (0.25 mmol) 2,5 TDC, and 0.021g (0.25 mmol) pyridine, were dissolved in 4.00g of ethanol (ratio of metal salt: linker: pyridine: solvent=1:1:1:34). The liner was transferred to a stainless steel autoclave and heated at 100°C for a period of 5 days. After cooling to room temperature, the resulting crystalline product was vacuum filtered and washed with ethanol. Elemental analysis for C, H, and N found 31.50% C, 2.76% H, <0.5% N (calc. 31.26%C, 2.62% H, 0.00% N).

3.3.2. Structure Determination

Representative single crystals of each sample suitable for single crystal x-ray diffraction were selected under a polarizing light microscope from the bulk sample. Data for compounds [3.1] and [3.2] were collected at room temperature (298 K) on a Bruker P4 four-circle diffractometer equipped with a SMART 1K CCD detector using Mo Kα radiation (λ=0.71073Å)

and φ and ω scans (Table 3.1). The raw intensity data were collected and integrated with the software packages SMART[70] and SAINT.[70] An empirical absorption correction was applied using SADABS.[70] The crystal structures were solved using direct methods (SHELXS[70]). Mg and S atoms were located first, followed by the determination of all other atom positions (O, C, N) from the Fourier difference map. Displacement parameters for non-hydrogen atoms were refined anisotropically using SHELXTL.[70] Methyl and aromatic hydrogen atoms were placed in position using geometrical constraints. Powder X-ray diffraction (PXRD) data to confirm phase purity were collected using a Scintag Pad X diffractometer (CuK_α, (λ = 1.5418 Å) at a range of 5 < 2θ <40°, with a 0.02 ° 2θ–step size and a counting time of and 1.5 s/step. Powder diffraction data is shown in Figures 3.1 and 3.2.

Table 3.1. Crystallographic data table for [3.1] and [3.2].

	[3.1]	[3.2]
Empirical Formula	$C_{27}H_{27}Mg_3N_3O_{15}S_3$	$C_6H_6MgO_6S$
Formula Weight	802.66	230.49
Collection Temperature (K)	298	298
Wavelength (Å)	0.71073	0.71073
Space Group	$P2_1/c$	*P*nma
a (Å)	17.747(4)	7.296(4)
b (Å)	9.805(2)	17.760(4)
c (Å)	21.359(4)	6.6631(3)
α (°)	90	90
β (°)	103.13(3)	90
γ (°)	90	90
Volume ($Å^3$)	3619.5(14)	863.4(3)
Z	4	4
Calculated Density (g/cm^{-3})	1.473	1.773
Absorption Coefficient (mm^{-1})	0.328	0.447
F(000)	1656	472
Crystal Size (mm)	0.15 x 0.12 x 0.075	0.18 x 0.15 x 0.06
θ range of data collection	1.18 to 27.10	2.29 to 26.37
Index range	$-22 \le h \le 22$ $-11 \le k \le 12$ $-27 \le l \le 26$	$-8 \le h \le 9$ $-22 \le k \le 22$ $-7 \le l \le 8$
Total reflections	23671	5125
Independent reflections	7781 [R(int) = 0.0429]	908 [R(int) = 0.0419]
Goodness of fit	1.030	1.043
Refinement method	Full-matrix least squares on F^2	Full-matrix least squares on F^2
Data/Restraints/Parameter	7770 / 0 / 460	906 / 0 / 67
R1 (on $F_o^2, I > 2\sigma(I)$)	0.042	0.0293
wR2 (on $F_o^2, I > 2\sigma(I)$)	0.1194	0.0844

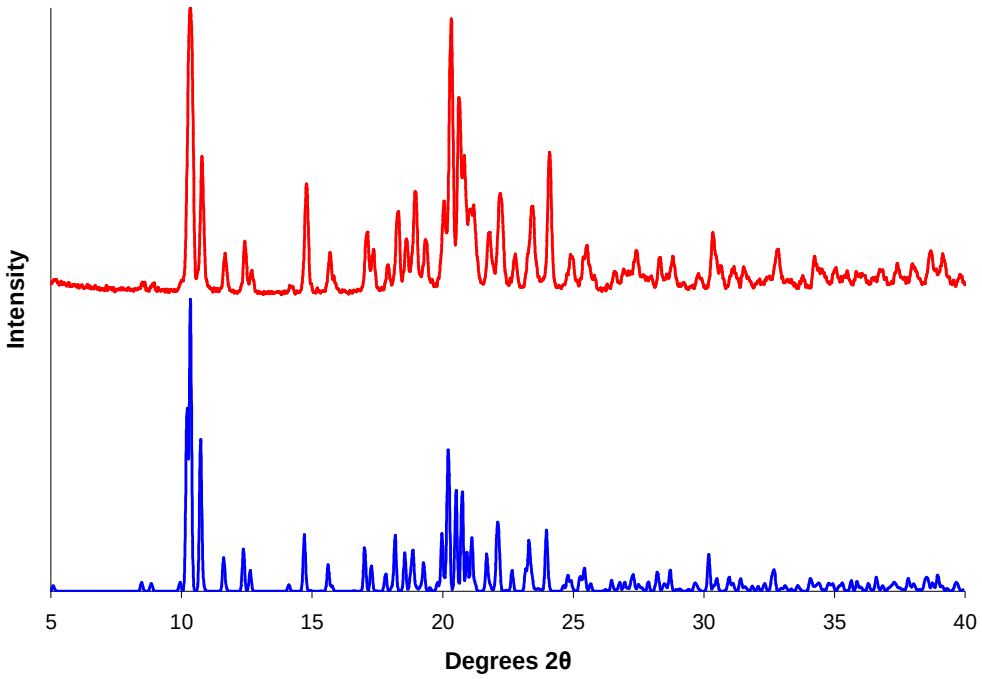

Figure 3.1. Calculated (bottom) and experimental (top) powder patterns of [3.1].

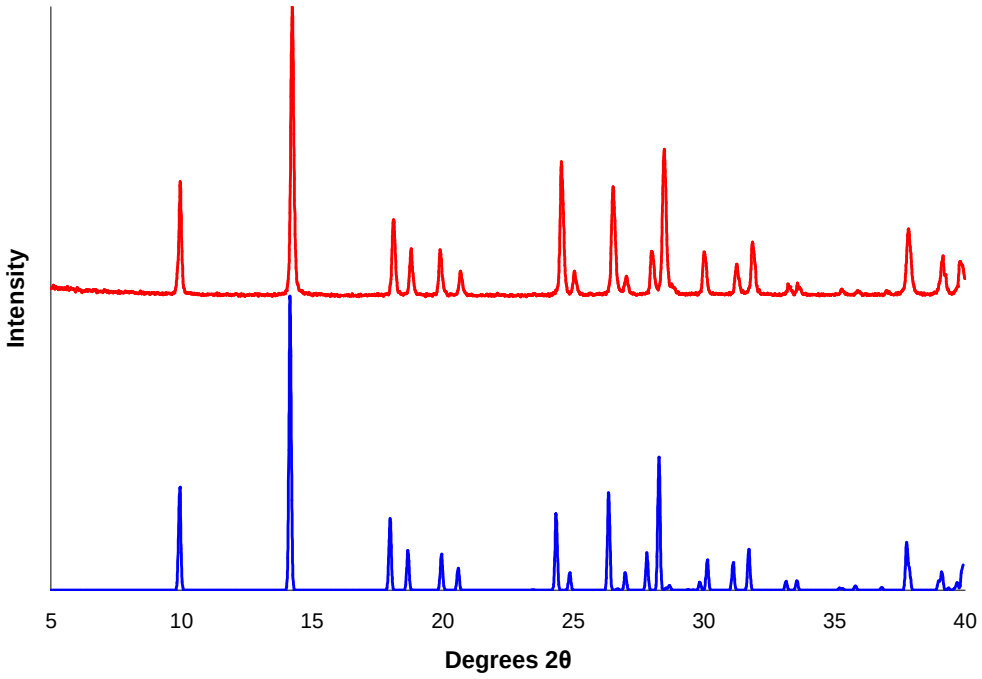

Figure 3.2. Calculated (bottom) and experimental (top) powder patterns of [3.2].

3.3.3. Thermal Data

Combined TGA-DSC data of [3.1] and [3.2] were collected using a STA 449 C Jupiter Netzsch Instrument. Powder samples were placed in an Al_2O_3 crucible for TGA-DSC and analyzed using a range of 30-650°C and 5 degrees per minute under N_2 atmosphere. Thermal data are shown in Figures 3.3 and 3.4.

The thermogravimetric analysis of [3.1] shows a gradual weight loss throughout heating, indicating the compound is thermally unstable. However, two major weight losses are observed during heating with first occurring at 100°C, corresponding to a removal of 2 coordinated DMF molecules; 18.2 wt. % loss calculated compared with 18.0 wt. % observed. The second major weight loss, which occurs at 420°C, can be matched to the loss of the remaining coordinated DMF molecule (calculated 70.2 wt.%; observed 69.7 wt %). Degassed samples of [3.1] at both 220° C and 320° C were checked for crystallinity by PXRD. Crystallinity is maintained after the initial loss of DMF molecules but is subsequently destroyed after heating to drive off the remaining coordinated solvent. When immersed in DMF for two days in an attempt to obtain the original compound, neither of the samples showed any change after PXRD analysis.

Thermogravimetric analysis of [3.1] also reveals two distinct weight losses during heating. The first major weight loss at 150°C corresponds to the dehydration of the compound; 15.6 wt. % calculated compared with 15.7 wt/. % observed. The second major weight loss occurs at 410°C and can be attributed to the elimination of half of the TDC linkers in the compound; 53.0 wt. % calculated compared to 53.1 wt. % observed.

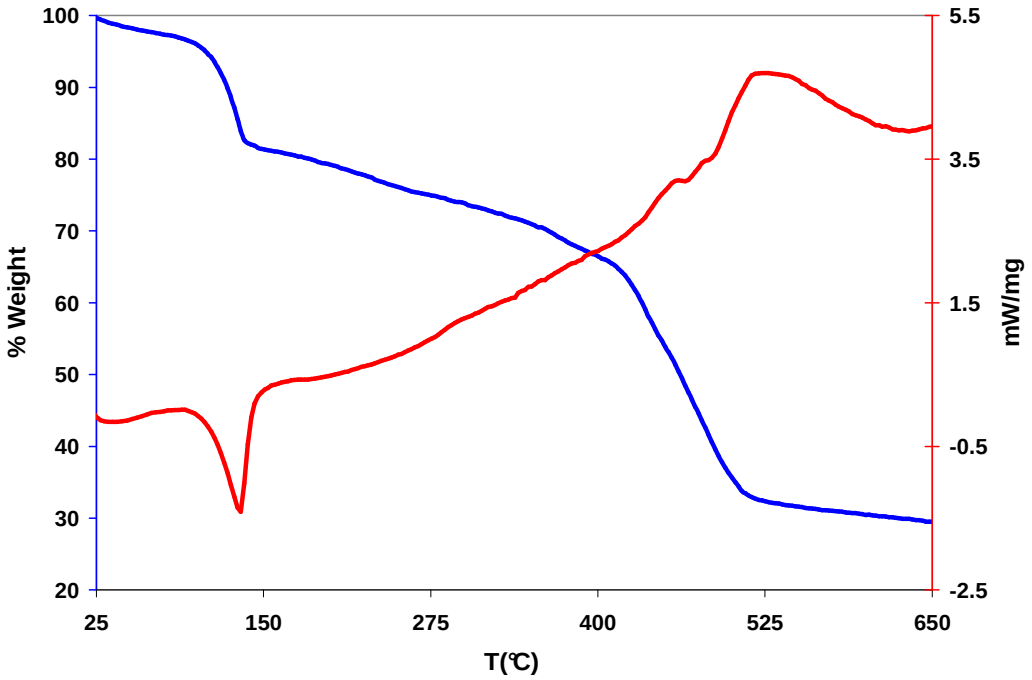

Figure 3.3. Combined TGA-DSC plot of compound [3.1]. The blue line represents the TGA plot while the red line shows the associated DSC signal.

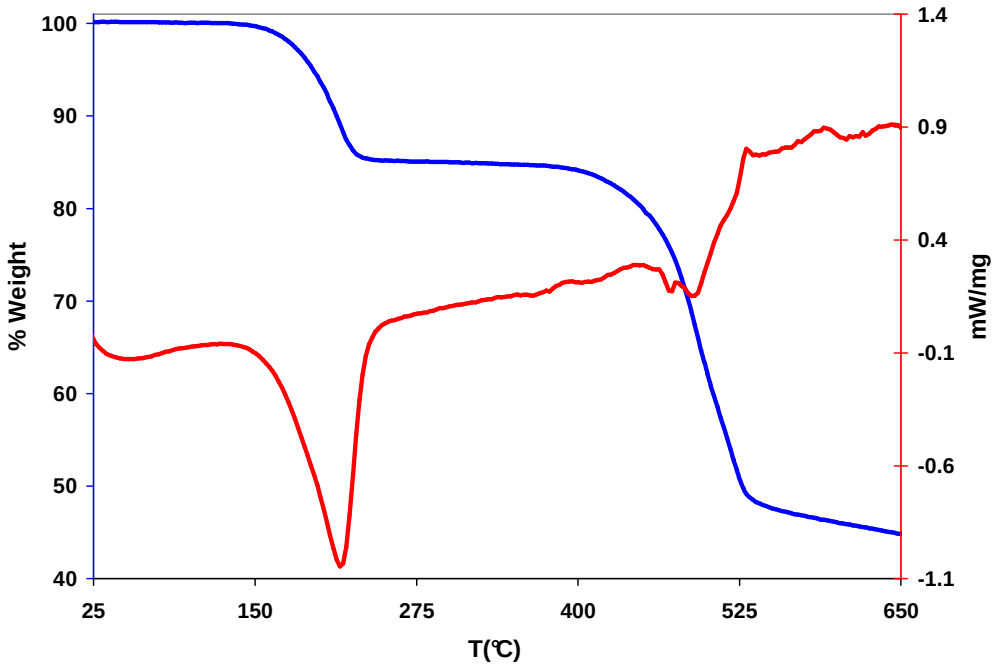

Figure 3.4. Combined TGA-DSC plot of compound [3.2]. The blue line represents the TGA plot while the red line shows the associated DSC signal.

3.3.4. Photoluminescence[x]

Powder samples of compounds [3.1] and [3.2] and the free organic linker were analyzed at room temperature on a FluoroLog-3 with a 10 s integration time using an excitation wavelength of 397 nm.

3.4. Results and Discussion

3.4.1. Structure of [3.1], Mg(TDC)(DMF)

Three unique Mg^{2+} ions grouped into a corner-sharing trimeric unit are observed in [3.1], **(**Figure 3.5). The polyhedral magnesium trimers form a secondary building unit, connected via a TDC^{2-} carboxylate bridge, creating one-dimensional chains (Figure 3.6). These 1D chains are further linked by the TDC ligand to six other chains to form the 3D array. The structure is built around solvent DMF molecules which coordinate to two of the three magnesium centers. The asymmetric unit of [3.1] includes three crystallographically unique magnesium centers, three TDC^{2-} linkers and three coordinated DMF molecules. Sites Mg1 and Mg2 are observed in octahedral coordination environments, while site Mg3 is found in a five-coordinate square pyramidal environment. The octahedral environments of Mg1 and Mg2 are different, as the coordinating oxygen atoms come from different sources. Each of the oxygen atoms coordinating to Mg1 are from the TDC^{2-} carboxylate oxygen atoms, with an average bond distance of 2.089Å (Table 3.2). The Mg1-O1 and Mg1-O6 bond distances are noticeably lengthened to 2.238(1)Å and 2.147(1)Å respectively, and the O1 site is coordinated to both Mg1- and Mg3-sites. Site Mg2 also adopts octahedral coordination, with five of its oxygen atoms coming from the carboxylate group of TDC, while site O1M, contributed by a coordinated DMF molecule, completes the octahedron. Similar to what is observed for Mg1, a lengthening of the Mg-O

[x] Assistance provided by Dr. Alexander Santulli and Dr. Stanislaus Wong

distance is observed in the Mg2-O11 and Mg2-O12 bonds to 2.262Å and 2.156Å, respectively. Site O11 also coordinates to both the Mg2 and Mg1 sites in the structure. Bond valence calculations for Mg3 reveal a sum of 2.04 v. u., supporting the observed five-coordination of magnesium. Two oxygen atoms, O2M and O3M, are contributed by coordinated DMF molecules. The interatomic distance between Mg3-O5 is notably shortened to 1.972(1)Å. Magnesium trimer units in which each Mg in the trimer group is octahedrally coordinated are commonly observed. However, [3.1] is unique in that one member of Mg trimer is five-coordinate while the other metals adopt octahedral coordination. It was also found that [3.1], a structural analog of a previously reported $Mn_3(TDC)_3(DMF)_3$,[97] has a theoretical void space of 46.2% after removal of coordinated solvent, (1670.8 $Å^3$). Compound [3.1] was found to be non-porous after BET analysis using N_2 gas.

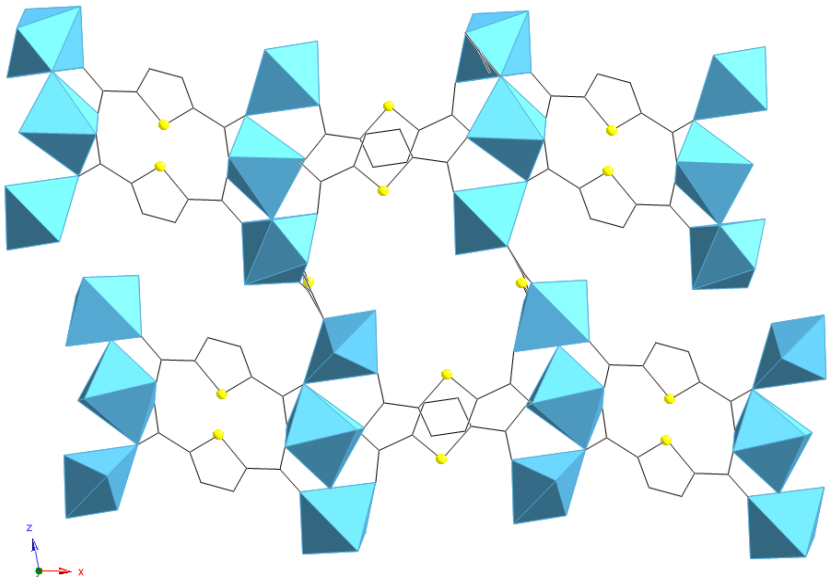

Figure 3.5. View of compound [3.1] along [0 1 0] direction showing the connectivity of the organic linker with the magnesium metal center. Magnesium atoms are represented as blue polyhedra, sulfur in gold, and carbon as wire bonds.

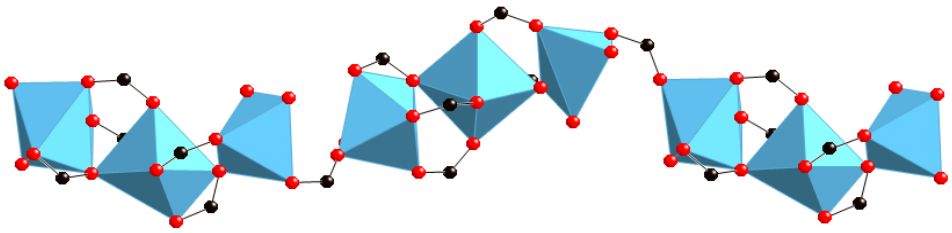

Figure 3.6. Representation of the connectivity of Mg_3 trimers along [0 0 1] direction of compound [3.1] highlighting the coordinating modes of the TDC carboxylate. Magnesium atoms are represented as blue polyhedra, oxygen in red, and carbon in black.

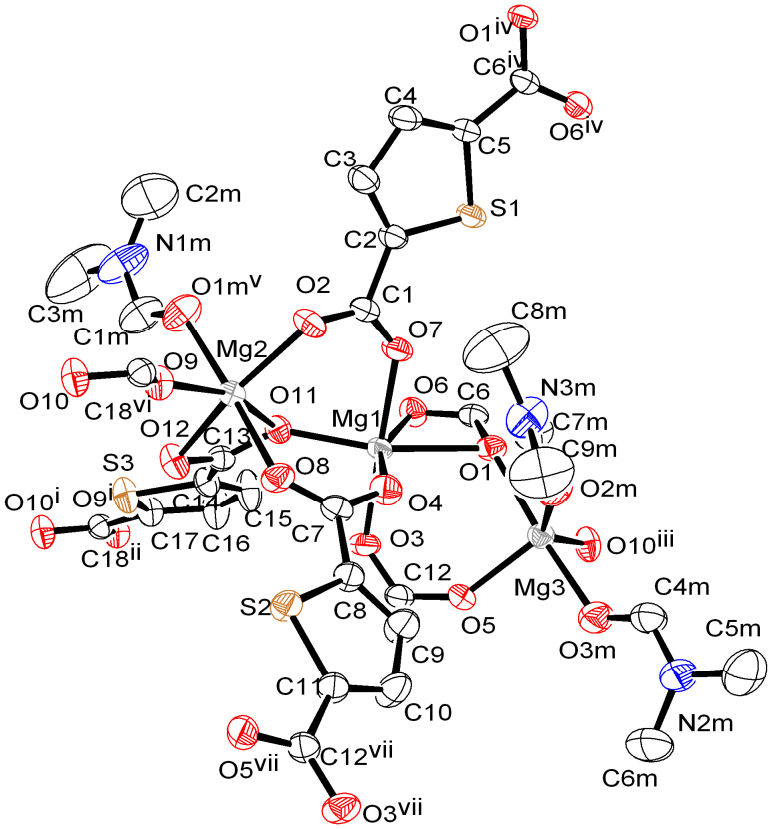

Figure 3.7. ORTEP representation of [3.1]. Ellipsoids are drawn at 50% probability. H atoms are omitted for clarity. Symmetry transformations used to generate equivalent atoms: (i) x, 1+y, z ; (ii) x, 5/2-y, 1/2+z ; (iii) x, 3/2-y, -1/2+z ; (iv) -x, -1/2+y, 1/2-z ; (v) -x, 1-y, 1-z ; (vi) x, 3/2-y, 1/2+z ; (vii) -1-x, -1/2+y, 1/2-z

Table 3.2. Selected bond lengths and angles for [3.1]

Mg(1)-O(4)	2.016(1)	C(18)-O(9)[2]	1.256(3)
Mg(1)-O(11)	2.021(1)	O(9)-C(18)[3]	1.256(3)
Mg(1)-O(3)	2.043(1)	O(10)-C(18)[3]	1.259(3)
Mg(1)-O(7)	2.066(1)	O(6)-C(6)	1.252(3)
Mg(1)-O(6)	2.147(1)	O(1)-C(6)	1.277(3)
Mg(1)-O(1)	2.238(1)	O(11)-C(13)	1.273(3)
Mg(2)-O(9)	1.990(1)	O(12)-C(13)	1.247(3)
Mg(2)-O(2)	2.006(1)	O(3)-C(12)	1.254(3)
Mg(2)-O(8)	2.036(2)	O(5)-C(12)	1.258(3)
Mg(2)-O(1M)[1]	2.109(2)	C(12)-O(5)-Mg(3)	141.86(17)
Mg(2)-O(12)	2.155(1)	C(6)-O(1)-Mg(3)	142.99(16)
Mg(2)-O(11)	2.261(1)	C(1)-O(2)-Mg(2)	134.47(16)
Mg(3)-O(5)	1.972(1)	C(18)[3]-O(9)-Mg(2)	150.74(17)
Mg(3)-O(10)[2]	2.008(1)	C(13)-O(12)-Mg(2)	92.30(14)
Mg(3)-O(2M)	2.031(2)	C(13)-O(11)-Mg(1)	142.45(16)
Mg(3)-O(3M)	2.039(2)	C(13)-O(11)-Mg(2)	86.82(13)
Mg(3)-O(1)	2.077(2)	C(6)-O(1)-Mg(1)	86.19(14)
O(7)-C(1)	1.253(3)	C(6)-O(1)-Mg(1)	86.19(14)
O(2)-C(1)	1.255(3)	Mg(1)-O(11)-Mg(2)	111.45(8)
O(8)-C(7)	1.258(3)	Mg(3)-O(1)-Mg(1)	111.98(8)
O(4)-C(7)	1.260(3)		

Symmetry transformations used to generate equivalent atoms: [1] -x,-y+1,-z+1; [2] x,-y+3/2,z-1/2; [3] x,-y+3/2,z+1/2

3.4.2. Structure of [3.2], $Mg(TDC)(H_2O)_2$

The structure of [3.2] can be described as one-dimensional chains of magnesium ocatahedra connected by TDC^{-2} ligands to form the 3D coordination network (Figure 3.8). Viewing along the [1 0 0] direction, the TDC^{-2} ligands are positioned as rungs in a step-ladder-like arrangement (Figure 3.9), with the rails of the ladder being created by the chains of magnesium. The asymmetric unit includes a unique magnesium ion and one coordinated water molecule, as well as a partial TDC^{2-} linker. The partial TDC^{2-} linker consists of a carboxylate

group and an incomplete thiophene ring of a sulfur atom connected to two carbon atoms. Site Mg1 is coordinated to four oxygen atoms from TDC^{2-} linkers and two oxygen atoms from coordinated water molecules. In the overall structure, the TDC^{2-} linker is associated with four magnesium ions, as each carboxylate oxygen (O1 and O3) coordinates to a metal independently. An average Mg-O distance of 2.078Å (Table 3.3) is observed in [3.2], with the water molecule at the O2 site coordinating at a distance of 2.080(3)Å from the magnesium center. Bond valence calculations for the Mg^{2+} ion revealed a value of 2.124 v. u. No void space was accessible after solvent removal. Compound [3.2] is a structural analog of a previously reported $Mn(TDC)(H_2O)_2$.[100]

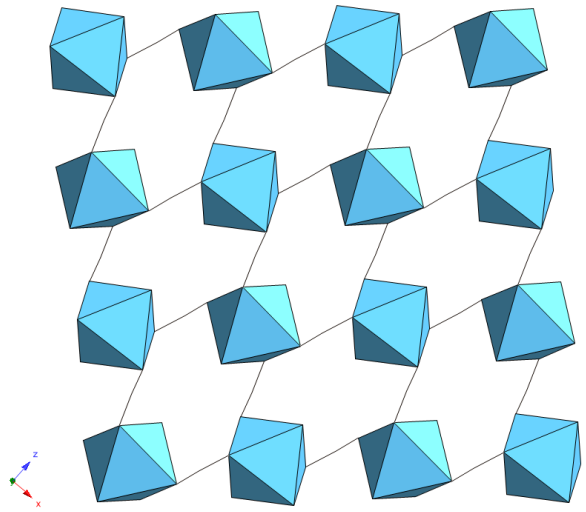

Figure 3.8. The arrangement of magnesium polyhedra (in blue) in compound [3.2] along [1 0 0] direction.

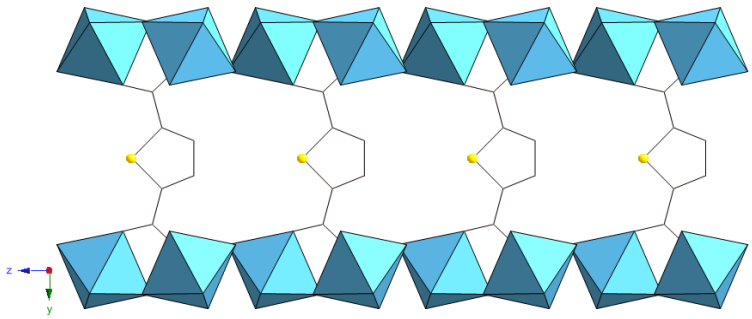

Figure 3.9. The connectivity of 2,5-TDC with metal polyhedra in compound [3.2]. Magnesium atoms are represented as blue polyhedra, sulfur in gold, and carbon as wire bonds.

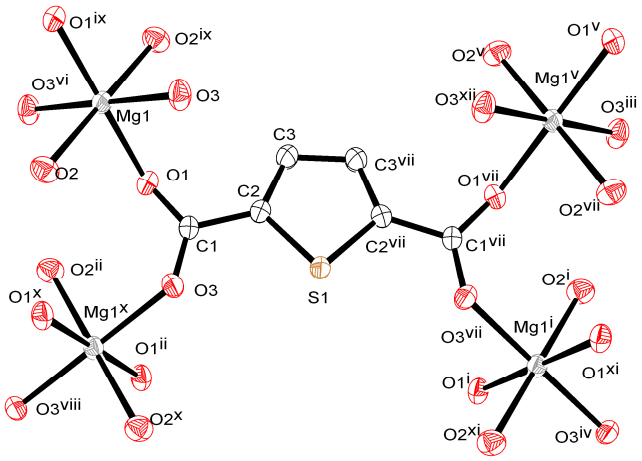

Figure 3.10. ORTEP representation of [3.2] illustrating the numbering scheme. Ellipsoids are drawn at 50% probability. H atoms are omitted for clarity. Symmetry transformations used to generate equivalent atoms: (i) -1/2+x, 1/2-y, 3/2-z ; (ii) -1/2+x, y, 3/2-z ; (iii) 1/2-x, 1/2+y, 1/2+z ; (iv) -x, 1/2+y, 1-z ; (v) 1-x, 1/2+y, 2-z ; (vi) 1/2-x, -y, 1/2+z ; (vii) x, 1/2-y, z ; (viii) -x, -y, 1-z ; (ix) 1-x, -y, 2-z ; (x) 1/2-x, -y, -1/2+z ; (xi) 1/2-x, 1/2+y, -1/2+z ; (xii) 1/2+x, 1/2-y, 3/2-z

Table 3.3. Selected bond length (Å) and bond angle (°) for compound [3.2]

Mg(1)-O(3)[1]	2.071(2)
Mg(1)-O(1)	2.079(2)
Mg(1)-O(2)	2.080(3)
O(1)-C(1)	1.273(2)
O(3)-C(1)	1.254(2)
C(1)-O(3)-Mg(1)[2]	133.27(1)
C(1)-O(1)-Mg(1)	132.51(1)
O(3)-C(1)-O(1)	124.49(5)
O(3)-C(1)-C(2)	118.29(4)
O(1)-C(1)-C(2)	117.20(4)

Symmetry codes: [1] x+1/2,y,-z+3/2; [2] -x+1/2,-y,z-1/2

3.4.3. Discussion

By varying the synthetic conditions of reaction temperature and solvent, and holding constant the metal-to-linker ratio, two new magnesium coordination networks were produced using 2,5 TDC as a linker. Reaction of magnesium salt and 2,5 TDC in pure DMF forms compound [3.1] while compound [3.2] forms in a pyridine/ethanol mixture. Though [3.1] includes solvent DMF in the structure, it is interesting to point out that the reaction producing

[3.2] did not result in a coordination network that incorporated either of its solvent components of pyridine or ethanol. Rather, the magnesium coordination sphere incorporates water molecules from the solution. Since the water content in the solvent ethanol and the waters of crystallization in the metal salt reactant are both present in sufficient quantities to hydrate the compound, the source of water in the ethanol/pyridine system of [3.2] cannot be definitively determined. However, we can conclude that solvation by water is more favorable than by ethanol since neither ethanol nor pyridine was included in the final structure.

A range of various solvent mixtures was used to conduct further experiments in order to determine if other structure types were possible through changes in solvent system. Solvent mixtures of DMF/methanol and DMF/methanol resulted in the formation of compound [3.1]**,** demonstrating a higher coordination capability of DMF compared to ethanol and methanol. For completeness, we extended our experiments further to check the relative coordination strength of DMF and water as a solvent. To our surprise, the reaction in 1:1 DMF/water solvent system produces a previously determined magnesium-formate compound, $[(CH_3)_2NH_2]Mg(HCOO)_3$,[101] due to the formation of formate anion via the hydrolysis of DMF molecules in the presence of water. Thus the relative coordination capability of DMF and water in this particular system remains inconclusive.

Photoluminescence (PL) analysis of [3.1] and [3.2] found that both compounds exhibit similar responses when excited at a wavelength of 397 nm, as can be seen in Figure 3.9. While the responses are similar to those acquired for free 2,5 TDC ligand excited at the same wavelength, there are significant differences in the spectra. The sharp peak centered on 436 nm in the free ligand is broadened and appears at a much higher intensity in the measurement of compounds [3.1] and [3.2]. These peaks can be attributed to the $\pi^* \rightarrow$ n transition of the TDC

ligand [96]. In addition, the broad peak centered on 440 nm in the free ligand is red shifted to 461 nm for [3.1] and shifted to 475 nm for [3.2]**.** Previous reports of PL in compounds containing the 2,5 TDC ligand coordinated to a cobalt have attributed the peak in this region to a ligand-to-metal charge transfer (LMCT) band.[96] Other LMCT effects have been previously noted with "closed shell" metal organic networks using zinc[102] and cadmium.[45,103] In an additional example, enhancement of PL intensity in a zinc-carboxylate based network[104] was attributed to the involvement of charge-transfer transitions from the oxygen atoms of the carboxylate ligands to the empty *4s* orbitals of the Zn^{2+} ions. We therefore suspect that the similar PL behavior occurring in [3.1] and [3.2] may be due to the presence of charge transfer between the 2,5 TDC ligand and the *3s* orbitals of the Mg.

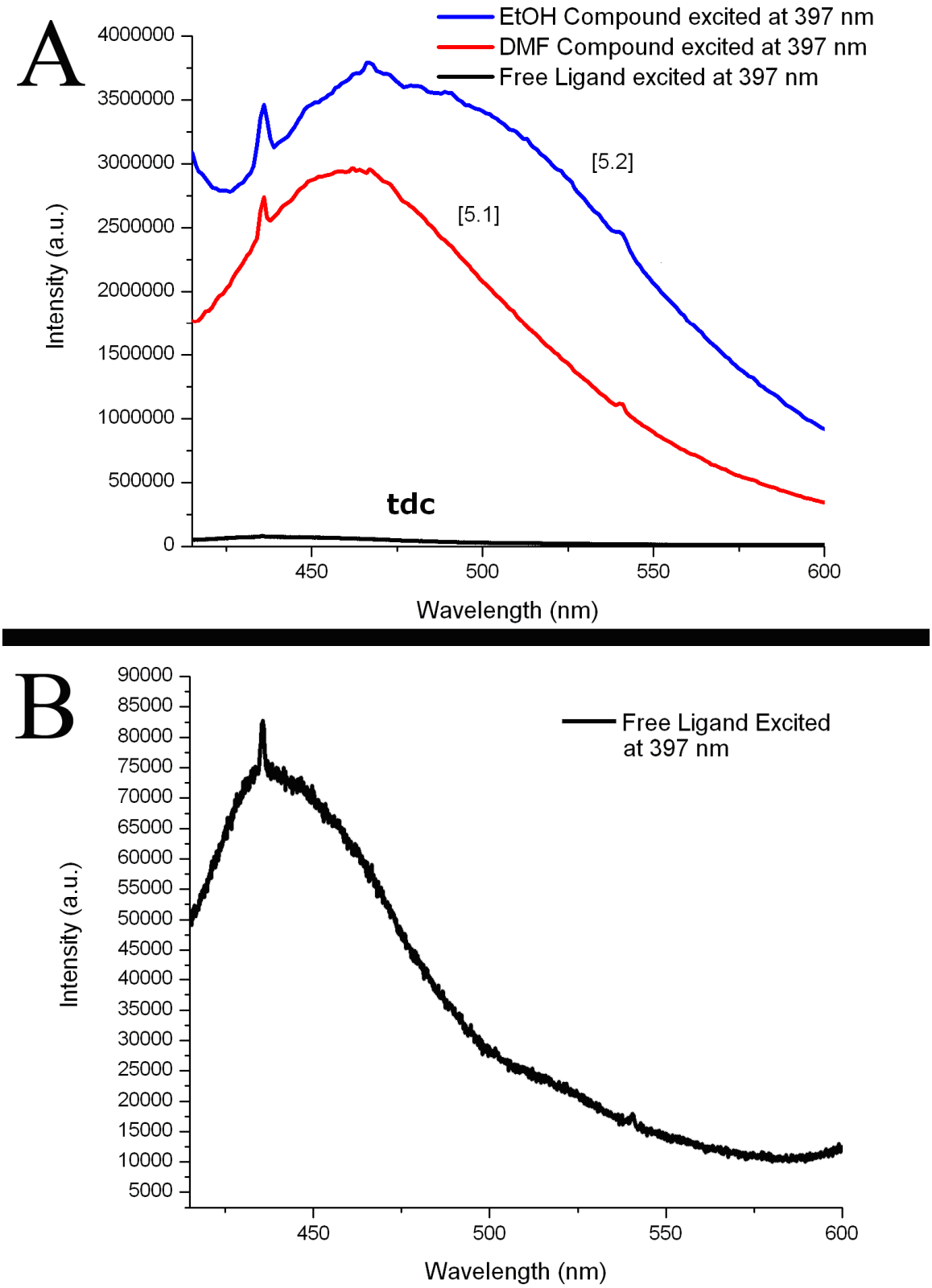

Figure 3.11. (A) Luminescence spectra comparison of [3.1] and [3.2] with free 2,5- TDC ligand (B) and zoom-in image of free 2,5-TDC spectrum excited at 397 nm.

3.5. Conclusion

Two new magnesium coordination networks were synthesized using the 2,5-thiophenedicarboxylate ligand. Changing the solvent and temperature of the reaction, while holding constant the metal-to-linker ratio, led to the formation of each individual network. Photoluminescence measurements reveal that, compared to that of the free TDC ligand, the intensity of luminescence is enhanced when the TDC ligand is used as the building block of these networks. Based on previously reported enhancements of luminescent properties after incorporation of TDC in Co- and Zn- coordination networks, the observed increase in photoluminescence intensity is believed to be due to charge transfer occurring between the ligand and the Mg metal center. These findings may be further applied to the development of luminescent coordination networks using main group metals.

Chapter 4

Temperature Dependent Structure Formation and Photoluminescence Studies of a Series of Magnesium-based Coordination Networks

4.1. Abstract

A series of three magnesium trimesate coordination networks was synthesized from identical reaction mixtures by varying synthetic temperature. $Mg(HBTC)(DMF)_2 \cdot[(CH_3)_2NH]$ ([4.1]; BTC = trimesate; space group $P6_3/m$, a = 16.596(4) Å, c = 14.351(8) Å) crystallizes at 65° C, $Mg_3(BTC)(HCOO)_3(DMF)_3$ ([4.2]; space group $P\text{-}3$, a = 13.928(2) Å, c = 8.025(6) Å) crystallizes at 100°C, and $Mg_3(BTC)_2(DMF)_4$ ([4.3]; space group $P2_1/c$, a = 17.490(4) Å, b= 11.940(2) Å, c= 18.460(4) Å, β = 116.87(3)°) crystallizes at a temperature of 180° C. Each network contains metal-coordinated solvent DMF molecules, but thermodynamics and solvent hydrolysis play major roles in structure determination. Compounds [4.1] and [4.2] are two-dimensional networks which incorporate hydrolysis byproducts. Compound [4.3] is a three-dimensional network and shows no inclusion of byproducts. The series follows the trend of increased network connectivity resulting from increased temperature. The networks show weak photoluminescence response in comparison to free linker, suggesting that coordinated solvent molecules and interlayer species play a role in quenching photoluminescence. Portions of this work come from Calderone, P. J.; Banerjee, D.; Plonka, Anna M.; Kim, S. J.; Parise, J. B. *Inorg. Chim. Acta*. **Submitted**.

4.2. Introduction

Functional hybrid materials, such as metal-organic frameworks (MOFs) and coordination networks (CNs), have promising applications in areas such as gas-storage,[1-3] separations,[105] catalysis,[106] magnetism[10-11] and sensing.[16,27,107] Accordingly, their potential uses stimulate exploratory synthetic chemistry and have lead to the discovery of a diverse collection of structures and topologies.[11-13] Attempts at tailoring MOFs or CNs for specific uses initially require consideration of the properties of their component parts, for example, using a transition metal in a prospective magnetic material[10] or a fluorescent ligand for photoluminescence properties.[15]

Synthetic variables like solvent and temperature can influence the topology and structure in a number of ways. For example, our group recently reported a series of magnesium pyridinedicarboxylate networks of diverse topologies using both pure and mixed solvents.[51] Other effects, like solvent breakdown, subsequent inclusion of breakdown products, and solvent coordination directly affect the assembly and properties of the compound.[50] The hydrolysis of dimethylformamide (DMF) when it is used as a solvent can often lead to the formation of structures containing formate anion ligands[22] or charge balancing dimethylammonium.[11-12] Varying temperature can influence the formation of different topologies and control solvent inclusion. This strategy for the selection of particular topologies was elegantly elaborated by Cheetham and co-workers who reported a change in metal-oxygen-metal (M-O-M) connectivity as a function of temperature.[52] Similarly, Gurunatha and coworkers used temperature to yield one-, two-, and three-dimensional magnesium-based networks of varying metal-linker connectivity.[53] noting that each increase in temperature led to a corresponding increase in dimensionality.

Networks based on the *s*-block metals are appealing targets for exploratory synthesis due to several possible applications. For instance, in gas storage applications, networks that combine lightweight metal centers like magnesium with carboxylate ligands[26,40] have a gravimetric advantage over heavier transition metal-containing networks. These materials retain the potential for high thermal stability due to the strong interactions of *s*-block metal centers with carboxylate oxygen atoms[26] In contrast, the photoluminescence (PL) properties of *s*-block CNs is underexplored[47-49,108] perhaps because as closed shell metal centers, they are unlikely to contribute to luminescent activity of networks. However, work with closed shell metals such as zinc and cadmium demonstrates that a sensible choice of the network linker can often lead to interesting PL properties.[109-115] Common PL active linkers include ligands with benzene rings or high degrees of conjugation, thereby allowing $\pi^* \rightarrow \pi$ or $\pi^* \rightarrow$ n emissions to occur.

Our group recently began to expand on the area of magnesium network photoluminescence by focusing on the importance of the ligand in luminescent activity. Continuing studies of magnesium CNs with PL activity could open the door for the development of lightweight photoluminescent or sensing materials. Our previous reports of magnesium thiophenedicarboxylate[49] and magnesium isophthalte[48] networks suggested that the makeup of the linker's conjugated ring plays a vital role in the PL response of the network. The ordering of conjugated linkers into a network material can also lead to π stacking, a PL effect caused by the interaction of π electrons from multiple linkers.[33-34] Trimesate (BTC) is one such PL active linker[109-111,116] that has the potential for π stacking interactions to lead to networks with luminescent activity.

Many MOFs and CNs, including magnesium-based networks, are based on trimesate because the three available carboxylate connection points lead to a variety of stable

topologies.[117-122] Our latest work, presented here, reports the synthesis and PL properties of three magnesium trimesate networks, $Mg(HBTC)(DMF)_2 \cdot[(CH3)2NH]$, $Mg_3(BTC)(HCOO)_3(DMF)_3$, and $Mg_3(BTC)_2(DMF)_4$. We highlight how from the same starting solution, solvent effects and synthesis temperature changes lead to three structurally unique networks. We also examine how the construction of each of these magnesium trimesate networks influences the ligand-based PL properties.

4.3. Experimental Details

4.3.1. Synthesis[x]

Compounds [4.1 – 4.3] were synthesized under solvothermal conditions using Teflon® – lined 23-mL Parr stainless steel autoclaves. Magnesium nitrate hexahydrate ($Mg(NO_3)_2 \cdot 6H_2O$ Acros organics, 99%), trimesic acid (H_3BTC, Acros organics, 98%), and N,N'-dimethylformamide (Sigma-Aldrich, 99%) were purchased and used as received.

Synthesis of [4.1 –4. 3]

In a 23 ml Teflon liner, 0.256 g (1 mmol) $Mg(NO_3)_2 \cdot 6H_2O$, and 0.210 g (1 mmol) H_3BTC were dissolved in 14 g of DMF (ratio of metal salt: linker: solvent = 1:1:192). For [4.1]**,** $Mg(HBTC)(DMF)_2 \cdot[(CH_3)_2NH]$**,** the liner was transferred to a stainless steel autoclave and heated at 65° C for a period of 5 days. After cooling to room temperature, the resulting crystalline product was vacuum filtered and washed with DMF and ethanol. A similar procedure is used for the 100° C synthesis of [4.2], $Mg_3(BTC)(HCOO)_3(DMF)_3$, and the 180° C synthesis of [4.3], $Mg_3(BTC)_2(DMF)_4$. Note: To yield pure [4.2] 100° C, two drops of concentrated HCl was added to the reaction mixture.

[x] Some synthesis done by Debasis Banerjee

4.3.2. Structure Determination[y]

Representative single crystals of samples [4.1 – 4.3] suitable for single crystal X-ray diffraction were selected under a polarizing light microscope from the bulk sample. Data for [4.1] were collected at room temperature (298 K) on an Oxford Gemini diffractometer equipped with an Atlas detector, using Mo Kα radiation (λ = 0.71073 Å) and 1.0° ω scans. Raw intensity data were integrated using the CrysAlisPro software package.[69] Data for [4.2] were collected at 100 K using a three-circle Bruker D8 diffractometer equipped with an APEXII detector (λ = 0.41328 Å) using 0.5° φ scans at Advanced Photon Source ChemMatCars beamline. The raw intensity data were integrated using the APEXII suite of programs.[71] Data for compound [4.3] were collected at room temperature (298 K) on a Bruker P4 four-circle diffractometer equipped with a SMART 1K CCD detector using Mo Kα radiation (λ=0.71073Å) and φ and ω scans (Table 1). Raw intensity data were integrated with the software packages SMART [70] and SAINT [70]. Empirical absorption corrections for [4.1 – 4.3] were applied using SADABS.[70] Structures were solved using direct methods and refined using SHELXS.[70] Mg atoms were located first, followed by the determination of all other atom positions (O, C, N) from the Fourier difference map. Most of the non-hydrogen atoms were refined with anisotropic displacement parameters, while hydrogen atoms were placed in idealized positions using geometric constraints. Powder X-ray diffraction (PXRD) data to confirm phase purity were collected using a Rigaku diffractometer (CuK_α, λ = 1.5418 Å) at a range of 5 < 2θ <40°, with a 0.02 ° 2θ–step size. Crystallographic details can be found in Table 4.1. Powder XRD are shown in Figures 4.1 – 4.3.

[y] Assistance in structure determination given by Anna Plonka

Table 4.1. Crystallographic data for [4.1 – 4.3]

	[4.1]	[4.2]	[4.3]
Empirical Formula	$C_{15}H_{18}MgN_2O_8$	$C_7H_9MgNO_5$	$C_{30}H_{34}Mg_3N_4O_{16}$
Formula Weight	378.62	211.46	779.54
Collection Temperature (K)	298	100	298
Wavelength (Å)	0.71073	0.41328	0.71073
Space Group	$P6_3/m$	$P\ -3$	$P2_1/c$
a (Å)	16.596(4)	13.928(2)	17.490(4)
b (Å)	16.596(4)	13.928(2)	11.940(2)
c (Å)	14.351(8)	8.025(6)	18.460(4)
α (°)	90	90	90
β (°)	90	90	116.87(3)
γ (°)	120	120	90
Volume (Å^3)	3422.9(3)	1348.1(3)	3438.9(5)
Z	6	6	4
Calculated Density (g/cm^{-3})	1.102	1.563	1.506
Absorption Coefficient (mm^{-1})	0.114	0.061	0.170
F(000)	1188	660	1624
Crystal Size (mm)	0.3 x 0.2 x 0.1	0.065 x 0.034 x 0.01	0.2 x 0.08 x 0.05
θ range of data collection	3.75 to 25.35	0.98 to 15.75	1.31 to 26.37
Index range	$-19 \le h \le 19$ $-19 < k < 19$	$-18 \le h \le 18$ $-18 < k < 18$	$-21 \le h \le 20$ $-14 < k < 14$
Data/Restraints/Parameters	2169/6/167	2093/2/133	7023/0/478
R1 (on $F_o^2, I > 2\sigma(I)$)	0.0617	0.0511	0.0428
wR2 (on $F_o^2, I > 2\sigma(I)$)	0.1834	0.1724	0.1124

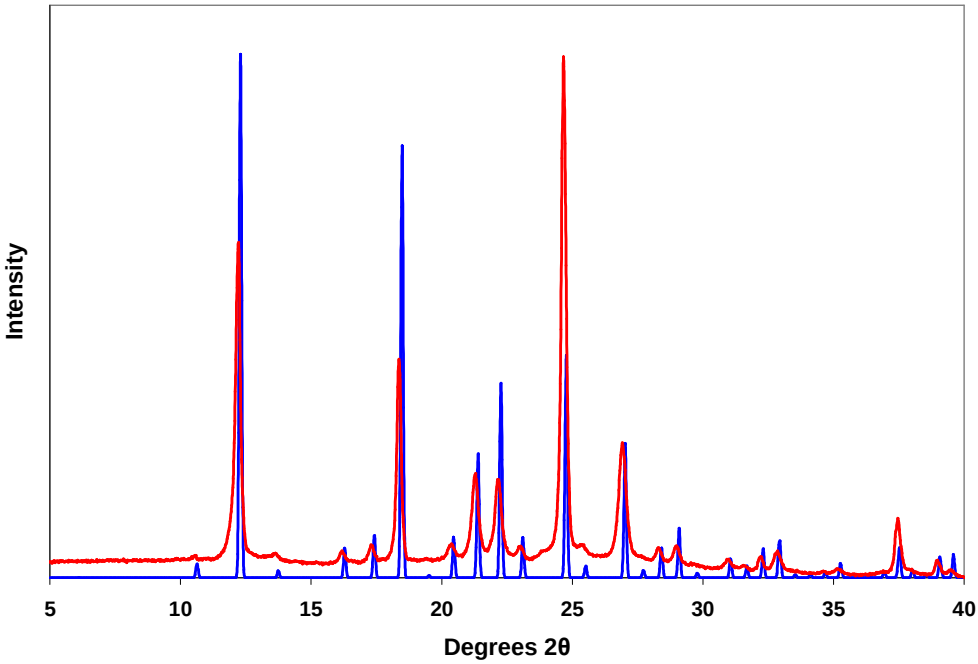

Figure 4.1. Calculated (blue) and experimental (red) powder XRD pattern of [4.1].

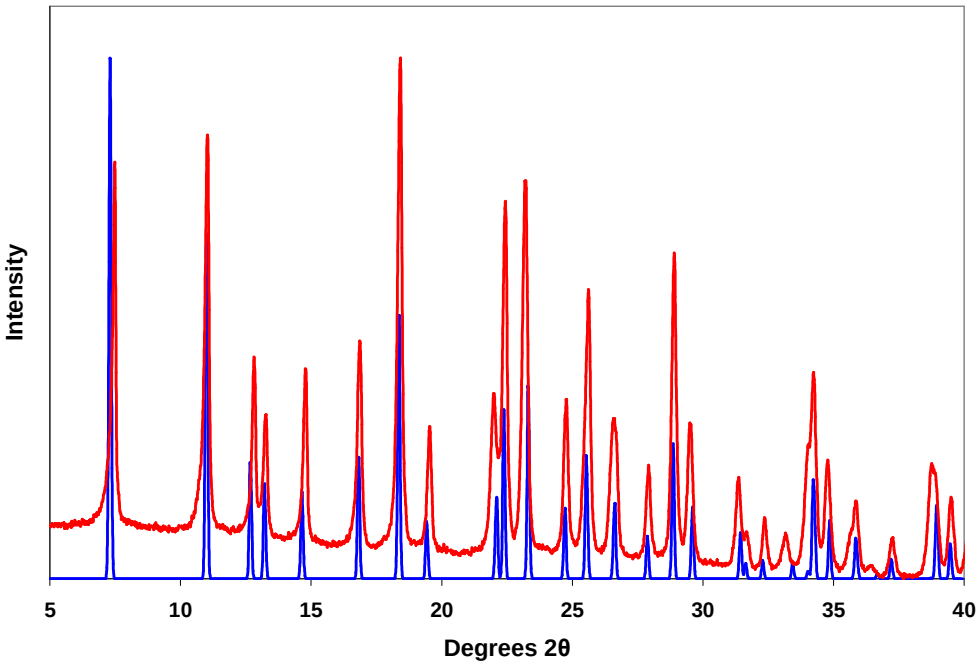

Figure 4.2. Calculated (blue) and experimental (red) powder XRD pattern of [4.2].

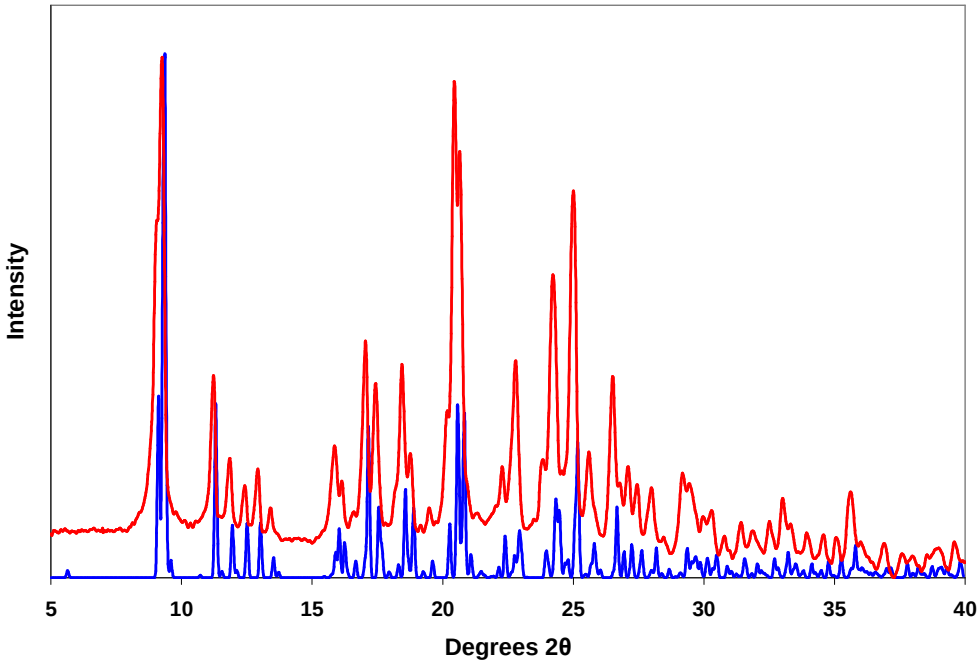

Figure 4.3. Calculated (blue) and experimental (red) powder XRD pattern of [4.3].

4.3.3. Thermal Data

Combined TGA-DSC data of [4.1 – 4.3] were collected using a STA 449 C Jupiter Netzsch Instrument. Powder samples were placed in an Al_2O_3 crucible for TGA-DSC and analyzed using a range of 30-800°C and 5 degrees per minute under N_2 atmosphere. Thermal data are shown in Figures 4.4 – 4.6.

The thermogravimetric data of [4.1] show no well-defined plateaus, but does exhibit three gradual weight losses, the first beginning at approximately 150° C and accounting for a loss of dimethylamine and one DMF molecule (27.8% calculated; 27.1% observed). A second DMF molecule is lost from [4.1] over the course of two weight losses (calculated 44.9%; observed 42.1%), beginning at approximately 350° C. Pyrolysis of the ligand follows after reaching a temperature of 550° C.

Thermogravimetric analysis of [4.2] also shows three gradual weight losses starting at approximately 200° C. The first weight loss corresponds to a loss of two DMF molecules (23.1 % calculated; 23.8 % observed). The next weight loss occurs at approximately 350° C and accounts for the loss of the last DMF molecule and two formate groups (48.8 % calculated; 47.5% observed). At approximately 550° C ligand pyrolysis occurs. Compound [4.3] shows two major weight losses that account for a loss of three DMF molecules (27.9% calculated; 25.4% observed). After approximately 550° C, pyrolysis of the remainder of the compound occurs.

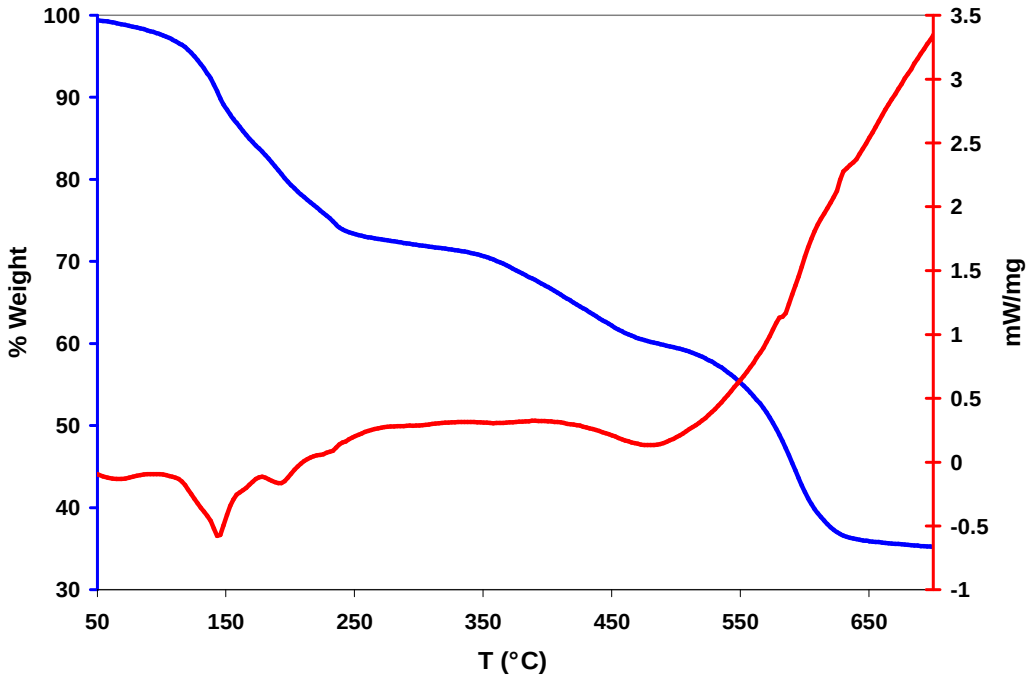

Figure 4.4. Combined TGA (blue) and DSC (red) data for [4.1].

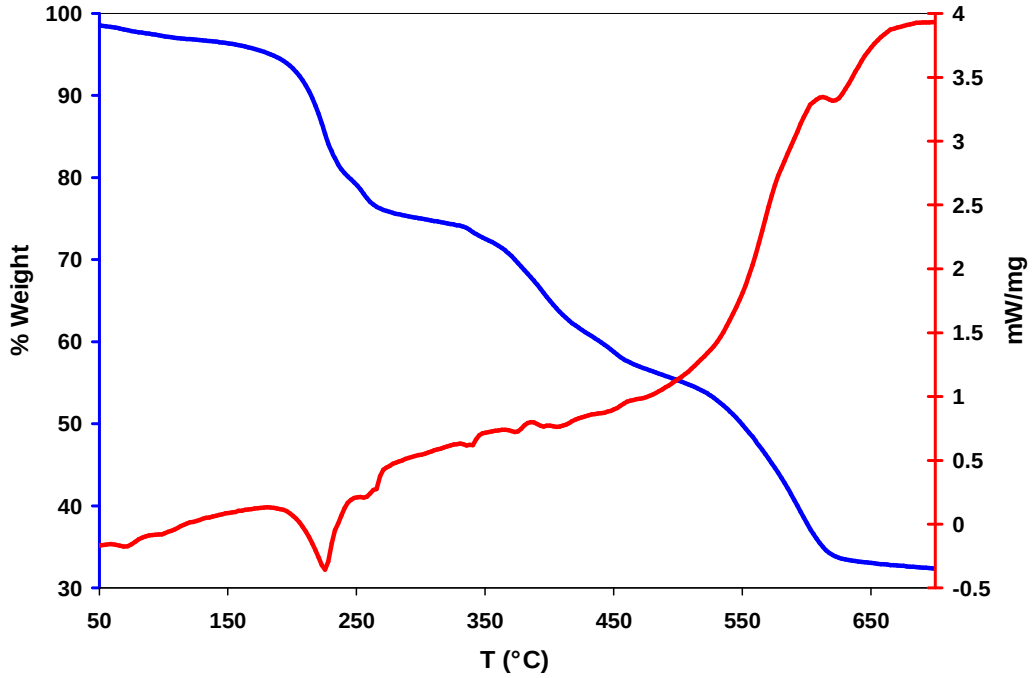

Figure 4.5. Combined TGA (blue) and DSC (red) data for [4.2].

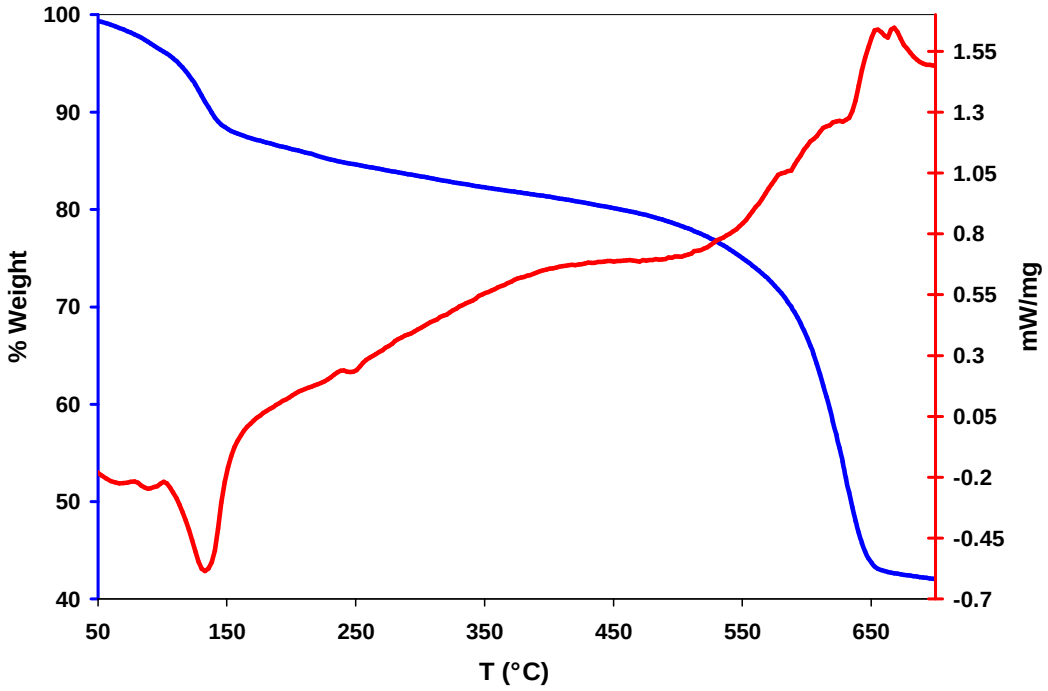

Figure 4.6. Combined TGA (blue) and DSC (red) data for [4.3].

4.3.4. Photoluminescence and UV-Vis absorption analysis[z]

The preparation of samples for fluorescence and UV-Vis analysis of [4.1 – 4.3] and free BTC followed the procedure as described below. Solid samples were ground into powder. Quartz slides of dimension 16mm x 60mm were first rinsed with de-ionized water and ethanol, dried, and then scotch (black) tape was applied to the lower half of the dried slide. The tape was then removed to leave behind a small amount of adhesive, onto which a continuous thin layer of sample was sprinkled. Excess sample was removed by gently tapping the slide face down. The effect of glass slide and adhesive was evaluated and found to be negligible. The UV-Vis absorption spectrum was measured for powdered solid samples of compounds [4.1 – 4.3] and free BTC on a Shimadzu UV-Vis spectrophotometer equipped with an integrating sphere. The excitation and emission spectra of thin layers of free BTC and [4.1 – 4.3] were measured on a Varian Cary Eclipse fluorescence spectrophotometer. The excitation spectra were obtained by varying excitation energy while fixing the emission wavelengths at 300 nm, the emission maxima of free BTC.

[z] Assistance provided by Zhichao Hu and Jing Li

4.4. Results and Discussion

4.4.1. Structure of [4.1], $Mg(HBTC)(DMF)_2 \cdot [(CH_3)_2NH]$

The structure of [4.1] is formed through the linking of individual magnesium octahedra into a two-dimensional net with both HBTC and BTC linkers (Fig. 4.7). A bidentate carboxylate group and two monodentate carboxylate groups form the connecting points to the net in the four equatorial positions of the magnesium octahedron. Disordered DMF molecules coordinate in the two axial positions (Fig. 4.8) and extend in between each net. The space between the nets is occupied by two disordered dimethylamine molecules, and their effects on the diffraction data were removed with the PLATON/SQUEEZE routine.[123] There are three unique linker positions in the compound's [4.1] structure, with the centroid of each located on the three-fold axis; consequently, the asymmetric unit contains one-third of each of the linker molecules, one Mg atom and a DMF molecule. The octahedral coordination environment of Mg1 is has six oxygen atoms. The BTC linkers are found in an exotridentate (κ^2)–(κ^2)–(κ^2)–μ_3 binding mode, while the HBTC linkers are also tridentate, but adopt a (κ^1)–(κ^1)–(κ^1)–μ_3 binding mode. Two carboxyl groups, each from a HBTC linker, contribute oxygen atoms O3 and O5 to equatorial positions *cis* to one another. The remaining two equatorial positions are also *cis* to one another and occupied by O1 and O2 from the bidentate carboxylate group. Axial positions of the octahedron are occupied by a DMF oxygen atom (O1D) and its symmetry generated counterpart. The octahedron is slightly distorted and has an average Mg-O bond length of 2.061 Å. Each magnesium octahedron is separated by a distance of 9.214(3) Å from its nearest neighbor. A topologically-related nickel structure of [4.1], $[Ni(HBTC)(DMF)_2 \cdot (guest)]$, has been previously reported.[124]

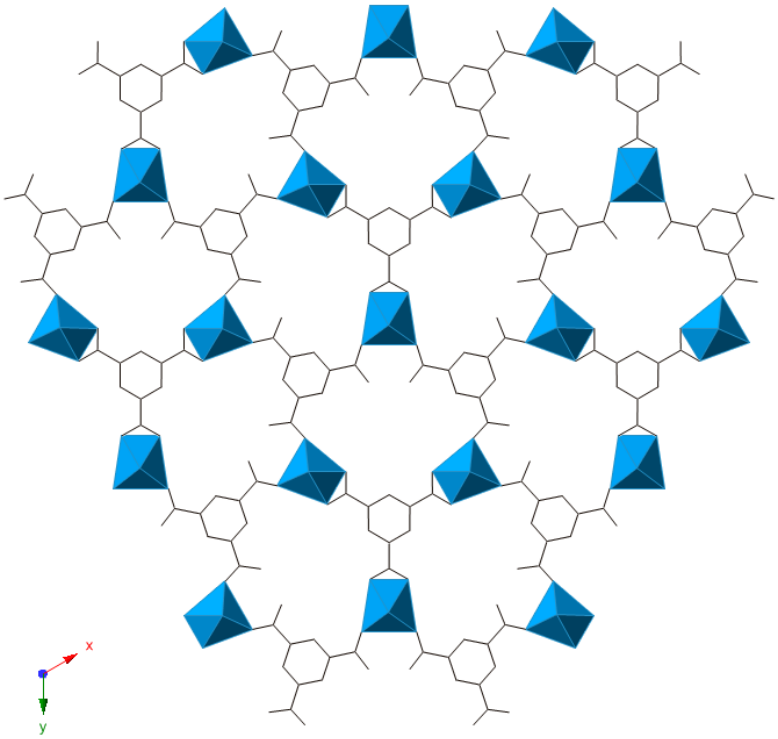

Figure 4.7. Network connectivity of the two-dimensional layers in [4.1], with Mg represented as light blue polyhedra and BTC linkers represented as wire bonds. DMF molecules are omitted for clarity.

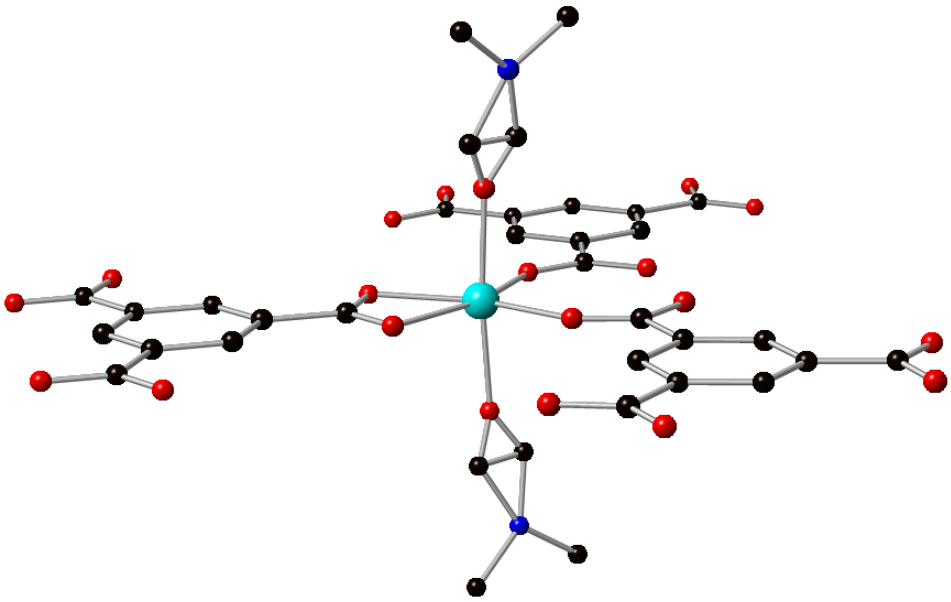

Figure 4.8. Local environment of [4.1]. Mg is shown in light blue, C in black, O in red, and N in blue.

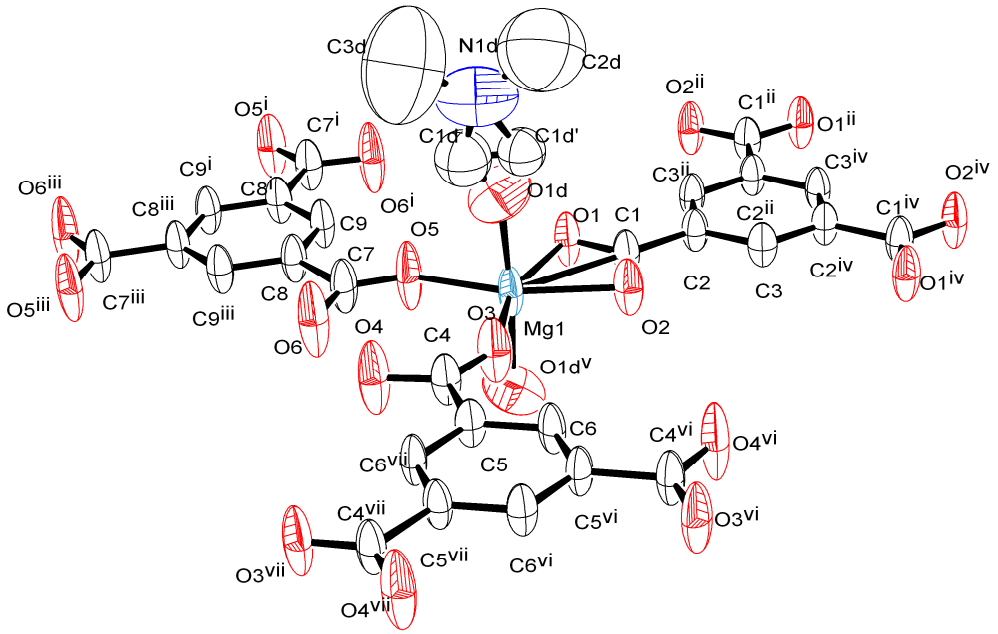

Figure 4.9. ORTEP representation of [4.1] with ellipsoids drawn at 50% probability. Symmetry operations used to generate equivalent atoms: (i) -y, x-y, z ; (ii) 1-x+y, 1-x, z ; (iii) -x+y, -x, z ; (iv) 1-y, x-y, z ; (v) x, y, 3/2-z ; (vi) 1-x+y, -x, z ; (vii) -y, -1+x-y, z

Table 4.2. Selected bond lengths (Å) and angles (°) for [4.1]

Mg(1)-O(1)	2.113(3)
Mg(1)-O(2)	2.121(3)
Mg(1)-O(3)	2.032(3)
Mg(1)-O(5)	2.018(3)
Mg(1)-O(1D)	2.041(4)
Mg(1)-O(1D)	2.041(4)
Mg(1)-O(1D)[a]	2.041(4)
O(3)-Mg(1)-O(1)	158.26(11)
O(5)-Mg(1)-O(1)	97.37(11)
O(3)-Mg(1)-O(1D)	87.82(9)
O(5)-Mg(1)-O(3)	104.37(11)
O(5)-Mg(1)-O(1D)	88.96(14)
O(1D)[a]-Mg(1)-O(1D)	174.5(2)

Symmetry transformations used to generate equivalent atoms: [a]x,y,-z+3/2

4.4.2. Structure of [4.2], $Mg_3(BTC)(HCOO)_3(DMF)_3$

Compound [4.2], consists of corner-shared magnesium octahedra linked into six member rings by bridging formate ligands to form a secondary building unit (Fig. 4.10). The rings of the secondary building unit are further connected into a two-dimensional layer by BTC linkers (Fig. 4.11), with the space between each layer occupied by metal-coordinating DMF molecules. The asymmetric unit is similar to [4.1], in that the centroid of the BTC linker is located at the three-fold axis, and therefore the asymmetric unit of [4.2], consists of one-third of the BTC linker, one Mg atom, a formate group, and one coordinated DMF molecule. Each carboxylate group of the BTC linker is bidentate binuclear and the BTC linker adopts an exohexadentate binding mode of $(\kappa^1\text{-}\kappa^1)\text{–}(\kappa^1\text{-}\kappa^1)\text{–}(\kappa^1\text{-}\kappa^1)\text{–}\mu_6$ Formate groups connect in the coordination mode of $(\kappa^1\text{-}\mu_2)\text{–}(\kappa^1)\text{–}\mu_3$. The equatorial positions in the coordination environment of Mg1 are occupied by two *cis*-related oxygen atoms contributed by a BTC carboxylate (O2; O3), and a formate group whose two oxygen atoms are also *cis* to one another (O4; O5). The axial positions are occupied by symmetry-generated O5 and a DMF oxygen atom, O1. The average Mg-O bond distance is 2.063 Å. Each magnesium atom is connected to its neighboring metal center at a distance of 3.580(2) Å. Centroids of the six-member Mg rings are separated in the two-dimensional net by a distance of 13.927 Å. The structure of [4.2], is previously reported[125] along with that of a cobalt structural analog $Co_3(BTC)(HCOO)_3(DMF)_3$.[126]

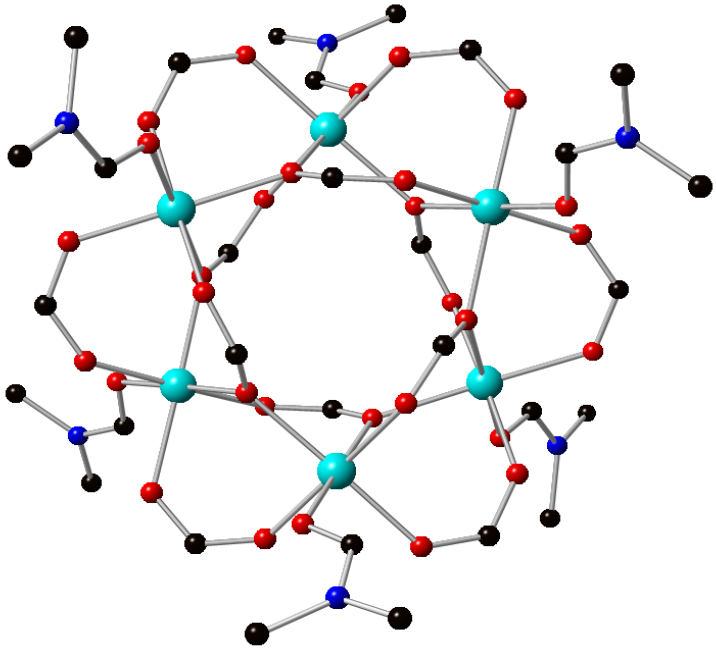

Figure 4.10. Hexagonal secondary building unit of [4.2] illustrating metal-bridging formates, with Mg represented in light blue, C in black, O in red, and N in blue.

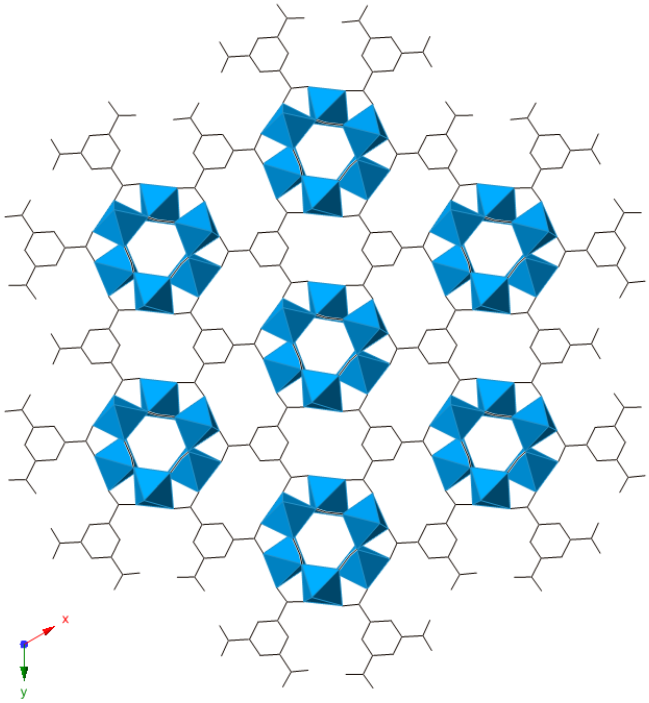

Figure 4.11. Layered network connectivity of the [4.2]. Mg polyhedra are shown in light blue and BTC linkers are shown as wire bonds. DMF is omitted for clarity.

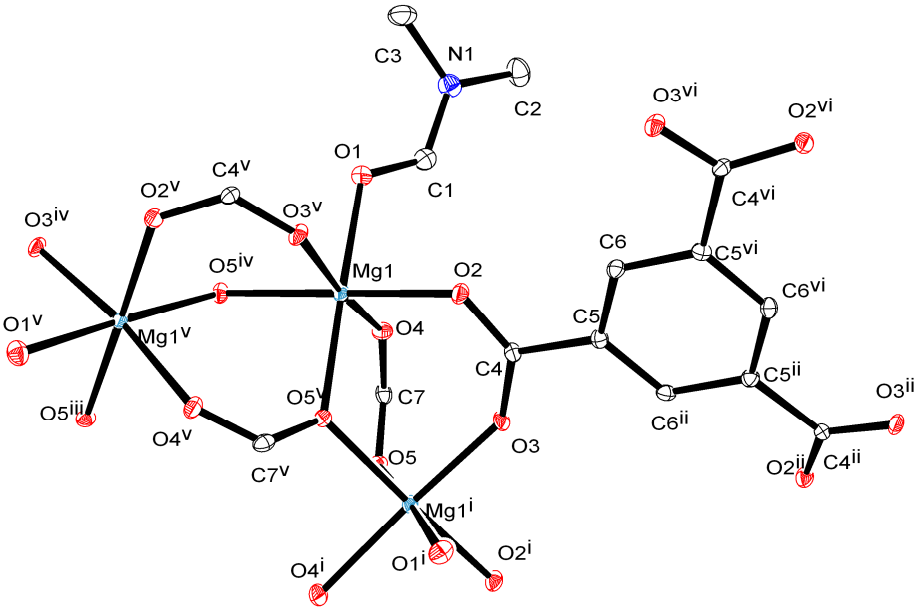

Figure 4.12. ORTEP representation of [4.2] with ellipsoids drawn at 50% probability. Symmetry operations used to generate equivalent atoms: (i) 1+y, 1-x+y, 2-z ; (ii) 2-x, -y, 2-z ; (iii) 1-y, -1+x-y, z ; (iv) 2-y, x-y, z (v) x-y, -1+x, 2-z ; (vi) 2-x+y, 2-x, z

Table 4.3. Selected bond lengths (Å) and angles (°) for [4.2].

Mg(1)-O(1)	2.107(2)
Mg(1)-O(2)	2.044(2)
Mg(1)-O(3)[a]	2.008(2)
Mg(1)-O(4)	2.072(2)
Mg(1)-O(5)[b]	2.118(2)
Mg(1)-O(5)[a]	2.118(2)
O(1)-Mg(1)-O(5)[b]	90.85(8)
O(2)-Mg(1)-O(5)[a]	89.59(8)
O(3)[a]-Mg(1)-O(1)	86.70(9)
O(3)[a]-Mg(1)-O(2)	88.75(8)
O(3)[a]-Mg(1)-O(5)[a]	95.85(8)
O(3)[a]-Mg(1)-O(5)[b]	89.37(8)
O(4)-Mg(1)-O(1)	84.53(8)
O(4)-Mg(1)-O(5)[a]	92.93(8)
O(5)[b]-Mg(1)-O(5)[a]	89.57(10)

Symmetry transformations used to generate equivalent atoms: [a] x-y,x-1,-z+2; [b]-y+1,x-y-1,z

4.4.3. Structure of [4.3], $Mg_3(BTC)_2(DMF)_4$

In compound [4.3], corner-shared triads of octahedral magnesium atoms are linked together into infinite chains by BTC carboxylate groups (Fig. 4.13). The chains are further linked into a three-dimensional network by a bridging BTC ligand (Fig. 4.14). DMF molecules coordinating to the magnesium metal center occupy the channels within the network. The asymmetric unit of [4.3] consists of three crystallographically unique Mg atoms, two BTC linkers, and four coordinated DMF molecules. The two BTC linkers each adopt the exohexadentate binding mode of $(\kappa^2\text{-}\kappa^1\text{-}\mu_2)\text{–}(\kappa^1\text{-}\kappa^1)\text{–}(\kappa^1\text{-}\kappa^1)\text{–}\mu_6$. The coordination of Mg1 consists of six oxygen atoms, each of which comes from a BTC carboxylate group. The equatorial positions are occupied by O1, O2, O3, and O5, with the combinations of O1; O3 and O2; O5 *cis* to one another. The axial positions are occupied by O8 and O13. Four oxygen atoms occupy the equatorial positions of Mg2; two *cis* oxygen atoms are contributed by BTC linkers (O2, O4), and *cis*-related oxygen atoms are contributed by DMF molecules (O1M, O3M). The axial positions are contributed by BTC linkers as well (O6, O9). The coordination environment of Mg3 is similar to Mg2 in that four oxygen atoms come from BTC linkers. The equatorial positions are occupied by the *cis*-related O8; O11 and O10; O12. The two axial oxygen atoms come from coordinated DMF molecules (O2M, O4M). Sites Mg1 and Mg2 are separated by a distance of 3.553(1) Å, while sites Mg1 and Mg3 are separated by a distance of 3.836(3) Å. The centroid of each triad is separated from its nearest neighbor at a distance of 9.797 Å. Structural collapse occurs when [4.3] is heated to remove coordinated DMF molecules. A manganese structural analog of [4.3], $Mn_3(BTC)_2(DMF)_4$, has been previously reported.[127]

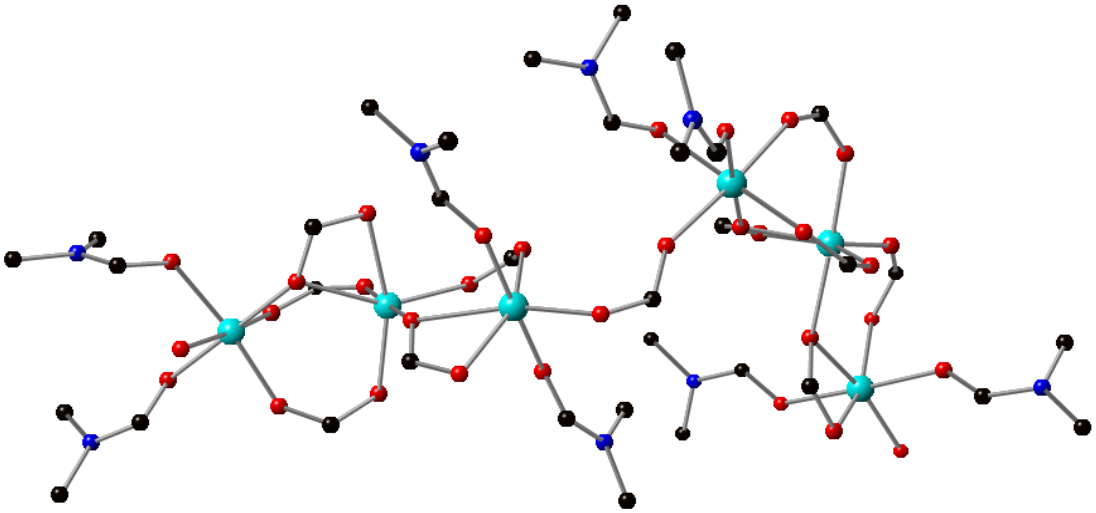

Figure 4.13. Illustration of the Mg triad chains observed in [4.3], with Mg representing in light blue, C in black, O in red, and N in blue.

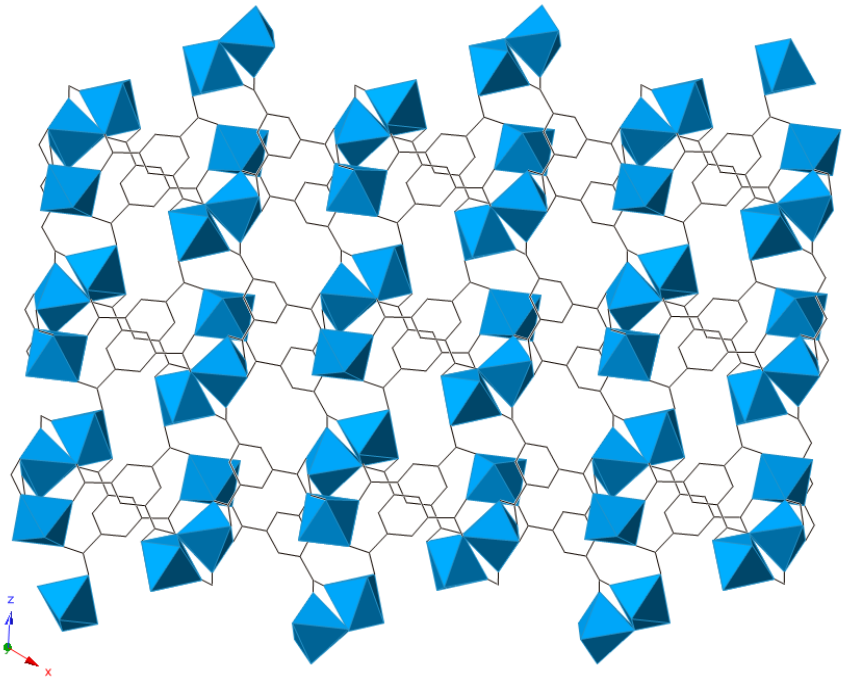

Figure 4.14. Illustration of the connectivity in the three dimensional network of [4.3], with Mg polyhedra represented in blue and BTC linkers as wire bonds. DMF is removed for clarity.

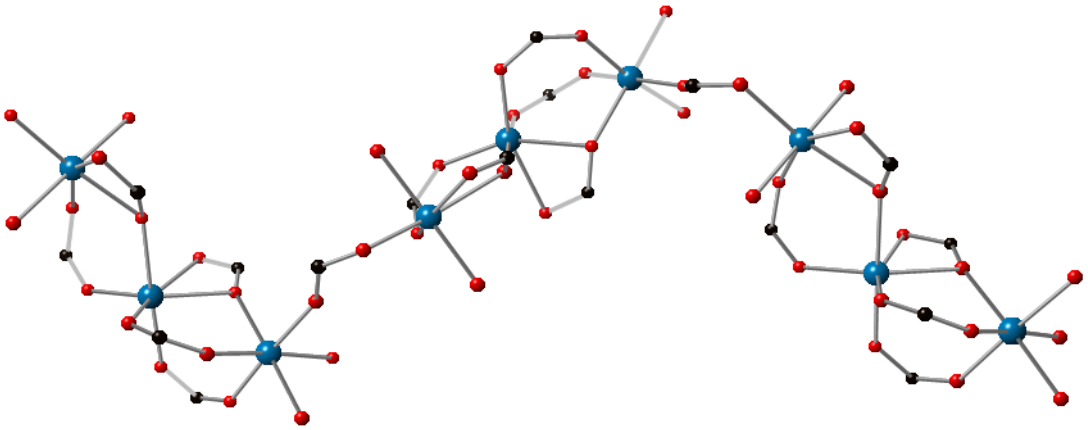

Figure 4.15. Mg carboxylate chain in compound [4.3] created by Mg triads and connecting BTC ligands.

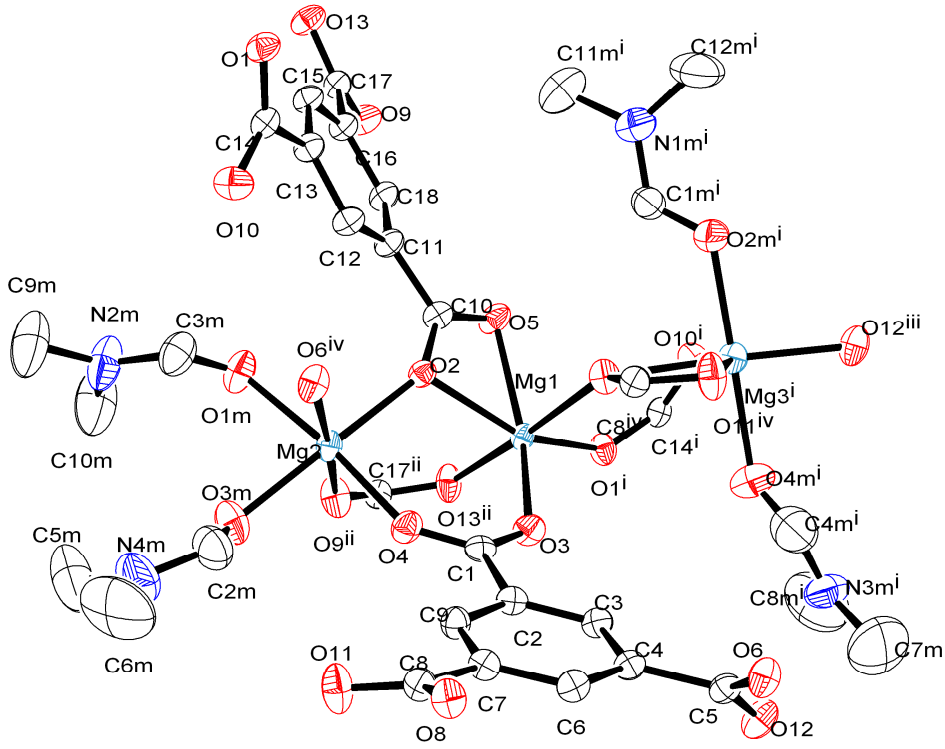

Figure 4.16. ORTEP representation of [4.3] with ellipsoids drawn at 50% probability. Symmetry operations used to generate equivalent atoms: (i) x, 1/2-y, -1/2+z ; (ii) 1-x, 1/2+y, 1/2-z ; (iii) -x, -1/2+y, -1/2-z ; (iv) -x, 1-y, -z ;

Table 4.4. Selected bond lengths (Å) and angles (°) for [4.3]

Mg(1)-O(1)	1.9977(17)	O(1)-Mg(1)-O(3)	109.14(8)
Mg(1)-O(2)	2.1537(16)	O(1)-Mg(1)-O(13)	85.63(7)
Mg(1)-O(3)	2.0323(17)	O(3)-Mg(1)-O(13)	99.30(8)
Mg(1)-O(5)	2.1909(18)	O(1)-Mg(1)-O(2)	151.75(7)
Mg(1)-O(8)	2.2161(18)	O(3)-Mg(1)-O(2)	99.07(7)
Mg(1)-O(13)	2.0657(18)	O(13)-Mg(1)-O(2)	88.54(7)
Mg(2)-O(2)	2.0587(17)	O(1)-Mg(1)-O(5)	92.47(7)
Mg(2)-O(4)	2.0050(19)	O(3)-Mg(1)-O(5)	156.44(7)
Mg(2)-O(6)	2.1090(18)	O(13)-Mg(1)-O(5)	91.39(8)
Mg(2)-O(9)	2.0120(18)	O(2)-Mg(1)-O(5)	60.03(6)
Mg(2)-O(1M)	2.074(2)	O(1)-Mg(1)-O(8)	94.64(7)
Mg(2)-O(3M)	2.079(2)	O(3)-Mg(1)-O(8)	83.47(7)
Mg(3)-O(8)	2.2690(17)	O(13)-Mg(1)-O(8)	176.97(8)
Mg(3)-O(10)	1.9898(18)	O(2)-Mg(1)-O(8)	89.81(7)
Mg(3)-O(11)	2.0984(18)	O(5)-Mg(1)-O(8)	85.58(7)
Mg(3)-O(12)	2.0275(19)		
Mg(3)-O(2M)	2.0819(19)		
Mg(3)-O(4M)	2.102(2)		

4.4.4. Discussion

Reaction temperature was used as the principal variable in our work, leading to the synthesis of three different magnesium BTC networks from identical starting solutions. The influence of the solvent DMF on the construction of the network changes with each change in temperature. Molecules of DMF are known to readily coordinate to metal centers,[10,43-44] and indeed, each of the three networks reported here contains metal-coordinated DMF molecules. However, DMF also has a tendency to hydrolyze during reactions and the byproducts of formate anions and dimethylammonium cations can be incorporated into the structure. The clearest example of this process is the formation of a class of transition metal and magnesium formates where charge is balanced by a dimethylammonium cation.[17,49] Breakdown of solvent DMF via hydrolysis also plays a vital role in the formation of two of the compounds presented in our work. Compound [4.1] is a layered network and the breakdown of DMF leads to the incorporation of dimethylamine molecules between the layers. Similarly, the formate linkers between metal centers in the two-dimensional compound [4.2] are also formed by DMF breakdown. It is interesting to note that compound [4.3] is a three-dimensional network that excludes both dimethylamine and formate.

Previous work in the synthesis of hybrid materials and coordination networks shows that increasing reaction temperature in a series of syntheses can also bring about a corresponding increase in network dimensionality.[19-20] Adding thermal energy to a system can drive a reaction that prefers one- or two-dimensional connectivity at lower temperatures to produce a three-dimensional structure. Similar effects are found in our work as two-dimensional [4.1] forms at the lowest temperature of 65° C. Raising the temperature to 100° C results in [4.2], a two dimensional network of BTC linkers that connect rings corner-shared magnesium octahedra.

Changing the temperature to 180° C leads to [4.3], in which BTC linkers connect corner-shared triads of Mg octahedra into a three dimensional network. The three-dimensional network and exclusion of any DMF breakdown byproducts means that thermodynamics plays a more important role in the formation of [4.3]. Similarly, the observation of increased M-O-M connectivity in the higher temperature phases also appears to be due to thermodynamic factors.

Recent work in our group has focused on exploring the photoactivity of magnesium coordination networks and how photoluminescence properties change when networks are constructed using different solvents or linkers.[48-49] The PL response of networks based on closed shell metals like Mg is almost exclusively linker-based, meaning that a judicious linker choice is the key to developing photoluminescent magnesium network materials. Trimesate (BTC) is known to be an emissive linker and will emit in closed shell Zn- and Cd-based networks.[15] The aromatic ring of BTC exhibits $\pi^* \rightarrow$ n and $\pi^* \rightarrow \pi$ transitions, and this allows for the comparison of ligand photoactivity when it is in the free acid state and when it is incorporated as a network linker. It would also be expected that the arrangement of ligands in a structure can facilitate an interaction between individual ring systems, leading to a more intense PL response for the network compounds. We have shown in previous studies of magnesium CNs that interactions between the ligands in the network materials can lead to shifts in the PL spectrum or an enhancement in luminescent intensity compared to the free linkers.[48-49]

Curiously, in our current work, the PL response of compounds [4.2] and [4.3] show very little PL activity over the free acid (Fig. 4.17). The two main peaks in each measurement can be attributed to the $\pi^* \rightarrow$ n and $\pi^* \rightarrow \pi$ transitions. The peak centered on 362 nm in the free linker red shifts in the fluorescence spectra of [4.2] and [4.3] to 363 nm with a slight increase in intensity. Compound [4.1] shows an even more diminished response, exhibiting no spectral shift

and in fact falling below the emission of the free ligand. The UV-Vis absorption spectrum of the free BTC ligand shows three broad absorbance peaks at 224, 266, and 284 nm. Compound [4.2] shows three broad peaks shifted to 221, 251, and 277 nm. Compound [4.3] absorbs the strongest of all network materials and the three peaks shift to 222, 257, and 282 nm. UV-Vis absorption analysis of [4.1] exhibits a similar response to the free ligand, with broad absorbance peaks at 221, 257, and 284 nm. We hypothesize that the lack of PL activity in the network materials could be partly due to quenching effects of DMF and the C−H oscillators of the methyl groups [128]. Additionally, the coordinated DMF molecules in each system can be causing an interruption of potential π system stacking. It is likely that the dimethylamine molecules within the layers of [4.1] further magnify the quenching effect leading to the reduced response observed.

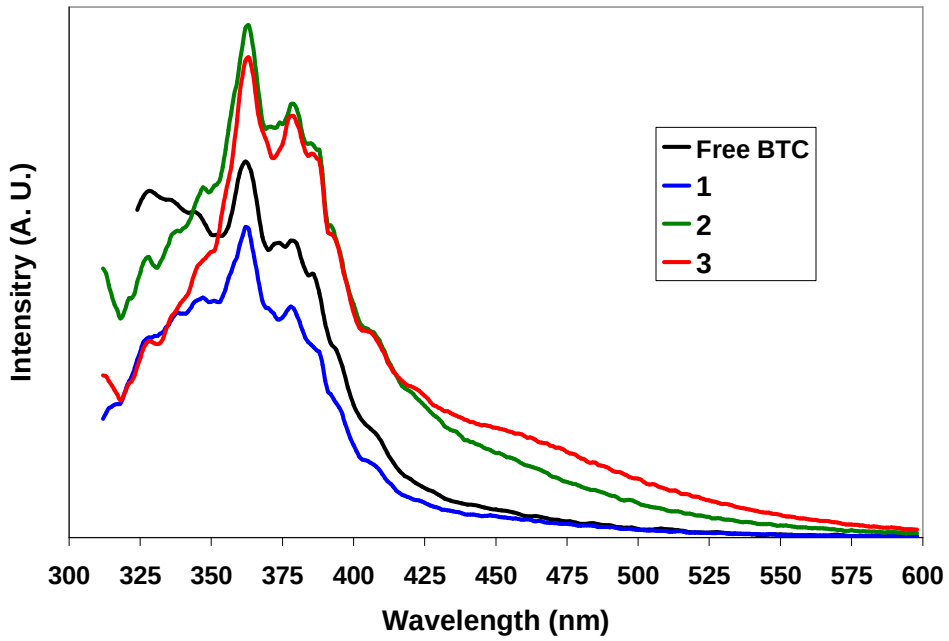

Figure 4.17. Fluorescence spectra of free BTC ligand and compounds [4.1 – 4.3], excited at 300 nm.

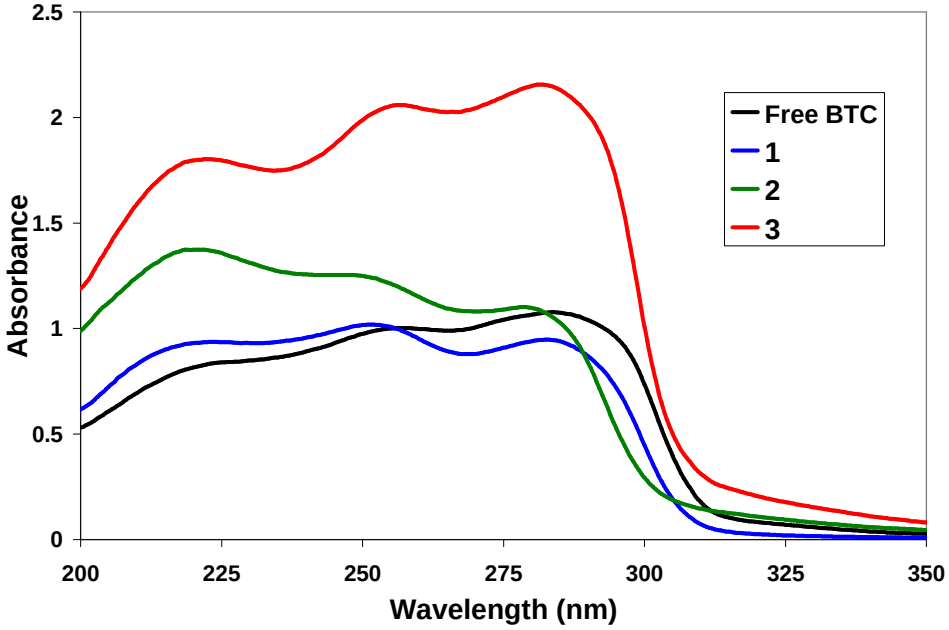

Figure 4.18. UV-Vis absorbance spectra of the free BTC ligand and compounds [4.1 – 4.3].

4.5. Conclusion

A series of three magnesium BTC coordination networks was synthesized from identical starting solutions using temperature as the synthetic variable. Our findings conform to the trend observed in previous studies in which network dimensionality and metal-oxygen connectivity increase along with increases in synthesis temperature. The effects of solvent hydrolysis and thermodynamics both play important parts in the formation of the networks in this series. At lower temperatures, the hydrolysis byproducts of DMF play the major roles in determining the network topologies, while thermodynamic factors dictate network formation at higher temperatures and lead to increased M-O-M connectivity and higher dimensionality. An examination of the photoluminescence properties of [4.1 – 4.3] reveals each has a slight red shift and weak PL response relative to that of the free BTC ligand, with the fluorescence intensity of [4.1] falling below the free ligand. These findings suggest that the metal-coordinated DMF and interlayer species are quenching the photoluminescence intensity and inhibiting the possible π system interactions of BTC ligands.

Chapter 5

Synthesis, Characterization, and Luminescence Properties of Magnesium Coordination Networks Synthesized Using an Isophthalate Linker

5.1. Abstract

Two new magnesium-based isophthalate coordination networks result from the variation of solvent and temperature: $Mg_4(IPA)_3(HCOO)_2(DMF)_2$ ([3.1]; IPA=isophthalate; space group *F*dd2, a=22.480(5) Å, b=38.210(8) Å, c=8.8690(2), *V*=7618(3) $Å^3$) is a three-dimensional network of edge-shared magnesium octahedra connected by IPA linkers. A formate group forms a bridge between the magnesium metal centers and a coordinated DMF molecule occupies the space within the channels of compound [5.1]. Mg(IPA)(EtOH) ([5.2]; space group *P*bca, a=14.1854(2) Å, b=16.326(2) Å, c=19.233(3) Å, *V*=4404.73(2) $Å^3$) also forms a three-dimensional network, which is constructed by connecting dimers of Mg_2 into chains with IPA linkers. Two solvent ethanol molecules coordinate to one of magnesium metal centers. Compound [5.1] forms using DMF as a solvent while ethanol is used as a solvent to form compound [5.2]. Topological analyses show that both structures can be described as trinodal nets with point symbols $(4^8\cdot6^2)_2(4^{10}\cdot6^5\}(4^{17}\cdot6^{11})_2$ for [5.1] and $(4^8\cdot6^2)(4^9\cdot6)(4^{31}\cdot6^{14})$ for [5.2]. Photoluminescence measurements of [5.2] and [5.2] reveal a red shift of the spectra of both compounds compared to the free IPA ligand when an excitation wavelength of 385 nm is used. Portions of this work, including structure, characterization, and properties have been published: Calderone, P. J.; Banerjee, D.; Nizami, Q.; LaDuca, R. L.; Parise, J. B. *Polyhedron* **2012**, *37*, 42.

5.2. Introduction

First row transition metals such as Mn,[1-2] Co,[129-130] and the post-transition metal Zn,[88,90,131] continue to be widely used to form MOFs and CNs, since their bonding interaction with carboxylate groups is so well-understood. More recently, the synthesis of CNs constructed with light *s*-block metals, such as lithium[36,132-133] and magnesium[40,119,134] has emerged as a means of producing lightweight networks aimed at optimizing gravimetric advantages for gas storage applications. Working with Mg^{2+} is very advantageous because it offers the benefit of a lightweight metal that behaves similarly to well-studied *3d* metal centers, such as zinc; Mg^{2+} (0.72 pm) has a similar ionic radius to Zn^{2+} (0.74 pm), both ions have comparable affinities for carboxylate ligands, and they both tend to adopt an octahedral coordination in networks[26,37].

The geometric conformation and functionality of the organic linkers play major roles in determining the topology of the final network.[135-137] This concept is illustrated when comparing magnesium CNs produced with similar ligands, as in the case of the aromatic-carboxylate linkers. For example, trimesate can coordinate from three carboxylate groups spaced 120° apart from one another on the aromatic ring,[12,19] while terephthalate linkers utilize two carboxylate groups in a 180° geometry to link metal centers.[119,134,138-139] Isophthalate (IPA) is similar to both trimesate and terephthalate in that it also has two coordinating carboxylate groups, but spaced 120° apart on the aromatic ring. Networks constructed using IPA as the sole linker are sparingly reported in the literature. The limited number of networks reported include those constructed using alkali,[140] and *3d*[23-26] metals. In fact, to date there are no reports of magnesium networks utilizing IPA as the sole linker. Furthermore, since IPA is an aromatic-carboxylate linker, excitation transitions may arise as a result of the conjugation in aromatic ring.[15-16] These $\pi \rightarrow \pi^*$ or $\pi \rightarrow$ n transitions make magnesium IPA networks good candidates for interesting

luminescence properties. Photoluminescence properties in magnesium coordination networks are rarely reported,[108,141-143] and this area may be a fruitful avenue for exploration in order to better understand the role the linker plays in their luminescent characteristics.

The solvent and temperature used in a reaction can be treated as tunable variables, since they are often identified as the factors that determine the structures of the products.[33-34] Solvents can coordinate to metal centers, reside as guests in the structure, or create *in situ* effects that alter or influence the ligands that link the metal centers.[50] For example, in recent work we have observed magnesium networks based on the same linker can have very different structures depending on which solvent is used in the synthesis. [51,143] Taking advantage of this knowledge and experience, we set out to explore the structural possibilities using different solvents and temperature for magnesium-based networks linked by IPA. Simultaneously, we have expanded the sparse reporting of luminescent properties in magnesium-based networks. Herein we report the synthesis and photoluminescence properties of two magnesium-isophthalate compounds, $Mg_4(IPA)_3(HCOO)_2(DMF)_2$ (compound [5.1]) and Mg(IPA)(EtOH) (compound [5.2]), synthesized using the solvents DMF and ethanol, respectively.

5.3. Experimental

5.3.1. Synthesis[x]

Compounds were synthesized under solvothermal conditions using Teflon®-lined 23 mL Parr stainless steel autoclaves. Magnesium nitrate hexahydrate ($Mg(NO_3)_2 \cdot 6H_2O$, Acros-organics, 99%), isophthalic acid, (Sigma-Aldrich, 95%), ethanol and N,N'-dimethylformamide (DMF, Sigma-Aldrich, 99%) were purchased and used as received.

Synthesis of [5.1], $[Mg_4(IPA)_3(HCOO)_2(DMF)_2]$

In a 23 ml Teflon liner, 0.256g (1 mmol) $Mg(NO_3)_2 \cdot 6H_2O$, and 0.166g (1 mmol) IPA were dissolved in 14.21 g DMF (molar ratio of metal salt: linker: solvent=1:1:191). The liner was transferred to a stainless steel autoclave and heated at 180°C for a period of 5 days. After cooling to room temperature, the resulting crystalline product was vacuum filtered and washed with DMF and ethanol (yield: 70% based on Mg salt, 0.150 g).

Synthesis of [5.2], Mg(IPA)(EtOH)

In a 23 ml Teflon liner, 0.256g (1 mmol) $Mg(NO_3)_2 \cdot 6H_2O$, and 0.166g (1 mmol) IPA were dissolved in 5.15 g EtOH (molar ratio of metal salt: linker: solvent=1:1:130). The liner was transferred to a stainless steel autoclave and heated at 100°C for a period of 5 days. The reaction solution was cooled and left undisturbed for 1 day to allow time for crystallization and then treated in the same manner as [5.1]. Compound [5.2] crystallizes along with a small quantity of an unidentified second phase, estimated to be roughly 14% of the bulk sample based on the heights of the most intense PXRD peaks in each phase and the TGA data obtained.

[x] Some synthesis done by Quddus Nizami

5.3.2. Structure Determination

Representative single crystals of each sample suitable for single crystal x-ray diffraction were selected under a polarizing light microscope from the bulk sample. Data for [5.1] and [5.2] were collected at room temperature (Table 1). Data for [5.1] were collected on a Bruker P4 four-circle diffractometer equipped with a SMART 1K CCD detector using Mo Kα radiation (λ=0.71073 Å) and φ and ω scans. The raw intensity data were collected and integrated with the software packages SMART[70] and SAINT[70] Data for [5.2] were collected on an Oxford Gemini diffractometer equipped with an Atlas detector, using Mo Kα radiation (λ = 0.71073 Å) and 0.5° ω scans. Raw intensity data were collected and integrated using the CrysAlisPro software package (Oxford Diffraction Ltd., Version 4, 2009). Empirical absorption corrections for [5.1] and [5.2] were applied using SADABS.[70] The crystal structures were solved using direct methods (SHELXS[70]). Mg atoms were located first, followed by the determination of all other atom positions (O, C, N) from the Fourier difference map. All non-hydrogen atoms were refined with anisotropic displacement parameters, while hydrogen atoms were placed in idealized positions using geometric constraints. One carbon atom (C20) of the ethyl group in compound [5.2] was found to be disordered and was modeled using the PART command in SHELXS.[70] The site occupancy C20 was refined to 0.42(3) for component.1 and 0.58(3) for component 2. Powder X-ray diffraction (PXRD) data were collected using a Scintag Pad X diffractometer (CuK_α; λ = 1.5418 Å) at a range of $5 < 2\theta < 40°$, with a 0.02 ° 2θ–step size and a counting time of and 1.5 s/step. The calculated and observed patterns were compared to obtain a measure of phase purity and determine how well the single crystal data represented the bulk sample from which it was taken. Powder XRD data are shown in Figures 5.1 and 5.2.

Table 5.1. Crystallographic data table for Compounds [5.1] and [5.2].

	[5.1]	[5.2]
Empirical Formula	$C_{16}H_{14}Mg_2NO_9$	$C_{20}H_{18}Mg_2O_{10}$
Formula Weight	412.90	466.96
Collection Temperature (K)	298	298
Wavelength (Å)	0.71073	0.71073
Space Group	*F*dd2	*P*bca
a (Å)	22.480(5)	14.154(3)
b (Å)	38.210(8)	16.251(4)
c (Å)	8.8690(2)	19.149(4)
α (°)	90	90
β (°)	90	90
γ (°)	90	90
Volume ($Å^3$)	7618(3)	4404.7(2)
Z	16	8
Calculated Density (g/cm^{-3})	1.440	1.408
Absorption Coefficient (mm^{-1})	0.328	0.163
F(000)	3408	1936
Crystal Size (mm)	0.40 x 0.20 x 0.15	0.60 x 0.40 x 0.30
θ range of data collection (°)	2.10 to 26.37	3.29 to 25.02
Index range	-26<=h<=28 -47<=k<=47 -11<=l<=10	-16<=h<=16 -18<=k<=19 -22<=l<=22
Total reflections	12235	28112
Independent reflections	3551 [R(int) = 0.0620]	3706 [R(int) = 0.0609]
Goodness of fit	1.048	1.029
Refinement method	Full-matrix least squares on F^2	Full-matrix least squares on F^2
Data/Restraints/Parameter	3551 / 1 / 254	3726 / 0 / 299
R1 (on $F_o^2, I > 2\sigma(I)$)	0.0490	0.0487
wR2 (on $F_o^2, I > 2\sigma(I)$)	0.1147	0.1236

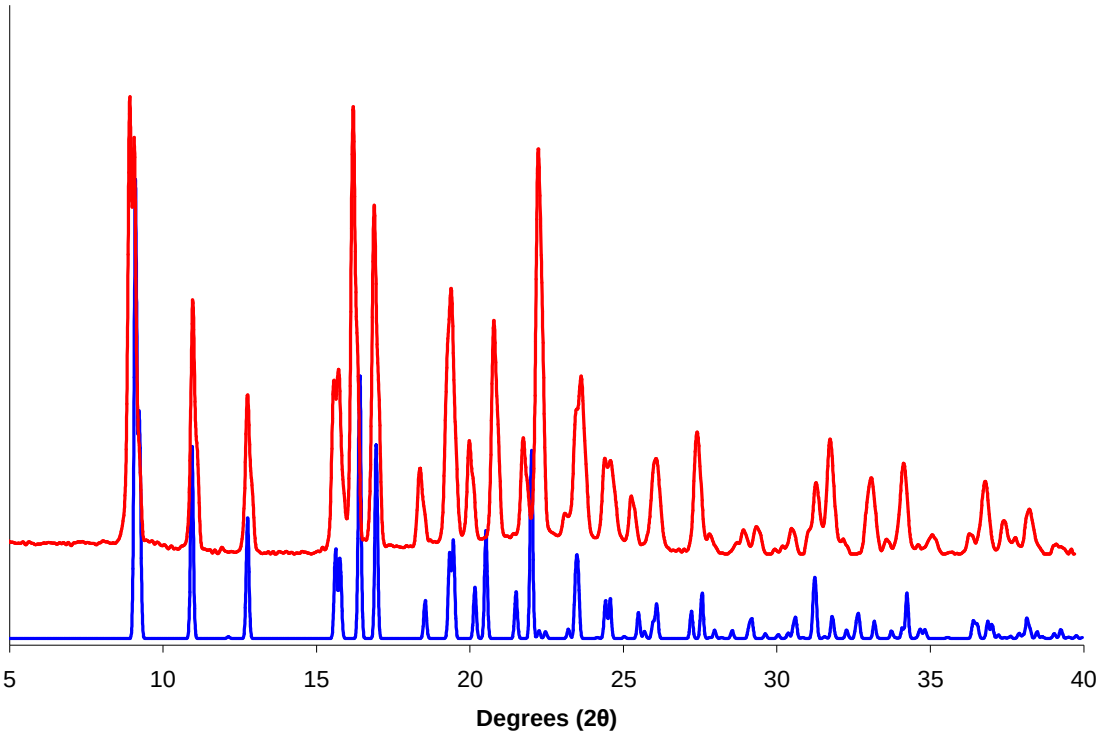

Figure 5.1. Simulated (blue) and experimental (red) powder diffraction pattern of [5.1]

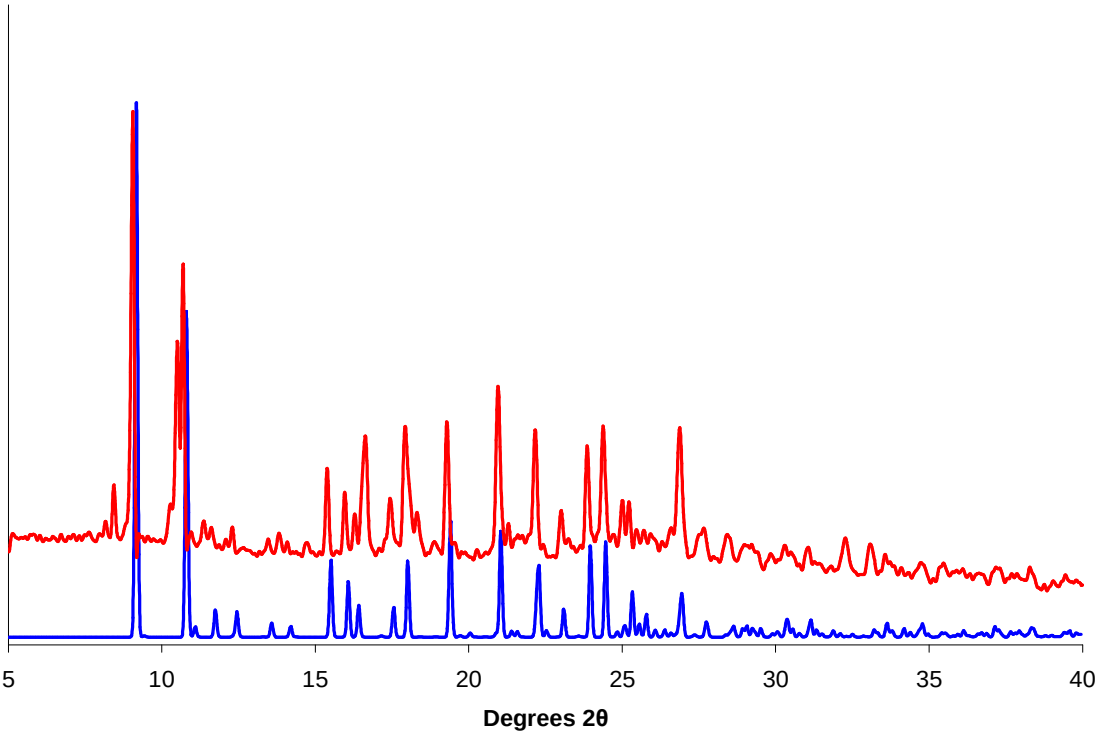

Figure 5.2. Simulated (blue) and experimental (red) powder diffraction pattern of [5.2].

5.3.3. Thermal Data

TGA/DSC data of [5.1] and [5.2] were collected using a STA 449 C Jupiter Netzsch Instrument. A powder sample was placed in an Al_2O_3 crucible for TGA-DSC and analyzed using a range of 30-650°C and 5 degrees per minute under N_2 atmosphere.

TGA analysis of compound [5.1] reveals two distinct weight losses on heating in N_2 atmosphere. The first loss occurs at 415°C and accounts for the loss of the solvent DMF molecule and formate linker (28.8% calculated; 28.6% observed), followed by a stable plateau until 500 °C. Pyrolysis of the ligand occurs after this point. Compound [5.2] also shows two distinct weight losses, and is estimated to have an impurity of 14% based on comparing the calculated and observed weight losses of the TGA. The first mass loss begins at 195 °C, corresponding to the loss of coordinated ethanol molecules (19.7% calculated; 22.7% observed) followed by a stable plateau until 475 °C where pyrolysis of the ligand occurs. Thermal data are shown in Figures 5.3 and 5.4.

5.3.4. Photoluminescence

Compounds [5.1], [5.2], and free isophthalic acid were analyzed at room temperature on a Jobin Yvon Spex Fluorolog 3 with a 10 s integration time using an excitation wavelength of 385 nm. Samples were ground into powder and then uniformly packed into the instrument sample holder.

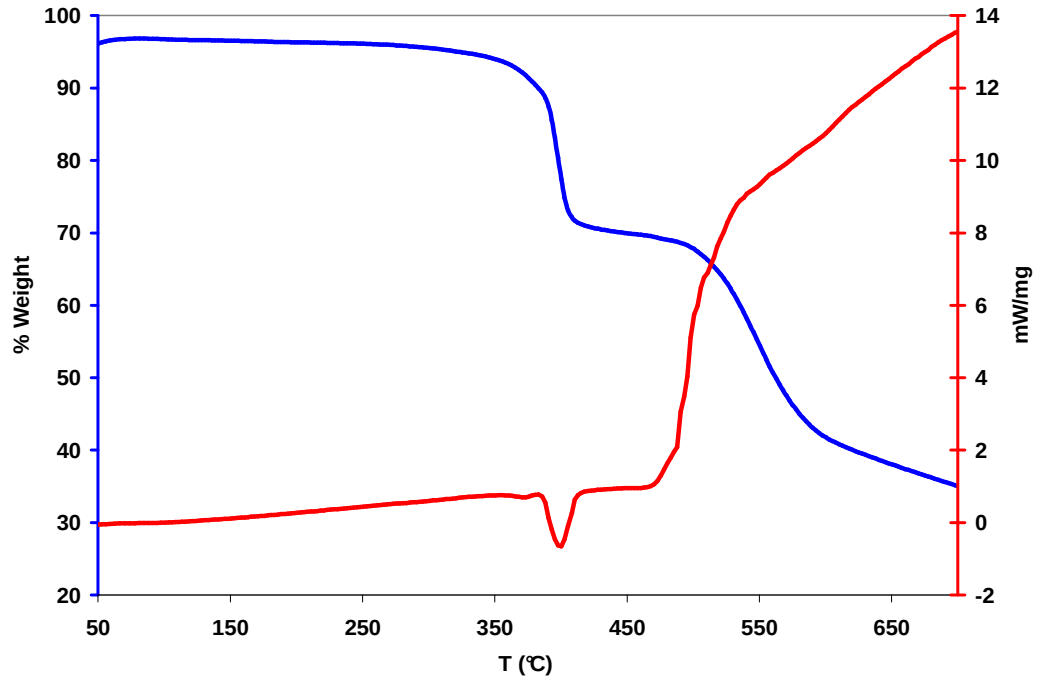

Figure 5.3. Combined TGA-DSC plot of compound [5.1]. The blue line represents the TGA plot while the red line shows the associated DSC signal.

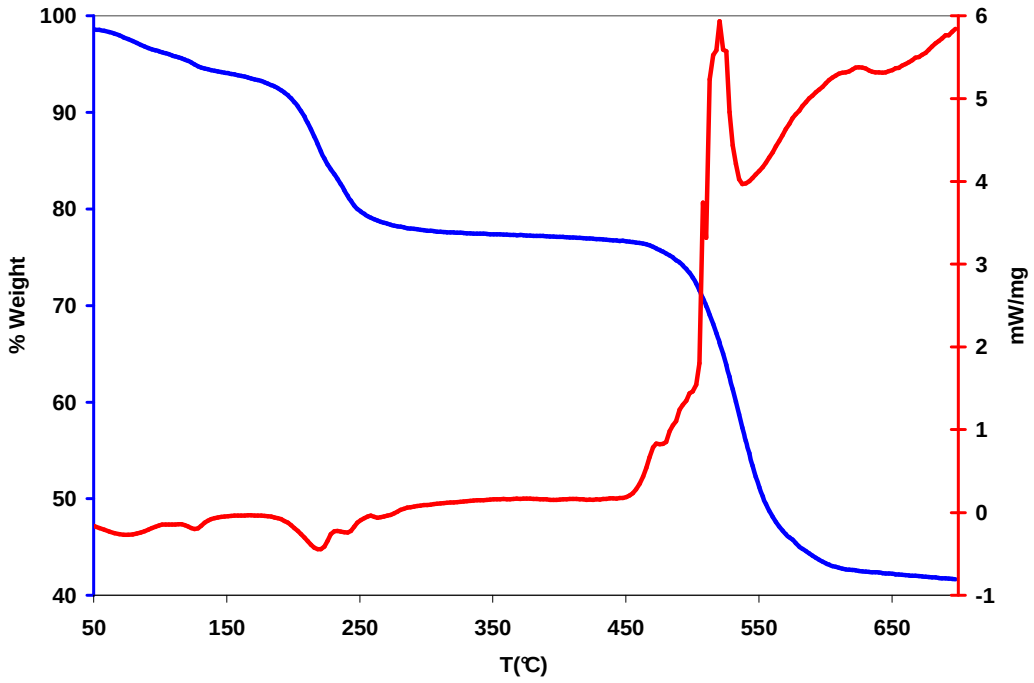

Figure 5.4. Combined TGA-DSC plot of compound [5.2]. The blue line represents the TGA plot while the red line shows the associated DSC signal.

5.4. Results and Discussion

5.4.1. Structure of [5.1], $Mg_4(IPA)_3(HCOO)_2(DMF)_2$

In compound [5.1], edge-shared dimers of magnesium octahedra connect in a corner-sharing manner to form pseudo-helical infinite chains (Figure 5.5), which are further connected into a 3-D network by two exotetradentate IPA linkers (Figure 5.6). A formate linker and two carboxylate groups from IPA linkers bridge the Mg polyhedra. The asymmetric unit consists of two crystallographically unique Mg centers, two IPA ligands, a single formate group, and a DMF molecule coordinated to Mg1 (Figure 5.7). Sites Mg1 and Mg2 are both octahedrally coordinated and separated by a distance of 3.275Å. Each dimer connects to its neighbor in the chain at a distance of 3.622Å. One IPA linker bridges the Mg chains in a $(\kappa^1\text{-}\kappa^1)\text{-}(\kappa^1\text{-}\kappa^1)\text{-}\mu_4$ coordination while the other IPA linker adopts a $(\kappa^2\text{-}\kappa^1\text{-}\mu_2)\text{-}(\kappa^1\text{-}\kappa^1)\text{-}\mu_4$ coordination (Figure 5.8). The coordination environment of site Mg1 consists of six oxygen atoms. IPA carboxylate groups contribute three of those oxygen atoms, one occupying the axial position (O3) and the other two (O6, O7) *trans* to one another in the equitoral positions. A formate group contributes two oxygen atoms which occupy the equatorial (O1) and axial (O5) positions. An oxygen atom contributed by a DMF molecule (O1M) coordinates equatorially to complete the octahedron. Site Mg2 also has six-fold oxygen coordination. The axial positions are occupied by two IPA carboxylate oxygen atoms (O2, O3). Equatorial positions are occupied by two IPA oxygen atoms *cis* to one another (O4, O8) and two formate oxygen atoms (O1, O5). Selected bond lengths and angles for [5.1] are shown in Table 5.2. The octahedral coordination of both Mg1 and Mg2 is supported by bond valence sums of 2.06 v. u. and 1.99 v. u., respectively.[144] BET analysis using N_2 gas showed that [5.1] is non-porous after solvent removal. To determine the

topology of the network an Mg_4 cluster and IPA linkers were defined as nodes, revealing the overall network to be a novel trinodal net with point symbol $(4^8 \cdot 6^2)_2(4^{10} \cdot 6^5\}(4^{17} \cdot 6^{11})_2$.

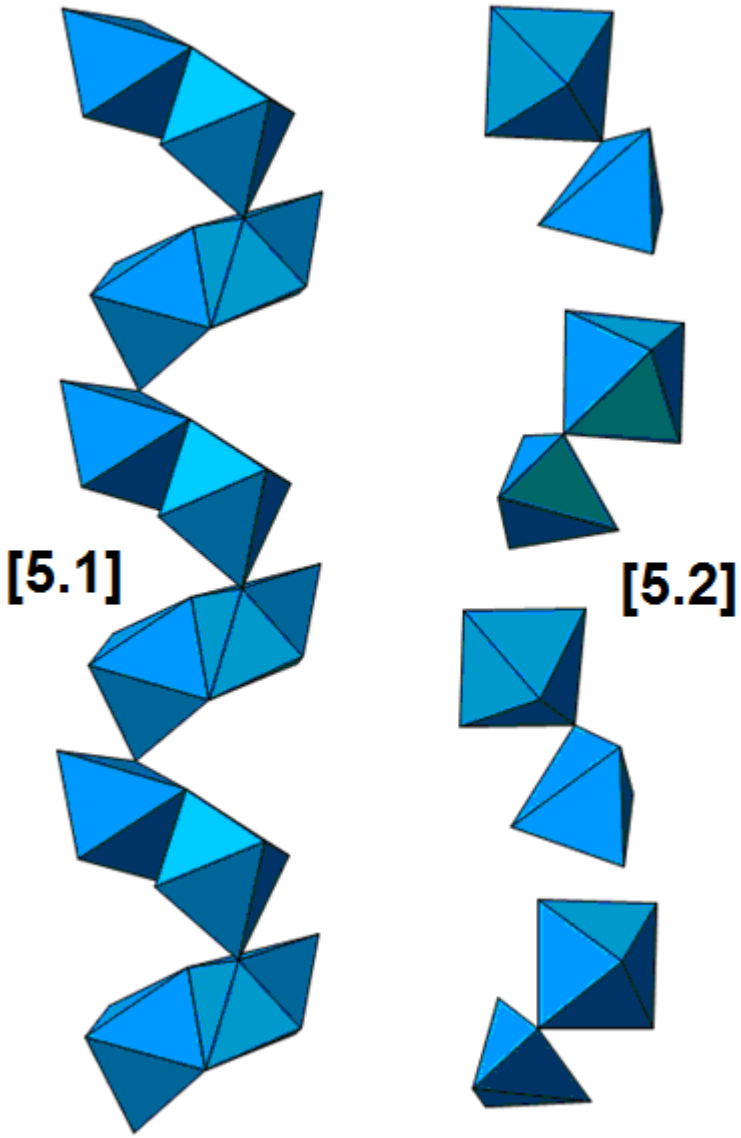

Figure 5.5. View of compounds [5.1] and [5.2] along the of the helical chains formed by Mg_2 dimers.

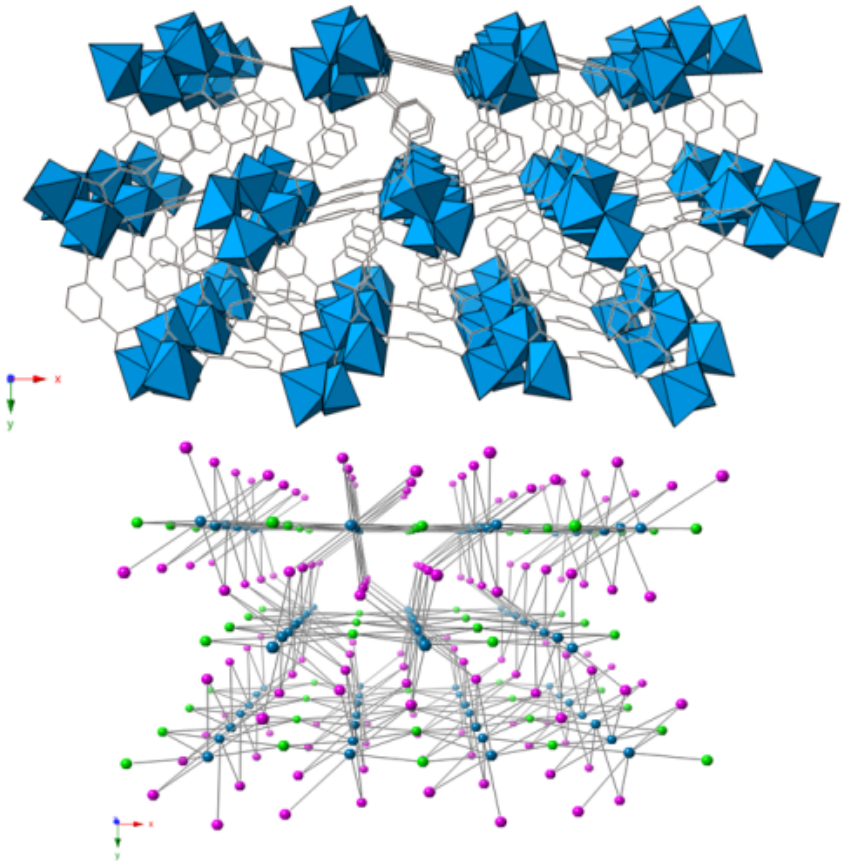

Figure 5.6. View of compound [5.1] along the [0 0 1] axis showing the overall structure (above) and simplified network connectivity (below). Mg polyhedra and metal clusters are represented in blue. IPA linkers are represented as wire bonds and nodes represented in cyan and green.

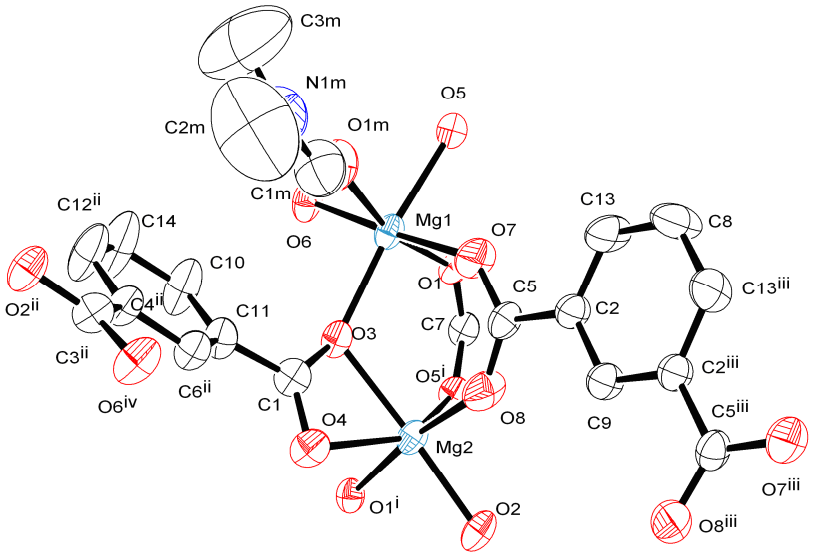

Figure 5.7. ORTEP representation of [5.1] illustrating the numbering scheme. Ellipsoids are drawn at 50% probability. Hydrogen atoms are omitted for clarity. Symmetry transformations used to generate equivalent atoms: (i) 1/2-x, -y, -1/2+z; (ii) 1/4-x, 1/4+y, 1/4+z; (iii) -x, -y, z ; (iv) -1/4+x, 1/4-y, -1/4+z

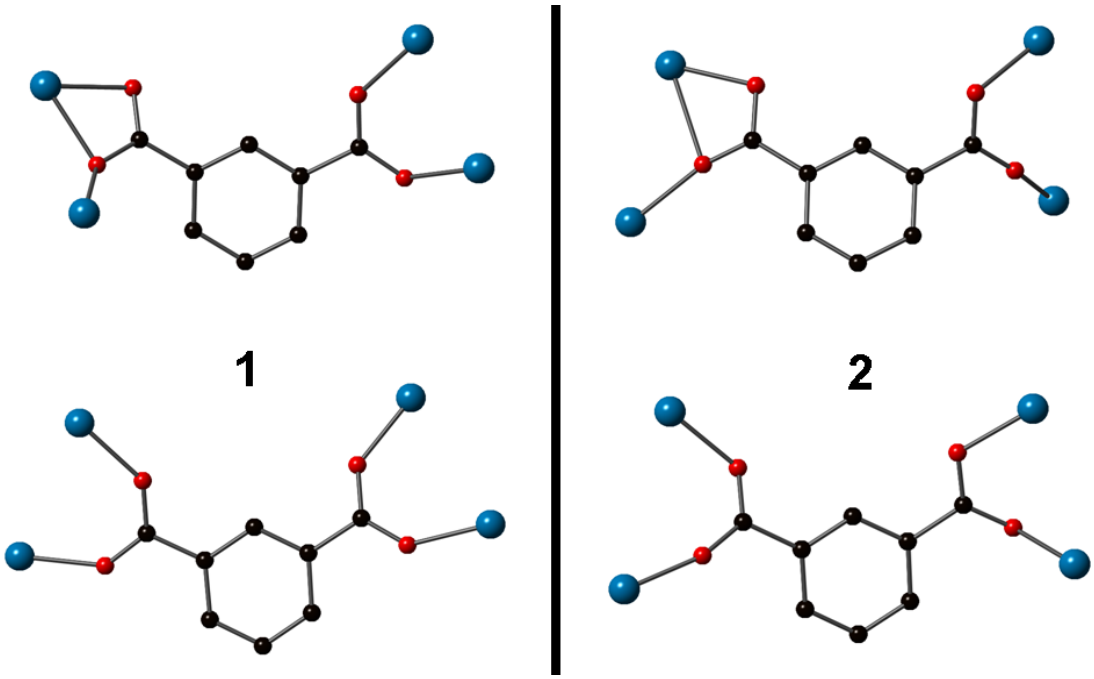

Figure 5.8. Binding modes of IPA linkers in [5.1] and [5.2].

Table 5.2. Selected bond lengths (Å) and angles (°) for [5.1]

Mg(1)-O(1)	2.153(3)	Mg(2)-O(2)	2.004(3)
Mg(1)-O(3)	2.103(3)	Mg(2)-O(3)	2.164(3)
Mg(1)-O(5)	2.201(3)	Mg(2)-O(4)	2.144(3)
Mg(1)-O(6)	2.007(3)	Mg(2)-O(5)[1]	2.102(3)
Mg(1)-O(7)	2.026(3)	Mg(1)-O(1)-Mg(2)[1]	97.28(1)
Mg(1)-O(1M)	2.072(3)	Mg(1)-O(3)-Mg(2)	116.18(13)
Mg(2)-O(1)[1]	2.211(3)	Mg(2)[1]-O(5)-Mg(1)	99.12(1)

Symmetry transformations used to generate equivalent atoms:

[1]-x+1/2,-y,z-1/2

5.4.2. Structure of [5.2], Mg(IPA)(EtOH)

Compound [5.2] is formed by corner-shared dimers of magnesium polyhedra which form a pseudo-helical chain (Figure 5.5). The chains are further connected by two exotetradentate IPA linkers to form the 3-D network (Figure 5.9). The asymmetric unit consists of two magnesium centers, two IPA linkers and two coordinating ethanol molecules (Figure 5.10). The two Mg centers are separated by a distance of 3.690Å, with each dimer connected to its neighbor at a distance of 4.173Å. The IPA coordination modes are similar to what is seen in [5.1], as one IPA linker bridges the Mg chains in a $(\kappa^1\text{-}\kappa^1)\text{-}(\kappa^1\text{-}\kappa^1)\text{-}\mu_4$ coordination, while the other IPA linker coordinates via a $(\kappa^2\text{-}\kappa^1\text{-}\mu_2)\text{-}(\kappa^1\text{-}\kappa^1)\text{-}\mu_5$ mode. Mg1 is found in an octahedral coordination consisting of six oxygen atoms. An IPA carboxylate oxygen (O5) coordinates to one equatorial position while two other IPA oxygen atoms occupy positions *cis* (O2) and *trans* (O3) to it. The octahedron is completed by two oxygen atoms contributed by ethanol molecules that coordinate in the remaining equatorial (O4) and axial (O6) positions. Mg2 is found in a distorted trigonal-bipyramidal coordination. The two Mg metal centers are joined together by carboxylate bridges, with O1 coordinating to both Mg1 and Mg2. The trigonal-bipyramidal coordination of Mg2 is formed by five carboxylate oxygen atoms of the IPA linker. The axial postions are occupied by O1 and O10. One equatorial position is occupied by O7, with O8 *cis* and O9 *trans* to O7. Selected bond lengths and angles for [5.2] are shown in Table 3. Bond valence calculations for ^{VI}Mg1 and ^{V}Mg2 result in valence sums of 2.12 v. u., and 1.99 v. u, respectively; this matches well with the theoretical value of +2.[144] The main structural feature of compound **2** is a rectangular shaped channel along the [100] direction, formed by the pseudo-chain type connectivity of carboxylate groups in the 010 and 001 directions. Coordinated ethanol molecules

are present within the channel. When an Mg_4 cluster and IPA linkers are defined as nodes, the network can be described as a novel trinodal net with point symbol $(4^8 \cdot 6^2)(4^9 \cdot 6)(4^{31} \cdot 6^{14})$

The five coordination of Mg2 was further detailed by calculating the tau parameter (τ), defined by Addison and Rao[145] to measure the degree of trigonality between trigonal bipyramidal and square pyramidal coordination. Generally, $\tau = (\beta - \alpha)/60$, where β and α are the two largest angles created in the metal coordination environment. A value of τ that is close to 1 indicates trigonal bipyramidal geometry, while a value close to 0 indicates square pyramidal geometry. In the case of Mg2, the angles of O(10)-Mg(2)-O(1) and O(9)-Mg(2)-O(7) are defined as β and α, respectively. Thus, our value of $\tau = 0.583$ indicates the Mg2 coordination has a slight trigonal bipyramidal character.

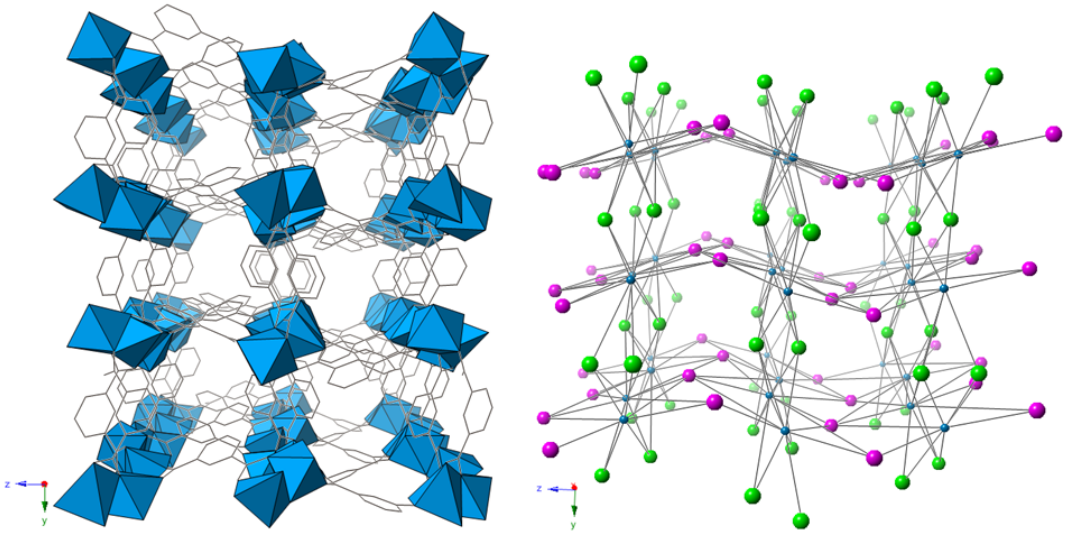

Figure 5.9. View of compound [5.2] along [1 0 0] axis showing the overall structure (left) and simplified network connectivity (right). Mg polyhedra and metal clusters are represented in blue. IPA linkers are represented as wire bonds and nodes represented in cyan and green.

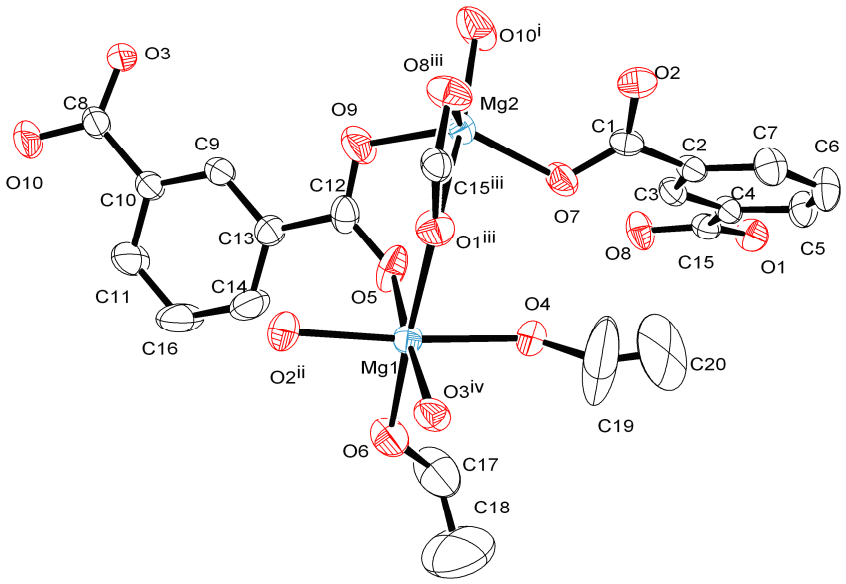

Figure 5.10. ORTEP representation of compound [5.2] illustrating the numbering scheme. Ellipsoids are drawn at 50% probability. Hydrogen atoms are omitted for clarity. Symmetry transformations used to generate equivalent atoms: (i) 1/2-x, 1/2+y, z; (ii) x, 1/2-y, -1/2+z; (iii) -1/2+x, y, 3/2-z

Table 5.3. Selected bond lengths (Å) and angles (°) for Compound [5.2].

Mg(1)-O(1)[3]	2.125(2)	Mg(2)-O(7)	1.984(2)
Mg(1)-O(2)[2]	2.060(2)	Mg(2)-O(8)[3]	2.012(2)
Mg(1)-O(3)[1]	2.024(2)	Mg(2)-O(9)	1.960(2)
Mg(1)-O(4)	2.118(2)	Mg(2)-O(10)[4]	1.923(2)
Mg(1)-O(5)	2.041(2)	Mg(1)[5]-O(1)-Mg(2)[5]	108.06(7)
Mg(1)-O(6)	2.086(2)	O(9)-Mg(2)-O(7)	125.35(9)
Mg(2)-O(1)[3]	2.429(2)	O(10)[4]-Mg(2)-O(1)[3]	160.38(9)

Symmetry transformations used to generate equivalent atoms:
[1]x,-y+1/2,z-1/2; [2]x+1/2,-y+1/2,-z+1; [3]-x+1/2,y+1/2,z; [4]x-1/2,y,-z+3/2; [5]-x+1/2,y-1/2,z

5.4.3. Discussion

Our current work provides the first examples of magnesium-based networks constructed using isophthalate as the linker. Topological analysis shows that two novel trinodal nets were produced using solvent and temperature as synthetic parameters. The use of DMF as a solvent leads to compound [5.1], in which two different effects of solvent DMF are observed. First, DMF molecules are found to coordinate to metal centers. Additionally, a breakdown of the DMF solvent to the formate anion occurs *in situ*, leading to the coordination of a formate bridge between the two metal centers. The breakdown of solvent DMF into the formate anion and the dimethylammonium cation is a well known effect, and is responsible for the formation of a number of transition metal formate frameworks[146] and a magnesium formate framework.[147] Compound [5.2] forms in EtOH and is similar to [5.1] in that it also has its solvent molecules of EtOH coordinating to the metal center. Further, it is interesting to note that one of the metal centers is 5-coordinate. The calculation of $\tau = 0.583$ indicates that the coordination can be classified as a distorted trigonal-bipyramidal geometry. Five-member coordination is uncommon for magnesium in coordination networks, as Mg shows preference for an octahedral environment in CNs.

In an attempt to gain a more complete understanding of the magnesium IPA compounds that were possible when different solvents were used in reactions, various solvent mixtures were tested at a synthesis temperature of 180°C. Solvent mixtures of DMF/EtOH and DMF/MeOH resulted in compound [5.1]. This shows that DMF is the more active solvent in these systems, demonstrating a higher coordination capability compared to EtOH and MeOH. Compound [5.1] dissolved completely in pure water and in all solvent mixtures that included water. However, [5.1] was insoluble in EtOH as well as a DMF/EtOH mixture.

Photoluminescence studies of magnesium coordination networks can provide more insight into the nature of the metal-linker interaction. When the spectrum of the magnesium CNs is compared with the spectrum of the free linker, we are able to examine how linker behavior changes when incorporated into a network material. Previous work by our group, reporting new magnesium thiophenedicarboxylate networks, noted that the observed luminescence spectra for the networks was both red-shifted, and of much higher intensity of than that of the free linker.[143] A similar effect was noted by Li et al. in a zinc coordination network using pyridine-2,4,6-tricarboxylate linkers,[148] where it was suggested that the rigid arrangement in the formation of the network led to both the enhancement and red shift. However, Fang et al. examined another zinc network linked by trimesate, noting only a red shift and not a significant increase in luminescence intensity.[116] While the presence of a heteroatom in the aromatic ring could be the reason for the enhanced the luminescence property reported in Li's work, such a physical effect also depends on a number of parameters including crystal packing and coordination environment of metal centers.

The magnesium IPA networks in our current work were examined in the same manner as our previous experiments in the hopes of better understanding the effect of linker choice on the luminescence properties of CNs. The free IPA ligand as well as compounds [5.1] and [5.2] show similar behavior when excited at 385 nm (Figure 5.11). While the broad peak centered on 438 nm in free IPA is red shifted to 480 nm in compound [5.1] and 455 nm in compound [5.2], no significant difference in intensity is noted when comparing the free ligand to the network compounds**.** In compound [5.2], it is expected that the small sample impurity has a negligible effect on the observed luminescence properties. The presence of the peaks in all spectra may be attributed to the $\pi \rightarrow \pi^*$ or $\pi \rightarrow$ n transitions of the ligand aromatic ring, while the observed shift

of the broad peaks in [5.1] and [5.2] likely occurs due to the coordination of the IPA ligand to the Mg metal center. In comparison to our previous work with 2,5 thiophenedicarboxylate[143] and to other results,[116,148] the lack of an increase in intensity observed when using the IPA ligand indeed suggests that heterocyclic aromatic ring based linkers may be a better choice to construct magnesium coordination networks for photoluminescence applications.

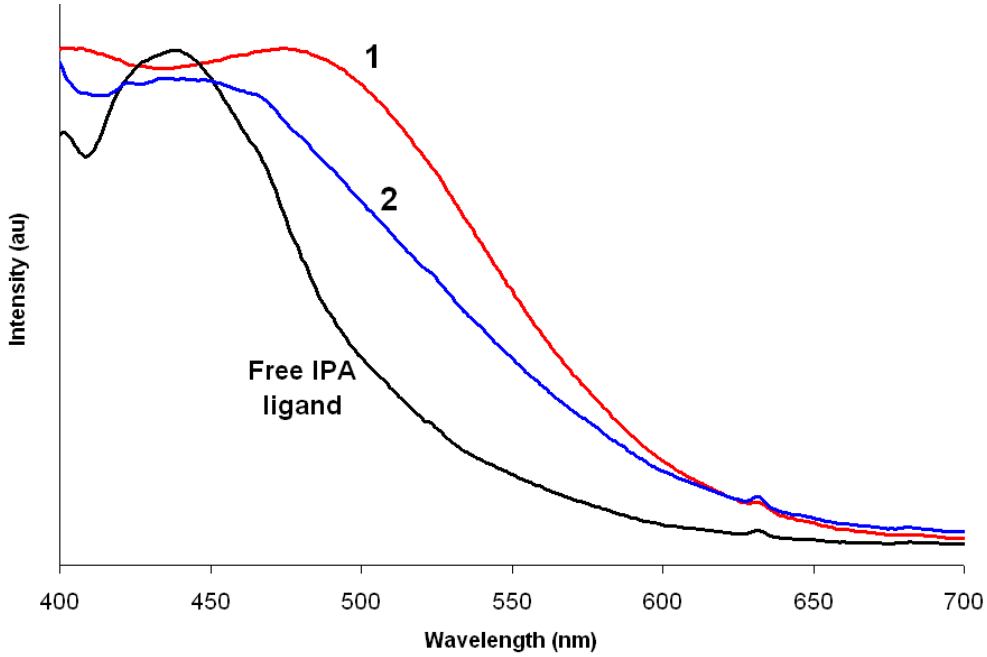

Figure 5.11. Photoluminescence spectra highlighting the red shift of compounds [5.1] (1) and [5.2] (2) compared to that of free IPA ligand (excitation wavelength at 385nm). Compound [5.2] contained a small percentage of impurity, which was unlikely to affect the photoluminescence behavior.

5.5. Conclusion

Two novel magnesium isophthalate networks were synthesized using identical metal-to-linker ratios. Topological analyses shows that [5.1] is a trinodal net with point symbol $(4^8 \cdot 6^2)_2(4^{10} \cdot 6^5)(4^{17} \cdot 6^{11})_2$ while [5.2] is a trinodal net with point symbol $(4^8 \cdot 6^2)(4^9 \cdot 6)(4^{31} \cdot 6^{14})$. The differences in the network topologies arise when either DMF or ethanol are used a reaction solvent. Photoluminescence measurements reveal that the predominant peak in the spectra of compounds [5.1] and [5.2] are red-shifted relative to the free IPA linker, likely due to the ligand coordination to the metal center. In contrast with our recently reported Mg-thiophenedicarboxylate networks,[143] no significant increase in photoluminescence intensity is noted for either network compound compared to the free ligand. These findings offer a better understanding of how linker choice can affect luminescence properties of resulting coordination networks**.**

Chapter 6

Lanthanide Metal-Organic Frameworks based on a Thiophenedicarboxylate Linker: Characterization and Luminescence Properties

6.1. Abstract

Three topologically-related lanthanide thiophenedicarboyxlate (TDC) metal-organic frameworks were synthesized using an identical metal:linker:solvet ratio. $Nd(TDC)_3(EtOH)_3(H_2O)\cdot H_2O$ ([6.1]**;** space group ***Cc***, a = 24.035(2) Å, b = 10.063(1) Å, c = 18.998(1) Å, β = 132.41(1)°) contains the same metal-TDC coordination modes as two other compounds which have the isostructural formula $Ln(TDC)_3(EtOH)_3(H_2O)\cdot H_2O$; Ln = Tb ([6.2]; space group $\boldsymbol{P\bar{1}}$, a = 12.807(9) Å, b = 14.557(1) Å, c = 19.128(1) Å, α =106.66(2)°, β = 105.62(2)°, γ = 93.691(2)°), Dy ([6.3]; space group $\boldsymbol{P\bar{1}}$, , a = 12.793(8) Å, b = 14.682(1) Å, c = 19.077(1) Å, α = 107.12(1)°, β = 105.54(1)°, γ = 93.518(2)°). An equimolar solvent mixture of water and ethanol causes both types of solvent molecules coordinating to metal centers. The fluorescence spectra of compounds [6.2] and [6.3] show characteristic bands related to their respective metal ions, but Dy-based [6.3] is very weak compared to Tb-based [6.2], indicating coordinating solvent molecules may be quenching Dy fluorescence. Portions of this work, including structure, characterization, and properties come from Calderone, P. J.; Plonka, Anna M.; Banerjee, D.; Nizami, Quddus A.; Parise, J. B. *Solid State Sci*. **Submitted**.

6.2. Introduction

Microporous MOFs are potentially selective sorbers of gases.[86,147,149-151] Further, the metal centers used to form frameworks can have variable coordination numbers which depend on metal-coordinated solvents and ligand geometry. This variance affects the species which can be incorporated within the pore volumes of these solids. Combining the potential for gas sorption with the characteristic luminescent properties of MOFs might lead to the discovery of gas-selective sensors. MOFs constructed with photoluminescent linkers and metals such as the lanthanides, have properties that can be tuned since their photoactivity depends dependent on the combination and interaction of the metal and linker.[16,76]

Lanthanide luminescence occurs with the excitation and subsequent relaxation of *f* electrons,[76] resulting in very specific color emissions unique to each metal ion. However, the low molar absorbtivity of the lanthanide ions leads to weak emission from direct metal excitation. One way around this is the use of coordinated or guest organic antenna ligands.[15,33,76,152] Through the "antenna effect", the ligands, often with high degrees of conjugation, further sensitize the metal excitation and enhance the luminescence intensity of the complex. When constructing lanthanide MOFs, the linkers serving as connective building blocks for the structure can also function as antennae for the metal.[28,153-156]

Networks based on lanthanide metals offer the possibility of new topologies not normally accessible when using other metals.[157-160] Lanthanide metal ions have variable coordination environments depending on the ligand used and can adopt larger coordination spheres than more common metal centers, such as the *3d* series. Additionally, the lanthanide contraction effect—a decrease in atomic radius with increasing atomic number—can influence how linkers coordinate and allows for additional degrees of freedom across the lanthanide series.[80,161] This makes the

coordination geometry and preferences of the ligand important factors in lanthanide MOF design. Carboxylate-based linkers are a good choice when constructing lanthanide networks because the Ln^{3+} ions are hard acceptors, making coordination with the hard carboxylate groups more favorable. To this end, the 2,5-thiophenedicarboxylate (TDC) has been used previously as a linker in lanthanide MOFs because its multiple coordination modes lead to a number of different topologies.[31,161-165]

Our synthetic approach builds on previous reports of lanthanide-TDC MOFs by using the alternative solvents and synthetic conditions. It has been shown that varying the solvent or temperature in a given synthetic system can cause changes in the topology and properties of the product.[51,166-167] Solvent activity can dictate how the molecules will coordinate to metal centers or occupy pore space, thus directing the assembly of the overall structure.[50] Our work sought to apply this knowledge using an equimolar water/ethanol mixture as a solvent and explore its effects on structure and properties in the resulting lanthanide networks. Herein, we report the synthesis and structural characterization, of a series of three related lanthanide-TDC MOFs, $Nd(TDC)_3(EtOH)_3(H_2O)$, and $Ln(TDC)_3(EtOH)_3(H_2O)\cdot 2H_2O$ (Ln = Tb, Dy). Additionally, the luminescence properties and structural origin of these compounds are examined and discussed.

6.3. Experimental Details

6.3.1. Synthesis[x]

Compounds [6.1 – 6.3] were synthesized under solvothermal conditions using Teflon – lined Parr stainless steel autoclaves. Starting materials, including neodymium nitrate pentahydrate ($Nd(NO_3)_3.5H_20$, 99.9%, Alfa Products), terbium nitrate pentahydrate ($Tb(NO_3)_3.5H_20$, 99.9%, Aldrich), dysprosium nitrate pentahydrate ($Dy(NO_3)_3.5H_20$, 99.99%,

[x] Some synthesis done by Quddus Nizami.

Reaction), 2,5-thophenedicarboxylic acid (2,5-TDC, $C_6H_4O_4S$, 97%, Sigma-Aldrich), ethanol (C_2H_5OH, 99%, Sigma-Aldrich) and distilled water (H_2O), were used without any further purification.

Synthesis of [6.1] Nd $(TDC)_3(EtOH)_3(H_2O)\cdot H_2O$

In a 23 ml Teflon liner, 1 mmol (0.435g) of $Nd(NO_3)_3\cdot 5H_2O$ and 1 mmol (0.172g) of 2,5-TDC were dissolved in 8.52 grams of EtOH and 3.33 grams of distilled H_2O and stirred for 3 hours to achieve homogeneity (molar ratio of metal salt:ligand:ethanol:water = 1:1: 185: 185]. The Teflon liner was transferred to stainless steel autoclave and the heated for a period of three days at 100°C. After cooling to room temperature, the product was recovered by filtration and subsequently washed with ethanol and water. Elemental analysis for C, H, and N found 29.70% C, 1.96% H, <0.5% N (calc. 30.21%C, 2.53% H, 0.00% N).

Synthesis of [6.2] $Tb(TDC)_3(EtOH)_3(H_2O)\cdot H_2O$

The synthesis was the same as [6.1], except that the metal source used was $Tb(NO_3)_3\cdot 5H_2O$ Elemental analysis for C, H, and N found 27.80% C, 2.39% H, <0.5% N (calc. 28.57%C, 2.53% H, 0.00% N).

Synthesis of [6.3] $Dy(TDC)_3(EtOH)_3(H_2O)\cdot H_2O$

The synthesis was the same as [6.1], except that the metal source used was $Dy(NO_3)_3\cdot 5H_2O$ Elemental analysis for C, H, and N found 27.72% C, 2.19% H, <0.5% N (calc. 28.56 C, 2.50% H, 0.00% N).

6.3.2. X-ray Crystallography[y]

Suitable crystal of compounds [6.1 – 6.3] were selected from the bulk samples and were mounted on a glass fiber using epoxy. Reflections were collected at ChemMatCars (Sector 15) at the Advanced Photon Source using a three-circle Bruker D8 diffractometer equipped with an APEXII detector at 100 K using synchrotron X-ray radiation (λ = 0.41328Å) and 0.5° φ scans. The raw intensity data were analyzed using the APEXII suite of software.[71] Raw intensity data were integrated with the software packages SMART[70] and SAINT.[70] Empirical absorption corrections for [6.1 – 6.3] were applied using SADABS.[70] Structures were solved using direct methods and refined using SHELXS.[70] Mg atoms were located first, followed by the determination of all other atom positions (O, C, N) from the Fourier difference map. Most of the non-hydrogen atoms were refined with anisotropic displacement parameters, while hydrogen atoms were placed in idealized positions using geometric constraints. Bulk sample identification and phase purity were determined using powder X-ray diffraction. The data were collected using a Scintag Pad-X diffractometer equipped with Cu Kα (λ = 1.5405 Å) radiation within a range of $5° \leq 2\theta \leq 40°$ (step size: 0.02°, counting time: 1s/step). Powder diffraction data are shown in Figures 6.1 – 6.3.

[y] Some crystallographic structure solution done by Anna Plonka

Table 6.1. Crystallographic data for [6.1 – 6.3]

	[6.1]	[6.2]	[6.3]
Empirical Formula	$C_{24}H_{25}Nd_2O_{17}S_3$	$C_{48}H_{50}Tb_4O_{34}S_6$	$C_{48}H_{50}Dy_4O_{34}S_6$
Formula Weight	970.13	1994.99	2013.24
Collection Temperature (K)	100	100	100
Wavelength (Å)	0.41328	0.41328	0.41328
Space Group	Cc	P -1	P -1
a (Å)	24.0351(2)	12.807(9)	12.793(8)
b (Å)	10.0634(1)	14.557(1)	14.682(1)
c (Å)	18.9982(1)	19.128(1)	19.077(1)
α (°)	90	106.66(2)	107.12(1)
β (°)	132.414(1)	105.62(2)	105.54(1)
γ (°)	90	93.691(2)	93.518(2)
Volume ($Å^3$)	3392.58(7)	3251.2(4)	3261.1(4)
Z	4	2	2
Calculated Density (g/cm-3)	1.899	2.038	2.047
Absorption Coefficient (mm-1)	0.771	1.083	0.170
F(000)	1892	1924	1936.8
Crystal Size (mm)	0.08 x 0.04 x 0.01	0.10 x 0.05 x 0.02	0.08 x 0.05 x 0.02
θ range of data collection	2.23 to 14.41	2.21 to 15.99	2.20 to 14.97
Index range	$-28 \le h \le 28$ $-12 \le k \le 12$ $-22 \le l \le 22$	$-17 \le h \le 16$ $-19 \le k \le 19$ $-21 \le l \le 25$	$-15 \le h \le 15$ $-18 \le k \le 18$ $-22 \le l \le 23$
Data/Restraints/Parameters	5868/341/353	15333/0/812	12779/0/778
R1 (on Fo2,I > 2σ(I))	0.0542	0.0423	0.0430
wR2 (on Fo2,I > 2σ(I))	0.1386	0.1011	0.1005

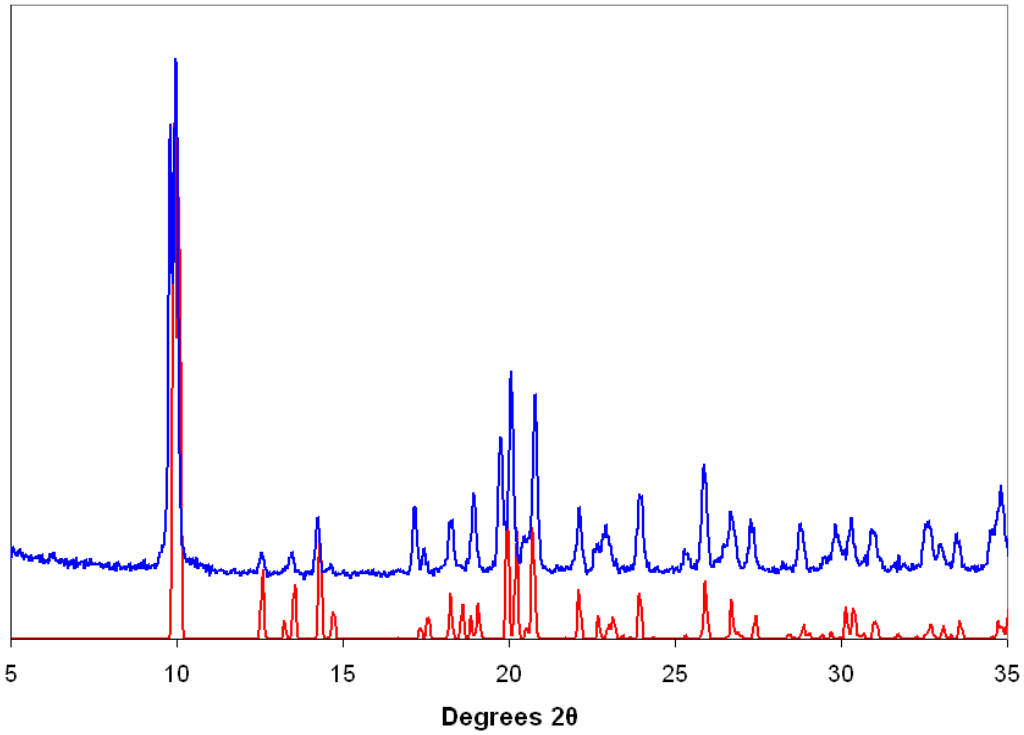

Figure 6.7. Calculated (red) and experimental (blue) powder XRD pattern of [6.1].

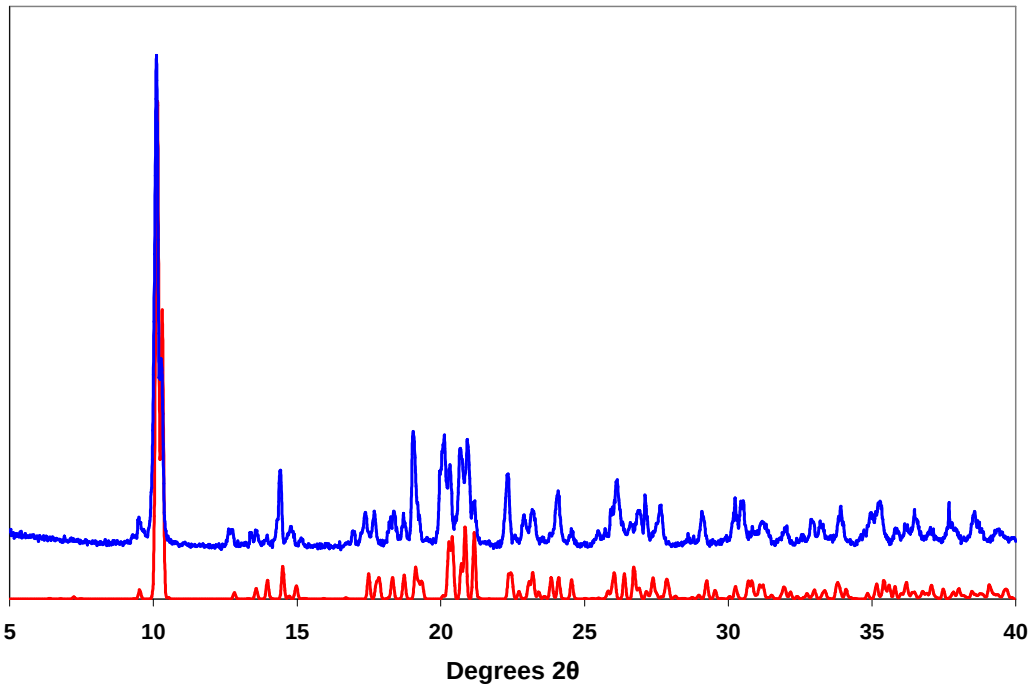

Figure 6.2. Calculated (red) and experimental (blue) powder XRD pattern of [6.2].

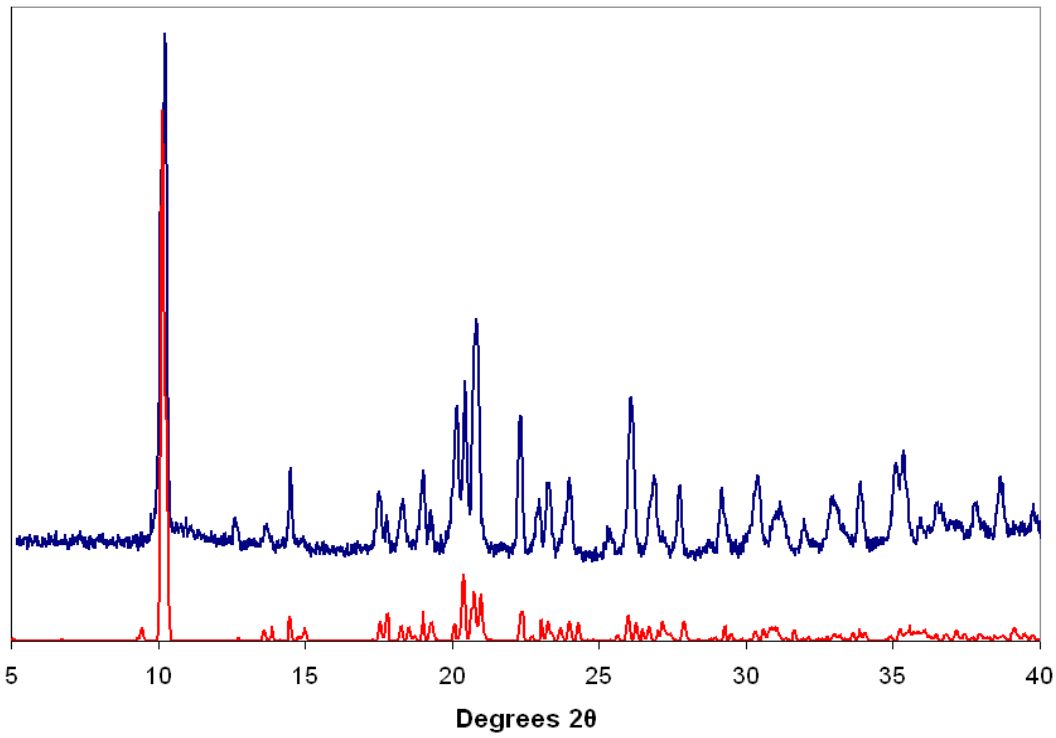

Figure 6.3. Calculated (red) and experimental (blue) powder XRD pattern of [6.3].

6.3.3. Thermal Data

Combined TGA-DSC data of [6.1 – 6.3] were collected using a STA 449 C Jupiter Netzch instrument. Powder samples were placed in an Al_2O_3 crucible for TGA-DSC and analyzed using a range of 30-650 °C and 5 degrees per minute temperature under N_2 atmosphere. Theremal data are shown in Figures 6.4 – 6.6.

The thermogravimetric data of [6.1] shows two weight losses with the first beginning at approximately 235° C and accounting for a loss of two ethanol molecules. After a plateau, the second weight loss begins at 415° C and accounts for the removal of remaining coordinating solvent and pyrolysis of the ligand.

Thermogravimetric data of [6.2] and [6.3] show no well defined weight losses before the first plateaus, beginning at approximately 210° C and 200° C, respectively and account for the loss of two ethanol molecules. The second major weight losses for [6.2] and [6.3] occur at 420° C and 445° C, respectively and account for the loss of remaining coordinated solvent and pyrolisis of the ligands.

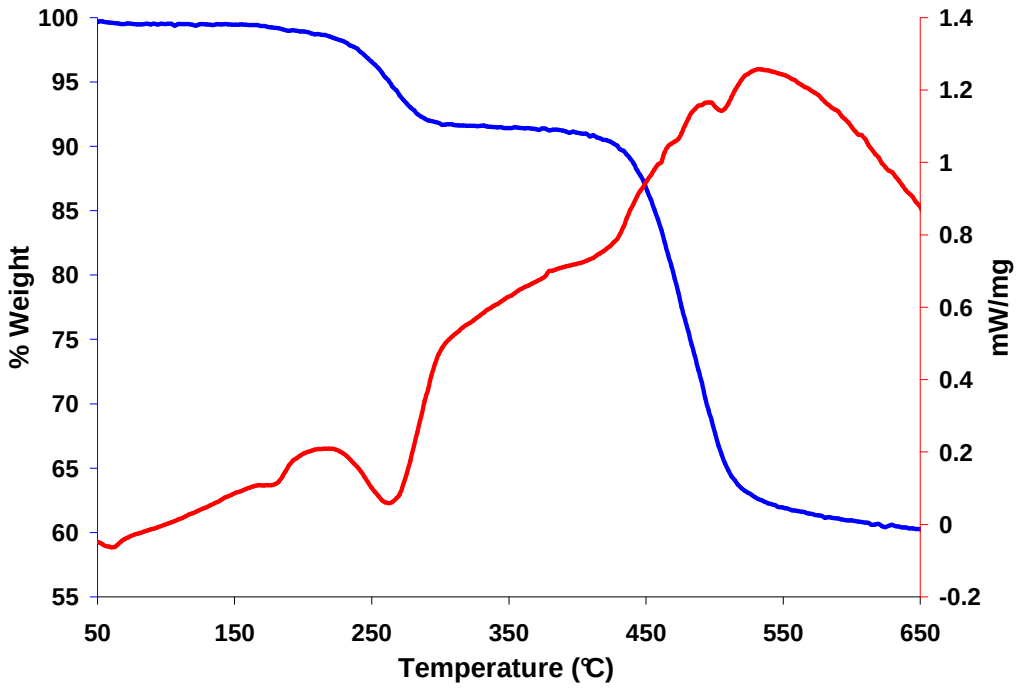

Figure 6.4. Combined TGA (blue) and DSC (red) data for [6.1].

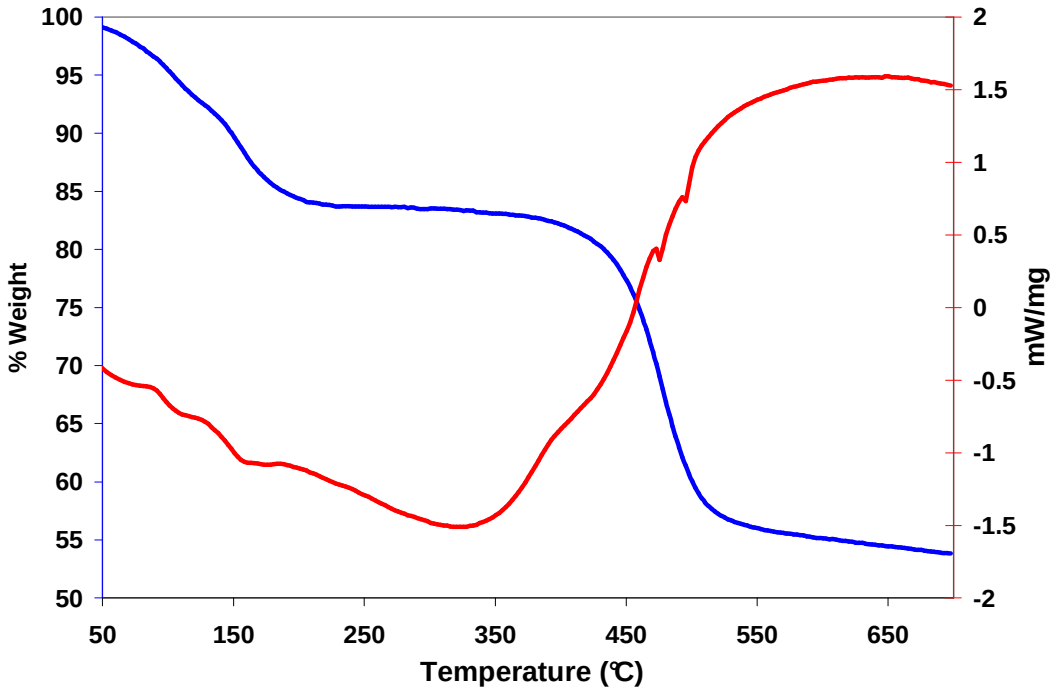

Figure 6.5. Combined TGA (blue) and DSC (red) data for [6.2].

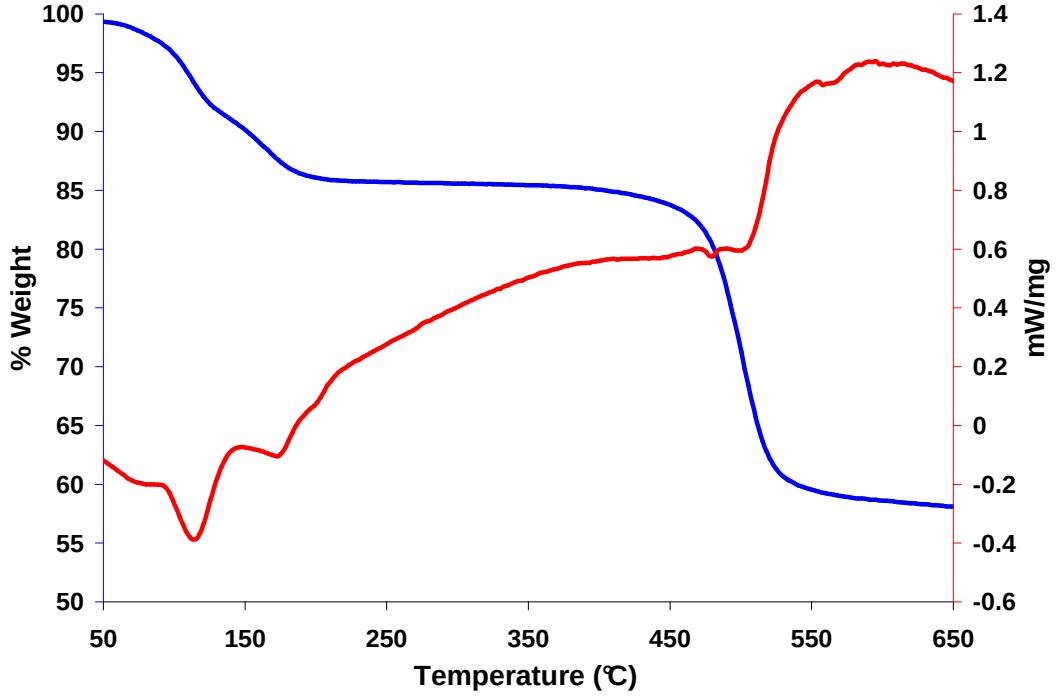

Figure 6.6. Combined TGA (blue) and DSC (red) data for [6.3].

6.3.4. Photoluminescence

The preparation of samples for fluorescence analysis of [6.1 – 6.3] and free TDC followed the procedure as described below. Solid samples were ground into powder. Quartz slides of dimension 16mm x 60mm were first rinsed with de-ionized water and ethanol, dried, and then scotch (black) tape was applied to the lower half of the dried slide. The tape was then removed to leave behind a small amount of adhesive, onto which a continuous thin layer of sample was sprinkled. Excess sample was removed by gently tapping the slide face down. The effect of glass slide and adhesive was evaluated and found to be negligible.

6.4. Results and Discussion

6.4.1. Structure of [6.1], $Nd(TDC)_3(EtOH)_3(H_2O)\cdot H_2O$

The structure of [6.1] consists of chains of individual 8-coordinate Nd polyhedra linked together with TDC caboxylate groups. The chains are connected via a TDC linker into a diamond-like three-dimensional network (Fig 6.7). Both EtOH molecules and H_2O molecules coordinate to the metal centers. The asymmetric unit of [6.1] consists of two unique Nd atoms, three TDC linkers, three metal-coordinated EtOH molecules, one metal-coordinated H_2O molecule, and one guest H_2O molecule. Two of the TDC linkers adopt the (κ^2)–$(\kappa^1$-$\kappa^1)$–μ_3 coordination mode, while the other TDC linker coordinates in the $(\kappa^1$-$\kappa^1)$–$(\kappa^1$-$\kappa^1)$–μ_4 mode (Fig. 6.8). The coordination environment of Nd1 consists of eight oxygen atoms at an average Nd-O distance of 2.444 Å (Table 6.2); two oxygen atoms come from a bidentate TDC carboxylate group (O3, O4), four from monodentate carboxylate groups (O2, O8, O10, O12), and two from coordinated ethanol molecules (O2E, O3E). Eight oxygen atoms also make up the coordination environment of Nd2 coordinating at an average distance of 2.455 Å; two oxygen atoms come from a bidentate TDC carboxylate group (O5, O6), four from monodentate carboxylate groups (O1, O7, O7, O11), one from a coordinated ethanol molecule (O1E) and one from a coordinated water molecule (O1W). A guest H_2O molecule (O2W) is also present. To determine the topology of the network, an Nd_3 cluster was defined as an 11-connected node and the three TDC linkers were defined as 3-, 4-, and 4-connected nodes respectively. A calculation using TOPOS software[168] was done, revealing a tetranodal net with a point symbol of $(4^2\cdot6)(4^{24}\cdot6^{30}\cdot8)(4^3\cdot6^3)(4^4\cdot6^2)$. Crystallographic details are shown in Table 6.1.

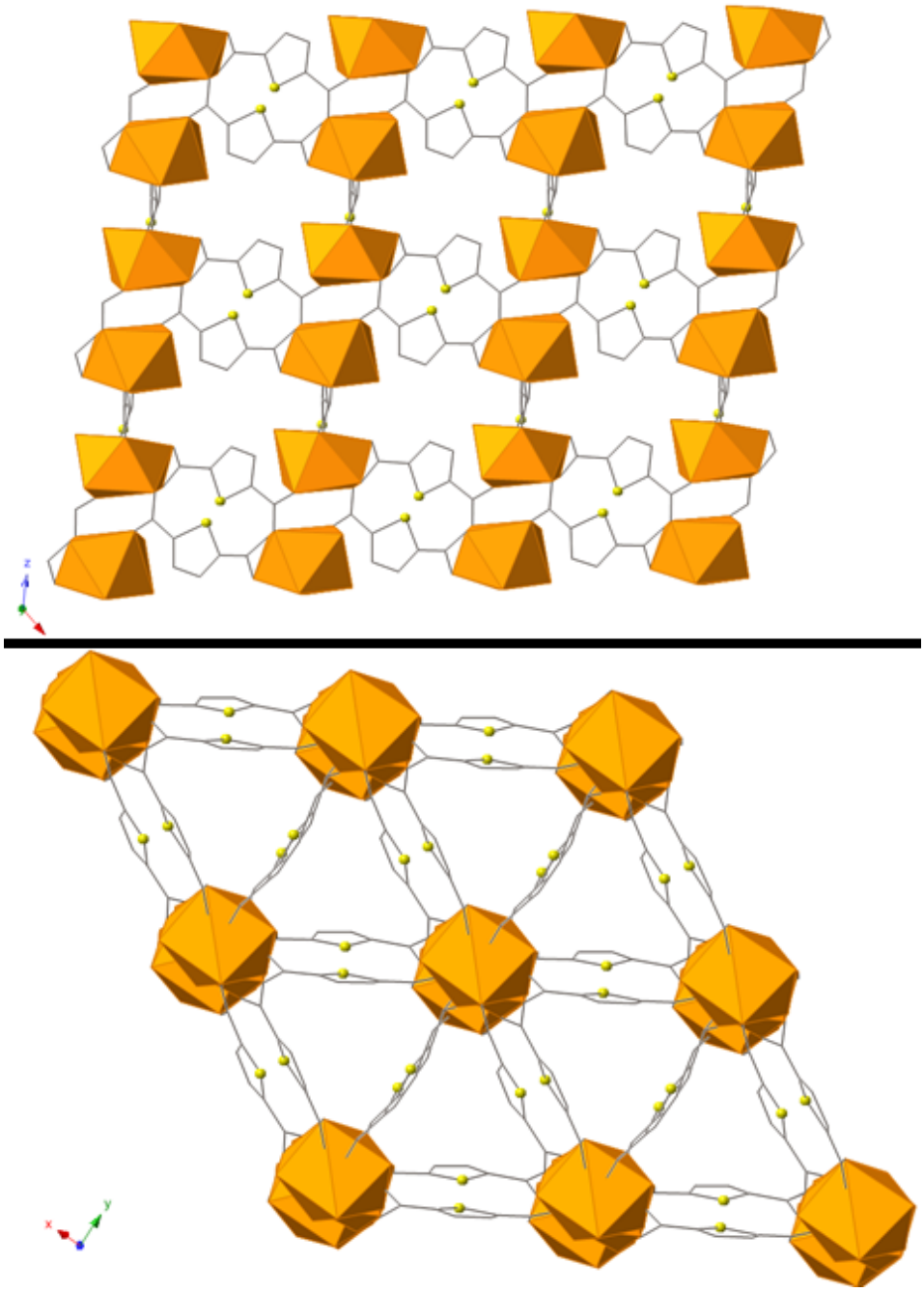

Figure 6.7. The network of [6.1] as viewed in the [0 1 0] (top) and [0 0 1] (bottom) directions. A similar network connectivity is observed in the networks of [6.2] and [6.3].

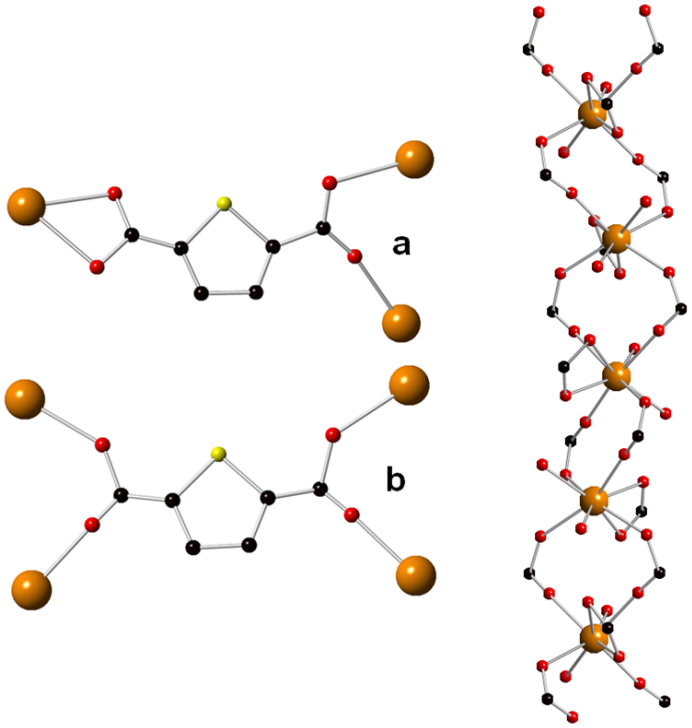

Figure 6.8. Coordination modes of (κ^2)–(κ^1-κ^1)–μ_3 (a) and (κ^1-κ^1)–(κ^1-κ^1)–μ_4 (b) for TDC (left) and the metal carboxylate chain (right) observed in [6.1 – 6.3].

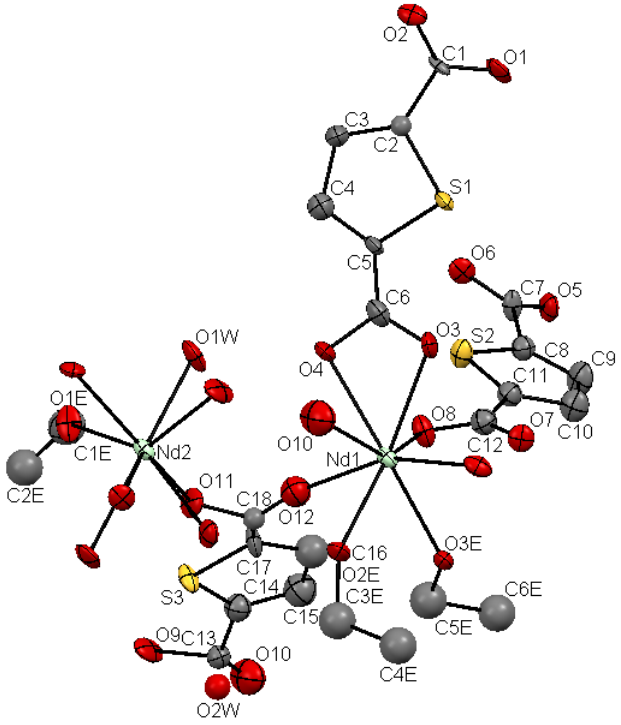

Figure 6.9. ORTEP representation of [6.1] with ellipsoids drawn at 50% probability.

Table 6.2. Selected bond lengths (Å) and angles (°) for [6.1].

Nd(1)-O(2)[b]	2.387(18)	O(2)[b]-Nd(1)-O(3)	74.5(7)
Nd(1)-O(3)	2.453(17)	O(10)[a]-Nd(1)-(12)	89.8(7)
Nd(1)-O(2E)	2.488(17)	O(3)-Nd(1)-O(4)	53.3(5)
Nd(1)-O(3E)	2.464(15)	O(2)[b]-Nd(1)-O(8)	111.5(5)
Nd(1)-O(4)	2.595(16)	O(10)[a]-Nd(1)-O(2)[b]	92.2(7)
Nd(1)-O(8)	2.431(15)	O(8)-Nd(1)-O(4)	74.1(6)
Nd(1)-O(10)[a]	2.320(2)	O(12)-Nd(1)-O(2)[b]	157.8(5)
Nd(1)-O(12)	2.325(19)	O(10)[a]-Nd(1)-O(8)	140.2(6)
Nd(2)-O(1)[d]	2.459(16)	O(12)-Nd(1)-O(8)	79.9(5)
Nd(2)-O(1E)	2.489(17)	O(10)[a]-Nd(1)-O(4)	66.3(7)
Nd(2)-O(1W)	2.488(16)	O(11)-Nd(2)-O(9)[a]	115.7(5)
Nd(2)-O(5)[e]	2.547(16)	O(6)[e]-Nd(2)-O(5)[e]	49.6(5)
Nd(2)-O(6)[e]	2.522(14)	O(11)-Nd(2)-O(1)[d]	73.2(5)
Nd(2)-O(12)[c]	2.368(17)	O(9)[a]-Nd(2)-O(1)[d]	142.3(5)
Nd(2)-O(9)[a]	2.396(13)	O(7)[c]-Nd(2)-O(9)[a]	79.4(5)
Nd(2)-O(11)	2.365(12)	O(11)-Nd(2)-O(6)[e]	127.9(5)
		O(7)[c]-Nd(2)-O(6)[e]	78.5(6)
		O(9)[a]-Nd(2)-O(5)[e]	72.1(6)
		O(11)-Nd(2)-O(7)[c]	150.8(5)
		O(7)[c]-Nd(2)-O(1)[d]	111.0(5)

Symmetry transformations used to generate equivalent atoms: [a]x,y-1,z ; [b]x+1/2,-y-1/2,z+1/2 ; [c]x,-y,z-1/2 ; [d] x+1/2,y+1/2,z ; [e]x+1/2,y-1/2,z

6.4.2. Structures of [6.2] and [6.3], $Ln(TDC)_3(EtOH)_3(H_2O)\cdot H_2O$, Ln = Tb, Dy

The structures of [6.2] and [6.3] are isostructural and topologically similar to the overall structure and net described in [6.1], with the main difference being the packing arrangement of connecting TDC ligands (Fig. 6.10). The asymmetric units of [6.2] and [6.3] consists of four unique Ln atoms, six TDC linkers, six metal-coordinated EtOH molecules, two metal-coordinated H_2O molecules, and two guest H_2O molecules. The coordination modes of TDC observed in [6.1] are also found in [6.2] and [6.3] as four TDC linkers coordinate in a (κ^2)–$(\kappa^1$-$\kappa^1)$–μ_3 mode and two TDC linkers adopt the $(\kappa^1$-$\kappa^1)$–$(\kappa^1$-$\kappa^1)$–μ_4 coordination mode.

Each Ln metal center in [6.2] and [6.3] is 8-coordinate, consisting of oxygen atoms from TDC carboxylate groups, ethanol molecules and water molecules. In [6.2], the environment of Tb1 is a bidentate TDC carboxylate group (O5, O6), four monodentate carboxylates (O1, O12, O14, O22) and two coordinated ethanol molecules (O1E, O2E). Tb2 also has a bidentate TDC carboxylate group (O15, O16) and four monodentate carboxylates (O2, O8, O11, O20), but only one coordinated EtOH molecule (O3E) is observed as the final position is occupied by a water molecule (O3W). Tb3 is similar to Tb1 with a bidentate TDC carboxylate group (O23, O24), four monodentate carboxylates (O3, O7, O9, O19) and two coordinated EtOH molecules (O4E, O5E). Likewise, Tb4 is similar to Tb2 with a bidentate TDC carboxylate group (O17, O18), four monodentate carboxylates (O4, O13, O10, O21), one coordinated EtOH (O6E), and one coordinated H_2O molecule (O4W). Two guest H_2O molecules (O1W, O2W) are also present. Selected bond lengths and angles for [6.2] are shown in Table 6.3.

In [6.3]**,** the environment of Dy1 consists of a bidentate TDC carboxylate group (O23, O24), four monodentate carboxylates (O4, O6, O10, O20) and two coordinated ethanol molecules (O1E, O2E). Dy2 has a bidentate TDC carboxylate group (O13, O14), four

monodentate carboxylates (O3, O5, O11, O21), one coordinated EtOH molecule (O3E), and one H_2O molecule (O1W). Dy3 has a bidentate TDC carboxylate group (O1, O2), four monodentate carboxylates (O9, O15, O19, O22), one coordinated EtOH molecule (O4E), and one H_2O molecule (O2W). Tb4 has a bidentate TDC carboxylate group (O7, O8), four monodentate carboxylates (O12, O16, O17, O21), and two coordinated EtOH molecules (O5E, O6E). The network also includes two guest H_2O molecules (O3W, O4W). Selected bond lengths and angles for **3** are shown in Table 6.4.

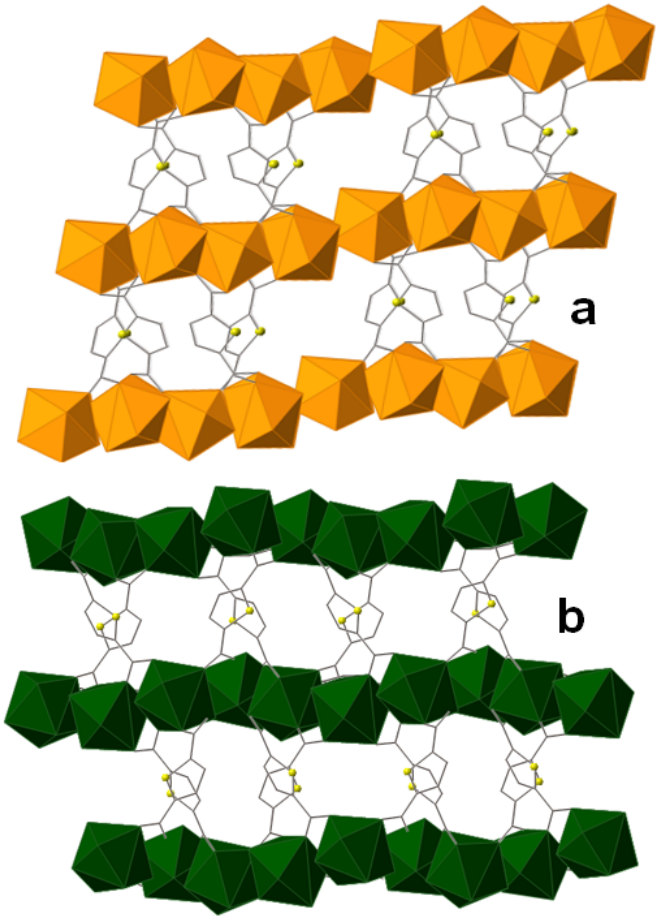

Figure 6.10. Difference in ligand packing between the network of [6.1] (a) and the networks of [6.2] and [6.3] (b).

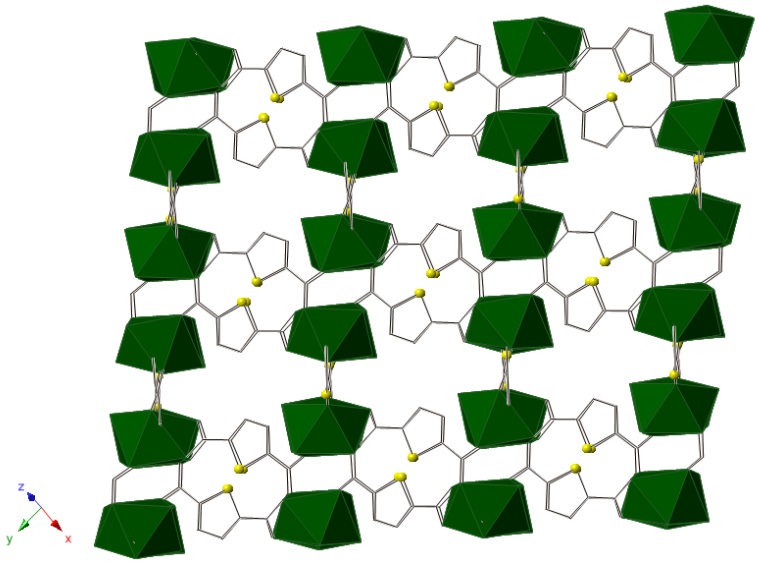

Figure 6.81. Network of [6.2] and [6.3] as viewed down the [1.2 0 1.2] direction. Metal polyhedra are represented in green, C as wire bonds, and S as yellow spheres.

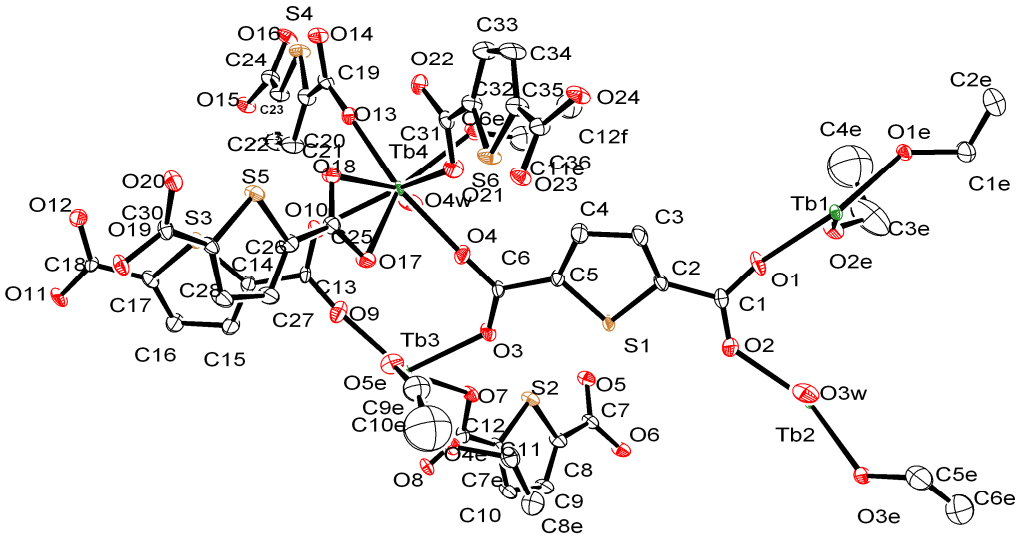

Figure 6.12. ORTEP representation of [6.2] with ellipsoids drawn at 50% probability.

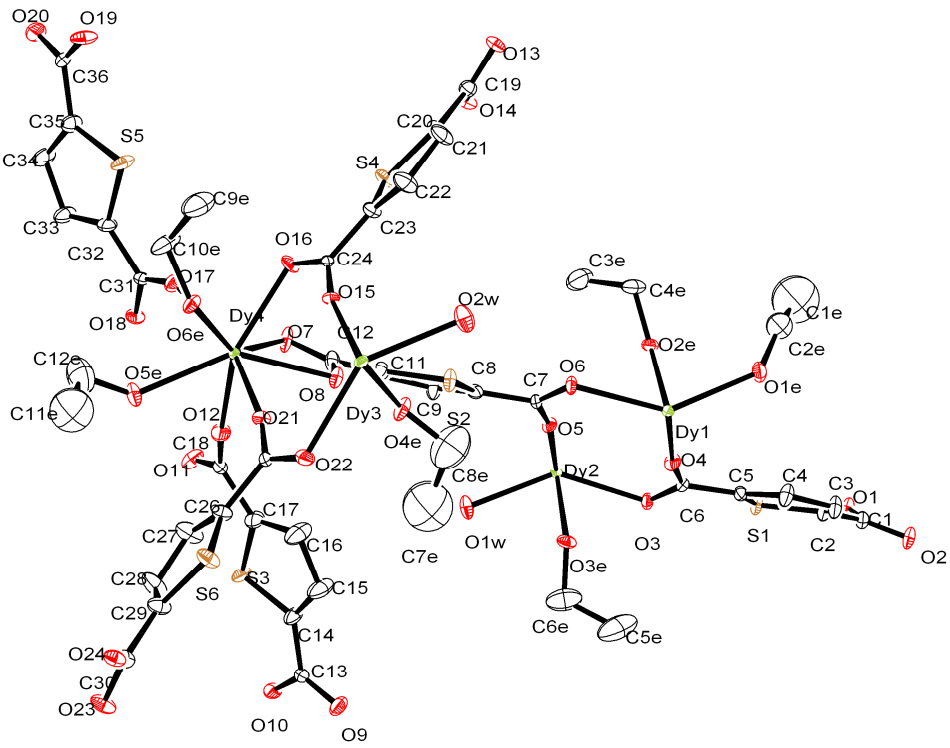

Figure 6.13. ORTEP representation of [6.3] with ellipsoids drawn at 50% probability.

Table 6.3. Selected bond lengths (Å) and angles (°) for [6.2].

Tb(1)-O1	2.273(4)	O(5)[a]-Tb(1)-O(6)[a]	51.86(15)
Tb(1)-O(5)[a]	2.432(4)	O(1)-Tb(1)-O(12)[g]	104.48(18)
Tb(1)-O(6)[a]	2.564(5)	O(22)[f]-Tb(1)-O(6)[a]	125.55(16)
Tb(1)-O(12)[g]	2.292(5)	O(12)[g]-Tb(1)-O(5)[a]	128.70(18)
Tb(1)-O(14)[f]	2.350(4)	O(14)[f]-Tb(1)-O(5)[a]	73.19(16)
Tb(1)-O(22)[f]	2.292(5)	O(13)-Tb(4)-O(18)	78.70(16)
Tb(2)-O(2)	2.332(5)	O(16)[c]-Tb(2)-O(15)[c]	52.81(14)
Tb(2)-O(8)[d]	2.272(4)	O(8)[d]-Tb(2)-O(20)[h]	109.67(15)
Tb(2)-O(11)[g]	2.236(4)	O(11)[g]-Tb(2)-O(8)[d]	156.75(17)
Tb(2)-O(15)[c]	2.511(5)	O(2)-Tb(2)-O(15)[c]	72.06(17)
Tb(2)-O(16)[c]	2.420(4)	O(8)[d]-Tb(2)-O(2)	80.60(17)
Tb(2)-O(20)[h]	2.372(4)	O(8)[d]-Tb(2)-O(16)[c]	77.88(15)
Tb(3)-O(3)	2.312(4)	O(23)[b]-Tb(3)-O(24)[b]	52.28(14)
Tb(3)-O(9)	2.269(5)	O(9)-Tb(3)-O(3)	104.44(17)
Tb(3)-O(7)	2.381(4)	O(9)-Tb(3)-O(24)[b]	70.20(18)
Tb(3)[e]-O(19)	2.262(4)	O(7)-Tb(3)-O(24)[b]	71.90(16)
Tb(3)[a]-O(23)	2.424(4)	O(7)-Tb(3)-O(23)[b]	72.49(16)
Tb(3)[a]-O(24)	2.536(5)	O(3)-Tb(3)-O(24)[b]	81.39(16)
Tb(4)-O(4)	2.234(5)	O(4)-Tb(4)-O(21)	81.12(17)
Tb(4)-O(10)	2.340(4)	O(13)-Tb(4)-O(10)	79.55(16)
Tb(4)-O(13)	2.278(4)	O(13)-Tb(4)-O(18)	78.70(16)
Tb(4)-O(17)	2.530(5)	O(18)-Tb(4)-O(17)	52.56(15)
Tb(4)-O(18)	2.418(4)	O(10)-Tb(4)-O(21)	143.26(18)
Tb(4)-O(21)	2.377(4)	O(13)-Tb(4)-O(17)	126.95(16)

Symmetry transformations used to generate equivalent atoms: [a]x-1,y,z ; [b]x+1,y,z ; [c]-x+2,-y+1,-z ; [d]-x+2,-y+2,-z ; [e]-x+2,-y+2,-z+1 ; [f]-x+1,-y+1,-z ; [g]x-1,y,z-1 ; [h]x,y,z-1

Table 6.4. Selected bond lengths (Å) and angles (°) for [6.3].

Dy(1)-O(4)	2.248(6)	O(20)[a]-Dy(1)-O(10)[b]	103.4(2)
Dy(1)-O(6)	2.359(5)	O(20)[a]-Dy(1)-O(24)[c]	80.6(2)
Dy(1)-O(10)[b]	2.300(6)	O(10)[b]-Dy(1)-O(23)[c]	80.8(2)
Dy(1)-O(20)[a]	2.267(6)	O(4)-Dy(1)-O(6)	108.8(2)
Dy(1)-O(23)[c]	2.509(6)	O(4)-Dy(1)-O(23)[c]	124.6(2)
Dy(1)-O(24)[c]	2.423(5)	O(20)[a]-Dy(1)-O(6)	142.4(2)
Dy(2)-O(3)	2.365(5)	O(5)-Dy(2)-O(3)	108.14(19)
Dy(2)-O(5)	2.261(5)	O(18)[f]-Dy(2)-O(11)[f]	105.6(2)
Dy(2)-O(11)[f]	2.325(6)	O(18)[f]-Dy(2)-O(14)[g]	125.5(2)
Dy(2)-O(13)[g]	2.486(6)	O(5)-Dy(2)-O(13)[g]	127.19(18)
Dy(2)-O(14)[g]	2.415(5)	O(14)[g]-Dy(2)-O(13)[g]	53.05(18)
Dy(2)-O(18)[f]	2.221(5)	O(18)[f]-Dy(2)-O(13)[g]	75.7(2)
Dy(3)-O(1)[e]	2.418(5)	O(15)-Dy(3)-O(22)	108.7(2)
Dy(3)-O(2)[e]	2.494(6)	O(9)[c]-Dy(3)-O(19)[d]	104.3(2)
Dy(3)-O(9)[c]	2.217(6)	O(15)-Dy(3)-O(2)[e]	127.01(19)
Dy(3)-O(15)	2.253(5)	O(9)[c]-Dy(3)-O(22)	81.6(2)
Dy(3)-O(19)[d]	2.332(6)	O(9)[c]-Dy(3)-O(2)[e]	75.1(2)
Dy(3)-O(22)	2.359(6)	O(15)-Dy(3)-O(1)[e]	78.04(19)
Dy(4)-O(7)	2.536(6)	O(21)-Dy(4)-O(16)	110.2(2)
Dy(4)-O(8)	2.420(5)	O(12)-Dy(4)-O(21)	86.9(2)
Dy(4)-O(12)	2.255(6)	O(21)-Dy(4)-O(7)	126.0(2)
Dy(4)-O(16)	2.339(5)	O(17)-Dy(4)-O(8)	129.4(2)
Dy(4)-O(17)	2.285(6)	O(17)-Dy(4)-O(7)	80.4(2)
Dy(4)-O(21)	2.264(6)	O(12)-Dy(4)-O(16)	142.1(2)

Symmetry transformations used to generate equivalent atoms: [a]x,y,z+1 ; [b]x-1,y,z ; [c]-x+2,-y,-z+2 ; [d] -x+1,-y,-z+1 ; [e]x,y-1,z-1 ; [f]-x+2,-y+1,-z+2 ; [g]-x+1,-y+1,-z+2 ; [h]x+1,y,z

6.4.3. Discussion

Compounds [6.1 – 6.3] were synthesized using the lanthanide metal centers Nd, Tb, and Dy, while holding constant solvent and reactant ratios. The lanthanide TDC networks that resulted are all topologically related with the structural formula $Ln(TDC)_3(EtOH)_3(H_2O)$. The TDC linker in [6.1 – 6.3] adopts the same coordination mode in each of the three compounds, but is arranged slightly different in compounds [6.2] and [6.3], which are isostructural. Though in both cases the metals are eight-coordinated, it is likely that the lanthanide contraction affects the way the linkers are able to coordinate to the metal. Eight-coordinate Nd^{3+} has an effective ionic radius of 1.11 Å, whereas eight-coordinate Tb^{3+} and Dy^{3+} are smaller and much similar to one another, having ionic radii of 1.04 Å and 1.03 Å, respectively. Further evidence for the lanthanide contraction effect comes from an unreported Er-based structure synthesized in the same way as [6.1 – 6.3].[a] The Er network has the same general $Er_2(TDC)_3$ formula and ligand coordination modes. However, rather than each metal being eight-coordinated as in [6.1 – 6.3], both six- and eight-coordination (Fig. 6.14) are observed and a completely different topology is formed (Fig. 6.15). We can conclude that the differences in ionic radii account for the observed differences in the structures.

Previous studies in the synthesis of lanthanide TDC networks have used a variety of solvents and solvent mixtures, including DMSO/DMF,[162] DMF/H_2O,[31] and H_2O/EtOH.[30] We set out to explore the possible topological differences in this family with a 1:1 molar EtOH/H_2O solvent mixture. Similar work by Wang and coworkers used an H_2O/EtOH mixture comprised of mostly H_2O and found that EtOH is not incorporated into the structure[30]. Curiously, we found that our use of an equimolar mixture of EtOH/H_2O led to coordination of both EtOH and H_2O to

[a] Structural formula $Er_2(TDC)_3$; Space group *Pbam*,, a = 20.9871(5)Å, b = 17.1421(2)Å, c = 19.2962(4)Å, V = 6942.0(9)$Å^3$. Structure refinement is not crystallographically acceptable due to crystal twinning, but we are confident general formula is correct.

the metal centers in each of the compounds, with the empirical ratio being three coordinated EtOH molecules to one coordinated H_2O. Previous work done in our group showed that mixtures of solvents have a unique character compared to pure solvents and lead to different topologies for a given metal/ligand combination[51]. Since EtOH coordinates preferentially, we can conclude it is a more active solvent than H_2O under these synthetic conditions.

The fluorescence spectra of [6.1 – 6.3] were analyzed based on the maximum ligand excitation wavelength, which was determined to be 300nm. Each compound shows the characteristic $\pi^* \rightarrow$ n and $\pi^* \rightarrow \pi$ transitions of the TDC linker, with a broad peak centered at 362 nm (Fig. 6.16). Compound [6.2] shows the characteristic Tb emission with lines corresponding to the $^5D_4 \rightarrow {}^7F_6$ (492 nm), $^5D_4 \rightarrow {}^7F_5$ (539 nm and 551 nm), $^5D_4 \rightarrow {}^7F_4$ (585 nm), and $^5D_4 \rightarrow {}^7F_3$ (621 nm) transitions (Fig. 6.17). When irradiated with a UV lamp on a benchtop, [6.2] emits bright green light (Fig. 6.18). The spectrum of [6.3] is comparatively weaker and shows an emission line at 479 nm that is characteristic of the $^4F_{9/2} \rightarrow {}^6H_{15/2}$ transition and another emission line at 575 nm corresponding to the $^4F_{9/2} \rightarrow {}^6H_{13/2}$ transition (Fig. 6.17). Other reported compounds have shown strong Dy emission using the TDC linker, but the weakness of emission lines in the Dy compounds reported in our work may be related to non-emissive luminescence quenching of the coordinated solvent molecules EtOH and H_2O.

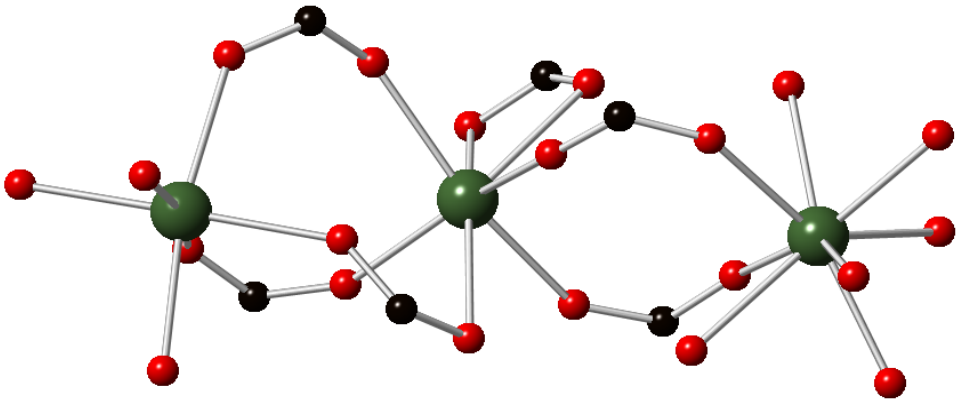

Figure 6.14. Coordination environment of metal atoms in Er-based compound.[a]

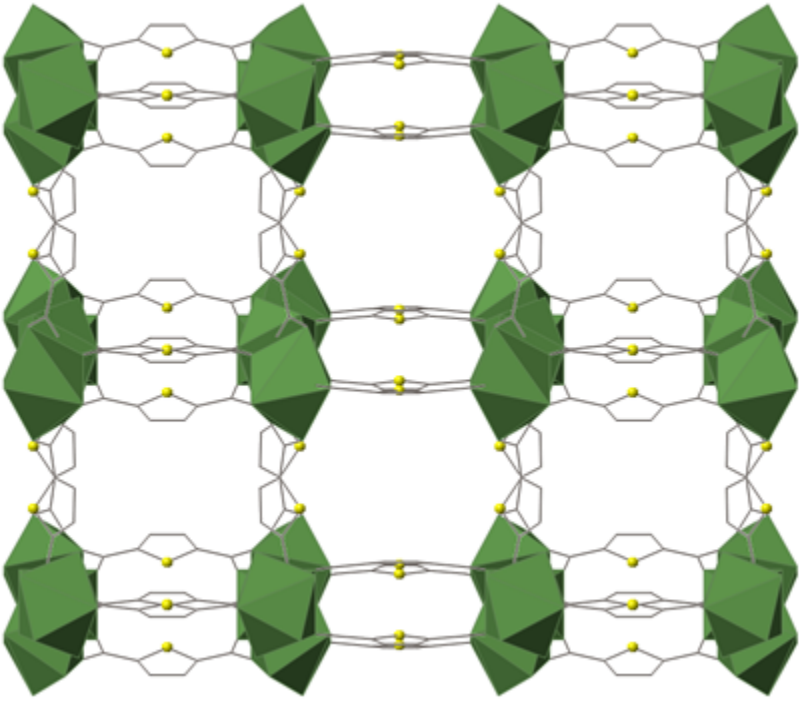

Figure 6.15. Different $Er_2(TDC)_3$ topology observed in Er-based compound.[a]

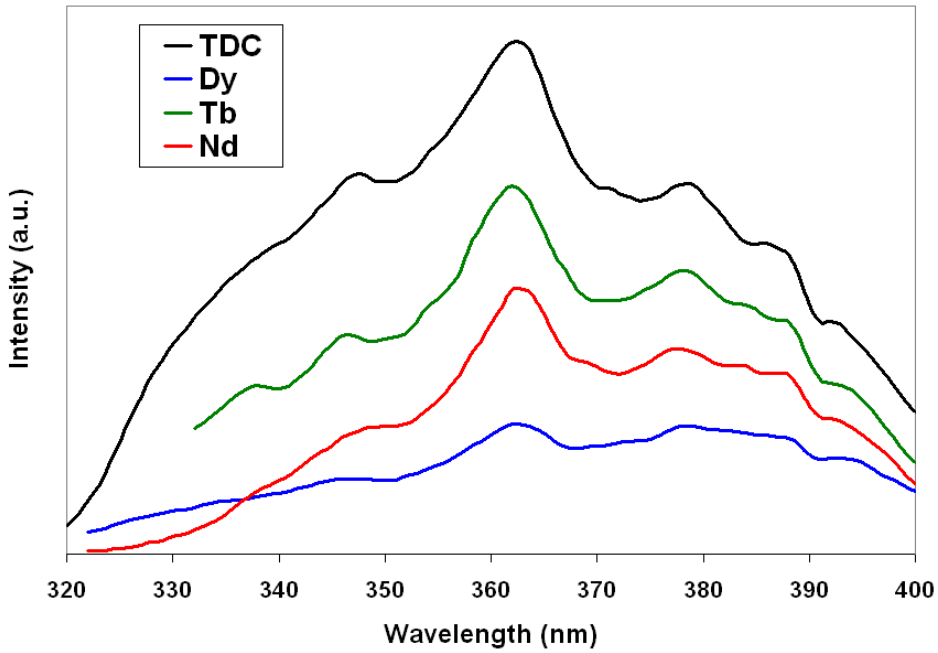

Figure 6.16. Fluorescence spectra of [6.1 – 6.3] and free H_2TDC acid showing emission of the TDC linkers.

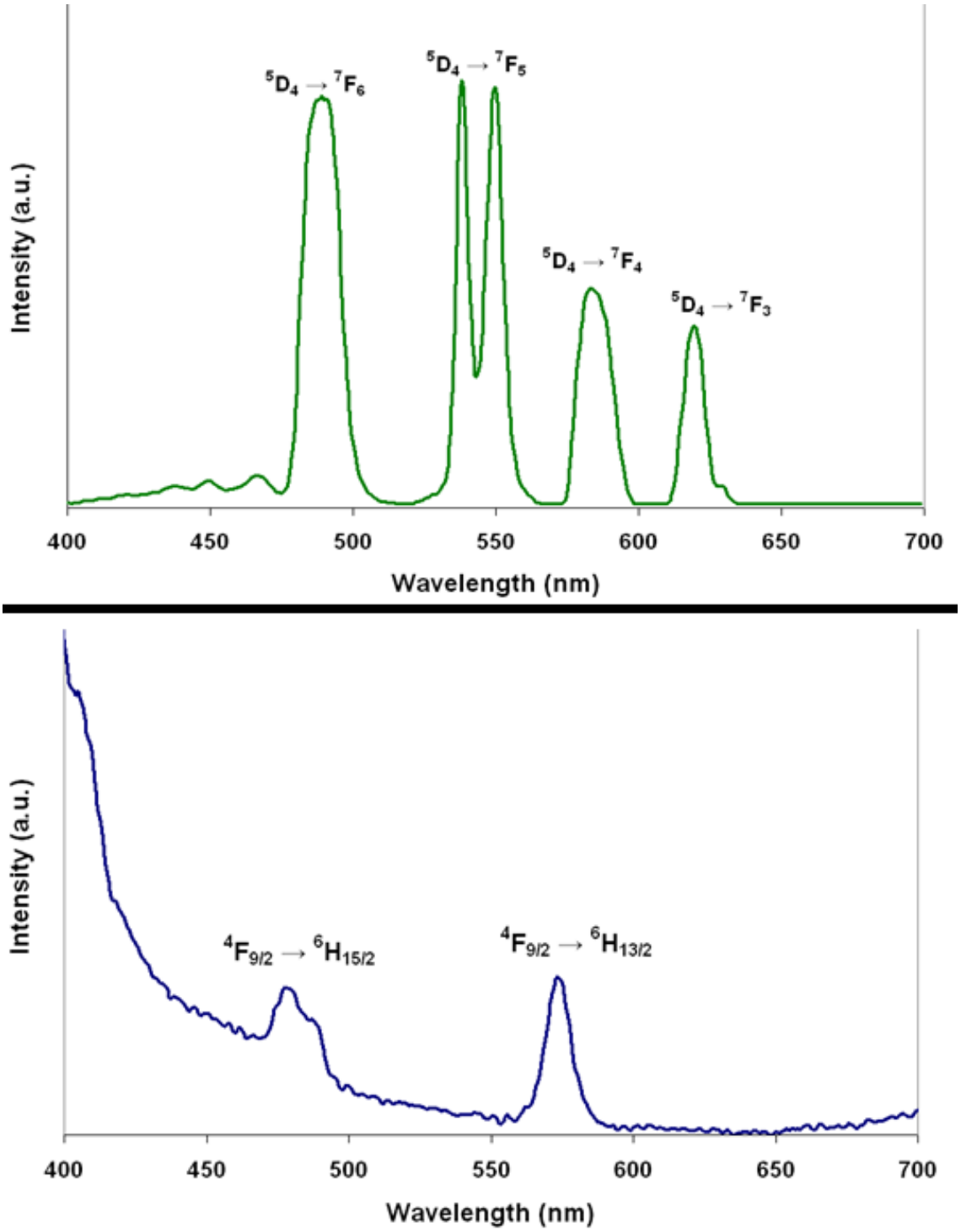

Figure 6.17. Photoluminescence emission spectra of compounds [6.2] and [6.3] obtained using an excitation wavelength of 300 nm.

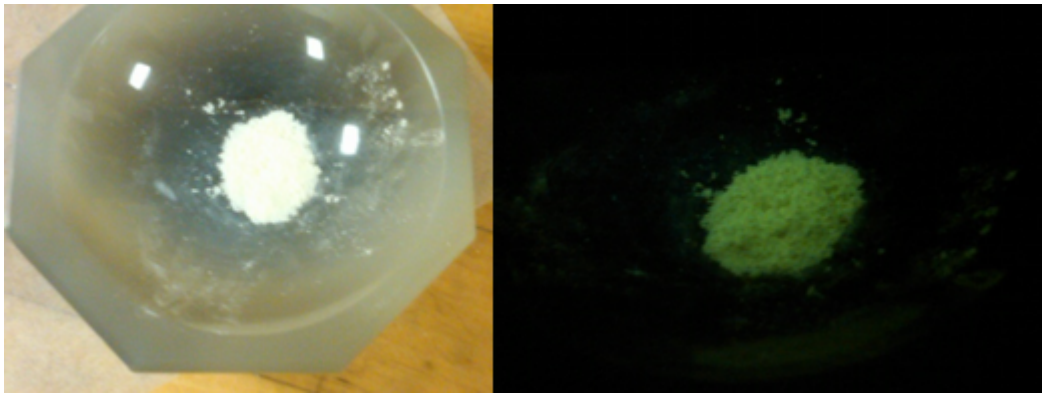

Figure 6.18. The response of compound [6.2] under visible light (left) and under UV light (right).

6.5. Conclusion

Three structurally-related lanthanide TDC coordination networks were synthesized using Nd, Tb, and Dy metal centers, with each reaction using the same metal:linker:solvent ratio. Each network shares the formula $Ln(TDC)_3(EtOH)_3(H_2O)\cdot H_2O$ and the same TDC linker coordination modes are observed. However, a difference in TDC linker packing due to the lanthanide contraction effect causes the topology of [6.1] to differ slightly from the isostructures [6.2] and [6.3]. Both water and ethanol solvent molecules were found to coordinate to the metal center when using a 1:1 mixture, but the ratio of three coordinated EtOH to one H_2O molecule suggests a preference for EtOH under these conditions. Fluorescence spectra show the characteristic Ln transitions in [6.2] and [6.3], but the emission in Dy-based [6.3] is considerably weaker indicating that the coordinating solvent molecules may be quenching the luminescence.

Chapter 7

Ionothermal Synthesis, Characterization, and Magnetic Studies of Novel Metal-Formate Frameworks

7.1. Abstract

Five novel two-dimensional frameworks containing formate-bridged metal-centered octahedra are synthesized ionothermally from two ionic liquids previously unused as solvents in hybrid synthesis, 2-hydroxyethylammonium (HEA) formate and 1-hydroxy, 3-proplyammonium (HPA) formate. Templating effects of the cation from each ionic liquid drive the formation of different structures. $[NH_3C_2H_4OH]_2[M(CHO_2)_4]$ (M=Co, [7.1]; Ni,[7.2]) exhibit the same stoichiometry and connectivity as their manganese analog (M=Mn, [7.3]), but the manganese form exhibits a different topology from [7.1] and [7.2]. $[NH_3C_3H_6OH][M(CHO_2)_3(H_2O)]$ (M=Co, [7.4]; Mn,[7.5]) were synthesized using the HPA formate ionic liquid with a metal-formate connectivity related to those of [7.1]–[7.3]. Canted antiferromagnetic ordering occurs at low temperatures ([7.1]: T_N = 7.5 K, [7.2]: T_N = 2.2 K, [7.3]: T_N = 8.1 K, [7.4]: T_N = 6.9 K, [7.5]: T_N = 9.5 K), similar to the magnetic properties previously reported for other metal-formate hybrid materials. Portions of the work described in this chapter, including the synthesis protocols, characterization, and property measurement have been published: Calderone, P. J.; Forster, P. M.; Borkowski, L. A.; Teat, S. J.; Feygenson, M.; Aronson, M. C.; Parise, J. B. *Inorg. Chem.* **2011**, *50*, 2159.

7.2. Introduction

Many of the important behaviors associated with transition metal oxides, such as electronic conductivity and magnetic ordering,[169] are now known to occur in MOFs as well.[10,170-171] Magnetic properties of transition metal MOFs offer great potential for exploration and of paramount importance is choosing short ligand bridges to effectively and efficiently transfer magnetic coupling between metal atoms.[21] Following this principle, examples of formate-bridged 3*d* transition metal systems utilizing short $HCOO^-$ metal connections have emerged as a means to construct new molecular magnets.[22-25,172-173] Cheetham and coworkers' recent discovery of a series of multiferroic MOFs based on transition metal-formates has created an even greater interest in the prospective uses of new MOF materials.[146] Multiferroic materials exhibit both magnetic and ferroelectric ordering, and the occurrence of both properties in the same compound is especially interesting in MOFs because only a small number of purely inorganic materials had previously been recognized as multiferroic.[174-175]

Given the success that reticular chemistry has achieved at envisioning and subsequently synthesizing new MOFs topologies, multiferroicity presents yet another property that can be considered in the targeting of new structures. In metal-formate MOFs, for example, the final structure and properties are often determined by the templating effects of organocations that are incorporated into the framework. This is well-documented in the formate-based transition metal multiferroics described by Cheetham which adopt an ABX_3 perovskite-type topology. In these compounds, multiferroic behavior occurs due to a ferroelectric order-disorder transition involving the ammonium cation (located at the A-site in the structure) and magnetic ordering between octahedral metal atoms (B-sites).[146] This cation order-disorder transition was further investigated by Sánchez-Andújar et al., finding that hydrogen-bonding of the charge-balancing

ammonium cation was a direct contributor to a low-temperature structural phase transition and the ferroelectric ordering.[176] A similar ferroelectric behavior has also been observed in the $[NH_4][Zn(HCOO)_3]$ system by Xu and coworkers.[177] Clearly, in order to better elucidate the nature of metal-formate framework systems, the effects that are created when the properties of ammonium cations are varied within a series must be studied. While previous attempts have explored variations of alkylammonium cations,[23-24] a more complete study can be carried out by varying the cation through changing alkyl chain length or adding functional groups, leading to the synthesis of related structure types.

We have chosen to explore the synthesis of hydroxyammonium metal formate MOFs utilizing two ionic liquids of hydroxyammonium cations and the formate anion, both of which can be easily produced in any laboratory. The two ionic liquids used in this work are derived from the inexpensive, readily available reagents formic acid, and the amino alcohols, 2-aminoethanol and 3-amino, 1-propanol. A previous report has characterized a 2-hydroxyethylammonium formate ionic liquid derived from formic acid and 2-aminoethanol.[178] Here, we use related ionic liquids to synthesize formate-bridged magnetic MOFs based on Co, Ni and Mn, finding that these ionic liquids offer the potential to act as solvent, organocation template source, and ligand source. We also compare the new frameworks generated in our ionic liquids to existing perovskite metal formates, finding that in the case of hydroxyammonium cations, templating effects and additional hydrogen bonding interactions drive structural dimensionality changes and lead to ordered structures with no potential for ferroelectric transitions.

7.3. Experimental

7.3.1. Syntheses

Ionic liquid constituents consist of formic acid (Acros) and either 2-aminoethanol (Acros) or 3-amino-1-propanol (Acros). Metal sources were cobalt (II) chloride hexahydrate (Aldrich), nickel (II) chloride hexahydrate (Acros), manganese (II) acetate tetrahydrate (Alfa), and cobalt (II) sulfate heptahydrate (Acros). Metal chlorides were dehydrated in an oven at 120°C for three hours prior to use.

Synthesis of ionic liquids

The preparation of the ionic liquid 2-hydroxyethylammonium (HEA) formate was modified from the procedure described in the literature.[1] To prepare HEA formate, 0.50g formic acid (11 mmol) was added dropwise to 0.66g 2-aminoethanol (11 mmol) in a 1 dram (3.70 ml) vial. The resulting liquid was stirred and allowed to cool to room temperature before adding metal source. The procedure to produce 1-hydroxy, 3-proplyammonium (HPA) formate was the same except that 3-amino-1-propanol (0.82g, 11 mmol) was used in place of 2-aminoethanol.

Synthesis of **[**7.1], $[NH_3C_2H_4OH]_2[Co(CHO_2)_4]$

Cobalt (II) chloride (0.156g, 1.16 mmol) was added to a vial containing the HEA formate liquid. The vial was capped and placed in a 100 °C oven for 4 hours then transferred to a 50 °C oven for 1 day. The resulting pink plate crystals showed susceptibly to breakdown in common solvents and in air after extended periods. For this reason, products were stored in the mother liquor.

Synthesis of [7.2], $[NH_3C_2H_4OH]_2[Ni(CHO_2)_4]$

The process was similar to the preparation of [7.1] except that nickel (II) chloride (0.153 g, 1.15 mmol) was the metal source used. Green plates resulted and were treated in the same manner as [7.1].

Synthesis of [7.3], $[NH_3C_2H_4OH]_2[Mn(CHO_2)_4]$

The process was similar to the preparation of [7.1] except that manganese (II) acetate tetrahydrate (0.29g, 1.1 mmol) was the metal source used. Pale pink plates resulted and were treated in the same manner as [7.1].

Synthesis of [7.4], $[NH_3C_3H_6OH][Co(CHO_2)_3(H_2O)]$

The process was similar to the preparation of [7.1] except that the liquid used was HPA formate, and the metal source was cobalt (II) sulfate heptahydrate (0.31g, 1.1 mmol). A molar ratio of 1 Co: 10 HPA formate was used. Pink plates resulted and were treated in the same manner as [7.1].

Synthesis of [7.5], $[NH_3C_3H_6OH][Mn(CHO_2)_3(H_2O)]$

The process was similar to the preparation of [7.1] except that manganese (II) acetate tetrahydrate (0.29g, 1.1 mmol) was used as a metal source. Pale pink laths resulted and were treated in the same manner as [7.1].

7.3.2. X-ray Diffraction and Structure Solution*

Representative single crystals of each sample suitable for single crystal x-ray diffraction were pulled directly from the bulk. The crystals were mounted either on a glass fiber using epoxy ([7.1], [7.2]) or a cryoloop using oil ([7.3 – 7.5]). Data for samples [7.1] and [7.2] were collected at room temperature on a Bruker P4 four-circle diffractometer equipped with a SMART CCD detector, using Mo Kα radiation (λ = 0.71073 Å) and 0.3° ω scans and were

* Some single crystal XRD and structure solution work done by Lauren Borkowski and Simon Teat

integrated using SMART/SAINT software packages.[2-3] Data for [7.3], [7.4], and [7.5] were collected at 100, 150, and 90K, respectively at the Advanced Light Source station 11.3.1 (λ = 0. 7749 Å) equipped with an Bruker AXS diffractometer, APEX2 CCD detector and APEX2 software.[4] The data were integrated using the SAINT software[5] through APEX2. Corrections for absorption in [7.1] were done via PsiScans[6] while [7.2 – 7.5] was corrected by SADABS 2008/1 for Bruker AXS area detectors.[7] Structure [7.1] was solved with SIR92,[8] [7.2] with SIR2004,[9] while structures for [7.3], [7.4], and [7.5] were solved using SHELXS.[10] All non-hydrogen atoms were refined anisotropically using SHELXTL[10] within the WINGX[11] suite of software and the hydrogen atoms on the formate groups were located in the Fourier map and the C - H distances were constrained. The remaining hydrogen atoms were placed in their calculated positions. A summary of crystallographic information can be found in Table 7.1. Powder X-ray diffraction data to determine phase purity (Fig 7.1 – 7.5) were collected using a Scintag Pad X diffractometer (CuK_α, 5-40° 2θ, 0.02 °step, 1.5 s/step).

Table 7.5. Crystallographic data table for [7.1-7.5]

	[7.1]	[7.2]	[7.3]	[7.4]	[7.5]
chemical formula	$C_8 H_{20} Co N_2 O_{10}$	$C_8 H_{20} Ni N_2 O_{10}$	$C_8 H_{20} Mn N_2 O_{10}$	$C_6 H_{15} Co N O_8$	$C_6 H_{15} Mn N O_8$
formula weight	363.19	362.97	359.20	288.12	284.13
crystal system	monoclinic	monoclinic	monoclinic	orthorhombic	orthorhombic
Space group	$P2_1/n$	$P2_1/n$	$P2_1/c$	*Pbca*	*Pbca*
a (Å)	6.866(1)	6.879(4)	8.925(9)	8.130(8)	8.270(7)
b (Å)	22.354(3)	22.363(1)	8.702(9)	16.131(1)	16.293(1)
c (Å)	9.582(1)	9.522(5)	9.230(1)	16.780(1)	17.015(1)
α (deg)	90	90	90	90	90
β (deg)	90.272(4)	90.362(1)	98.405(2)	90	90
γ (deg)	90	90	90	90	90
V(Å^3)	1470.7(4)	1464.7(1)	709.1(1)	2200.7(4)	2292.8(3)
Z	4	4	2	8	8
λ	0.71073	0.71073	0.77490	0.77490	0.77490
D_{calc} (gcm^{-3})	1.640	1.646	1.682	1.739	1.646
μ (mm^{-1})	1.218	1.376	1.835	2.000	1.485
temp (K)	298	298	100	150	90
R1 (on $F_o^2, I > 2\sigma(I)$)	0.0491	0.0311	0.0204	0.0262	0.0263
wR2 (on $F_o^2, I > 2\sigma(I)$)	0.0785	0.0783	0.0557	0.0720	0.0715

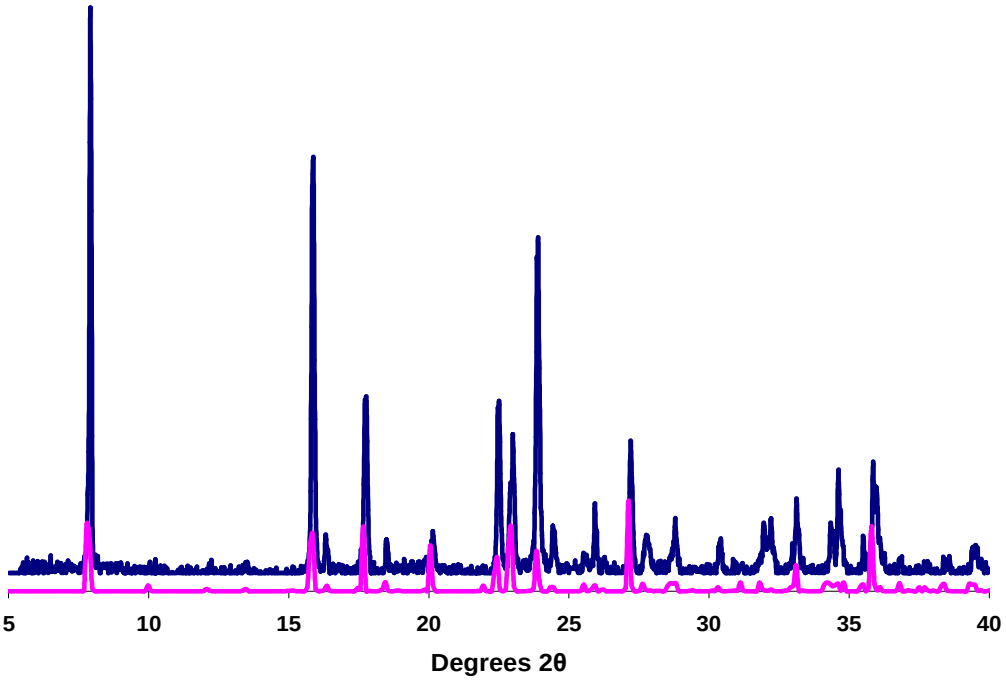

Figure 7.1. Calculated (bottom) and experimental (top) powder patterns of [7.1].

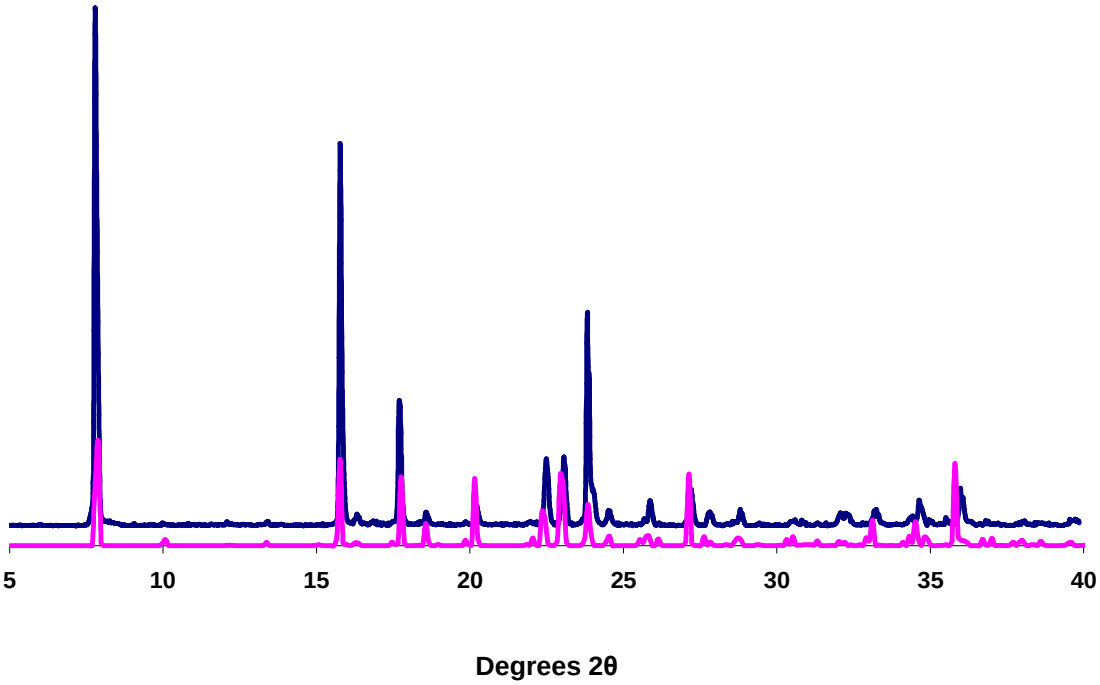

Figure 7.2. Calculated (bottom) and experimental (top) powder patterns of [7.2].

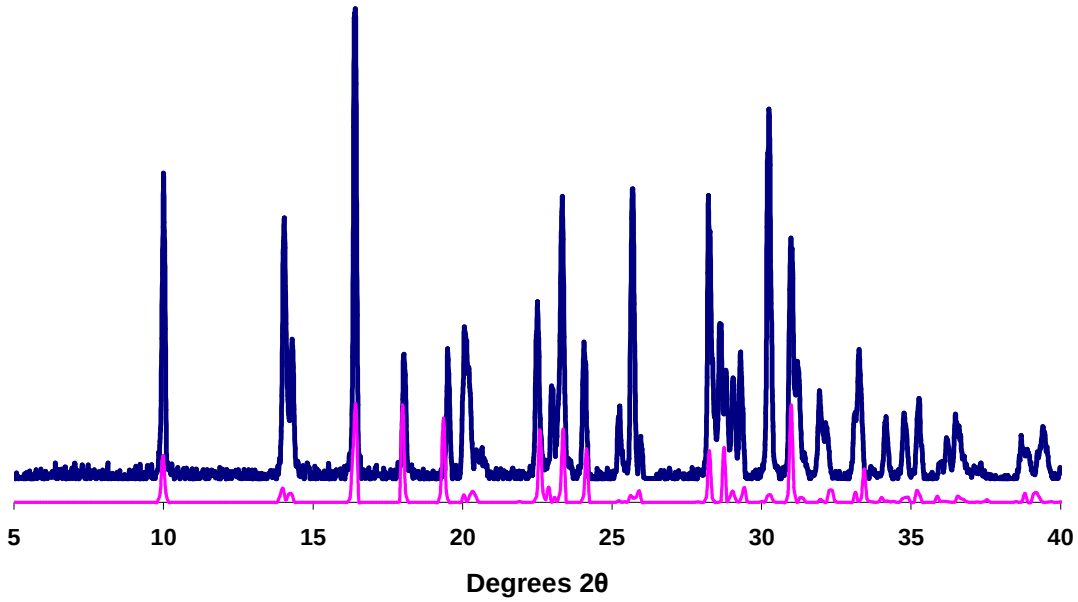

Figure 7.3. Calculated (bottom) and experimental (top) powder patterns of [7.3].

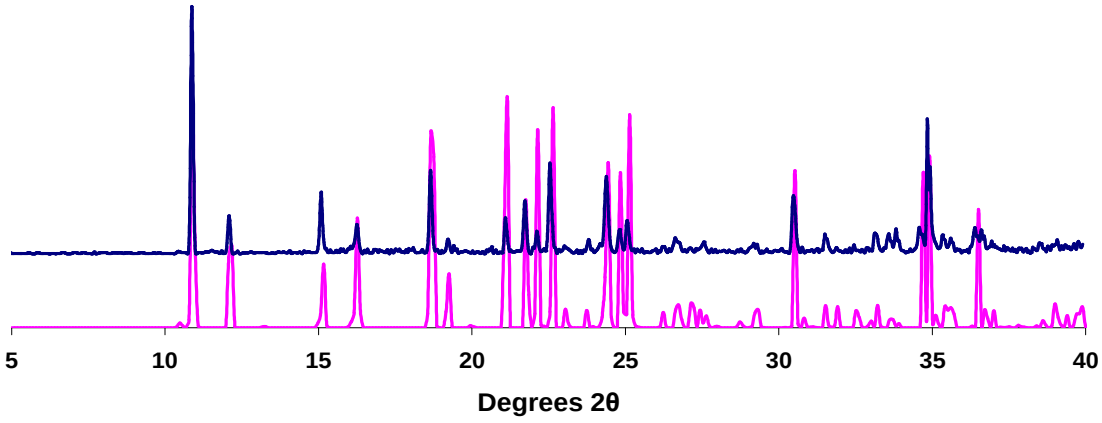

Figure 7.4. Calculated (bottom) and experimental (top) powder patterns of [7.4].

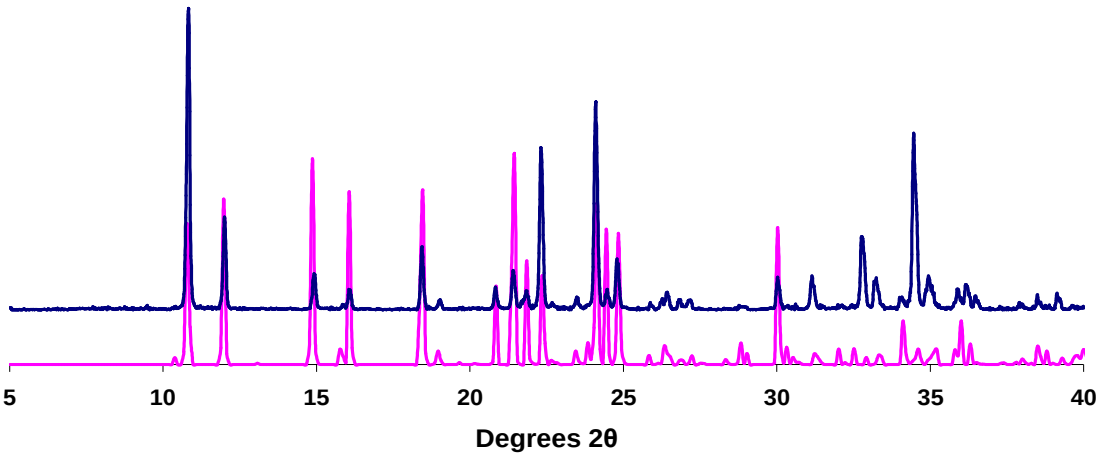

Figure 7.5. Calculated (bottom) and experimental (top) powder patterns of [7.5].

7.3.3. Magnetization Measurements[b]

AC susceptibility and dc magnetization measurements of each sample were carried out using the Quantum Design Magnetic Property Measurement System (model XL-7). The powdered sample was contained in a standard gelatin capsule and was introduced into the magnetometer at room temperature. After subsequent cooling to 2 K in zero magnetic field, the magnetization was measured as a function of applied magnetic fields in the range -50 to 50 kOe at temperatures of 2, 30, 150 and 300 K, respectively. The temperature dependent dc magnetization was measured using standard zero–field cooled (ZFC) and field–cooled (FC) protocols in an applied field of 500 Oe in the temperature range 2 – 300 K. The temperature dependence of the ac susceptibility was measured in a 17 Hz ac field, with a root mean square amplitude of 4.17 Oe. The diamagnetic background of the gelatin capsule was measured to be ~10^{-5} emu, and is only weakly temperature dependent. Since this amounts to no more than 5% of the total measured sample+capsule magnetization in any sample at any temperature, we report

[b] Magnetic susceptibility measurements completed by Mikhail Feygenson in the lab of Meigan Aronson.

here the entire sample + capsule magnetization. The values of the ac susceptibilities and dc magnetizations were normalized by the nominal masses of the moment bearing atoms (i.e. Co, Ni, Mn).

7.3.4. Thermal Analysis

Thermal data for all samples were collected with using a STA 449 C Jupiter from Netzsch Instruments at a range of 30-600°C and 5 degrees per minute under air/nitrogen atmosphere. Thermal data are shown in Figures 7.6 – 7.10.

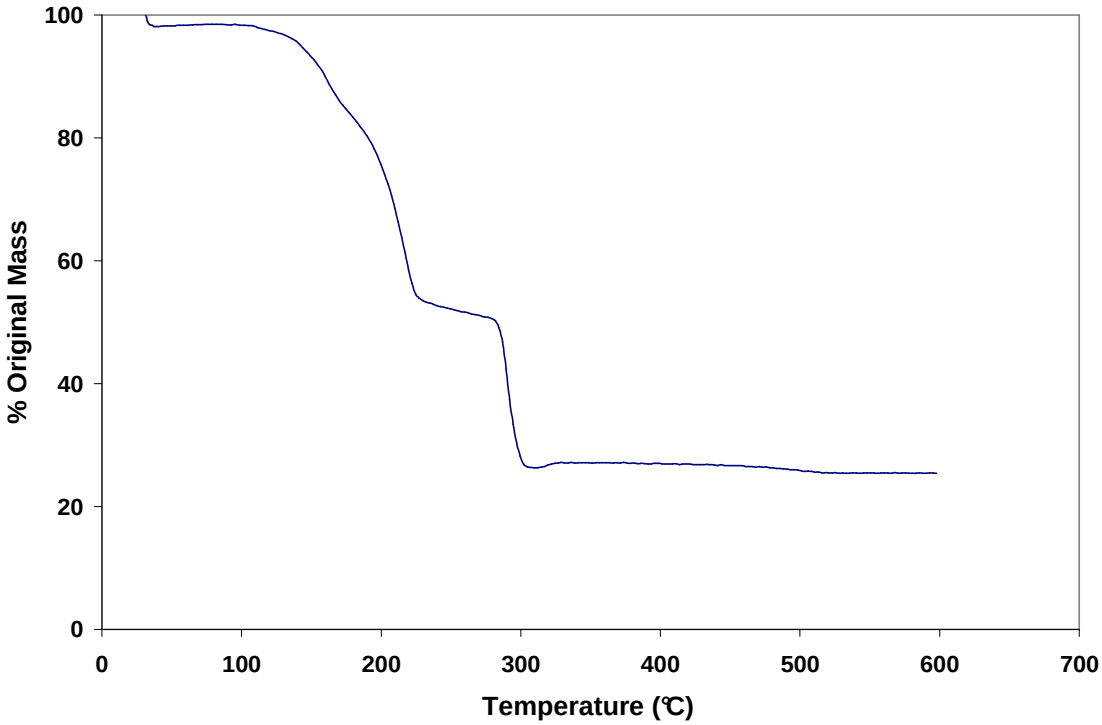

Figure 7.6. TGA curve of [7.1].

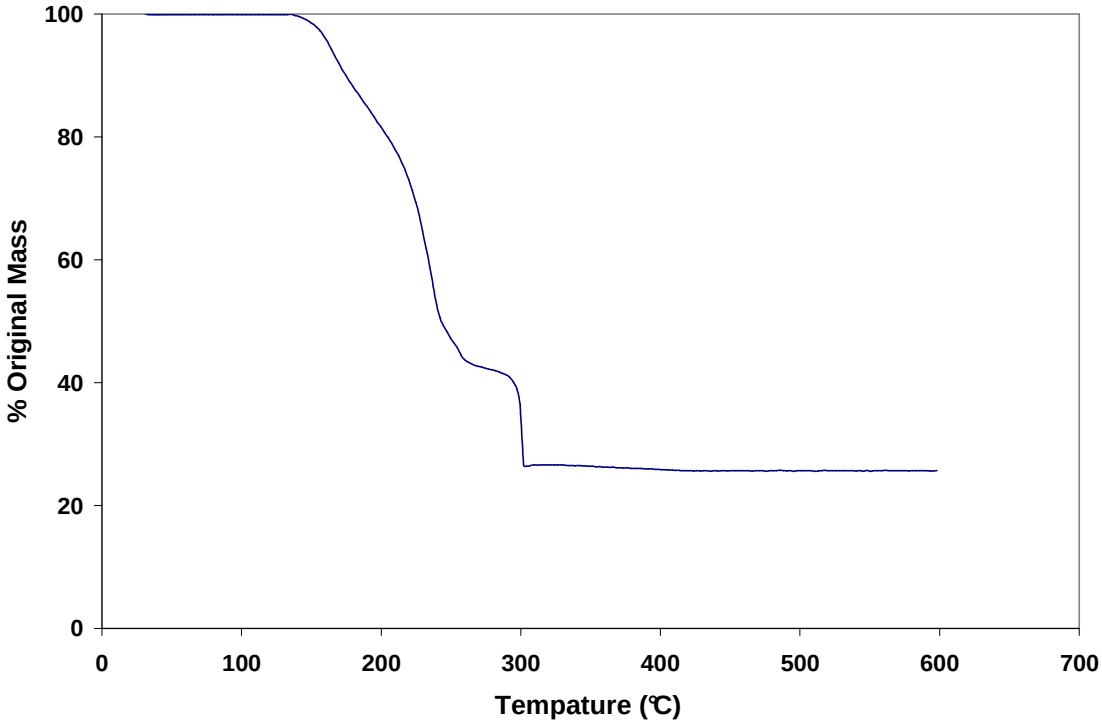

Figure 7.7. TGA curve of [7.2].

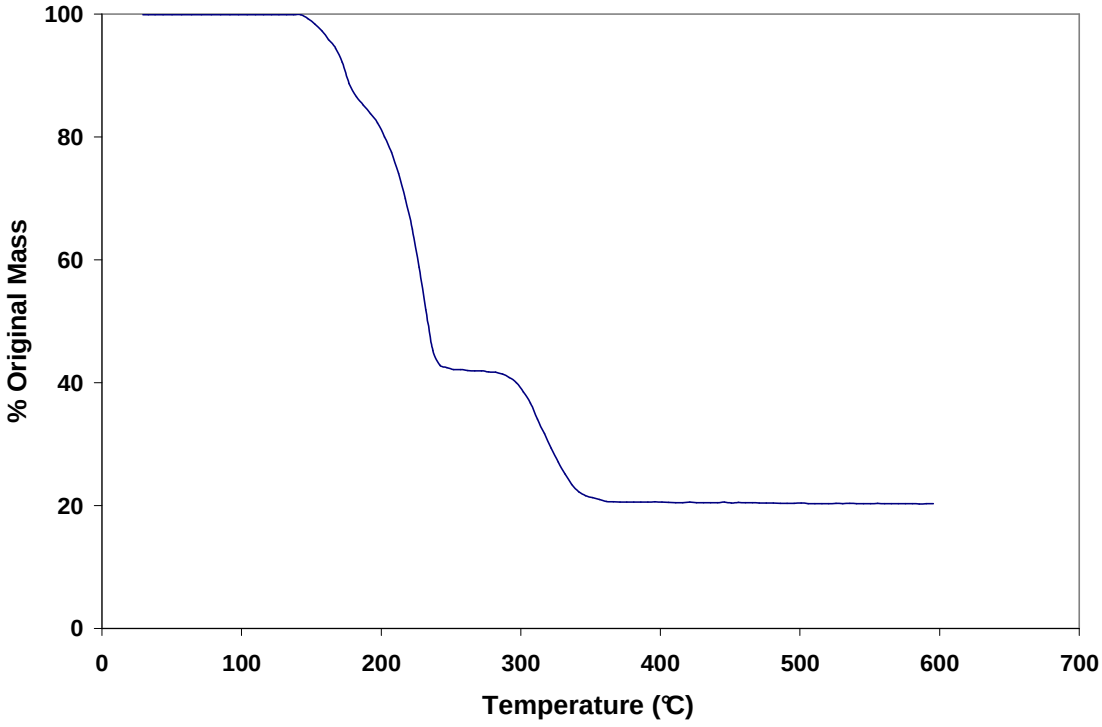

Figure 7.8. TGA curve of [7.3].

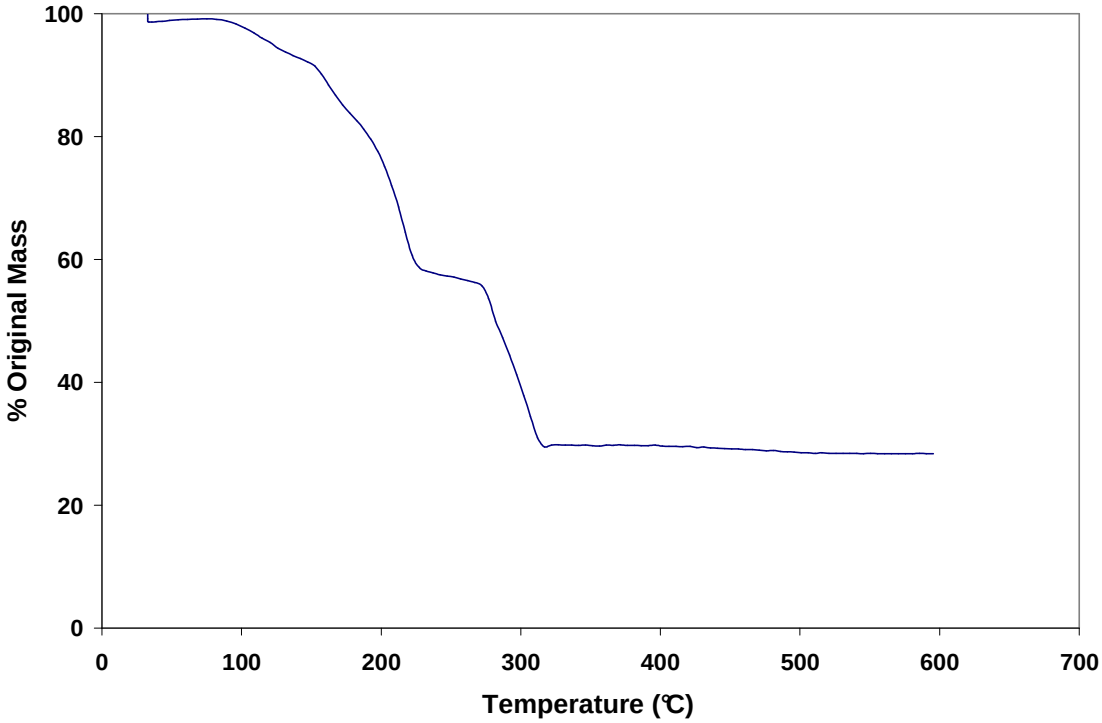

Figure 7.9. TGA curve of [7.4].

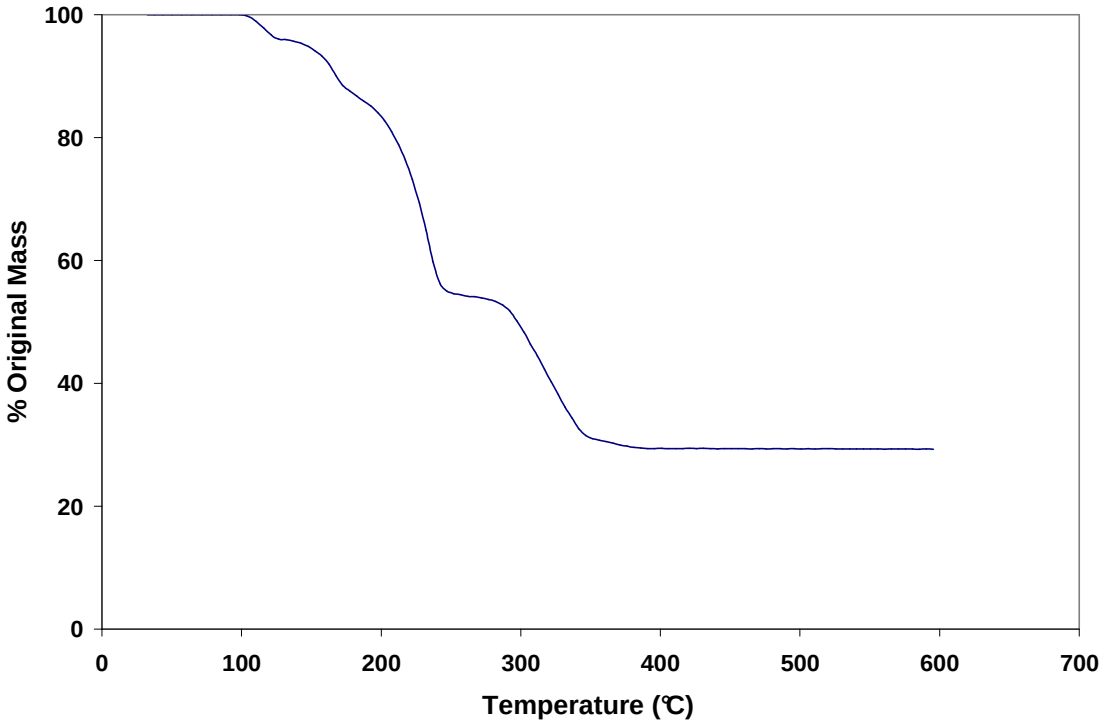

Figure 7.10. TGA curve of [7.5].

7.4. Results and Discussion

7.4.1. Structure Description

Where the multiferroic formates reported by the Cheetham group can be described based on the perovskite structure, compounds 1-5 resemble n=1 Ruddlesden-Popper phases.[169] Compounds [7.1 – 7.3], $[NH_3C_2H_4OH]_2[M(CHO_2)_4]$ (M= Co, Ni, Mn, respectively), consist of two-dimensional metal-formate nets created by formates bridging from the equatorial positions of the metal octahedra (Figure 7.11). Two non-linking formates coordinate in the axial positions of the metal octahedra and the terminal oxygen atoms extend in between the layers. Two HEA cations sit in between the anionic layers to serve as charge balance (Figures 7.12, 7.13). Compounds [7.1] and [7.2] are isostructural with each other but [7.3], which shares the same stoichiometry and connectivity, exhibits a distinct structure as can be seen by comparison of Figures 7.12 and 7.13. Compounds [7.4] and [7.5], $[NH_3C_3H_6OH][M(CHO_2)_3(H_2O)]$ (M = Co and Mn, respectively), are two-dimensional networks exhibiting a similar overall connectivity to that seen in [7.1 – 7.3] (Fig. 7.11). However, only one non-linking formate group occupies an axial position of the octahedron rather than two as for [7.1 – 7.3]. The remaining axial position is occupied by a bound water molecule while one HPA cation, required for charge balance, occupies the space between the layers (Fig. 7.14). For compounds [7.1 – 7.5], hydrogen-bonding interactions are observed between the non-linking formate oxygen and the protonated ammonium group, as summarized in Table 7.3. These hydrogen-bonding interactions are more numerous, and presumably lead to greater stabilization, than observed for 3D perovskite formates due both to the presence of additional groups on the cations capable of hydrogen bonding as well as the presence of uncoordinated formate oxygen atoms.

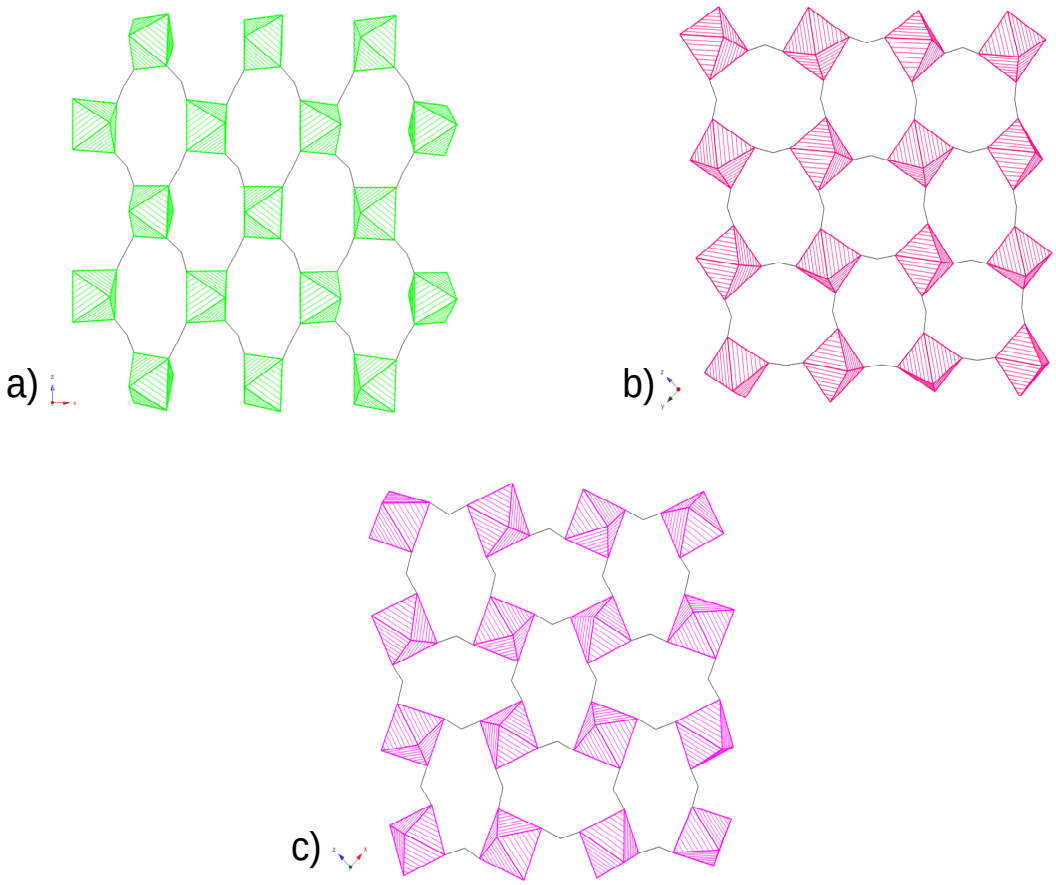

Figure 7.11 . A view of illustrating the different two-dimensional metal-formate-metal nets seen in [7.1-7.2] (a), [7.3] (b), and [7.4 -7.5] (c). The networks are shown as metal octahedra bridged by wire bond formates. Network (a) is viewed in the [010] direction, (b) in the [100] direction, and (c) in the [010] direction.

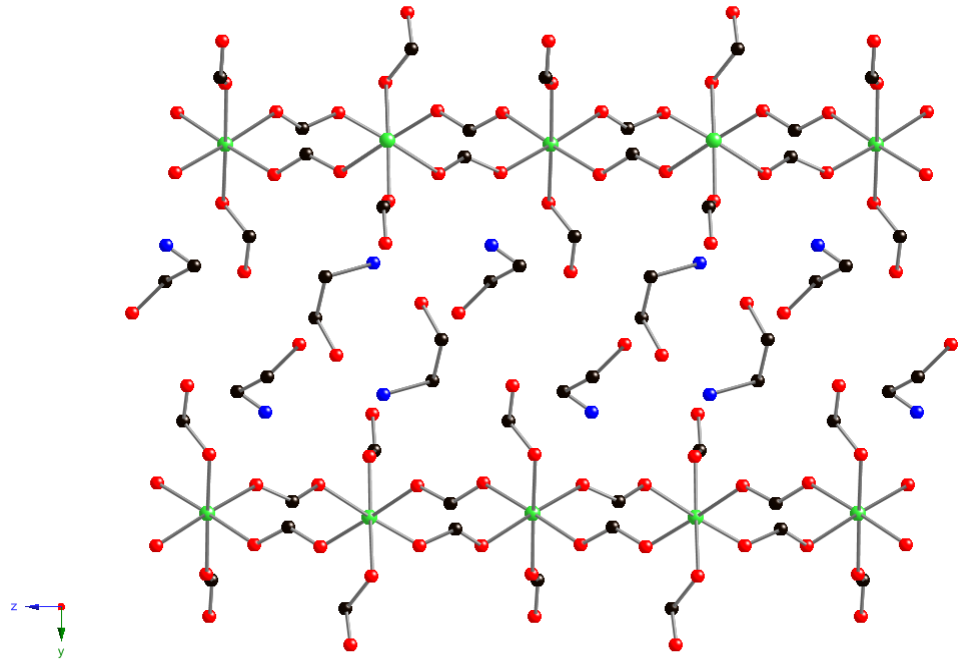

Figure 7.12. Illustration looking into the metal-formate network layers in [7.1] and [7.2] as viewed in the [100] direction. Non-linking formate groups extend from the axial positions to interact with HEA cations between the layers. Metal atoms are shown in green. C atoms are in black. O atoms are shown in red. N atoms are shown in blue.

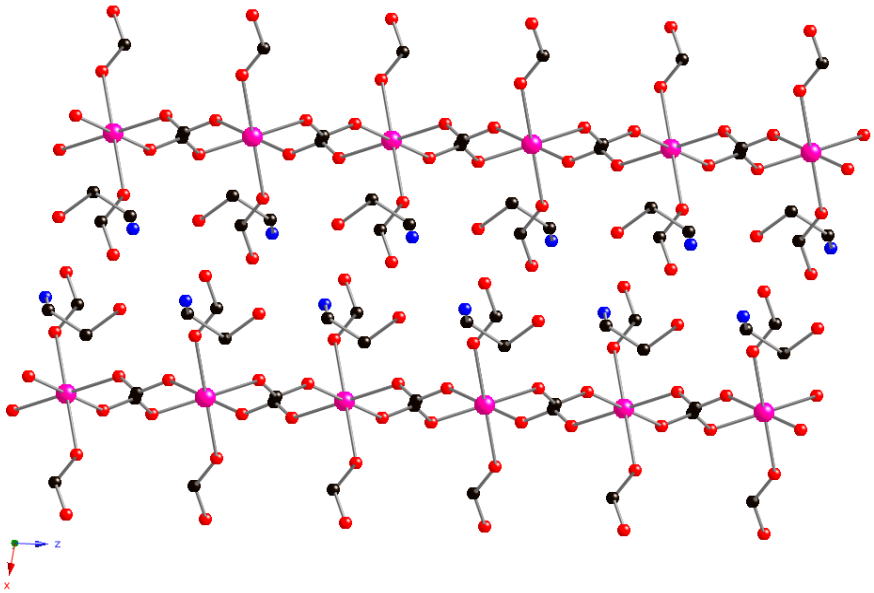

Figure 7.13. Illustration of [7.3] in the [010] direction looking into Mn-formate network layers. Non-linking formates extend from axial positions of the octahedra to interact with HEA cations in the layers. Mn atoms are shown in pink. C atoms are shown in black. O atoms are in red. N atoms are in blue.

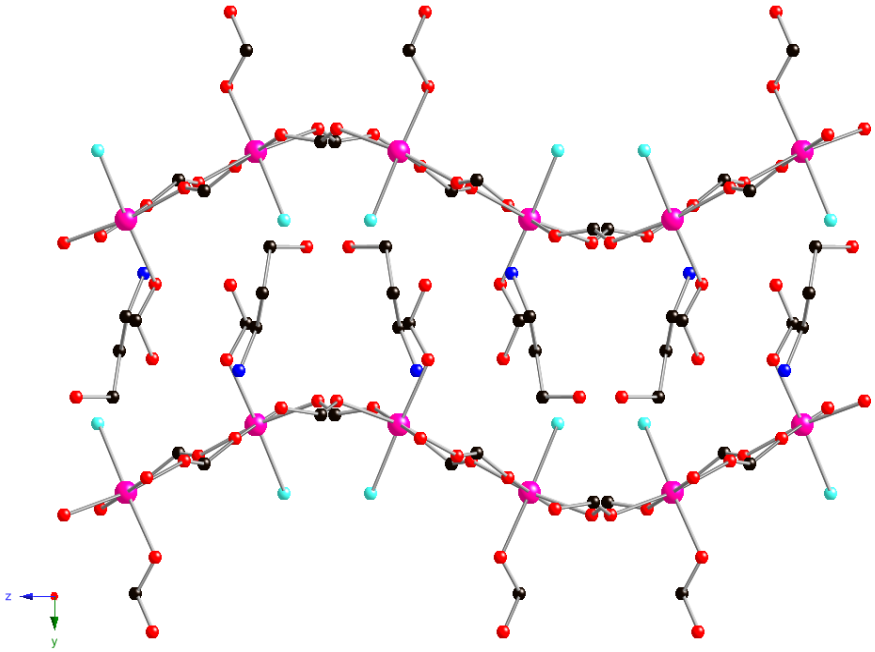

Figure 7.14. View of [100] direction looking into the distorted metal-formate layers of [7.4] and [7.5]. Non-linking formate groups coordinated to an axial position interact with HPA cations in the layers while a bound water molecule occupies the other axial position. Metal atoms are shown in violet. C atoms are shown in black. O atoms are in red. N atoms are in blue. Water molecules are represented in aqua.

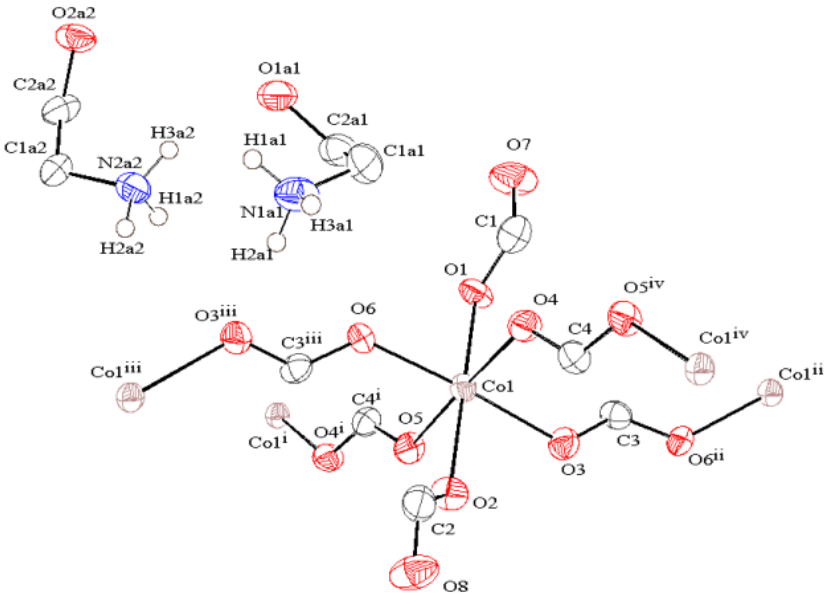

Figure 7.15. ORTEP representation of [7.1] illustrating the numbering scheme. Ellipsoids are drawn at 50% probability. Hydrogen atoms are included on the protonated ammonium N1A1 and N2A2 for distinction. All other H atoms are omitted for clarity. Symmetry codes: i) (1/2+x, 1/2-y, 1/2+z), ii) (1/2+x, 1/2-y, -1/2+z), iii) (-1/2+x, 1/2-y, 1/2+z) or iv) (-1/2+x, 1/2-y, -1/2+z).

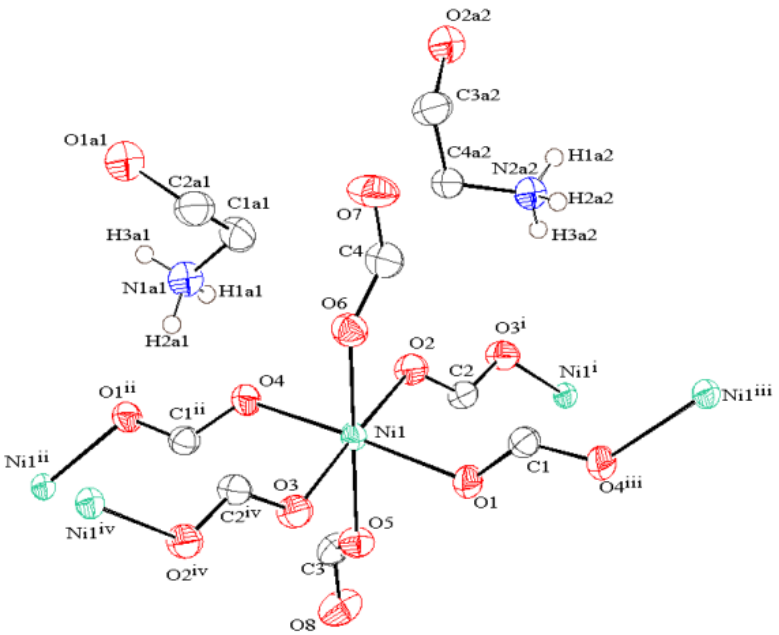

Figure 7.16. ORTEP representation of [7.2] illustrating the numbering scheme. Ellipsoids are drawn at 50% probability. Hydrogen atoms are included on the protonated ammonium N1A1 and N2A2 for distinction. All other H atoms are omitted for clarity. Symmetry codes: i) (-1/2+x, 1/2-y, -1/2+z), ii) (-1/2+x, 1/2-y, 1/2+z), iii) (1/2+x, 1/2-y, -1/2+z), iv) (1/2+x, 1/2-y, 1/2+z).

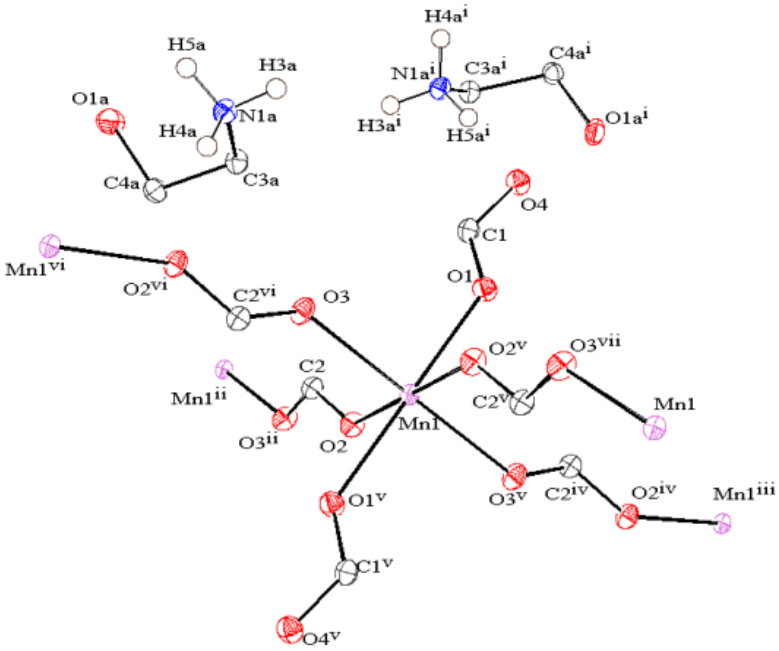

Figure 7.17. ORTEP representation of [7.3] illustrating the numbering scheme. Ellipsoids are drawn at 50% probability. Hydrogen atoms are included on the protonated ammonium N1A for distinction. All other H atoms are omitted for clarity. Symmetry codes: i) (-x, -1/2+y, 1/2-z), ii) (1-x, -1/2+y, 1/2-z) iii) (1-x, -1/2+y, -1/2-z), iv) (x, 1/2-y, -1/2+z), v) (1-x, 1-y, -z), vi) (1-x, 1/2+y, 1/2-z) vii) (x, 3/2-y, -1/2+z).

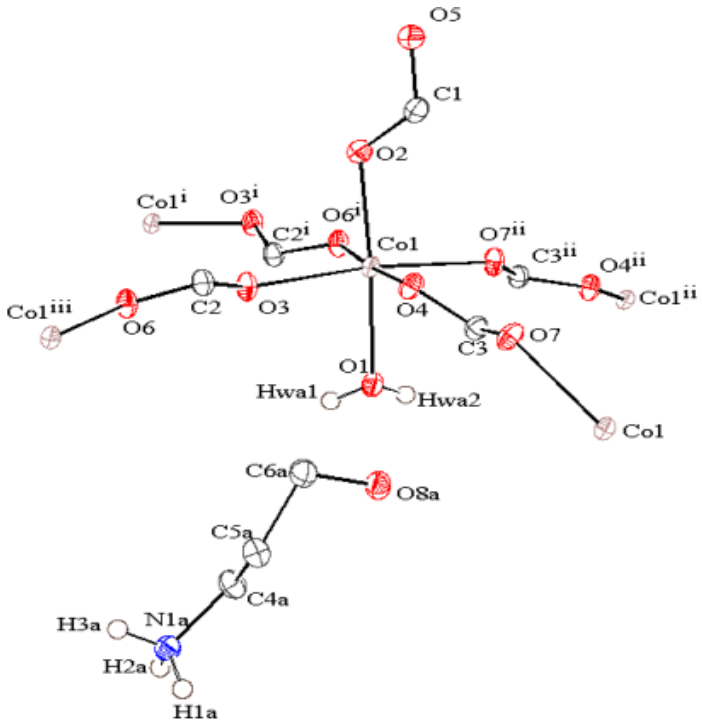

Figure 7.18. ORTEP representation of [7.4]. Ellipsoids are drawn at 50% probability. Hydrogen atoms part of the bound water molecule and protonated ammonium N1A are included for distinction. Symmetry codes: i) (-1/2+x, 1/2-y, 1-z), ii) (-1/2+x, y, 3/2-z), iii) (1/2+x, 1/2-y, 1-z).

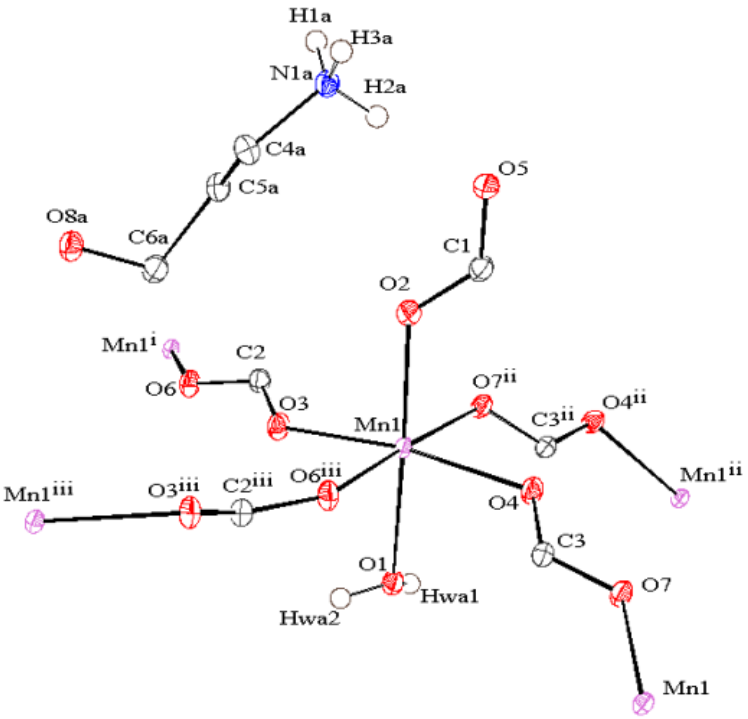

Figure 7.19. ORTEP representation of [7.5]. Ellipsoids are drawn at 50% probability. Hydrogen atoms part of the bound water molecule and protonated ammonium N1A are included for distinction. Symmetry codes: i) (-1/2+x, 1/2-y, 1-z), ii) (-1/2+x, y, 3/2-z) iii) (1/2+x, 1/2-y, 1-z).

Table 7.2. Selected bond lengths* for [7.1-7.5]

Structure		Length (Å)	Structure		Length (Å)
[7.1]	Co(1)-O(6)	2.059(4)	[7.3]	Mn(1)-O(3)	2.1656(7)
	Co(1)-O(5)	2.062(4)		Mn(1)-O(2)	2.1849(7)
	Co(1)-O(4)	2.079(4)		N(1A)-C(3A)	1.4951(1)
	Co(1)-O(3)	2.084(4)	[7.4]	Co(1)-O(1)	2.1278(1)
	Co(1)-O(1)	2.138(4)		Co(1)-O(2)	2.0557(1)
	Co(1)-O(2)	2.142(4)		Co(1)-O(3)	2.0868(9)
	N(1A1)-C(1A1)	1.495(9)		Co(1)-O(4)	2.1097(9)
	N(2A2)-C(1A2)	1.487(8)		Co(1)-O(6)[1]	2.1000(9)
[7.2]	Ni(1)-O(3)	2.0381(2)		Co(1)-O(7)[2]	2.1146(9)
	Ni(1)-O(4)	2.043(2)		N(1A)-C(4A)	1.4865(2)
	Ni(1)-O(2)	2.0543(2)	[7.5]	Mn(1)-O(1)	2.2431(9)
	Ni(1)-O(1)	2.0692(2)		Mn(1)-O(2)	2.1392(9)
	Ni(1)-O(6)	2.097(2)		Mn(1)-O(3)	2.1591(8)
	Ni(1)-O(5)	2.112(2)		Mn(1)-O(4)	2.1888(9)
	N(1A1)-C(1A1)	1.488(5)		Mn(1)-O(6)[3]	2.1789(9)
	N(2A2)-C(4A2)	1.481(4)		Mn(1)-O(7)[2]	2.1858(9)
[7.3]	Mn(1)-O(1)	2.1930(7)		N(1A)-C(4A)	1.4888(2)

*Symmetry transformations used to generate equivalent atoms: [1](x-1/2,-y+1/2,-z+1), [2](x-1/2,y,-z+3/2), [3](x+1/2,-y+1/2,-z+1)

Table 7.3. Selected hydrogen bonding data* for [7.1-7.5] (Å and deg).

Structure	D-H...A	d(D-H) (Å)	d(H...A) (Å)	d(D...A) (Å)	<(DHA) (deg)
[7.1]	N(1A1)-H(3A1)...O(7)[1]	0.92(2)	2.32(5)	2.971(7)	127(5)
	N(2A2)-H(1A2)...O(8)[2]	0.93(2)	1.96(3)	2.851(8)	159(6)
[7.2]	N(1A1)-H(1A1)...O(7)[3]	0.86(2)	2.39(3)	2.973(4)	126(3)
	N(2A2)-H(2A2)...O(8)[4]	0.86(3)	1.99(3)	2.843(3)	168(4)
[7.3]	N(1A)-H(3A)...O(4)[5]	0.90(1)	2.00(1)	2.870(1)	163(1)
[7.4]	N(1A)-H(3A)...O(5)[6]	0.90(2)	1.88(2)	2.762(2)	167(2)
[7.5]	N(1A)-H(2A)...O(5)	0.90(1)	1.89(2)	2.776(1)	167(2)

*Symmetry transformations used to generate equivalent atoms: [1](x-1,y,z), [2](x+1/2,-y+1/2,z+1/2), [3](x-1,y,z), [4](x+1/2,-y+1/2,z-1/2), [5](-x,-y+1,-z), [6](x+1/2,-y+1/2,-z+1).

7.4.2. Discussion

In this work, we present an alternative route to the synthesis of magnetic metal-formate MOFs through the use of formate-based ionic liquids, allowing us to better investigate the role of hydroxyammonium cations on the resulting formate structures. To our knowledge, these formate-bridged MOFs are the first examples where structures are produced from an ionic liquid providing both the bridging ligand as well as the extra-framework cation. All of the reported structures obtained in our experiments are two-dimensional, layered compounds which is contrary to the three-dimensional frameworks produced when the templating effect of alkylammonium cations was investigated. When alkylammonium cations were used, the now well-established three-dimensional metal-formate connectivity resulted based on both the size and limited hydrogen bonding character of the extra-framework cations.[22-24,172] However, this study utilizing hydroxyammonium cations and ionothermal synthesis found two-dimensional metal-formate layers formed with extensive hydrogen bonding between the non-bridging formates and the hydroxyammonium ions. This is unlikely to be due to a factor of size or chain length, as both alkylammonium and hydroxyammonium cations are of comparable size. Instead, increased framework-cation hydrogen-bonding interactions stabilize the 2D structure.

To further test this hypothesis, we prepared two additional formate-based ionic liquids with the amines ethylenediamine (EN) and 1,3-diaminopropane (DAP)[a]. Again, the ammonium species templated each of the formate network types, but three-dimensional connectivity was observed. The reaction of the ethylenediamine IL gave the network [EN] $[M(HCOO)_3]$ (M= Mn[b], Nic[c], Co[d]), in which ethylenediammoium cations sit in the cavities of a $(4^9 \cdot 6^6)$ net (Figs.

[a] Synthesis followed the same procedure as compounds [3.1-3.5], except that the ILs were formed with the reaction of two equivalents of formic acid to one equivalent of amine.
[b] [EN] $[Mn(HCOO)_3]$; space group *P3*, a = 8.1916(2) Å, c= 7.7027(4) Å, V=447.62(3) $Å^3$
[c] [EN] $[Ni(HCOO)_3]$; space group *P3*, a = 8.0170(4) Å, c= 7.2744(2) Å, V=404.91(2) $Å^3$

7.20, 7.21). Likewise, the 1,3-diaminopropane IL was used in a similar manner, and the $(4^{12}\cdot6^3)(4^9\cdot6^6)$ net of 2[DAP] $[M_2(HCOO)_6]\cdot H_2O$ (M=Mn[e], Co[f]) was formed (Figs. 7.22, 7.23). In each case, the charge balancing cations influence the formation of their respective networks. From the observations and comparision to the two-dimensional networks, we can conclude that the formation of a two- or three-dimensional net appears to be influenced by the presence or absence of the hydroxyl group.

In comparison to the 3D formates discussed and cited above,[173] the 2D formates also follow a 2.11 *anti-anti* linking mode (Fig. 7.11). The principle difference between the two structure types arises from the non-bridging formates, preventing 3D connectivity (Fig. 7.12-7.14). As a result, the hydroxyammonium cations of each compound do not sit inside pores, as in the three-dimensional structure, but instead occupy space between two-dimensional formate nets. The size of the ionic liquid cation also influences the topology. A logical assumption for the HPA cation, with an additional CH_2 group compared to HEA, would lead to an increase the inter-layer spacing. However, the increased size appears to destabilize the structure type observed in [7.1 – 7.3] in favor of one where half of the terminal formate anions are replaced by neutral water molecules. Consequently, only half as many HPA cations are needed to balance charge, leading to a smaller interlayer spacing and a distortion of the 2-D nets to accommodate the cation (Fig. 7.14). It is also notable that when similar reactions were attempted with formate liquids derived from still larger amino alcohols, 4-amino, 1-butanol and 5-amino, 1-pentanol, the products obtained the well-known metal formate dihydrate structure type,[179-181] implying that these cations were too large to allow organocation-containing structures to form at all.

---

[d] [EN] $[Co(HCOO)_3]$; single crystals were not obtained, but powder diffraction matching the Mn and Ni phases suggests the same network formula and similar cell parameters.
[e] 2[DAP] $[Mn_2(HCOO)_6]\cdot H_2O$; space group *P-31c*, a = 8.4798(5) Å, c= 28.978(2) Å, V= 1804.6(2) $Å^3$
[f] 2[DAP] $[Co_2(HCOO)_6]\cdot H_2O$; space group *P-31c*, a = 8.3738(1) Å, c= 27.793(3) Å, V= 1687.7(3) $Å^3$

In contrast with a three-dimensional connectivity, where the tilts and bond lengths of the octahedra are inherently constrained, two-dimensional connectivity allows for more structural freedom. A comparison of the isostructures produced with the HEA formate, [7.1 – 7.3], demonstrates larger structural variability between different metal atoms compared to the 3D structures. Differences can be seen clearly when the O-C-O connections between neighboring metal octahedra are approximated as linear bonds and torsion angles defined by the O-M-M-O connections measured. The average torsion angle between octahedra in [7.1] and [7.2] is 54.7° and 54.9°, respectively, while [7.3] has an average torsion angle of 29.3° between Mn octahedra. The positioning of the non-linking formates is then directly affected in each structure, as an increase in octahedral torsion angles leads to an increase in distance between O atoms of the non-linking formates. Furthermore, the orientation of ammonium cations that hydrogen-bond to the non-linking formates affects interlayer stacking. The respective inter-layer distances of [7.1] and [7.2] (12.42 Å and 12.44 Å) are significantly larger than the inter-layer distance observed in [7.3] (8.925 Å).

Adjustments in the framework can also be made through distortions of the metal octahedra. As shown in Table 7.2, the metal-oxygen bonds for [7.1] and [7.2] show a greater distortion along their respective axial planes—the location of the non-linking formates—than those of [7.3]. The extent of distortion also has an effect on how the respective structures fit together. A different pattern of octahedral tilting is observed in [7.3], causing the void spaces in the two-dimensional net to alternate orientation (Fig 7.11). This is not seen in [7.1] and [7.2], as the void spaces are ordered uniformly throughout that network. This effect also gives rise to an increased metal to metal distance in [7.3] of 6.343 Å, nearly 0.5 Å more than [7.1] and [7.2].

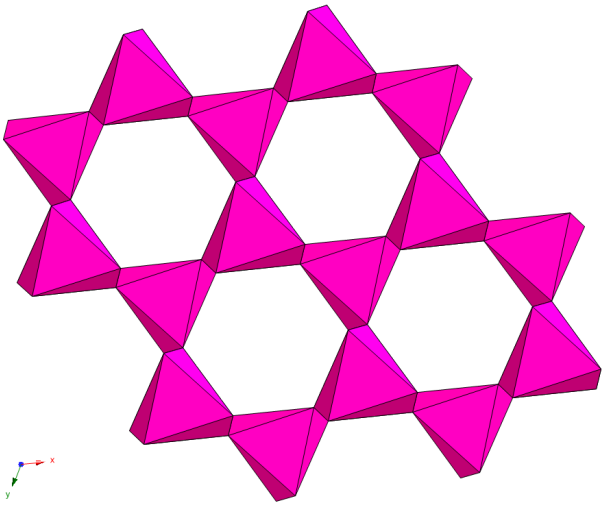

Figure 7.20. The $(4^9 \cdot 6^6)$ topology observed in the [EN] $[M(HCOO)_3]$ network.

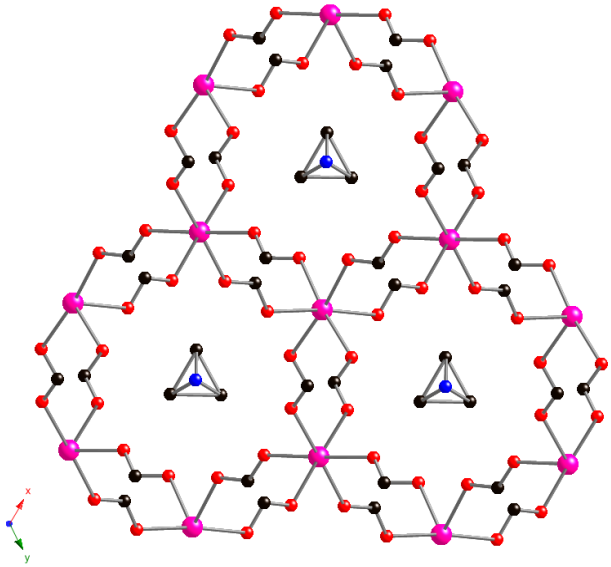

Figure 7.21. Structural view of trigonally distorted ethylenediammonium cations within the cavities of [EN] $[M(HCOO)_3]$.

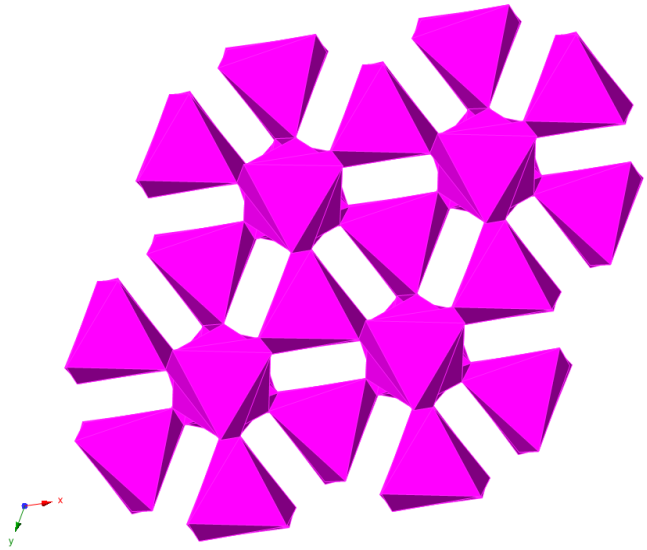

Figure 7.22. The $(4^{12}\cdot6^{3})(4^{9}\cdot6^{6})$ topology observed in the 2[DAP] $[M_2(HCOO)_6]\cdot H_2O$ network.

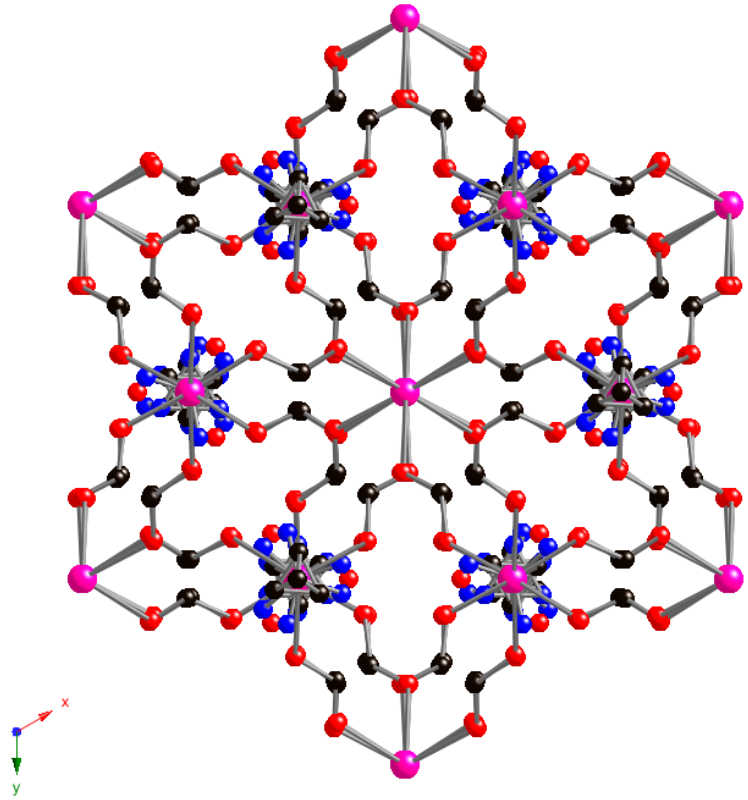

Figure 7.23. A view of the overall connectivity in 2[DAP] $[M_2(HCOO)_6]\cdot H_2O$. The triginally distorted 1,3-propanediammonium as well as a water molecule sit in the cavities of the formate bridges.

7.4.3. Magnetic Properties

The temperature T and magnetic field H dependencies of the dc magnetizations M(T,H) and the temperature dependence of the real χ' and imaginary χ'' parts of the ac susceptibility $\chi(T)$ were measured for each of the five samples. The temperature dependencies of the FC and ZFC dc magnetizations are depicted in Fig. 7.24**.** M(T) generally appears to increase monotonically with decreasing temperature, however the insets of Fig. 7.24 suggest that magnetic order occurs in each of the samples at low temperatures. Separation of the FC and ZFC magnetizations is one indication of magnetic order, and this effect is particularly pronounced in samples [7.1] and [7.5], where the magnetic ordering temperatures are 7 K and 9.2 K, respectively. The separation is less dramatic in samples [7.2]**,** [7.3]**,** and [7.4] where the separation of the FC/ZFC magnetizations occurs at 4.6 K, 8 K, and 7 K. These measurements of T_N are summarized in Table 7.2.

The separation of the FC and ZFC magnetizations only reveals the presence of a net uncompensated moment in the ordered phase, and cannot unambiguously differentiate ferromagnetic ordering from a complex form of antiferromagnetic order, such as the canted antiferromagnetism that was previously reported in this class of compounds.[22-23,73,172,182] Antiferromagnetic phase transitions are distinguished by a peak in the temperature derivative of the real part of the ac susceptibility χ' at the Néel temperature T_N, where an accompanying peak in the imaginary part of the susceptibility χ'' reflects the enhanced dissipation associated with the phase transition. We will determine T_N from the maximum in $\chi''(T)$. Measurements of the temperature dependencies of χ' and χ'' for [7.1 – 7.5] are shown in Fig. 7.25. In Co-based [7.1], we observe a strong peak in χ' and a very weak peak in χ'' at 7.3±0.1 K (Fig. 7.25a), close to the temperature where the FC and ZFC magnetizations separate, but there are additional peaks in χ'

and χ'' at 5.1±0.1 K, where weak features are also found in the FC and ZFC magnetizations (Fig. 5a, inset). Qualitatively similar observations are made in [7.4] (Fig. 7.25d), which is also Co-based. It is possible the initial magnetic structure that appears at 7 K in [7.1] and [7.4] is unstable, and transforms into a second structure at 5.2 K, and indeed a similar second transition was previously reported by Wang et al[22] who proposed that this behavior corresponds to a net rotation of the uncompensated moment. Samples [7.2] and [7.5] show single magnetic transitions, where the peaks in $\chi''(T_N)$ occur very near the same temperatures where the FC and ZFC magnetizations separate in [7.5], while we take the peak in $\chi''(T_N)$ to be a more accurate determination of the onset of order than the separation of the FC/ZFC magnetizations in [7.2]. No peak in χ'' is found in 3, but there is a broad peak in χ' at 8.0±0.15 K that agrees with the ordering temperature taken from the FC/ZFC magnetizations. The good agreement between the magnetic ordering temperatures determined from the ac susceptibility and FC/ZFC M(T) measurements is summarized for all five samples in Table 7.4.

The temperature dependence of the dc susceptibility $\chi(T)=M(T)/H$, measured in a dc field H of 500 Oe, increases monotonically with decreasing temperatures, and for temperatures between 10 K and 300 K is well described by the Curie-Weiss law, $\chi = C / (T - \theta)$. We have plotted $1/\chi$ as a function of temperature in Fig. 7.26, allowing us to determine the Curie constant C and the Weiss constant θ as parameters of straight line fits to these data. We calculated the effective paramagnetic moment $\mu_{eff} = (8 \cdot C)^{1/2}$ of each metal ion using the measured values of C for each sample, and the results are compared to the previously reported values of μ_{eff} for Co^{2+}, Ni^{2+} and Mn^{2+} in Table 7.4, showing good agreement. We find that the Weiss constant θ is negative for [7.1 – 7.5], indicating that the mean field for the fluctuating moments is overall antiferromagnetic, supporting the conclusions of the ac susceptibility analyses, above.

The field dependence of the dc magnetization is different above and below the antiferromagnetic phase transition. Below T_N, the magnetization is almost linear at high magnetic fields (Fig. 7.27), while at lower fields it is hysteretic with small coercive fields H_C (insets, Fig. 7.27). No hysteresis was detected above T_N. The values of H_C for all samples are summarized in Table 7.4. At the lowest temperature (2 K) and highest applied field (50 kOe), the saturation magnetization M_S per metal ion is much smaller than the value calculated for the corresponding isolated metal ion $M_S = gJ\mu_B$, where g is a Landé factor and J is a total angular momentum (Table 7.4).

In summary, we have determined from measurements of the ac and dc susceptibility that all five metal formate samples are moment bearing, and order antiferromagnetically below 10 K. The antiferromagnetic order is not simple, since the ordered state displays hysteresis between field cooled and zero field cooled magnetizations, as well as a pronounced coercive field. Our observations are consistent with earlier measurements that concluded that the ordered state of metal-formate hybrids can best be described as a canted antiferromagnet.

Table 7.4. Summary of magnetic properties of samples [7.1 – 7.5]. T_N is the magnetic ordering temperature defined from the separation of the FC and ZFC measurements of the dc magnetization, T_N^* is the ordering temperature defined from ac susceptibility measurements, θ is the Weiss constant, μ_{eff}, is the effective paramagnetic moment per metal atom, and μ_{th} is the calculated theoretical value of μ_{eff}, . M_S is the saturation magnetization at 2 K at 50 kOe, M_S^{free} is the calculated saturation magnetization, H_C is the coercive field at 2 K.

Sample	T_N (K)	T_N^* (K)	θ (K)	μ_{eff} (μ_B/atom)	μ_{th}(μ_B/atom)	M_S(μ_B)	M_S^{free}(μ_B)	H_C (Oe)
[7.1] Co^{2+}	7.0	7.3±0.1 5.1±0.1	-46	4.1	4.8	1.5	3	400
[7.2] Ni^{2+}	4.6	1.9±0.1	-33	3.3	3.2	0.3	2	700
[7.3] Mn^{2+}	8.0	8.0±0.15	-10	6.1	5.9	1.9	5	20
[7.4] Co^{2+}	7.0	6.7±0.15, 4.7±0.1	-30	5.1	4.8	0.9	3	300
[7.5] Mn^{2+}	9.2	9.6±0.1	-14	6.1	5.9	1.6	5	100

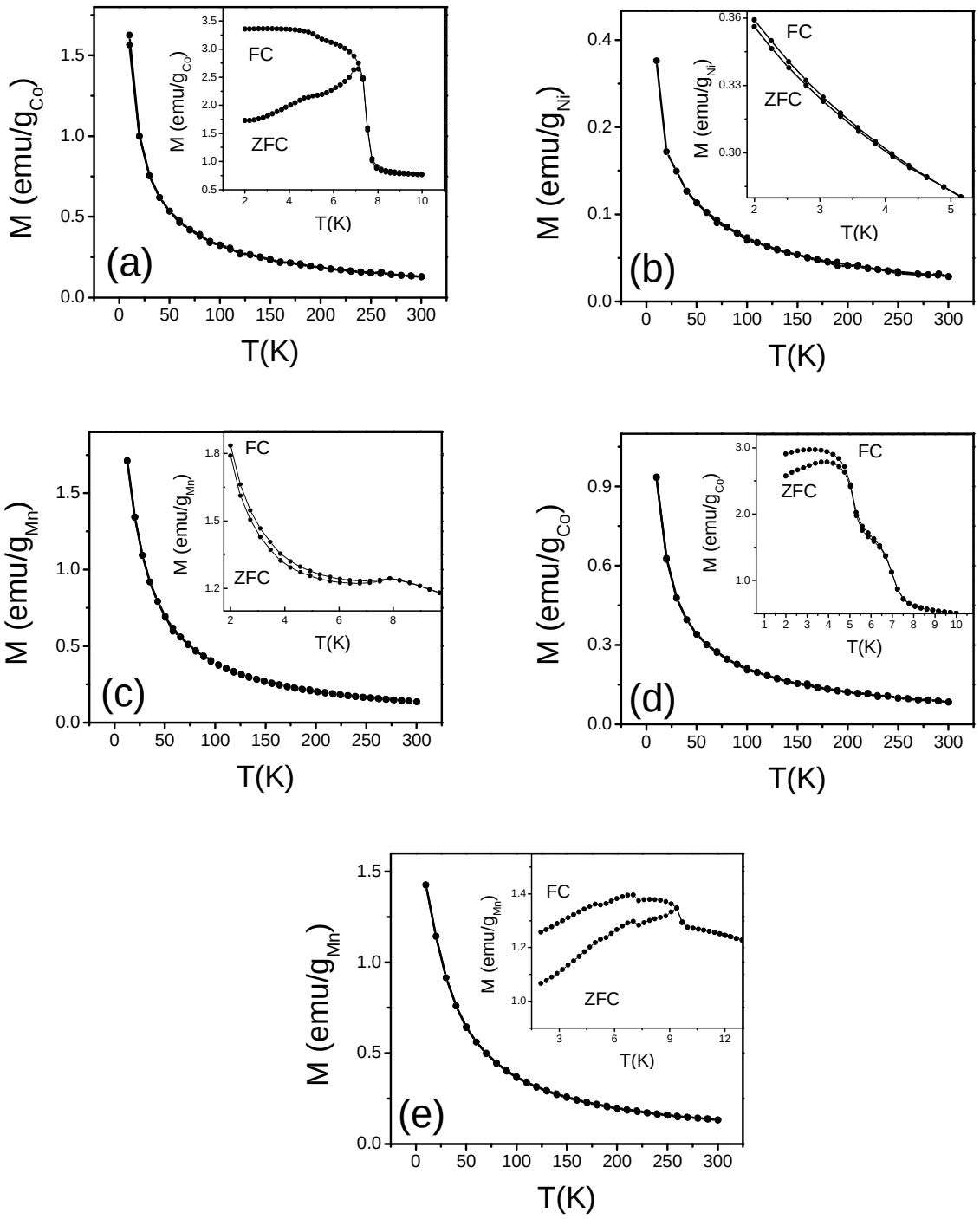

Figure 7.24. The temperature dependencies of the ZFC and FC magnetizations in a magnetic field of 500 Oe for samples (a) [7.1], (b) [7.2], (c) [7.3], (d) [7.4] and (e) [7.5]. Insets: expanded view of low temperatures regimes.

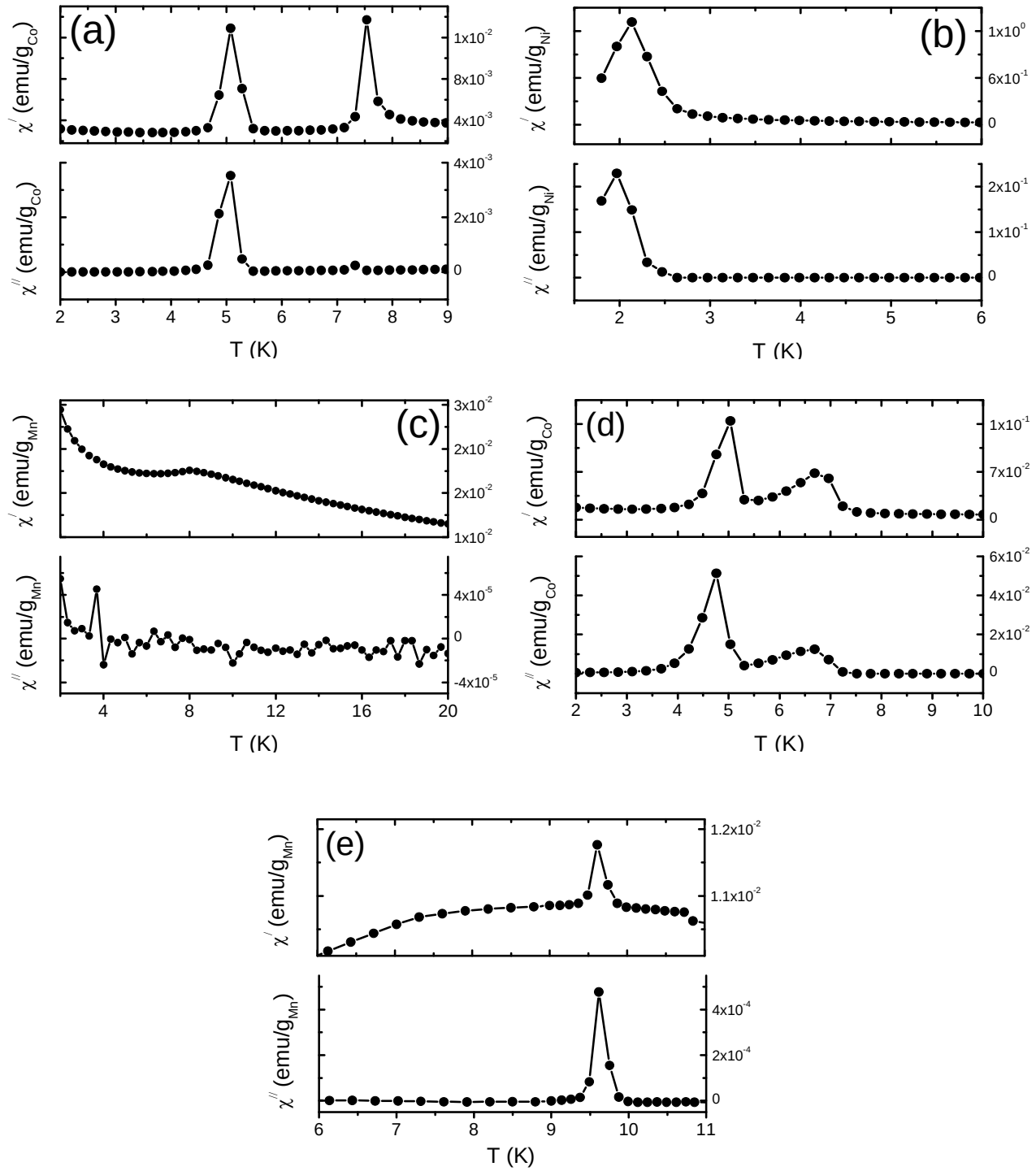

Figure 7.25. The temperature dependencies of the real part χ' and imaginary part χ'' of the ac susceptibility for samples (a) [7.1], (b) [7.2], (c) [7.3], (d) [7.4] and (e) [7.5].

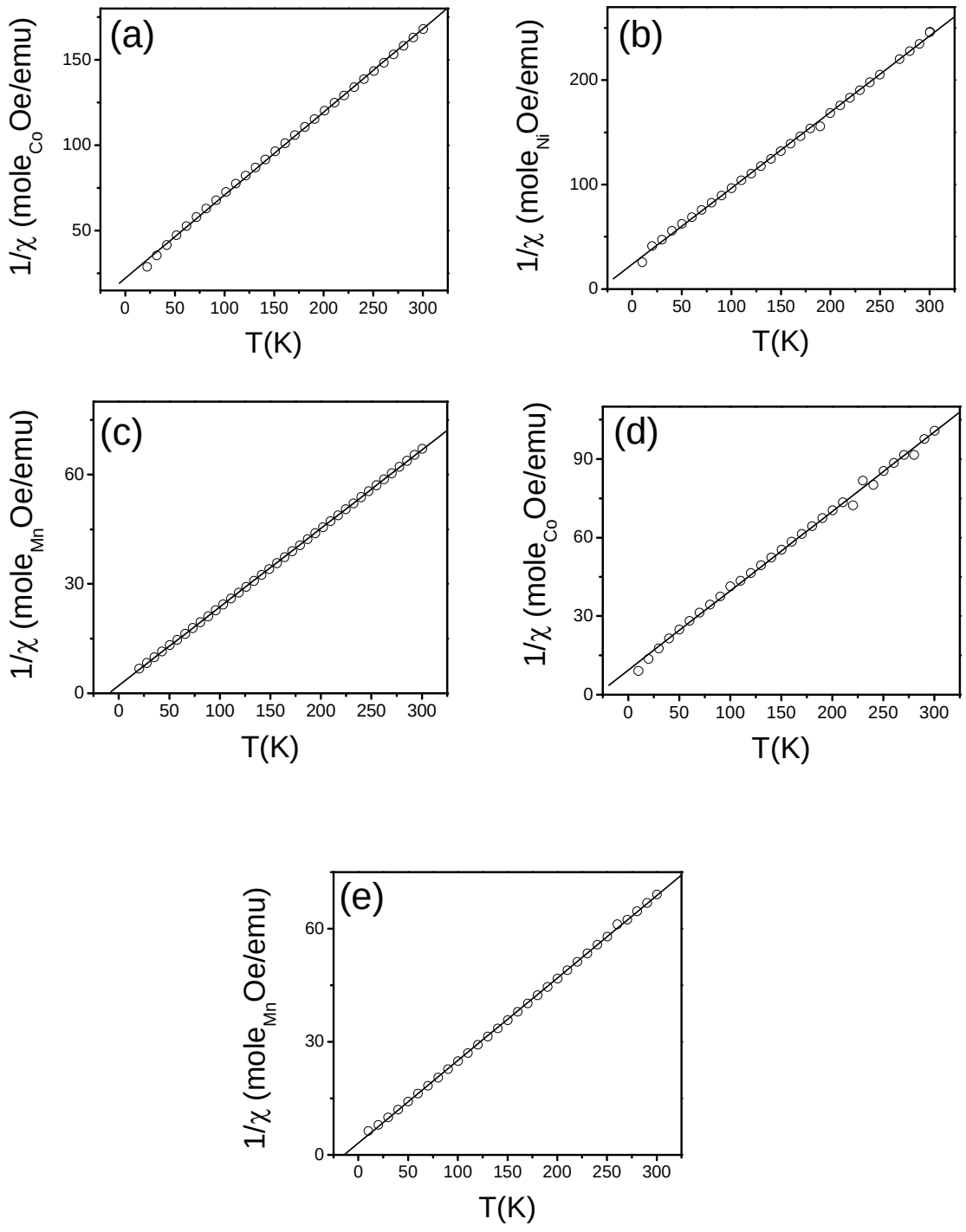

Figure 7.26. The inverse molar susceptibility χ as a function of temperature for samples (a) [7.1], (b) [7.2], (c) [7.3], (d) [7.4] and (e) [7.5]. The solid lines are the fits to Curie-Weiss expression, as described in the text.

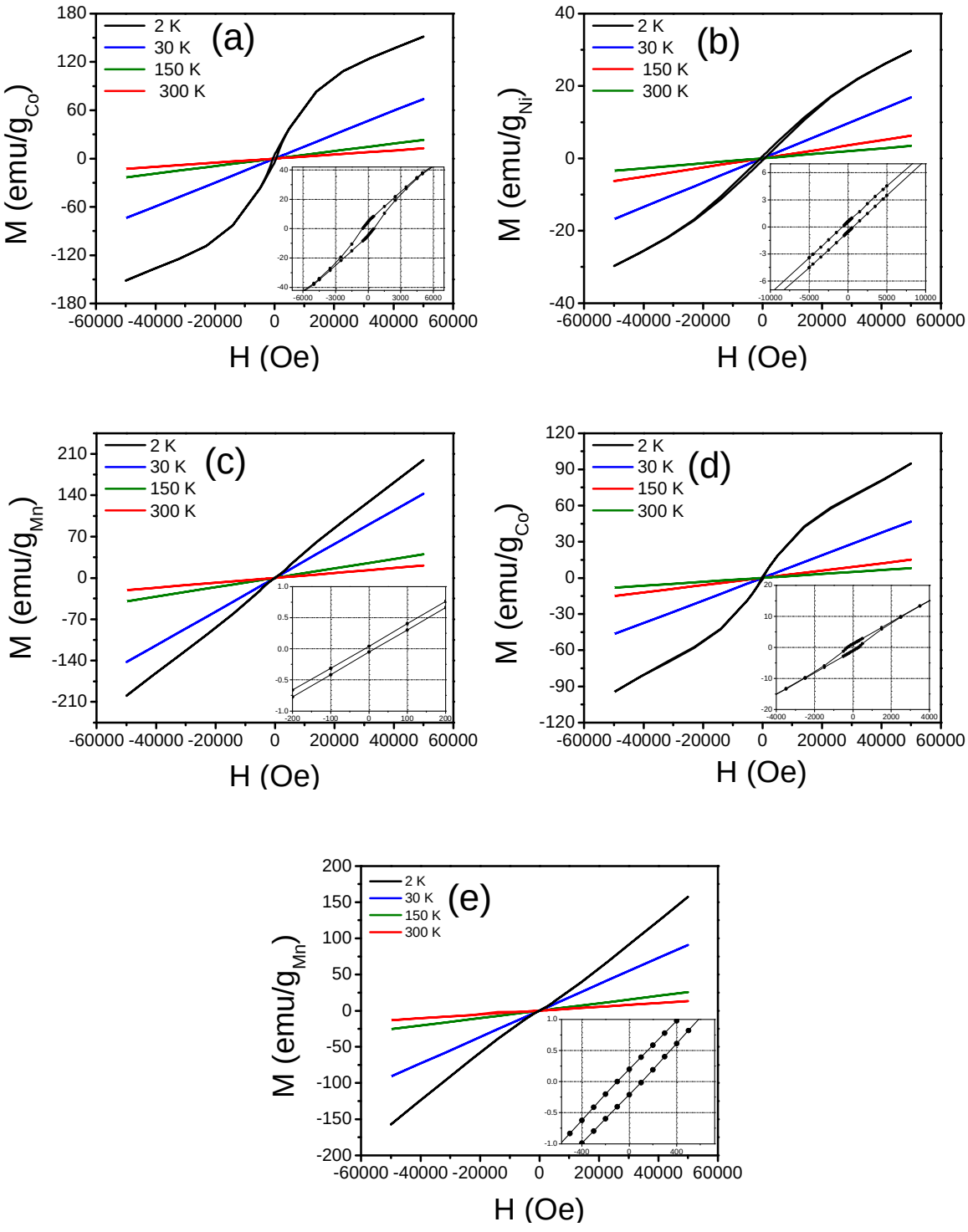

Figure 7.27. The magnetization M as a function of magnetic fields H at different temperatures for samples (a) [7.1], (b) [7.2], (c) [7.3], (d) [7.4] and (e) [7.5]. Insets: Expanded view of the low field magnetization at 2 K for samples (a) [7.1], (b) [7.2], (c) [7.3], (d) [7.4] and (e) [7.5].

7.5. Conclusion

The five magnetic metal-formate frameworks presented here were synthesized ionothermally by utilizing two different ionic liquid solvents, hydroxyethylammonium (HEA) formate and 1-hydroxy, 3-proplyammonium (HPA) formate. The use of HEA formate in [7.1 – 7.3] yielded a metal-formate network with two non-linking formate groups in the axial positions, while using HPA formate in [7.4] and [7.5] produced a 2-D metal-formate framework with the axial Co(II) coordination sites occupied by one formate anion and a water molecule. In each compound, the ionic liquid cation is incorporated into the resulting structure as a charge balancing species, demonstrating that the choice of ionic liquid cation can greatly affect the resulting metal-organic framework. It was found that all samples can be classified as canted antiferromagnets, a magnetic behavior consistent with other previously reported magnetic metal formate hybrids. Minor reaction modifications, such as a change in metal center or ammonium cation, produced each compound described in this work, demonstrating that ionothermal synthesis of formate-based ionic liquids is a simple, yet effective means for the discovery of new varieties of magnetic metal-formate frameworks. Future work will continue to utilize ionothermal methods in this system, targeting new multiferroic materials.

Chapter 8

Synthesis and Structural Characterization of *s*-block Coordination Networks

8.1. Abstract

A three-dimensional magnesium-lithium coordination network, $Mg_2Li(BTC)(HBTC)(DMF)_2$ [8.1] (BTC=1,3,5-benzenetricarboxylate; DMF=N,N-dimethylformamide), the first example of a mixed-metal Mg-Li coordination network, was synthesized using solvothermal techniques. Structural characterization was completed using single crystal x-ray techniques while thermal properties and surface area measurements were conducted by thermogravimetric and BET analysis, respectively. Three potassium-based coordination networks K were also synthesized. The structures of $K_2(NDC)\cdot xH_2O$ [8.2] (NDC=1,4-naphthalenedicarboxylate), $K_2(TDC)$ [8.3] (TDC=2,5-thiophenedicarboxylate), and $K_2(SDB)\cdot$(guest) [8.4] (SDB=4,4′-sufonyldibenzoate) are dependent on the coordination and geometry of the linker, as chains of potassium are the predominant network features. The structure and characterization of [8.1] has been published: Calderone, P. J.; Banerjee, D.; Borkowski, L. A.; Parise, J. B. *Inorg. Chem. Commun.* **2011**, *14*, 741.

8.2. Introduction

Transition and other *3d* metal centers such as Mn,[85] Co,[86] and Zn[88] continue to be used most frequently in CN synthesis since their chemistry and bonding behavior with polycarboxylate linkers is well known. In contrast, the synthetic possibilities of CNs based on *s*-block metal centers remain relatively underexplored.[183] Aside from their relative abundance in nature, the other rationale for using *s*-block metals in CNs is that their variety of metal coordination environments results in a high degree of structural diversity.[26] However, the ionic bonding character of the metal centers makes structure predictability and synthetic control a challenge. Moreover, the small number of reports of *s*-block metal CNs in the literature provides only limited guidance for future work. To remedy this, our research group is further exploring *s*-block metal chemistry in CNs, specifically those based on the lightweight metals potassium, lithium, and magnesium.

Lightweight metal-CNs possess gravimetric advantage over more common CNs based on heavier, *3d* metals and are desired for materials intended for storage or sequestration applications. Potassium-based networks are sparsely reported,[184-187] but the use of an appropriate linker has led to compounds thought to be the basis for new redox-active materials[188] and possible alternatives to sequester radioactive alkali cations from spent nuclear fuel.[185] Also, the connectivity of potassium CNs depends largely on the choice of ligand due to the preference of the K^+ coordination sphere. Potassium CNs tend to form chains where coordinated oxygen atoms are shared between metal centers. Consequently, a predominate feature in many potassium carboxylates CNs is increased metal connectivity no matter what the linker used. Therefore, the geometry of the ligand is the determining factor in the network topology. .

Magnesium- and lithium-based CNs are more common targets and their chemistries are better understood in *s*-block CN research. Work specifically targeting magnesium CNs has grown significantly,[38,93-94,151,189-190] and our group has previously synthesized a series of lithium CNs that utilize a number of multifunctional organic ligands.[34-36,92] However, lithium metal centers favor tetrahedral coordination with carboxylate oxygen, thus restricting the topological possibilities. The incorporation of another metal center in addition to lithium allows new degrees of freedom for topological variation. Taking this into account, we have begun to explore the advantages of mixed metal/lithium coordination networks (CNs).

Many mixed metal coordination networks have fascinating coordination environments and building units, and examples of combinations of transition [191-193], rare earth,[194-195] and *s*-block,[93,196-198] metals are known. However, heterometallic coordination networks present a synthetic challenge not encountered in homometallic synthesis in that the chemistry of two different metal centers must be considered. It is difficult to find a balance in reaction conditions that favor incorporation of two metals into the structure, primarialy because the coordination preferences of both metals must be accommodated. Additionally, if the targeted material were intended to minimize the gravimetric contributions of metal centers to the overall compound, frameworks that include heavier transition and rare earth metals would be poor targets for exploratory synthesis. However, extended networks combining the lightweight s-block metals magnesium and lithium could be used to construct lightweight MOFs with new, interesting structures.

Hybrid inorganic-organic materials combining lithium and magnesium are known in a few organometallic complexes.[199-201] Yet, to date, extended lithium-magnesium coordination networks have not been reported. Considering the lack of examples of lithium-magnesium

networks and the prospects of further expansion on lightweight s-block metal MOF synthesis, we decided to explore the possibility of mixed lithium-magnesium MOFs. This has resulted in $Mg_2Li(BTC)(HBTC)(DMF)_2$, [8.1], the first example of a lithium-magnesium heterometallic coordination network. Simultaneously, we also expand on the limited understanding of the chemistry in potassium CNs with the synthesis of three new networks, $K_2NDC \cdot xH_2O$ [8.2], K_2TDC [8.3], and $K_2(SDB) \cdot (guest)$ [8.4].

8.3. Experimental Section

8.3.1. Synthesis of $Mg_2Li(HBTC)_2(DMF)_2$ [8.1], $K_2NDC \cdot xH_2O$ [8.2], K_2TDC [8.3], and $K_2(SDB) \cdot (guest)$ [8.4]

All compounds were synthesized under solvothermal condition using Teflon lined stainless steel Parr autoclaves. Starting materials were purchased and used as received and include: Magnesium nitrate hexahydrate (Acros-organics, 99%), lithium nitrate (Acros-organics, 99%), lithium hydroxide (Alfa-Aesar, 98%), potassium nitrate (Acros-organics, 99%) trimesic acid (Sigma-Aldrich, 95%), 1,4-naphthalenedicarboxyic acid (J.K. Baker 96%), 2,5-thiophenedicarboxylic acid (Acros 97%), 4,4′-sulfonyldicarboxylic acid (Acros 95%) and N,N'-dimethylformamide (Sigma-Aldrich, 99%).

The synthesis procedures were similar for all four compounds [8.1 - 8.4]. For [8.1] 1.25 mmol (0.323 g) of $Mg(NO_3)_2 \cdot 6H_2O$, 2.5 mmol (0.173 mmol) $LiNO_3$, 0.5 mmol (0.023 g) LiOH, 5 mmol (1.051 g) trimesic acid, were mechanically stirred for 4 hours in 14.15 g DMF. For [8.2], 1 mmol (0.101 g) $K(NO_3)$ and 0.5 mmol (0.108 g) 1,4-naphthalenedicarboxylic acid was dissolved in 10.10 g DMF. For [8.3], 2 mmol (0.202 g) $K(NO_3)$ and 1 mmol (0.172 g) 2,5-thiophenedicarboxylic acid were dissolved in 14.20 g DMF. Finally, for [8.4], 2 mmol (0.202 g)

$K(NO_3)$ and 1 mmol (0.306 g) 4,4´-sufonyldibenzoic acid were dissolved in 14.05 g DMF. The mixtures were reacted in autoclaves at 180°C for three days, and then the resultant white crystalline products, were washed with DMF and ethanol.

8.3.2. X-ray Diffraction and Structure Solution[*]

A representative single crystal of [8.1][#] ($Mg_2Li(HBTC)_2(DMF)_2$) suitable for single crystal x-ray diffraction was pulled directly from the bulk. The crystal was mounted on a cryoloop using oil and data were collected at 100K on an Oxford Gemini diffractometer equipped with an Atlas detector, using Mo Kα radiation (λ = 0.71073 Å) and 0.5° ω scans. Raw intensity data were collected and integrated using the CrysAlisPro software package (Oxford Diffraction Ltd., Version 1.171.33.41, 2009). An empirical absorption correction was applied using SADABS.[70] The crystal structure for [8.1] was solved via direct methods (SHELXS).[70] Mg atoms were located first, followed by the determination of all other atom positions (O, C, N, Li) from the Fourier difference map. Non-hydrogen atoms were refined anisotropically using SHELXTL[70] within the WINGX[202] suite of software. Methyl group and aromatic hydrogen atoms were placed in calculated positions. The hydrogen atom on the protonated carboxyl group was located in the Fourier difference map Powder X-ray diffraction data (Fig. 8.1) were collected on a Scintag Pad X diffractometer (CuK_α, (λ = 1.5418 Å) at a range of 5-40° 2θ, 0.02 °step, 1.5 s/step).

A similar procedure was used for the partial structure determination of [8.2][a], [8.3][b], and [8.4][c]. Crystallographically acceptable structure refinements were not possible due to crystal

[*] Some structure solution work completed by Debasis Banerjee and Lauren Borkowski.

[#] Crystal data for [4.1]: Space group *C*2/*c*, M_r=618.00, *a*=17.1200(7)Å, *b*=8.8749(4)Å, *c*=17.1186(8)Å, β=95.728(4)°, *V*=2588.0(2)Å^3, Formula= $C_{24}H_{22}LiMg_2N_2O_{14}$, *Z*=4, ρ_o= 1.586mg/m^3, *T*=100(2) K, *R*1[I>2σ(I)]= 0.0553, wR_2= 0.1631, GOF= 1.106.

merohedral twinning in each sample. However, we are confident in the structural formulas, space groups and cell parameters reported here.

8.3.3. Thermal Analysis

Thermal TG/DSC data for [8.1] (Fig 8.2) were collected with using a STA 449 C Jupiter Netzsch Instrument at a range of 30-700°C and 5 degrees per minute under N_2 atmosphere using an Al_2O_3 crucible for TGA-DSC analysis.

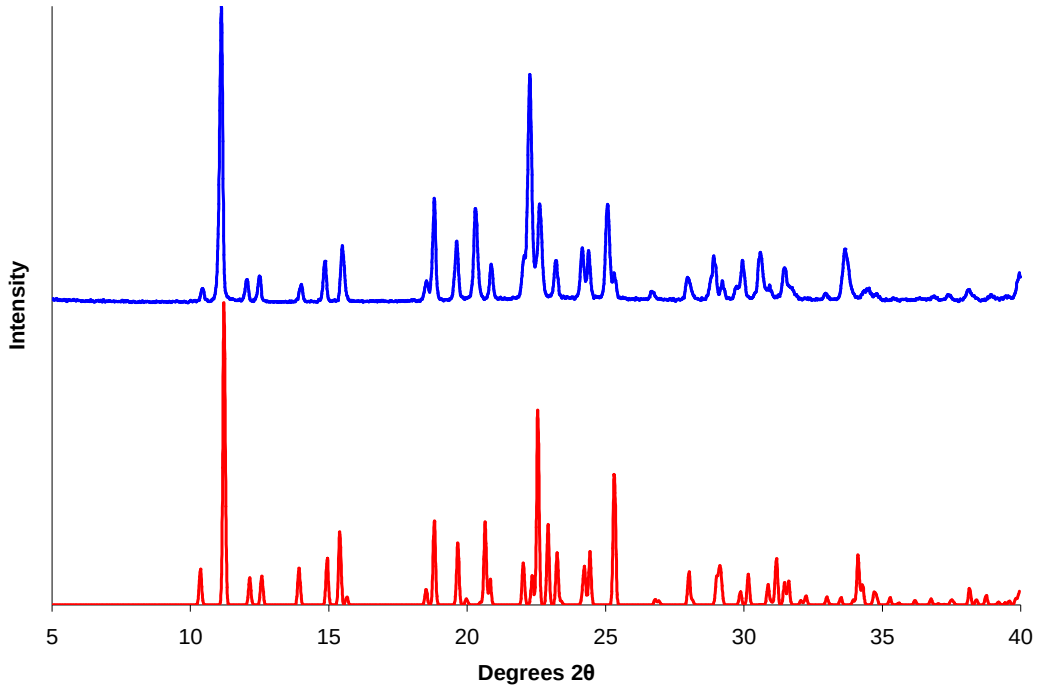

Figure 8.1. Experimental (top) and simulated (bottom) powder XRD pattern comparison for [8.1].

8.3.3. Thermal Analysis and Surface Area Measurement

[a] Space group $P2_1/c$, a= 11.6576(5)Å, b= 27.7194(2) Å, c= 16.4248(7) Å, β= 110.279(2)°, V= 4978.6(4) Å^3
[b] Space group $A2_1am$, a= 3.9320(8) Å, b= 18.743(4) Å, c= 5.6915(2)Å, V= 419.45(15)Å^3
[c] Space group $P2_1/n$, a= 13.6526(8) Å, b= 6.0026(8) Å, c= 22.367(3) Å, β=105.776(3)°, V=1764.0(4) Å^3

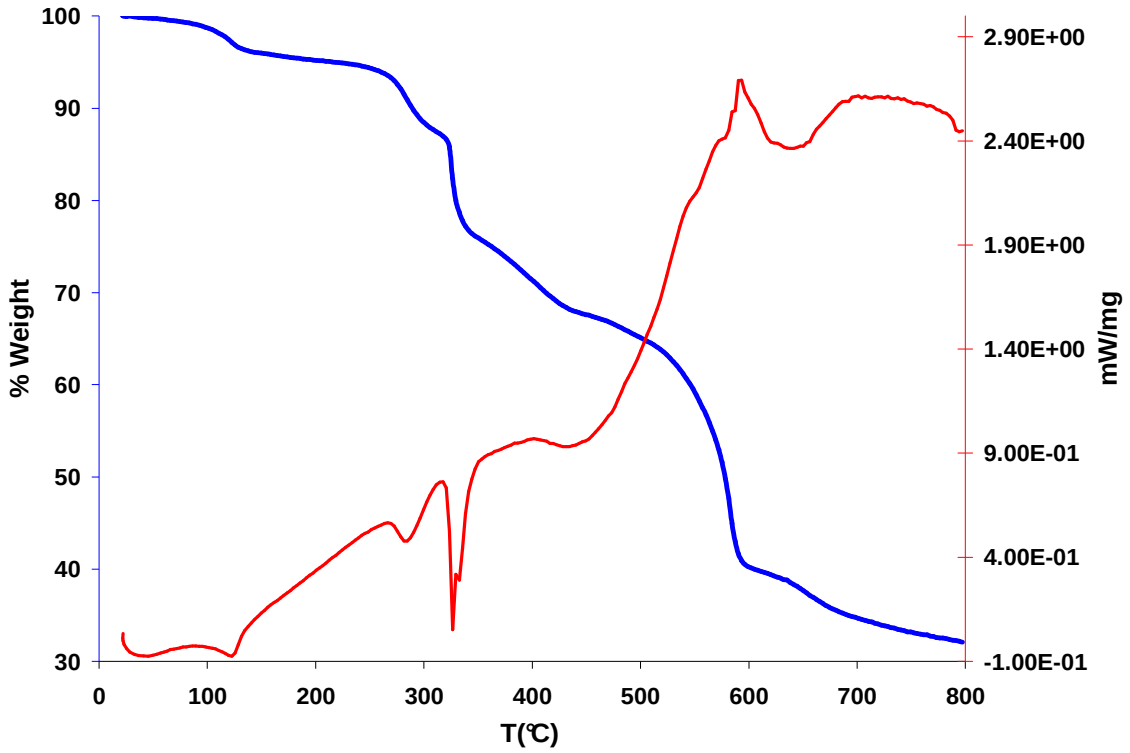

Fig 8.2. Thermal data curves of [8.1] showing thermogravimetric analysis (blue) and corresponding differential scanning calorimetry (red, mW/mg) up to 800 °C.

8.4. Results and Discussion

8.4.1 Structural description of [8.1], $Mg_2Li(BTC)(HBTC)(DMF)_2$

Compound [8.1] consists of dimeric units of distorted, 5-coordinated magnesium trigonal-bipyramids linked by irregular corner-shared Li tetrahedra to form Mg-Li-Mg triads arranged in one-dimensional chains running along the [010] direction (Fig 8.3). These one-dimensional chains are set in a diamond-shaped array and connected into a three-dimensional network by both a BTC ligand and a protonated HBTC ligand. We are confident that the unbound carboxylate oxygen is protonated due to the lengthening of the C-O bond in comparision to others. These two linkers produce one-dimensional channels along the [001] direction (Fig. 8.4). The HBTC ligand contains three carboxylate groups each found in different coordination environments: tridentate-trinuclear, bidentate-binuclear, and monodentate (Fig 8.5). The tridentate-trinuclear carboxylate group is bound to two magnesium and one lithium center and connects the triads into an extended network. The bidentate-binuclear group is bound to both a magnesium and a lithium center whereas the monodentate group is bound to only one magnesium center. The second oxygen atom of the monodentate group remains protonated. The coordination environment of the magnesium centers is completed by DMF molecules in the axial positions that extend into the channels (Fig 8.4).

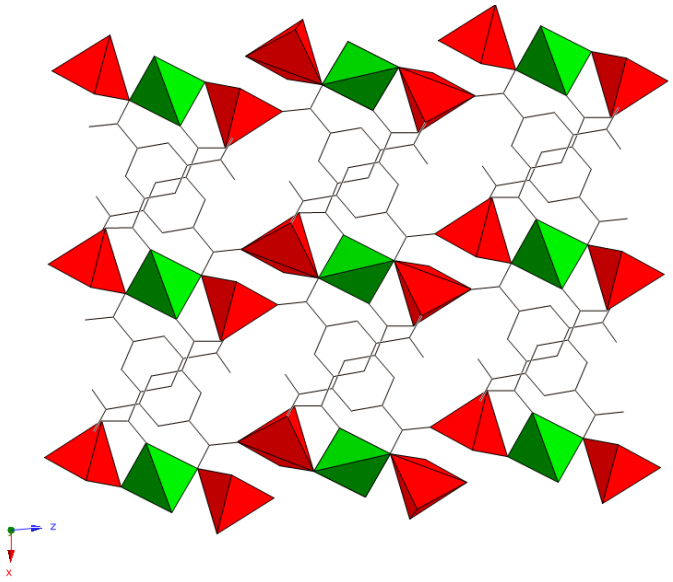

Figure 8.3. View of [8.1] down the [010] axis showing the coordination of the HBTC ligand and the Mg-Li-Mg triads. Mg polyhedra a represented in red, Li polyhedra in green, and HBTC ligands are represented as wire bonds. Coordinated DMF molecules and hydrogen atoms are not shown for clarity.

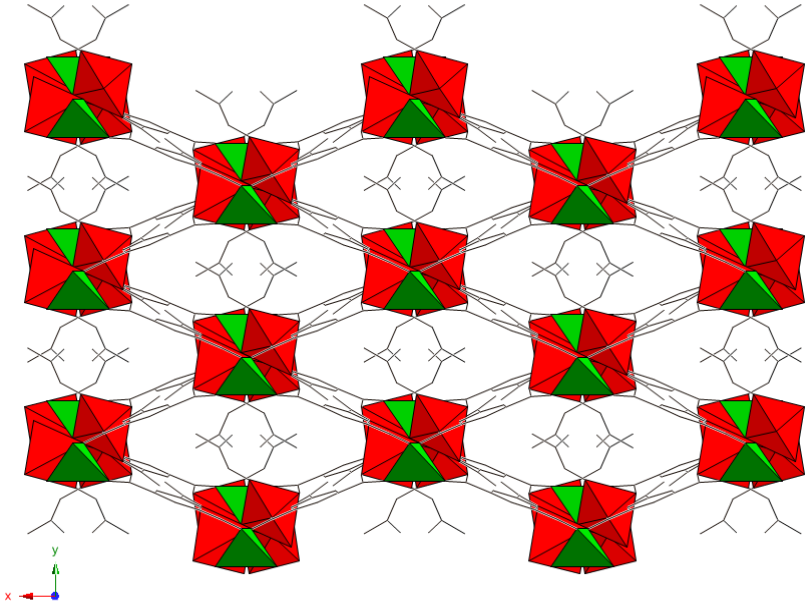

Figure 8.4. View of the diamond-shaped 1D channels in [8.1] formed by the arrangement of Mg-Li-Mg chains as viewed down the [001] direction. A coordinated DMF molecule extends into the channels. Mg polyhedra a represented in red, Li polyhedra in green, and HBTC ligands and DMF molecules are represented as wire bonds. Hydrogen atoms removed for simplicity.

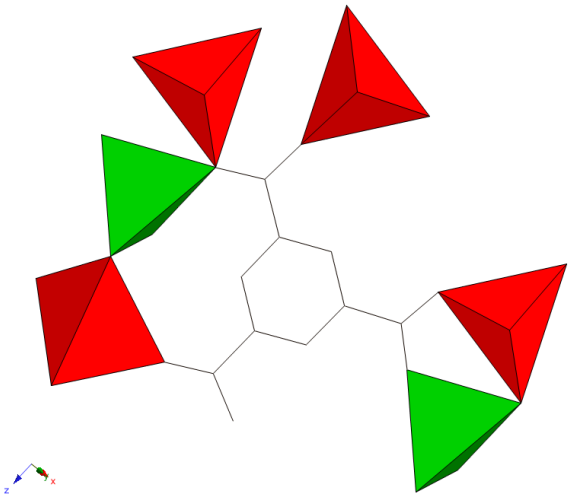

Figure 8.5. Coordination environment of HBTC ligand in [8.1]. Mg polyhedra a represented in red, Li polyhedra in green, and HBTC ligands are represented as wire bonds. Hydrogen atoms removed for simplicity.

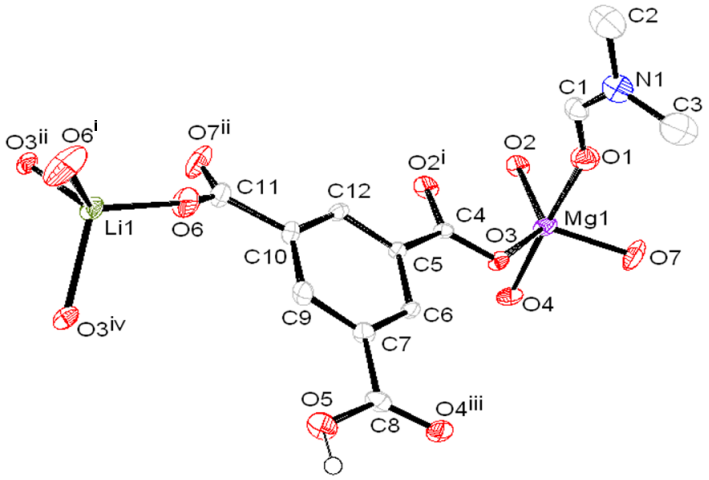

Figure 8.6. ORTEP representation of [8.1]. Thermal ellipsoids are drawn at 50% probability. Hydrogen atoms are omitted for clarity except for the protonated carboxyl group. Symmetry codes used to generate equivalent atoms: Symmetry-generated atoms labeled with i or ii are at symmetry positions (x+1, y+1, z+1), or (-x, y, -z+1/2), respectively while atoms labeled with iii or iv are at symmetry positions (x+1/2, y+1/2, -z+1/2), or (-x+1/2, y+1/2, -z+1/2), respectively.

Table 8.1. Selected bond distances (Å) and angles (deg) for 1*

Mg(1)-O(2)	1.977(2)
Mg(1)-O(7)	1.977(2)
Mg(1)-O(1)	2.040(2)
Mg(1)-O(3)	2.045(2)
Mg(1)-O(4)	2.094(2)
O(6)-Li(1)	1.853(4)
Li(1)-O(3)	2.054(4)
O(5)-C(8)	1.277(3)
O(4)-C(8)#1	1.240(3)
O(5)-H(5)	0.82
O(2)-Mg(1)-O(7)	111.26(10)
O(2)-Mg(1)-O(1)	91.90(10)
O(7)-Mg(1)-O(1)	88.62(10)
O(2)-Mg(1)-O(3)	130.87(9)
O(7)-Mg(1)-O(3)	117.75(10)
O(1)-Mg(1)-O(3)	86.18(9)
O(2)-Mg(1)-O(4)	91.79(9)
O(7)-Mg(1)-O(4)	89.42(9)
O(1)-Mg(1)-O(4)	176.25(10)
O(3)-Mg(1)-O(4)	91.90(8)
O(6)-Li(1)-O(6)#2	125.1(4)
O(6)-Li(1)-O(3)#3	99.27(11)
O(6)-Li(1)-O(3)#4	109.75(9)
O(3)#3-Li(1)-O(3)#4	114.5(3)

*Symmetry transformations used to generate equivalent atoms:
#1 -x+1,y,-z+1/2 #2 -x+2,y,-z+1/2
#3 x+1/2,y+1/2,z #4 -x+3/2,y+1/2,-z+1/2

8.4.2. Structural description of [8.2], $K_2(NDC)\cdot xH_2O$

The structure of [8.2] consists of potassium chains that are linked together by carboxylate groups. In turn, the chains are connected into a three dimensional network by 1,4-naphthalenedicarboxylate linkers (Fig 8.7, 8.8). The naphthalene rings alternate orientation in the [1 0 0] direction which creates an interpenetrated network. Guest water molecules are also found in the structure. Due to incomplete structure refinement, the exact number of guest water molecules could not be determined.

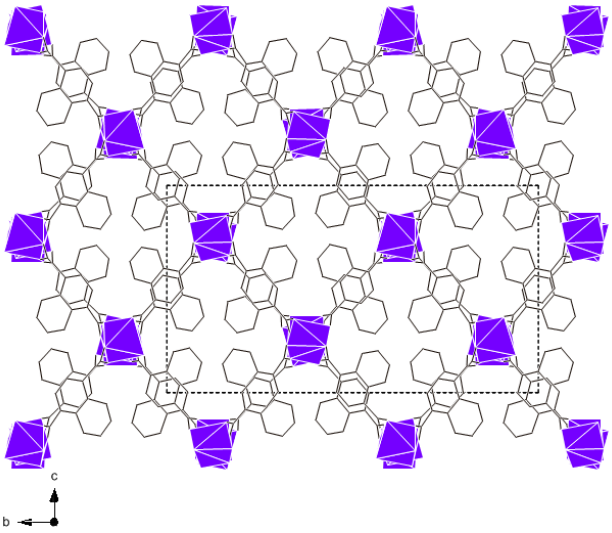

Figure 8.7. View down the [1 0 0] direction of [8.2] showing the interpenetrated network of created by 1,4-napthalenedicarboxylate linkers.

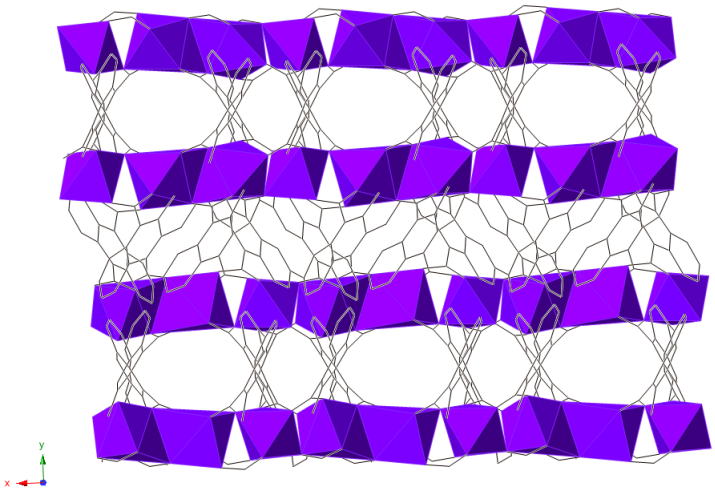

Figure 8.8. View of [8.2] in the [0 0 1] direction illustrating the one-dimensional potassium chains.

8.4.3. Structural description of [8.3], K_2(TDC)

Compound [8.3] is an overall dense structure created by layers of potassium layers linked together by TDC ligands (Fig 8.9, 8.10). The alternating potassium and TDC creates a "step ladder"-like structure, with the TDC linkers representing "steps" and the potassium layers representing as "rungs". No incorporated solvent is observed in [8.3].

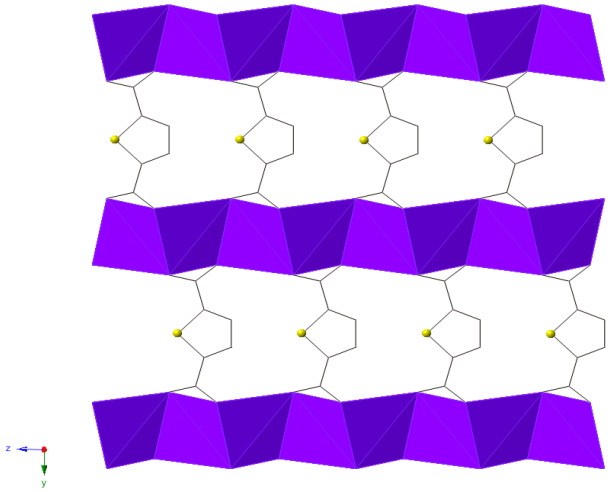

Figure 8.9. Network of [8.3] illustrating the "step ladder"-like arrangement of TDC linkers connected by "rungs" of potassium.

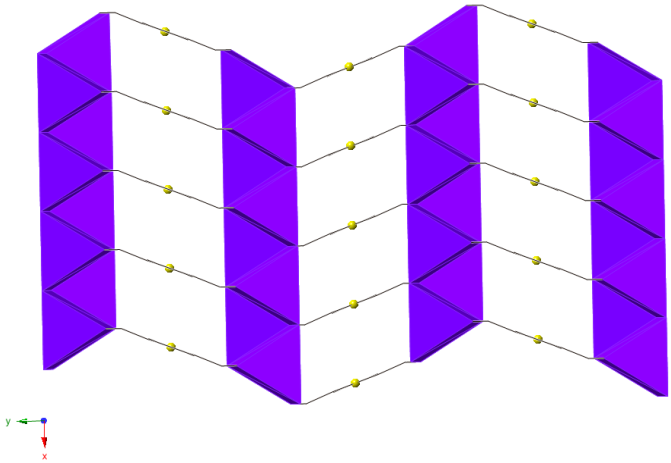

Figure 8.10. Alternating layers of potassium layers and TDC in [8.3].

8.4.4. Structural description of [8.4], K_2(SDB)·(guest)

In [8.4], chains of potassium are linked by carboxylate groups of the SDB ligand. The SDB linker forms a three-dimensional network by connecting to three different potassium chains with three connection points; oxygen atoms of both carboxylate groups as well as the sulfonyl group oxygen atoms coordinate to potassium metal centers (Fig 8.11, 8.12). Guest molecules (likely dimethylamine resulting from the breakdown of DMF) sit within the openings created by the "V" shape of the SDB linkers. Due to crystal twinning, full structure refinement was not possible.

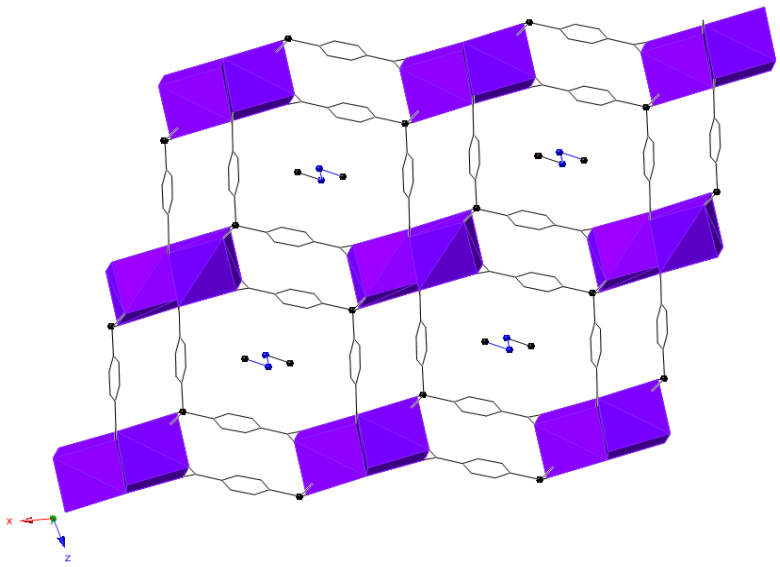

Figure 8.11. The network observed in [8.4] viewed down [0 1 0] illustrating the topology created by the "V"-shape of the 4,4´-sulfonyldibenzoate linkers.

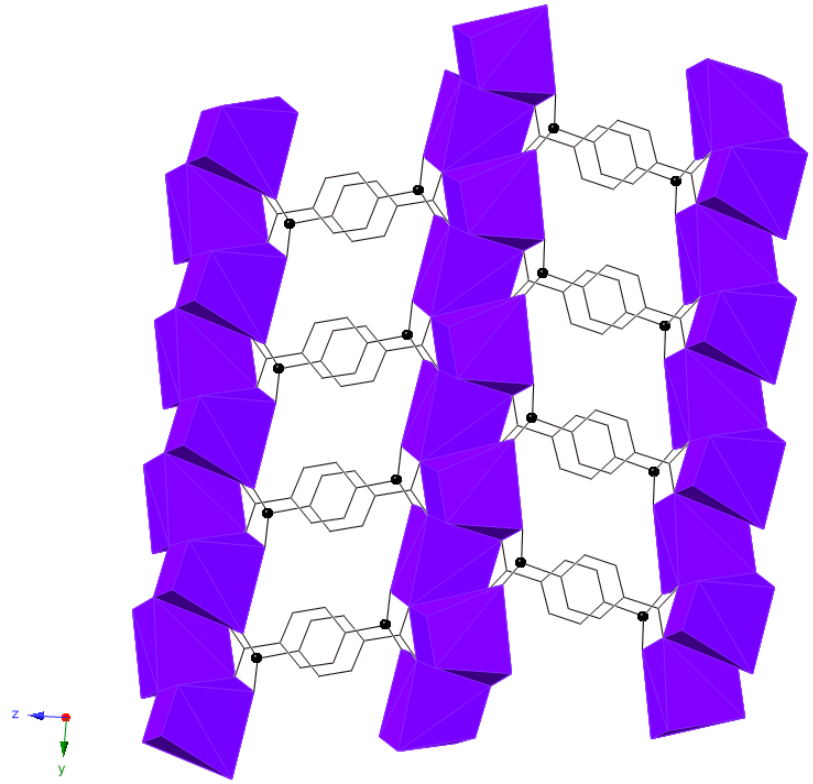

Figure 8.92. The potassium chains in [8.4] as viewed down [1 0 0].

8.4.5. Discussion

Coordinated DMF molecules were removed after heating to a temperature of 340°C, at which point the crystallinity is destroyed. Elemental analysis of this heated sample shows that only trace amounts of DMF remain when heating to this temperature [30] and the framework components remain despite no long-range order being present. The total potential solvent accessible volume after DMF removal was calculated with PLATON to be 793.7 $Å^3$ (30.7% unit cell volume), and a successive surface area measurement revealed a surface area of 13 m^2/g, indicating a collapse of the framework upon solvent removal.

All potassium coordination networks reported here share the common trait of dense potassium chains or layers. Ultimately, the structure of the networks is dictated by the geometry of the ligand. In [8.2], the naphthalene ring forces the potassium chains to accommodate for the increased size and an interpenetrated network is formed. Compound [8.3] is similar in that potassium forms dense layers which are connected by TDC linkers. Potassium chains are also observed in the network of [8.4], and "V" shape geometry of the SDB ligand allows it to connect to three different chains. This forms an open network which is occupied by a guest dimethylamine molecule.

8.5. Conclusion

The new mixed *s*-block heterometallic coordination network, $Mg_2Li(BTC)(HBTC)(DMF)_2$, is the first such compound to employ both lithium and magnesium as metal centers. Mg-Li-Mg triads constructed of magnesium trigonal bipyrimids and lithium tetrahedra are arranged into one-dimensional chains, which are in turn connected by BTC and HBTC ligands to form a three-dimensional array. One-dimensional diamond-shaped channels formed along the [001] direction are occupied by DMF molecules coordinated to the magnesium ion. Three potassium coordination networks are also studied. Chains of K-O form in each compound, leaving the topology of the network to be determined by the geometry of the linker. The naphthalene ring of the NDC linker in the $K_2(NDC)$ network generates an interpenetrated network. The network of K_2TDC forms a dense network of alternating K-O and TDC layers. The "V" shape of the SDB linker creates channels in the network of K_2SDB. This work provides an insight into the chemistry of *s*-block metals systems that are not well-studied, and determining trends in these systems will help establish a starting point for the future targeting of *s*-block networks and their properties.

Chapter 9

Conclusion

This project sought to expand the knowledge and elucidate the synthetic trends of carboxylate-based metal-organic frameworks (MOFs) and coordination networks (CNs). Various metal centers, ligands, and synthetic conditions were used and structure/property relationships were examined. All compounds herein were characterized using single-crystal X-ray diffraction. Magnetic susceptibilities were determined using a SQUID magnetometer. Standard measurements were done to determine photoluminescence properties including solid-state UV-Vis absorption and fluorescence analyses.

Carboxylate networks based on lightweight *s*-block metals centers were explored in order to improve upon our limited understanding of their chemistry in forming CNs. Based on the solvents, temperatures, and components used, a series of networks with varying topologies and properties was formed. The use of temperature as a synthetic variable generally leads to a correlation between increased temperature and increased network connectivity. Solvent variance in *s*-block metal synthesis had even more of an effect on the resulting structure. Metal-coordinated solvents influence the construction of the network and ultimately affect the physical properties.

Magnesium-based CNs were studied using different ligands, solvents, and temperatures. Two series of magnesium CNs based on 2,5 thiopehendicarboxylate and 1,3-benzenedicarboxylate were synthesized by using solvent as the principal variable and holding constant the metal:linker ratio. The resulting networks were heavily influenced by the solvent used, with the coordination of solvent molecules to metal centers leading to completely different

topologies. Similarly, the examination of a series of magnesium CNs based on 1,3,5-benzenetricarboxylate found that temperature had had a high degree of influence on network formation as well. Network dimensionality and metal-oxygen connectivity increased along with the temperature, as a competition between the effects of solvent breakdown byproducts and thermodynamic effects was noted. The photoluminescence studies of each of these networks expanded an underexplored area that could one day lead to the development of lightweight sensing materials. As the photoactivity in magnesium CNs is ligand-based, the fluorescence response was studied using a number of linkers. While the two linkers with homocyclic rings showed a relatively insignificant response, the heterocyclic thiophene ring of 2,5-thiophenedicarboxylate enhanced the photoluminescence properties of the networks due to π-stacking interactions between rings and increased electron localization around the large S atom.

The 2,5-thiophenedicarboxylate linker was also used to construct a series of lanthanide MOFs based on eight-coordinate Nd, Tb, and Dy metal centers under the same synthetic conditions. Using an equimolar mixture of ethanol and water, three structurally-related networks were produced. Ethanol preferentially coordinates to the metal centers at a ratio of three EtOH to one H_2O. While each of the networks has the same topological formula and ligand coordination modes, slight differences in ligand packing are observed due to the lanthanide contraction effect. This effect is further noted in the synthesis of an Er-based compound where lanthanide contraction causes the structure to form with a combination of six- and eight-coordinate metal centers. To test the activity of the thiophenedicarboxylate ligand as an antenna, photoluminescence measurements were done. Observations show that the Tb-based network is effectively sensitized, and a bright green emission was observed when put under UV light. On

the other hand, the emission of Dy is weak in this system and is possibly due to the quenching of metal-coordinated solvent molecules.

Transition metal formate MOFs were constructed using formate-based ionic liquids as synthetic solvents in ionothermal syntheses. Formate anions, which can link metal centers together with short three atom bridges, are also a judicious choice when constructing magnetic metal-organic frameworks because the charge is more effectively transferred between metal ions. Furthermore, the use of ionothermal synthesis to produce MOFs is a novel approach that opens the possibility of synthesizing magnetic materials at lower temperatures and with more synthetic control. In this work, formate-based ionic liquids were used to produce transition metal formate MOFs based on Mn^{2+}, Co^{2+}, and Ni^{2+}. Charge is balanced in the networks by the cationic ammonium species of the ionic liquids. The metal-formate topologies depended on the presence or absence of hydroxyl functional group on the cation. Two-dimensional networks crystallized when using hydroxyammonium cations, while a change to diammonium cations led to three-dimensional networks. From the observation of non-linking formate groups in the structure, it is evident that the hydrogen bonding of hydroxyl group influences the connectivity of the network. Magnetic susceptibilities of the two-dimensional networks showed that they ordered antiferromagnetically.

Alkali and alkaline earth metal-carboxylate networks, specifically those based on the lightweight metals magnesium, lithium, and potassium, are thought to be ideal starting points for the development of gas storage materials. Since reports of CNs based on these metals are small compared to more common metal centers, exploratory synthesis is necessary in order to better understand the chemistry and enable future progress in this area. To this end, the first lithium-magnesium heterometallic coordination network was synthesized. Tetrahedrally-coordinated Li

metal centers were used as an additional degree of freedom, and building blocks of Mg-Li-Mg triads were linked by 1,3,5-benzenetricarboxylate. In addition, three potassium-based coordination networks linked with 1,4-naphthalenedicarboxylate, 2,5-thiopehendicarboxylate, and 4,4′-sufonyldibenzoate, respectively, were highlighted. In each case, the geometry and coordination of the ligand dictated the structure of the network, as K^+ metal centers prefer to form dense one-dimensional chains in carboxylate CNs.

In contrast to the seemingly routine chemistry and structure prediction touted in the solvothermal synthesis of transition metal and *3d* coordination networks, research employing other metals, ligands, and synthetic conditions lags behind. The reasons for this discrepancy lie not only with the differences in chemistry, but the comparative lack of literature and experience in this area. In order to unlock the potential from the methods and network types described in this thesis, more systematic exploratory syntheses, coupled with theoretical studies, are necessary to reveal important trends.

References

(1) Ferey, G. *Chem. Soc. Rev.* **2008**, *37*, 191.

(2) Ferey, G. *Dalton Trans.* **2009**, 4400.

(3) Cheetham, A. K.; Rao, C. N. R.; Feller, R. K. *Chem. Commum.* **2006**, 4780.

(4) Rao, C. N. R.; Cheetham, A. K.; Thirumurugan, A. *J. Phys.: Condens. Matter* **2008**, *20*.

(5) Collins, D. J.; Zhou, H. C. *J. Mater. Chem.* **2007**, *17*, 3154.

(6) Suh, M. P.; Park, H. J.; Prasad, T. K.; Lim, D.-W. *Chem. Rev.* **2011**, *112*, 782.

(7) Xiao, B.; Wheatley, P. S.; Zhao, X. B.; Fletcher, A. J.; Fox, S.; Rossi, A. G.; Megson, I. L.; Bordiga, S.; Regli, L.; Thomas, K. M.; Morris, R. E. *J. Am. Chem. Soc.* **2007**, *129*, 1203.

(8) Ma, S. Q.; Eckert, J.; Forster, P. M.; Yoon, J. W.; Hwang, Y. K.; Chang, J. S.; Collier, C. D.; Parise, J. B.; Zhou, H. C. *J. Am. Chem. Soc.* **2008**, *130*, 15896.

(9) Nouar, F.; Eckert, J.; Eubank, J. F.; Forster, P.; Eddaoudi, M. *J. Am. Chem. Soc.* **2009**, *131*, 2864.

(10) Kurmoo, M. *Chem. Soc. Rev.* **2009**, *38*, 1353.

(11) Dechambenoit, P.; Long, J. R. *Chem. Soc. Rev.* **2011**, *40*, 3249.

(12) Cui, H. B.; Wang, Z. M.; Takahashi, K.; Okano, Y.; Kobayashi, H.; Kobayashi, A. *J. Am. Chem. Soc.* **2006**, *128*, 15074.

(13) Li, W.; Jia, H. P.; Ju, Z. F.; Zhang, J. *Dalton Trans.* **2008**, 5350.

(14) Cheng, X. N.; Zhang, W. X.; Lin, Y. Y.; Zheng, Y. Z.; Chen, X. M. *Adv. Mater.* **2007**, *19*, 1494.

(15) Allendorf, M. D.; Bauer, C. A.; Bhakta, R. K.; Houk, R. J. T. *Chem. Soc. Rev.* **2009**, *38*, 1330.

(16) Cui, Y.; Yue, Y.; Qian, G.; Chen, B. *Chem. Rev.* **2011**.

(17) Hoskins, B. F.; Robson, R. *J. Am. Chem. Soc.* **1990**, *112*, 1546.

(18) Li, H.; Eddaoudi, M.; O'Keeffe, M.; Yaghi, O. M. *Nature* **1999**, *402*, 276.

(19) Rowsell, J. L. C.; Yaghi, O. M. *J. Am. Chem. Soc.* **2006**, *128*, 1304.

(20) Eddaoudi, M.; Kim, J.; Rosi, N.; Vodak, D.; Wachter, J.; O'Keeffe, M.; Yaghi, O. M. *Science* **2002**, *295*, 469.

(21) Wang, X. Y.; Wang, Z. M.; Gao, S. *Chem. Commum.* **2008**, 281.

(22) Wang, X. Y.; Gan, L.; Zhang, S. W.; Gao, S. *Inorg. Chem.* **2004**, *43*, 4615.

(23) Wang, Z. M.; Zhang, X. Y.; Batten, S. R.; Kurmoo, M.; Gao, S. *Inorg. Chem.* **2007**, *46*, 8439.

(24) Wang, Z. M.; Zhang, B.; Otsuka, T.; Inoue, K.; Kobayashi, H.; Kurmoo, M. *Dalton Trans.* **2004**, 2209.

(25) Wang, Z. M.; Zhang, B.; Zhang, Y. J.; Kurmoo, M.; Liu, T.; Gao, S.; Kobayashi, H. *Polyhedron* **2007**, *26*, 2207.

(26) Banerjee, D.; Parise, J. B. *Cryst. Growth Des.* **2011**, *11*, 4704.

(27) Rocha, J.; Carlos, L. D.; Paz, F. A. A.; Ananias, D. *Chem. Soc. Rev.* **2011**, *40*, 926.

(28) Serre, C.; Millange, F.; Thouvenot, C.; Gardant, N.; Pelle, F.; Ferey, G. *J. Mater. Chem.* **2004**, *14*, 1540.

(29) Wang, H.-S.; Zhao, B.; Zhai, B.; Shi, W.; Cheng, P.; Liao, D.-Z.; Yan, S.-P. *Cryst. Growth Des.* **2007**, *7*, 1851.

(30) Huang, W.; Wu, D. Y.; Zhou, P.; Yan, W. B.; Guo, D.; Duan, C. Y.; Meng, Q. J. *Cryst. Growth Des.* **2009**, *9*, 1361.

(31) Wang, J. G.; Huang, C. C.; Huang, X. H.; Liu, D. S. *Cryst. Growth Des.* **2008**, *8*, 795.

(32) MacNeill, C. M.; Day, C. S.; Gamboa, S. A.; Lachgar, A.; Noftle, R. E. *Journal of Chemical Crystallography* **2010**, *40*, 222.

(33) de Lill, D. T.; de Bettencourt-Dias, A.; Cahill, C. L. *Inorg. Chem.* **2007**, *46*, 3960.

(34) Banerjee, D.; Borkowski, L. A.; Kim, S. J.; Parise, J. B. *Cryst. Growth Des.* **2009**, *9*, 4922.

(35) Banerjee, D.; Kim, S. J.; Borkowski, L. A.; Xu, W. Q.; Parise, J. B. *Cryst. Growth Des.* **2010**, *10*, 709.

(36) Banerjee, D.; Kim, S. J.; Li, W.; Wu, H. H.; Li, J.; Borkowski, L. A.; Philips, B. L.; Parise, J. B. *Cryst. Growth Des.* **2010**, *10*, 2801.

(37) Shannon, R. *Acta Crystallogr. Sect. A* **1976**, *32*, 751.

(38) Dinca, M.; Long, J. R. *J. Am. Chem. Soc.* **2005**, *127*, 9376.

(39) Dietzel, P. D. C.; Blom, R.; Fjellvåg, H. *Eur. J. Inorg. Chem.* **2008**, *2008*, 3624.

(40) Caskey, S. R.; Wong-Foy, A. G.; Matzger, A. J. *J. Am. Chem. Soc.* **2008**, *130*, 10870.

(41) Wibowo, A. C.; Vaughn, S. A.; Smith, M. D.; zur Loye, H.-C. *Inorg. Chem.* **2010**, *49*, 11001.

(42) Yang, E.-C.; Li, J.; Ding, B.; Liang, Q.-Q.; Wang, X.-G.; Zhao, X.-J. *Crystengcomm* **2008**, *10*, 158.

(43) Hu, R.; Cai, H.; Luo, J. *Inorg. Chem. Commun.* **2011**, *14*, 433.

(44) Stylianou, K. C.; Heck, R.; Chong, S. Y.; Bacsa, J.; Jones, J. T. A.; Khimyak, Y. Z.; Bradshaw, D.; Rosseinsky, M. J. *J. Am. Chem. Soc.* **2010**, *132*, 4119.

(45) Fan, J.; Zhu, H. F.; Okamura, T. A.; Sun, W. Y.; Tang, W. X.; Ueyama, N. *New J. Chem.* **2003**, *27*, 1409.

(46) Zhang, D. J.; Song, T. Y.; Zhang, P.; Shi, J.; Wang, Y.; Wang, L.; Ma, K. R.; Yin, W. R.; Zhao, J.; Fan, Y.; Xu, J. N. *Inorg. Chem. Commun.* **2007**, *10*, 876.

(47) Jayaramulu, K.; Kanoo, P.; George, S. J.; Maji, T. K. *Chem. Commum.* **2010**, *46*, 7906.

(48) Calderone, P. J.; Banerjee, D.; Nizami, Q.; LaDuca, R. L.; Parise, J. B. *Polyhedron* **2012**, *37*, 42.

(49) Calderone, P. J.; Banerjee, D.; Santulli, A. C.; Wong, S. S.; Parise, J. B. *Inorg. Chim. Acta* **2011**, *378*, 109.

(50) Li, C.-P.; Du, M. *Chem. Commum.* **2011**, *47*, 5958.

(51) Banerjee, D.; Finkelstein, J.; Smirnov, A.; Forster, P. M.; Borkowski, L. A.; Teat, S. J.; Parise, J. B. *Cryst. Growth Des.* **2011**, *11*, 2572.

(52) Forster, P. M.; Burbank, A. R.; Livage, C.; Ferey, G.; Cheetham, A. K. *Chem. Commum.* **2004**, 368.

(53) Gurunatha, K. L.; Uemura, K.; Maji, T. K. *Inorg. Chem.* **2008**, *47*, 6578.

(54) Morris, R. E. *Chem. Commum.* **2009**, 2990.

(55) Jin, K.; Huang, X.; Pang, L.; Li, J.; Appel, A.; Wherland, S. *Chem. Commum.* **2002**, 2872.

(56) Cooper, E. R.; Andrews, C. D.; Wheatley, P. S.; Webb, P. B.; Wormald, P.; Morris, R. E. *Nature* **2004**, *430*, 1012.

(57) Liao, J.-H.; Wu, P.-C.; Huang, W.-C. *Cryst. Growth Des.* **2006**, *6*, 1062.
(58) Hulvey, Z.; Wragg, D. S.; Lin, Z. J.; Morris, R. E.; Cheetham, A. K. *Dalton Trans.* **2009**, 1131.
(59) Lin, Z. J.; Slawin, A. M. Z.; Morris, R. E. *J. Am. Chem. Soc.* **2007**, *129*, 4880.
(60) Lin, Z. J.; Wragg, D. S.; Warren, J. E.; Morris, R. E. *J. Am. Chem. Soc.* **2007**, *129*, 10334.
(61) Lin, Z.; Li, Y.; Slawin, A. M. Z.; Morris, R. E. *Dalton Trans.* **2008**, 3989.
(62) Calderone, P. J.; Forster, P. M.; Borkowski, L. A.; Teat, S. J.; Feygenson, M.; Aronson, M. C.; Parise, J. B. *Inorg. Chem.* **2011**, *50*, 2159.
(63) Rabenau, A. *Angew. Chem.-Int. Edit. Engl.* **1985**, *24*, 1026.
(64) Walton, R. I. *Chem. Soc. Rev.* **2002**, *31*, 230.
(65) Parnham, E. R.; Morris, R. E. *Acc. Chem. Res.* **2007**, *40*, 1005.
(66) Torimoto, T.; Tsuda, T.; Okazaki, K.; Kuwabata, S. *Adv. Mater.* **2010**, *22*, 1196.
(67) SMART; v5.053 ed.; Bruker AXS, Inc.: Madison, WI, 1998.
(68) SAINTPLUS; v7.34a ed.; Bruker AXS, Inc.: Madison, WI, 2006.
(69) Oxford Diffraction (2012), *CRYSALIS*, Oxford Diffraction Ltd, Abingdon, England.
(70) Sheldrick, G. M. *Acta Crystallogr.* **2008**, *A64*, 112.
(71) Bruker (2007), *APEX2*, Bruker AXS Inc., Madison, Wisconsin, USA.
(72) Cullity, B. D.; Graham, C. D. *Introduction to Magnetic Materials*; 2 ed.; Wiley-IEEE Press, 2008.
(73) Kittel, C. *Introduction to Solid State Physics*; Wiley: New York, 1996.
(74) Lacheisserie, É. D. T. d.; Gignoux, D.; Schlenker, M. *Magnetism: Materials and Applications*; Springer, 2005.
(75) Kleiner, R.; Koelle, D.; Ludwig, F.; Clarke, J. *Proceedings of the IEEE* **2004**, *92*, 1534.
(76) Binnemans, K. *Chem. Rev.* **2009**, *109*, 4283.
(77) Harris, D. C. *Quantitative Chemical Analysis*; Sixth ed.; W. H. Freeman and Company, 2002.
(78) Werts, M. H. V. *Sci. Prog.* **2005**, *88*, 101.
(79) Crosby, G. A.; Whan, R. E.; Freeman, J. J. *Journal of Physical Chemistry* **1962**, *66*, 2493.
(80) Cotton, S. *Lanthanide and Actinide Chemistry*; Wiley-VCH, 2006.
(81) Lin, X.; Champness, N. R.; Schroder, M. *Top Curr Chem* **2010**, 35.
(82) Millward, A. R.; Yaghi, O. M. *J. Am. Chem. Soc.* **2005**, *127*, 17998.
(83) Corma, A.; García, H.; Llabrés i Xamena, F. X. *Chem. Rev.* **2010**, *110*, 4606.
(84) Farrusseng, D.; Aguado, S.; Pinel, C. *Angew. Chem. Int. Ed.* **2009**, *48*, 7502.
(85) Dinca, M.; Dailly, A.; Liu, Y.; Brown, C. M.; Neumann, D. A.; Long, J. R. *J. Am. Chem. Soc.* **2006**, *128*, 16876.
(86) Ma, S. Q.; Zhou, H. C. *J. Am. Chem. Soc.* **2006**, *128*, 11734.
(87) Wang, Y.; Bredenkotter, B.; Rieger, B.; Volkmer, D. *Dalton Trans.* **2007**, 689.
(88) Wong-Foy, A. G.; Matzger, A. J.; Yaghi, O. M. *J. Am. Chem. Soc.* **2006**, *128*, 3494.
(89) Park, H.; Britten, J. F.; Mueller, U.; Lee, J.; Li, J.; Parise, J. B. *Chem. Mater.* **2007**, *19*, 1302.
(90) Park, H.; Moureau, D. M.; Parise, J. B. *Chem. Mater.* **2005**, *18*, 525.

(91) Senkovska, I.; Kaskel, S. *Eur. J. Inorg. Chem.* **2006**, *2006*, 4564.
(92) Banerjee, D.; Kim, S. J.; Parise, J. B. *Cryst. Growth Des.* **2009**, *9*, 2500.
(93) Hulvey, Z.; Cheetham, A. K. *Solid State Sci.* **2007**, *9*, 137.
(94) Rood, J. A.; Noll, B. C.; Henderson, K. W. *Inorg. Chem.* **2006**, *45*, 5521.
(95) Demessence, A.; Mesbah, A.; Francois, M.; Rogez, G.; Rabu, P. *Eur. J. Inorg. Chem.***2009**, 3713.
(96) Gong, Y.; Wang, T.; Zhang, M.; Hu, C. W. *J. Mol. Struct.* **2007**, *833*, 1.
(97) Yuan, H.-B.; Yang, S.-Y.; Xie, Z.-X.; Huang, R.-B.; Batten, S. R. *Inorg. Chem. Commun.* **2009**, *12*, 755.
(98) Chen, Z.; Zuo, Y.; Li, X. H.; Wang, H.; Zhao, B.; Shi, W.; Cheng, P. *J. Mol. Struct.* **2008**, *888*, 360.
(99) Sun, X. Z.; Huang, Z. L.; Wang, H. Z.; Ye, B. H.; Chen, X. M. *ZAAC* **2005**, *631*, 919.
(100) Chen, B.-L.; Mok, K.-F.; Ng, S.-C.; G. B. Drew, M. *New J. Chem.* **1999**, *23*, 877.
(101) Rossin, A.; Ienco, A.; Costantino, F.; Montini, T.; Di Credico, B.; Caporali, M.; Gonsalvi, L.; Fornasiero, P.; Peruzzini, M. *Cryst. Growth Des.* **2008**, *8*, 3302.
(102) Fang, Q. R.; Zhu, G. S.; Xue, M.; Sun, J. Y.; Sun, F. X.; Qiu, S. L. *Inorg. Chem.* **2006**, *45*, 3582.
(103) Fang, Q. R.; Zhu, G. S.; Shi, X.; Wu, G.; Tian, G.; Wang, R. W.; Qiu, S. L. *J. Solid State Chem.* **2004**, *177*, 1060.
(104) Chen, W.; Wang, J. Y.; Chen, C.; Yue, Q.; Yuan, H. M.; Chen, J. S.; Wang, S. N. *Inorg. Chem.* **2003**, *42*, 944.
(105) Li, J.-R.; Sculley, J.; Zhou, H.-C. *Chem. Rev.* **2011**, *112*, 869.
(106) Yoon, M.; Srirambalaji, R.; Kim, K. *Chem. Rev.* **2011**, *112*, 1196.
(107) Kreno, L. E.; Leong, K.; Farha, O. K.; Allendorf, M.; Van Duyne, R. P.; Hupp, J. T. *Chem. Rev.* **2011**, *112*, 1105.
(108) Liu, H. K.; Tsao, T. H.; Zhang, Y. T.; Lin, C. H. *Crystengcomm* **2009**, *11*, 1462.
(109) Chen, W.; Wang, J.-Y.; Chen, C.; Yue, Q.; Yuan, H.-M.; Chen, J.-S.; Wang, S.-N. *Inorg. Chem.* **2003**, *42*, 944.
(110) Dai, J.-C.; Wu, X.-T.; Fu, Z.-Y.; Cui, C.-P.; Hu, S.-M.; Du, W.-X.; Wu, L.-M.; Zhang, H.-H.; Sun, R.-Q. *Inorg. Chem.* **2002**, *41*, 1391.
(111) Dai, J.-C.; Hu, S.-M.; Wu, X.-T.; Fu, Z.-Y.; Du, W.-X.; Zhang, H.-H.; Sun, R.-Q. *New J. Chem.* **2003**, *27*, 914.
(112) Li, Z.-Q.; Qiu, L.-G.; Wang, W.; Xu, T.; Wu, Y.; Jiang, X. *Inorg. Chem. Commun.* **2008**, *11*, 1375.
(113) Chen, J.-X.; Liu, S.-X.; Gao, E.-Q. *Polyhedron* **2004**, *23*, 1877.
(114) Fang, Q.; Zhu, G.; Shi, X.; Wu, G.; Tian, G.; Wang, R.; Qiu, S. *J. Solid State Chem.* **2004**, *177*, 1060.
(115) Bauer, C. A.; Timofeeva, T. V.; Settersten, T. B.; Patterson, B. D.; Liu, V. H.; Simmons, B. A.; Allendorf, M. D. *J. AM. CHEM. SOC.* **2007**, *129*, 7136.
(116) Fang, Q.; Zhu, G.; Xue, M.; Sun, J.; Sun, F.; Qiu, S. *Inorg. Chem.* **2006**, *45*, 3582.
(117) Gao, C.; Liu, S.; Xie, L.; Sun, C.; Cao, J.; Ren, Y.; Feng, D.; Su, Z. *Crystengcomm* **2009**, *11*, 177.
(118) Fu, Y.; Su, J.; Yang, S.; Li, G.; Liao, F.; Xiong, M.; Lin, J. *Inorg. Chim. Acta* **2010**, *363*, 645.

(119) Davies, R. P.; Less, R. J.; Lickiss, P. D.; White, A. J. P. *Dalton Trans.* **2007**, 2528.

(120) Ma, S.; Fillinger, J. A.; Ambrogio, M. W.; Zuo, J.-L.; Zhou, H.-C. *Inorg. Chem. Commun.* **2007**, *10*, 220.

(121) Song, L. F.; Jiang, C. H.; Zhang, J. A.; Sun, L. X.; Xu, F.; Tian, Y. Q.; You, W. S.; Cao, Z.; Zhang, L.; Yang, D. W. *J. Therm. Anal. Calorim.* **2010**, *101*, 365.

(122) Calderone, P. J.; Banerjee, D.; Borkowski, L. A.; Parise, J. B. *Inorg. Chem. Commun.* **2011**, *14*, 741.

(123) Spek, A. L. *J. Appl. Crystallogr.* **2003**, *36*, 7.

(124) Gao, C.; Liu, S.; Xie, L.; Ren, Y.; Cao, J.; Sun, C. *Crystengcomm* **2007**, *9*, 545.

(125) Yeh, C.-T.; Liu, H.-K.; Lin, C.-J.; Lin, C.-H. *Acta Crystallogr. Sect. E* **2010**, *66*, m1289.

(126) He, J.; Zhang, Y.; Pan, Q.; Yu, J.; Ding, H.; Xu, R. *Microporous Mesoporous Mater.* **2006**, *90*, 145.

(127) Xue, M.; Zhu, G.; Fang, Q.; Guo, X.; Qiu, S. *J. Mol. Struct.* **2006**, *796*, 165.

(128) Beeby, A.; Faulkner, S. *Chem. Phys. Lett.* **1997**, *266*, 116.

(129) Lama, P.; Aijaz, A.; Sañudo, E. C.; Bharadwaj, P. K. *Cryst. Growth Des.* **2009**, *10*, 283.

(130) Luo, F.; Che, Y.-x.; Zheng, J.-m. *Crystallogr. Growth Des.* **2008**, *9*, 1066.

(131) Wang, J.; Lin, Z.; Ou, Y.-C.; Yang, N.-L.; Zhang, Y.-H.; Tong, M.-L. *Inorg. Chem.* **2007**, *47*, 190.

(132) Zheng, S. T.; Li, Y. F.; Wu, T.; Nieto, R. A.; Feng, P. Y.; Bu, X. H. *Chem.–Eur. J.* **2010**, *16*, 13035.

(133) Abrahams, B. F.; Grannas, M. J.; Hudson, T. A.; Robson, R. *Angew. Chem. Int. Ed.* **2010**, *49*, 1087.

(134) Williams, C. A.; Blake, A. J.; Wilson, C.; Hubberstey, P.; Schröder, M. *Crystallogr. Growth Des.* **2008**, *8*, 911.

(135) Martin, D. P.; Braverman, M. A.; LaDuca, R. L. *Cryst. Growth Des.* **2007**, *7*, 2609.

(136) Wang, S. N.; Xing, H.; Li, Y. Z.; Bai, J. F.; Pan, Y.; Scheer, M.; You, X. Z. *Eur. J. Inorg. Chem.* **2006**, 3041.

(137) Blake, K. M.; Braverman, M. A.; Nettleman, J. H.; Sposato, L. K.; LaDuca, R. L. *Inorg. Chim. Acta* **2010**, *363*, 3966.

(138) Kaduk, J. *Acta Crystallogr. Sec. B* **2002**, *58*, 815.

(139) Rood, J. A.; Noll, B. C.; Henderson, K. W. *Main Group Chem.* **2006**, *5*, 21.

(140) Clegg, W.; Russo, L. *Crystallogr. Growth Des.* **2009**, *9*, 1158.

(141) Zhang, D.-J.; Song, T.-Y.; Zhang, P.; Shi, J.; Wang, Y.; Wang, L.; Ma, K.-R.; Yin, W.-R.; Zhao, J.; Fan, Y.; Xu, J.-N. *Inorg. Chem. Commun.* **2007**, *10*, 876.

(142) Guo, Z.; Li, G.; Zhou, L.; Su, S.; Lei, Y.; Dang, S.; Zhang, H. *Inorg. Chem.* **2009**, *48*, 8069.

(143) Calderone, P. J.; Banerjee, D.; Santulli, A. C.; Wong, S. S.; Parise, J. B. *Inorg. Chim. Acta*.

(144) Brese, N. E.; O'Keeffe, M. *Acta Crystallogr. Sec. B* **1991**, *47*, 192.

(145) Addison, A. W.; Rao, T. N.; Reedijk, J.; van Rijn, J.; Verschoor, G. C. *J. Chem. Soc., Dalton Trans.* **1984**, 1349.

(146) Jain, P.; Ramachandran, V.; Clark, R. J.; Zhou, H. D.; Toby, B. H.; Dalal, N. S.; Kroto, H. W.; Cheetham, A. K. *JACS* **2009**, *131*, 13625.

(147) Rood, J. A.; Noll, B. C.; Henderson, K. W. *Inorg. Chem.* **2006**, *45*, 5521.

(148) Li, X.; Wang, X.-W.; Zhang, Y.-H. *Inorg. Chem. Commun.* **2008**, *11*, 832.

(149) Yaghi, O. M.; Davis, C. E.; Li, G. M.; Li, H. L. *J. AM. CHEM. SOC.* **1997**, *119*, 2861.

(150) Li, J. R.; Kuppler, R. J.; Zhou, H. C. *Chem. Soc. Rev.* **2009**, *38*, 1477.

(151) Cheon, Y. E.; Park, J.; Suh, M. P. *Chem. Commum.* **2009**, 5436.

(152) Balzani, V.; Ballardini, R.; Bolletta, F.; Gandolfi, M. T.; Juris, A.; Maestri, M.; Manfrin, M. F.; Moggi, L.; Sabbatini, N. *Coord. Chem. Rev.* **1993**, *125*, 75.

(153) Chandler, B. D.; Cramb, D. T.; Shimizu, G. K. H. *J. Am. Chem. Soc.* **2006**, *128*, 10403.

(154) Soares-Santos, P. C. R.; Cunha-Silva, L. s.; Paz, F. A. A.; Ferreira, R. A. S.; Rocha, J.; Trindade, T.; Carlos, L. s. D.; Nogueira, H. I. S. *Cryst. Growth Des.* **2008**, *8*, 2505.

(155) Li, H. H.; Shi, W.; Xu, N.; Zhang, Z. J.; Niu, Z.; Han, T.; Cheng, P. *Cryst. Growth Des.* **2012**, *12*, 2602.

(156) Wang, H.; Liu, S. J.; Tian, D.; Jia, J. M.; Hu, T. L. *Cryst. Growth Des.* **2012**, *12*, 3263.

(157) Deng, Z.-P.; Huo, L.-H.; Wang, H.-Y.; Gao, S.; Zhao, H. *Crystengcomm* **2010**, *12*, 1526.

(158) Cui, Y.; Xu, H.; Yue, Y.; Guo, Z.; Yu, J.; Chen, Z.; Gao, J.; Yang, Y.; Qian, G.; Chen, B. *J. Am. Chem. Soc.* **2012**, *134*, 3979.

(159) Qin, C.; Wang, X.-L.; Wang, E.-B.; Su, Z.-M. *Inorg. Chem.* **2005**, *44*, 7122.

(160) Wang, X.-L.; Qin, C.; Wang, E.-B.; Su, Z.-M.; Xu, L.; Batten, S. R. *Chem. Commum.* **2005**, 4789.

(161) Xu, J.; Cheng, J.; Su, W.; Hong, M. *Cryst. Growth Des.* **2011**, *11*, 2294.

(162) Marques, L. F.; dos Santos, M. V.; Ribeiro, S. J. L.; Castellano, E. E.; Machado, F. C. *Polyhedron* **2012**, *38*, 149.

(163) Huang, W.; Wu, D.; Zhou, P.; Yan, W.; Guo, D.; Duan, C.; Meng, Q. *Cryst. Growth Des.* **2009**, *9*, 1361.

(164) Zhan, C.-H.; Wang, F.; Kang, Y.; Zhang, J. *Inorg. Chem.* **2011**, *51*, 523.

(165) Wang, M.-X.; Long, L.-S.; Huang, R.-B.; Zheng, L.-S. *Chem. Commum.* **2011**, *47*, 9834.

(166) Huang, X.-C.; Li, D.; Chen, X.-M. *Crystengcomm* **2006**, *8*, 351.

(167) Chen, S.-C.; Zhang, Z.-H.; Huang, K.-L.; Chen, Q.; He, M.-Y.; Cui, A.-J.; Li, C.; Liu, Q.; Du, M. *Cryst. Growth Des.* **2008**, *8*, 3437.

(168) Blatov, V. A.; Shevchenko, A. P.; Serezhkin, V. N. *J. Appl. Crystallogr.* **2000**, *33*, 1193.

(169) Rao, C. N. R.; Raveau, B. *Transition Metal Oxides*; 2nd ed.; Wiley-VCH, 1998.

(170) Zhang, W.; Ye, H. Y.; Xiong, R. G. *Coord. Chem. Rev.* **2009**, *253*, 2980.

(171) Rogez, G.; Viart, N.; Drillon, M. *Angew. Chem. Int. Ed.* **2010**, *49*, 1921.

(172) Wang, Z. M.; Zhang, B.; Inoue, K.; Fujiwara, H.; Otsuka, T.; Kobayashi, H.; Kurmoo, M. *Inorg. Chem.* **2007**, *46*, 437.

(173) Wang, Z. M.; Hu, K. L.; Gao, S.; Kobayashi, H. *Adv. Mater.* **2010**, *22*, 1526.

(174) Spaldin, N. A.; Fiebig, M. *Science* **2005**, *309*, 391.

(175) Hill, N. A. *J. Phys.Chem. B* **2000**, *104*, 6694.

(176) Sanchez-Andujar, M.; Presedo, S.; Yanez-Vilar, S.; Castro-Garcia, S.; Shamir, J.; Senaris-Rodriguez, M. A. *Inorg. Chem.* **2010**, *49*, 1510.

(177) Xu, G.-C.; Ma, X.-M.; Zhang, L.; Wang, Z.-M.; Gao, S. *J. Am. Chem. Soc.* **2010**, *132*, 9588.

(178) Bicak, N. *Journal of Molecular Liquids* **2005**, *116*, 15.

(179) Osaki, K.; Nakai, Y.; Watanabe, T. *J. Phys. Soc. Jpn.* **1964**, *19*, 717.

(180) Krogman, K.; Mattes, R. *Z. Kristallogr* **1963**, *118*.

(181) Antsyshkina, A. S.; Guseinova, M. K.; Porai-Koshits, M. A. *J. Struct. Chem.* **1966**, *8*, 321.

(182) Wang, Z. M.; Zhang, B.; Kurmoo, M.; Green, M. A.; Fujiwara, H.; Otsuka, T.; Kobayashi, H. *Inorg. Chem.* **2005**, *44*, 1230.

(183) Fromm, K. M. *Coord. Chem. Rev.* **2008**, *252*, 856.

(184) Kaduk, J. *Acta Crystallogr. Sec. B* **2000**, *56*, 474.

(185) Kim, M. K.; Jo, V.; Lee, D. W.; Shim, I.-W.; Ok, K. M. *Crystengcomm* **2010**, *12*, 1481.

(186) Turner, D. R.; Strachn-Hatton, J.; Batten, S. R. *ZAAC* **2009**, *635*, 439.

(187) An, C.; Lu, Y.; Shang, Z.; Zhang, Z. *Inorg. Chim. Acta* **2008**, *361*, 2721.

(188) Nguyen, T. L. A.; Demir-Cakan, R.; Devic, T.; Morcrette, M.; Ahnfeldt, T.; Auban-Senzier, P.; Stock, N.; Goncalves, A.-M.; Filinchuk, Y.; Tarascon, J.-M.; Férey, G. r. *Inorg. Chem.* **2010**, *49*, 7135.

(189) Grirrane, A.; Pastor, A.; Alvarez, E.; Galindo, A. *Inorg. Chem. Commun.* **2005**, *8*, 453.

(190) Cote, A. P.; Shimizu, G. K. H. *Chem.–Eur. J.* **2003**, *9*, 5361.

(191) Caskey, S. R.; Matzger, A. J. *Inorg. Chem.* **2008**, *47*, 7942.

(192) Lim, C. S.; Schnobrich, J. K.; Wong-Foy, A. G.; Metzger, A. J. *Inorg. Chem.* **2010**, *49*, 5271.

(193) Zhang, J. P.; Ghosh, S. K.; Lin, J. B.; Kitagawa, S. *Inorg. Chem.* **2009**, *48*, 7970.

(194) Zhao, B.; Cheng, P.; Dai, Y.; Cheng, C.; Liao-Zheng, D.; Yan, S. P.; Jiang, Z. H.; Wang, G. L. *Angew. Chem. Int. Ed.* **2003**, *42*, 934.

(195) Zhai, B.; Yi, L.; Wang, H. S.; Zhao, B.; Cheng, P.; Liao, D. Z.; Yan, S. P. *Inorg. Chem.* **2006**, *45*, 8471.

(196) Su, Z.; Bai, Z. S.; Fan, J.; Xu, J.; Sun, W. Y. *Cryst. Growth Des.* **2009**, *9*, 5190.

(197) Majeed, Z.; Mondal, K. C.; Kostakis, G. E.; Lan, Y. H.; Anson, C. E.; Powell, A. K. *Chem. Commum.* **2010**, *46*, 2551.

(198) Chen, B. L.; Fronczek, F. R.; Maverick, A. W. *Inorg. Chem.* **2004**, *43*, 8209.

(199) Zuniga, M. F.; Kreutzer, J.; Teng, W.; Ruhlandt-Senge, K. *Inorg. Chem.* **2007**, *46*, 10400.

(200) Garcia-Alvarez, J.; Graham, D. V.; Hevia, E.; Kennedy, A. R.; Mulvey, R. E. *Dalton Trans.* **2008**, 1481.

(201) Yamashita, M.; Suzuki, Y.; Segawa, Y.; Nozaki, K. *J. Am. Chem. Soc.* **2007**, *129*, 9570.

(202) Farrugia, L. J. *J. Appl. Cryst.* **1999**, *32*, 837.